EverWing Design

Ultra-Low Impact 150 Passenger Commercial Aircraft

AE3200 Design Synthesis Final Report

DSE Group 27

Delft University of Technology

TU Delft

This page was intentionally left blank

EverWing Design

Ultra-Low Impact 150 Passenger Commercial Aircraft

by

DSE Group 27

Student name	Student number
Bart Andriessen	5781140
Floris Briedé	5551358
Berit Corben	5772508
Ethan Garrett	5910145
Bence Gecseg	5922704
Roann Kersbergen	5742501
Martijn Kochuijt	5447216
Sander Lammers	5948339
Jelle Ruigrok	5992249
Jose Salazar Lopez	5970334

Tutor/Coordinator:	Dr. ir. J.M.J.F. (Julien) van Campen
Coaches:	Ir. O. Stroosma & Ir. N. Papanikolatos
Project Duration:	April - June, 2026
Faculty:	Faculty of Aerospace Engineering, Delft
Version:	1.0
Style:	TU Delft Report Style, with modifications by Daan Zwaneveld
Cover:	Generated with ChatGPT, using the following prompt; ’Remake this picture (Blender model), make a cloudy sky and colour the aircraft.’

TU Delft

Contents

Contents i

Nomenclature iii

1 Executive Overview 1
- 1.1 Problem and Objective . . . 1
- 1.2 Concept Selection . . . 1
- 1.3 Converged Design . . . 1
- 1.4 Performance . . . 3
- 1.5 Sustainability and End of Life . . . 3
- 1.6 Cost and return on investment . . . 3

2 Project Objective and User Requirements 4
- 2.1 Project Objective . . . 4
- 2.2 User and Product Requirements . . . 4
- 2.3 Market Analysis . . . 4
  - 2.3.1 The Market . . . 4
  - 2.3.2 Stakeholder Identification . . . 5
  - 2.3.3 SWOT Analysis . . . 6
  - 2.3.4 Segmentation Strategies . . . 9
- 2.4 Technical Risk Assessment . . . 10

3 Budget Breakdown and Functional Analysis 15
- 3.1 Budget Breakdown . . . 15
- 3.2 Interface Definition . . . 15
- 3.3 Functional Analysis . . . 16

4 Initial Design 19
- 4.1 Trade-Off . . . 19
- 4.2 Summary of Design . . . 21

5 Performance Analysis 22
- 5.1 Information Dependencies . . . 22
- 5.2 Assumptions . . . 22
- 5.3 Methods . . . 23
  - 5.3.1 Aerodynamic Performance . . . 23
  - 5.3.2 Load Diagram . . . 25
  - 5.3.3 Detailed Weight Estimation . . . 27
  - 5.3.4 Climb Performance . . . 28
  - 5.3.5 Noise Analysis . . . 29
- 5.4 Results . . . 30
  - 5.4.1 Airfoil Selection . . . 30
  - 5.4.2 Lift and Drag Performance . . . 30
  - 5.4.3 Aircraft Loading . . . 31
  - 5.4.4 Weight Results . . . 31
  - 5.4.5 Climb Performance . . . 31

6 Fuselage Design and Payload Storage 33
- 6.1 Information Dependencies . . . 33
- 6.2 Assumptions . . . 33
- 6.3 Fuselage Design . . . 34
  - 6.3.1 Packaging . . . 34
  - 6.3.2 Cabin Design . . . 35
  - 6.3.3 Cross Sectional Design . . . 35
  - 6.3.4 Length Sizing . . . 36
  - 6.3.5 Cockpit Visibility . . . 36
- 6.4 Results . . . 36
- 6.5 Structural Analysis . . . 39
  - 6.5.1 Structural Analysis Methodology 40
  - 6.5.2 Structural Analysis Results . . . 44
  - 6.5.3 Total Mass Estimate . . . 46

7 Wing Subsystem 47
- 7.1 Information Dependencies . . . 47
- 7.2 Assumptions . . . 47
- 7.3 Methods . . . 48
  - 7.3.1 Loading Diagram . . . 48
  - 7.3.2 Wing Planform Design . . . 50
  - 7.3.3 Tail Design . . . 50
  - 7.3.4 Winglet Design . . . 51
  - 7.3.5 Longitudinal Stability . . . 51
- 7.4 Results . . . 52
  - 7.4.1 Design Point Selection Results . 52
  - 7.4.2 Wing Sizing Results . . . 53
  - 7.4.3 Tail Sizing Results . . . 53
  - 7.4.4 Winglet Results . . . 54
  - 7.4.5 Stability Results . . . 54
- 7.5 Wing Box Design: Wing and Tail . . . 55
  - 7.5.1 Load Calculation . . . 56
  - 7.5.2 Material Selection and Mass Calculation . . . 59
  - 7.5.3 Fuselage Connection . . . 59
  - 7.5.4 Results . . . 60

8 Fuel Storage and Propulsion Subsystem 62
- 8.1 Information Dependencies . . . 62
- 8.2 Assumptions . . . 62
- 8.3 Methods . . . 63
  - 8.3.1 Hydrogen Storage . . . 63
  - 8.3.2 Hydrogen Distribution . . . 65
  - 8.3.3 Propulsion System . . . 67
- 8.4 Results . . . 69
  - 8.4.1 Hydrogen Storage . . . 69
  - 8.4.2 Hydrogen Distribution . . . 70
  - 8.4.3 Propulsion System Results . . . 70

9 Control Surface Subsystem 72
- 9.1 Information Dependencies . . . 72
- 9.2 Assumptions . . . 72
- 9.3 Methods . . . 73
  - 9.3.1 Aileron . . . 73
  - 9.3.2 Elevator . . . 74
  - 9.3.3 Ruddervator . . . 74
  - 9.3.4 Critical Design Cases . . . 75
  - 9.3.5 Trim Conditions . . . 77
- 9.4 Results . . . 78
  - 9.4.1 Aileron Results . . . 78
  - 9.4.2 Ruddervator Results . . . 78
  - 9.4.3 Elevator Results . . . 79
  - 9.4.4 Trim Conditions . . . 80

10 Landing Gear Subsystem 81
- 10.1 Information Dependencies . . . 81
- 10.2 Assumptions . . . 81
- 10.3 Methods . . . 82

10.3.1 Force Calculation 82
10.3.2 Wheel Design 83
10.3.3 Shock absorber 83
10.3.4 Brakes design 83
10.3.5 Motor Sizing 84
10.3.6 Undercarriage Positioning 85
10.3.7 Retraction Procedure 86
10.4 Results 89

11 Detailed Aircraft Description 91
11.1 Final Design 91
11.2 Design Configuration Diagrams 91
11.2.1 Hardware / Software Diagram . . 91
11.2.2 Electrical and Data Handling Block Diagram 93

12 Operations Concept 96
12.1 Operations and Logistics Concept Description 96
12.1.1 Ground Operations 96
12.1.2 Flight Operations 97

13 Production Plan and Remanufacturing 99
13.1 Production Plan 99
13.1.1 Material Acquisition 99
13.1.2 Part Manufacturing 99
13.1.3 Final Assembly 99
13.2 Recycling and Re-manufacturing Plan . 101
13.2.1 Aircraft Disassembly 101
13.2.2 Inspection of Parts 101
13.2.3 Re-manufacturing of Parts . . . 101
13.2.4 Recycling of Material 102
13.2.5 Second Hand Market 102

14 Reliability, Availability, Maintainability, and Safety Analysis 103
14.1 Safety Analysis 103
14.2 Maintainability Analysis 106
14.3 Availability Analysis 106
14.4 Reliability Analysis 107
14.4.1 Methods 107
14.4.2 Results 107
14.5 Future Recommendations 107

15 Sustainability Development Strategy 108
15.1 Sustainability Framework 108
15.2 Ex-ante Life Cycle Assessment 108
15.2.1 Goal & Scope 108
15.2.2 Life Cycle Inventory 109
15.2.3 Impact Assessment Results . . . 111
15.2.4 Limitations & Uncertainties . . . 112
15.2.5 Interpretation & Design recommendations 112

16 Future Product Development 113
16.1 Cost Breakdown Structure 113
16.1.1 Production Costs 113
16.1.2 Recycling and Re-manufacturing Costs 114
16.1.3 Direct Operating Costs (DOC) . 115
16.2 Return on Investment 116
16.2.1 Market Volume and Achievable Share 116
16.2.2 Results and Expected Market Price 117
16.3 Post Project Gantt Chart 117

17 Product Compliance 120
17.1 Requirement Compliance 120
17.2 Sensitivity Analysis 122
17.2.1 Fuel Cell Efficiency 122
17.2.2 CFR-PEEK material properties . 123
17.2.3 H_2 production emissions 123

18 Project Methodology Verification and Validation 124
18.1 Aircraft Development Model Functional Flow 124
18.1.1 Code Hierarchy 124
18.2 Verification methods 125
18.2.1 Unit Testing 125
18.2.2 Integrated Testing 125
18.3 Validation Methods 126
18.3.1 Wing Loading 126
18.3.2 OEW Fraction 126
18.3.3 Cruise L/D Ratio 126
18.4 Verification and Validation results 126

19 Conclusion 129

References 130

A Requirements 134
A.1 Stakeholder Requirements 134
A.2 Mission Requirements 134
A.3 System Requirements 134
A.4 Subsystem Requirements 137

B Formulas and Relations 138
B.1 Torenbeek's Procedure 138
B.2 Performance Analysis 139
B.3 Longitudinal stability 139

Nomenclature

Abbreviations

Abbrev.	Definition	Abbrev.	Definition
AEO	All-Engines-Operating	FFD	Functional Flow Diagram
AFP	Automated Fibre Placement	FH	Flight Hour
ALC	Aircraft Leasing Companies	FHA	Functional Hazard Assessment
AM	Aircraft Manufacturer	FL400	Flight Level 400
AMC	Acceptable Means of Compliance	H_2	Hydrogen
AOC	Air Operator Certificate	HC	H_2 Control Unit
AP	Acidification Potential	HEX	Heat Exchanger
APSI	Accessory drives, Powerplant controls, Starting and Ignition systems	HTP	Human Toxicity Potential
APU	Auxiliary Power Unit	IATA	International Air Transport Association
AR	Aspect Ratio	ICAO	International Civil Aviation Organization
ASK	Available Seat-Km	ISA	International Standard Atmosphere
ASME	American Society of Mechanical Engineers	IPS	Integrated Propulsion System
ATC	Air Traffic Control	LCA	Life-cycle assessment
B2F	Buy-to-Fly	LCC	Low Cost Carrier
BH	Block Hours	LHV	Lower Heating Value
BOP	Balance of Plant	LH_2	Liquid Hydrogen
BWB	Blended-Wing Body	LT-PEM	Low-Temperature Proton Exchange Membrane
CASK	Cost per Available Seat-Km	MLG	Main Landing Gear
CCP	Climate Change Potential	MM	Material Manufacturer
CEM	Compressor-Expander Module	MRO	Maintenance, Repair, and Overhaul
CFR-PEEK	Carbon Fibre Reinforced Polyether Ether Ketone	MTOM	Maximum Take-Off Mass
CFRP	Carbon Fibre Reinforced Polymer	MTOW	Maximum Take-Off Weight
CG	Centre of Gravity	NACA	National Advisory Committee for Aeronautics
CHS	Centralised Hydraulic Servo	NASA	National Aeronautics and Space Administration
CO_2	Carbon Dioxide	NLG	Nose Landing Gear
DC	Direct Current	NO_x	Nitrogen Oxides
DOC	Direct Operating Costs	OEI	One-Engine-Inoperative
DSE	Design Synthesis Exercise	OEM	Operating Empty Mass
EASA	European Union Aviation Safety Agency	PCU	Power Control Unit
EHA	Electro-Hydrostatic Actuator	PEM	Proton Exchange Membrane
EII	Environmental Impact Indicators	PIM	Power-Influence Matrix
EMA	Electro-Mechanical Actuator	PSM	Propulsion System Manufacturers
EOL	End-of-Life	PV	Photovoltaic
ES	Energy Supplier	RAM	Rapid Air Movement
FAA	Federal Aviation Administration	ROI	Return on Investment
FAL	Final Assembly Line	RPM	Revolutions per minute
FBS	Functional Breakdown Structure	SAF	Sustainable Aviation Fuel
FCU	Flight Control Unit	SU	Service Unit
		SWOT	Strengths, Weaknesses, Opportunities, Threats

Latin Symbols

Symbol	Definition	Unit	Symbol	Definition	Unit
a_1	Elevator / Aileron Spanwise Start Position	m	P	Roll Rate	deg/s
a_{brake}	Braking Deceleration	m/s^2	P	Design Pressure	Pa
A_{cap}	Spar Cap Area	m^2	P_a	Power Available	W
A_{δ_e}	Elevator Aspect Ratio	–	$P_{a_{SL}}$	Power Available at Sea-Level	W
A_{δ_r}	Ruddervator Aspect Ratio	–	P_{aux}	Auxiliary Electrical Load	W
A_{HEX}	HEX Frontal Area	m^2	$P_{aux,eng}$	Auxiliary Load per Engine	W
a_{LOF}	Lift-Off Deceleration	m/s^2	P_{BOP}	Balance of Plant Power	W
A_{mem}	Membrane Area	m^2	P_{CEM}	CEM Power	W
AR	Aspect Ratio	–	P_{cr}	Cruise Roll Rate	deg/s
A_{ring}	HEX Annular Area	m^2	P_{gross}	Gross Stack Power	W
AR_t	Tail Aspect Ratio	–	P_{land}	Landing Roll Rate	deg/s
AR_w	Wing Aspect Ratio	–	P_M	Load on MLG strut	N
A_s	Stringer Area	m^2	P_N	Load on NLG strut	N
ASM_{FC}	Area Specific Stack Mass	kg/m^2	P_{net}	Net Stack Power	W
b	Aircraft Wing Span	m	P''_{gross}	Gross Power Density	W/m^2
b_1	Wing / Aileron Spanwise Start/End Position	m	P_r	Power Required	W
B_{21}	Radiative Configuration Factor	–	P_{shaft}	Individual Shaft Power	W
b_{fus}	Fuselage Span / Width	m	p_{stack}	Fuel Cell Stack Pressure	Pa
b_t	Tail Span	m	P_{TO}	Take-Off Power	W
b_{tail}	V-Tail Span	m	P_{to}	Take-Off Roll Rate	deg/s
b_w	Half-Wing Span	m	q	Dynamic Pressure	Pa
c	Rate of Climb	m/s	Q_{cond}	Conductive Heat Transfer	W
c_a/c_w	Aileron-to-Wing Chord Ratio	–	q_∞	Freestream Dynamic Pressure	Pa
C_D	Drag Coefficient	–	Q_{rad}	Radiative Heat Transfer	W
C_{D_0}	Zero-Lift Drag Coefficient	–	Q_{waste}	Waste Heat	W
$C_{D,nac}$	Nacelle Drag Coefficient	–	r	Tank Radius	m
C_L	Lift Coefficient	–	R	Shell Radius	m
$C_{l_{\alpha_{fus}}}$	Fuselage Airfoil Lift Curve Slope	1/rad	Re	Reynold's Number	–
$C_{L_{\alpha,r}}$	Ruddervator Lift Curve Slope	1/rad	R_{ferry}	Ferry Range	m
$C_{l_{\alpha_{tail}}}$	Tail Airfoil Lift Curve Slope	1/rad	R_{lost}	Lost Range Equivalent	m
$C_{L_{\alpha,w}}$	Wing Lift Curve Slope	1/rad	R_{nom}	Nominal Range	km
C_{l_β}	Rolling Moment Derivative due to Sideslip	1/rad	ROC	Rate of Climb	m/s
$C_{l_{\beta_{\Lambda,w}}}$	Wing Dihedral/Sweep Contribution to C_{l_β}	1/rad	$(ROC)_{max}$	Maximum Rate of Climb	m/s
$C_{l_{\beta_{tail}}}$	Tail Contribution to C_{l_β}	1/rad	S	Allowable Material Stress	Pa
$C_{l_{\delta_a}}$	Rolling Moment Derivative due to Aileron Deflection	1/rad	SB_{21}	Radiation Exchange Factor	–
$C_{L_{\delta_e}}$	Elevator Lift Derivative	1/rad	s_{brake}	Braking Distance	m
$C_{L_{\delta_r}}$	Ruddervator Lift Derivative	1/rad	S_{δ_e}	Elevator Reference Area	m^2
C_{l_e}	Engine-Out Rolling Moment Coefficient	–	S_{δ_r}	Ruddervator Reference Area	m^2
$C_{L,\max}$	Maximum Lift Coefficient	–	S_{fgs}	Total Fuselage Wetted Area	m^2
C_{l_p}	Roll Damping Derivative	1/rad	S_{fus}	Fuselage Reference Area	m^2
$C_{L,r,tot}$	Total Ruddervator Lift Coefficient	–	SP_{CEM}	CEM Specific Power	kW/kg
$C_{L,w,tot}$	Total Wing Lift Coefficient	–	SP_{fan}	Fan Specific Energy	W/kg
C_m	Pitch Moment Coefficient	–	SP_{HEX}	HEX Specific Power	kW/kg
C_{m_α}	Pitch Moment Stability Derivative	1/rad	SP_i	Specific Power of Component i	kW/kg
$C_{m_{\delta_e}}$	Pitching Moment Derivative due to Elevator Deflection	1/rad	S_{ref}	Reference Wing Area	m^2
$C_{m_{\delta_{rv}}}$	Pitching Moment Derivative due to Ruddervator Deflection	1/rad	S_t	Tail Area	m^2
C_{n_β}	Yawing Moment Derivative due to Sideslip	1/rad	S_v	Vertical Tail Area	m^2
$C_{n_{\delta_{rv}}}$	Yawing Moment Derivative due to Ruddervator Deflection	1/rad	S_w	Wing Area	m^2

Symbol	Definition	Unit	Symbol	Definition	Unit
C_{n_e}	Engine-Out Yawing Moment Coefficient	–	S_{wet}	Wetted Area	m^2
C_{n_r}	Yaw Damping Derivative	1/rad	T	Torque	Nm
c_p	Specific Heat Capacity	J/(kg K)	t	Structural Thickness	m
C_r	Wing Root Chord	m	t_{avail}	Available Time for Retraction	s
C_t	Wing Tip Chord	m	t_{block}	Block Time	hr/yr
c_{tail}	Tail Chord Length	m	t/c	Thickness-to-Chord Ratio	–
c_w	Wing Chord Length	m	t_{cl}	Climbing Time to Cruise Altitude	s
C_{Y_β}	Side Force Derivative due to Sideslip	1/rad	T_e	External Temperature	K
$C_{y_{\beta_{tail}}}$	Tail Airfoil Side Force Slope	1/rad	t_i	Insulation Layer Thickness	m
$C_{Y_{\delta_{rv}}}$	Side Force Derivative due to Ruddervator Deflection	1/rad	T_i	Internal Temperature	K
C_{Y_r}	Side Force Derivative due to Yaw Rate	1/rad	T_{idle}	Idle Thrust	N
D	Drag Force	N	t_{inner}	Inner Tank Shell Thickness	m
D_{core}	Core Duct Diameter	m	t_{outer}	Outer Tank Shell Thickness	m
ΔAR	Extra Aspect Ratio	–	t_r	Wing Root Thickness	m
D_{nac}	Nacelle Diameter (HEX)	m	t_{skin}	Skin Thickness	m
D_{trim}	Trim Drag	N	t_{spar}	Spar Web Thickness	m
$\left(\frac{dW_{LH_2}}{dt}\right)_{TO}$	Fuel Flow at Take-Off	kg/s	T_{stack}	Fuel Cell Stack Temperature	K
e	Oswald Efficiency Factor	–	$T_{t,2}$	Fan Inlet Total Temperature	K
E	Young's Modulus	Pa	T_{TO}	Take-Off Thrust	N
e_1	Elevator Spanwise Start Position	m	U	Steady-State Flight Velocity	m/s
e_2	Elevator Spanwise End Position	m	$u_{e,c}$	Core Nozzle Exit Velocity	m/s
E_{cell}	Cell Voltage	V	V	Velocity / Shear Force	m/s, N
e_{δ_e}	Elevator Oswald Efficiency Factor	–	v	Poisson's Ratio	–
e_{δ_r}	Ruddervator Oswald Efficiency Factor	–	V_{app}	Approach Speed	m/s
E_{OCV}	Open Circuit Voltage	V	V_{cr}	Cruise Speed	m/s
E_{op}	Operating Cell Voltage	V	$V_{crosswind}$	Crosswind Velocity	m/s
E_{th}	Thermoneutral Voltage	V	V_D	Dive Speed	m/s
f	Darcy Friction Factor	–	$V_{D_{min}}$	Velocity at Minimum Drag	m/s
F	Faraday Constant	C/mol	V_{HEX}	HEX Inlet Velocity	m/s
F_{11}	Surface 1 Self-View Factor	–	V_{LO}	Placard Velocity	m/s
F_{12}	View Factor from Surface 1 to 2	–	V_{LOF}	Lift-Off Velocity	m/s
F_{21}	View Factor from Surface 2 to 1	–	V_{max}	Maximum Velocity	m/s
F_{22}	Surface 2 Self-View Factor	–	V_{min}	Minimum Velocity	m/s
f_{CEM}	CEM Power Fraction	–	V_{pax}	Passenger Cabin Volume	m^3
F_{cruise}	Cruise Thrust Requirement	N	$V_{Pr_{min}}$	Velocity at Minimum Power Required	m/s
FF	Form factor	-	V_s	Stall Speed	m/s
F_{req}	Thrust Target Per Engine	N	V_{TD}	Touchdown Velocity	m/s
g	Gravitational Acceleration	m/s^2	V_{TO}	Take-Off Speed	m/s
G	Shear Modulus / Climb Gradient	Pa, –	V_y	Velocity at $(ROC)_{max}$	m/s
h_{cg}	distance ground to CG	m	W_{api}	Air-Conditioning, Pressurisation, Anti- and De-Icing Weight	kg
h_{CR}	Cruise Altitude	m	W_{apsi}	APSI Weight	kg
h_f	Fuselage Maximum Height	m	W_{bc}	Baggage and Cargo Handling Equipment Weight	kg
h_{MLG}	Height of MLG	m	W_{cem}	Compressor-Expander Module Weight	kg
h_{NLG}	Height of NLG	m	W_{els}	Electrical Systems Weight	kg
i	Current Density	A/cm^2	W_{emp}	Empennage Subsystem Weight	kg
i_{AEO}	AEO Cruise Current Density	A/cm^2	W_{eng}	Engine Components Weight	kg
i_{op}	Operating Current Density	A/cm^2	w_f	Fuselage Maximum Width	m

Symbol	Definition	Unit	Symbol	Definition	Unit
I_{xx}	Second Moment of Area	m^4	W_{fan}	Total Fan Weight	kg
I_{yy}	Pitch Mass Moment of Inertia	$kg\,m^2$	W_{fc}	Fuel Cell Stack / Flight-Control Systems Weight	kg
$I_{yy,MLG}$	Pitch Mass Moment of Inertia About MLG	$kg\,m^2$	W_{feq}	Fixed Equipment Weight	kg
I_{zz}	Yaw Mass Moment of Inertia	$kg\,m^2$	W_{fur}	Furnishings Weight	kg
k	Thermal Conductivity	W/mK	W_{fus}	Fuselage Subsystem Weight	kg
K_f	Fuselage Scaling Factor	–	W_{hex}	Heat Exchanger Weight	kg
K_{g_r}	Fuselage Scaling Factor (runway)	–	W_{iae}	Instrumentation, Avionics and Electronics Weight	kg
K_r	Yaw Damper Gain	–	W_{lg}	Landing Gear Subsystem Weight	kg
L	Lift Force	N	W_{LH_2}	Liquid Hydrogen Weight	kg
L_{air}	HEX Air Channel Length	m	W_{misc}	Miscellaneous Weight	kg
l_f	Wing Quarter-Chord to Empennage Quarter-Chord	m	W_{mot}	Electric Motors Weight	kg
$\mathcal{L}_{LFL}$	Landing Field Length	m	W_{MZF}	Maximum Zero-Fuel Weight	kg
l_m	distance MLG to CG	m	W_{nac}	Nacelles Weight	kg
l_n	distance NLG to CG	m	W_{OEW}	Operative Empty Weight	kg
l_{pax}	Passenger Cabin Length	m	W_{ox}	Oxygen System Weight	kg
$\mathcal{L}_{TO}$	Take-Off Field Length	m	W/P	Power Loading	N/W
M	Bending Moment	Nm	W_{paint}	Paint Weight	kg
m	Aircraft Mass	kg	W_{pwt}	Powertrain Subsystem Weight	kg
MAC	Mean Aerodynamic Chord	m	W_{rib}	Rib Weight	kg
m_{CEM}	CEM Mass	kg	W/S	Wing Loading	N/m^2
$\dot{m}_{core}$	Core Air Mass Flow Rate	kg/s	W_{skin}	Skin Weight	kg
M_{cr}	Cruise Mach Number	–	W_{spar}	Spar Weight	kg
M_f	Material Performance Factor	–	$W_{stringer}$	Stringer Weight	kg
$\dot{m}_{fan}$	Fan Mass Flow Rate	kg/s	W_{tail}	Tail Weight	kg
m_{FC}	Stack Mass	kg	W_{tnk}	Tanks Weight	kg
$\dot{m}_{H_2}$	H_2 Mass Flow Per Engine	g/s	W_{TO}	Take-Off Weight	N
$\dot{m}_{H_2,total}$	Total Hydrogen Mass Flow Rate	kg/s	$W_{v\text{-}tail}$	V-Tail Weight	kg
m_{HEX}	HEX Mass	kg	W_w	Wing Subsystem Weight	kg
M_{HEX}	HEX Entrance Mach Number	–	W_{wing}	Wing Weight	kg
$\dot{m}_{HEX}$	HEX Air Mass Flow Rate	kg/s	$W_{wingbox}$	Wing Box Weight	kg
m_{IPS}	IPS Mass	kg	x	Longitudinal Position	m
MM_{H_2}	Hydrogen Molar Mass	kg/mol	$x_{ac,tail}$	Tail Aerodynamic Centre Location	m
m_{motor}	Motor Mass	kg	x_{cg}	Centre of Gravity Location	m
m_{MTO}	Maximum Take-Off Mass	kg	X_{cg}	Centre of Gravity Location	m
m_p	Pipe Mass	kg	$x_{cg,fwd}$	Forward Centre of Gravity Location	m
m_t	Tank Mass	kg	X_{LEMAC}	Leading Edge MAC Location	m
n	Load Factor	–	x_{MLG}	Longitudinal position of MLG	m
N_β	Yawing Moment due to Sideslip	s^{-2}	X_n	Neutral Point Location	m
n_{cells}	Cell Count	–	x_{NLG}	Longitudinal position of NLG	m
N_e	Number of Engines	–	y	Lateral Position	m
$N_{M_{struts}}$	Number of MLG struts	-	Y	Material Coefficient	–
N_{MW}	Number of MLG wheels	-	Y_β	Side Force due to Sideslip	m/s^2
N_{NW}	Number of NLG wheels	-	y_e	Engine Spanwise Position	m
N_{pax}	Number of Passengers	–	y_{mac}	Spanwise MAC Position	m
N_r	Yawing Moment due to Yaw Rate	s^{-1}	y_{MLG}	MLG Lateral Position	m
n_{sold}	Number of Aircraft Sold	–	y_{NLG}	NLG Lateral Position	m
n_{ult}	Ultimate Load Factor	–	Y_r	Side Force due to	

Greek Symbols

Symbol	Definition	Unit	Symbol	Definition	Unit
α	Angle of Attack	rad	λ	Taper Ratio	–
α_i	Ruddervator Incidence Angle	rad	λ_t	Tail Taper Ratio	–
α_p	Power Lapse Factor	–	$\Lambda_{1/4}$	Quarter-Chord Sweep Angle	deg
$\alpha_{0,r}$	Ruddervator Zero-Lift Angle of Attack	rad	$\Lambda_{1/2}$	Wing Half-Chord Sweep Angle	deg
$\alpha_{0,w}$	Wing Zero-Lift Angle of Attack	rad	Λ_{LE}	Leading Edge Sweep Angle	deg
β	Sideslip Angle	deg	$\Lambda_{v,c/2}$	Vertical Tail Half-Chord Sweep Angle	deg
$\beta_{crosswind}$	Crosswind Sideslip Angle	deg	μ	Absolute Viscosity	Pa s
δ	HEX Inclination Angle	deg	μ_{brake}	Dynamic Friction Coefficient of Brakes	–
δ_a	Aileron Deflection Angle	deg	μ_{roll}	Dynamic Friction Coefficient of Surface	–
$\delta_{a,crosswind}$	Aileron Deflection (Crosswind)	deg	ν	Poisson's Ratio	–
$\delta_{a,EIO,\beta=0}$	Aileron Deflection (Engine Out, $\beta = 0$)	deg	ω_n	Dutch Roll Natural Frequency	rad/s
$\delta_{a,max}$	Maximum Aileron Deflection	deg	ϕ	V-Tail Inclination w.r.t. the Vertical	deg
δ_e	Elevator Deflection Angle	deg	π_f	Fan Pressure Ratio	–
δ_r	Rudder Deflection Angle	deg	π_x	HEX Stagnation Pressure Ratio	–
δ_{rv}	Ruddervator Deflection Angle	deg	Ψ	Turnover Angle	deg
$\delta_{rv,crosswind}$	Ruddervator Deflection (Crosswind)	deg	ρ	Air / Material Density	kg/m^3
$\delta_{rv,EIO,\beta=0}$	Ruddervator Deflection (Engine Out, $\beta = 0$)	deg	ρ_{HEX}	HEX Inlet Density	kg/m^3
ΔE_{act}	Activation Voltage Loss	V	σ	Normal Stress	Pa
ΔE_{conc}	Concentration Voltage Loss	V	σ_{cr}	Critical Buckling Stress	Pa
ΔE_{deg}	Fuel Cell Degradation Voltage Loss	V	σ_y	Yield Stress	Pa
ΔE_{ohm}	Ohmic Voltage Loss	V	σ_{yield}	Material Yield Stress	Pa
Δh_{vap}	Latent Heat of Vaporisation	J/kg	τ	Shear Stress	Pa
ΔP	Pressure Difference	Pa	τ_a	Aileron Effectiveness Factor	–
ΔT	Temperature Difference	K	τ_e	Elevator Effectiveness Factor	–
ΔT_p	Lost Engine Thrust	N	τ_r	Rudder Effectiveness Factor	–
$\ddot{\theta}$	Pitch Angular Acceleration	deg/s^2	$\tau_{rv,e}$	Ruddervator Pitch Effectiveness Factor	–
$\ddot{\theta}_{to}$	Pitch Angular Acceleration at Take-Off	deg/s^2	$\tau_{rv,r}$	Ruddervator Yaw Effectiveness Factor	–
ϵ	Radiation Emissivity	–	θ	Wing Twist Angle	deg
η_{elec}	Electrical Efficiency	–	φ	Bank Angle	deg
η_{fan}	Fan Efficiency	–	ζ	Dutch Roll Damping Ratio	–
η_{FC}	Fuel Cell Efficiency	–	ζ_{BOP}	Balance-of-Plant Power Fraction	–
η_p	Propeller Efficiency	–	$\frac{d\varepsilon}{d\alpha}$	Downwash Gradient	–
η_{sys}	System Efficiency	–	Γ	Wing Dihedral Angle	deg
Γ_t	Tail Dihedral Angle	deg	Γ_{tail}	V-Tail Dihedral Angle	deg
γ	Ratio of Specific Heats	–			

1. Executive Overview

1.1. Problem and Objective

Commercial aviation faces two major challenges regarding sustainability. The first is the climate and resource impact during its operation: in-flight combustion releases CO_2 and NO_x along every route, polluting the atmosphere. The second is the underlying linear supply chain: building airframes from virgin materials that are largely scrapped or downcycled at retirement.

DSE Group 27, at the Faculty of Aerospace Engineering of Delft University of Technology, responded to this problem by designing a 150-passenger commercial transport vehicle that removes in-flight CO_2 and NO_x emissions and is built to be remanufactured and recycled at end of life. The project objective was to design a commercial 150-passenger, 4000 km range, net-zero-emission aircraft for 2050 service entry with full end-of-life upcycling, completed in ten weeks by ten students. Sustainability and circularity were treated as the design objective, end-of-life recovery and low-impact operation was carried as a primary driver from the concept trade-off through to the lifecycle assessment.

The resulting design is an blended wing body (BWB) powered by liquid-hydrogen fuel cells. It cruises at Mach 0.80 and FL400 over a 4000 km design range, is sized for a 30-year service life, and targets entry into service in 2050. The top-level mission and economic targets the design was held to are summarised in Table 1.1.

Table 1.1: Top-level mission and economic targets.

Parameter	Target value
Passengers and cabin crew	150 passengers + 3 cabin crew
Design range	4000 km
Cruise	Mach 0.80
Service life	30 years
Entry into service	2050
Acquisition cost	FY 2026 EUR 150M
Operating cost	FY 2026 EUR 0.050 per seat-km

1.2. Concept Selection

Five strawman configurations were carried into a structured trade-off: a box wing, a blended wing body, a flying wing, a dual wing, and a conventional tube-and-wing reference. Each was scored against six criteria that condensed the most important stakeholder and mission requirements into design drivers: re-manufacturability and recyclability (20%), propulsive performance (25%), cost (15%), aerodynamic performance (15%), mass performance (15%), and design schedule risk (10%). The high weighting on re-manufacturability reflects the project objective, which placed circularity ahead of raw performance.

The blended wing body with a liquid hydrogen fuel cell propulsion system scored highest, as shown in Table 1.2. Benefits of this planform include its lift-producing centrebody and high lift-to-drag ratio, and the volumetric efficiency of its fuselage for liquid-hydrogen storage. As for the propulsion system, its zero in-flight CO_2 and NO_x emissions and low required fuel mass drove the design choice.

Table 1.2: Concept trade-off result

Configuration	Weighted score
Blended wing body	3.90
Conventional	3.80
Box wing	3.65
Dual wing	3.30
Flying wing	3.20

A sensitivity analysis confirmed the blended wing body as the robust top choice, holding its lead under reasonable variation of the criteria weights. The conventional utilising sustainable aviation fuel configuration ranked second and remains the lower-risk fallback. The final score of each concept is presented in Table 1.2

1.3. Converged Design

Geometry

The wing and powertrain were sized from a design point at a wing loading of 1875 N/m^2 and a power loading of 0.0504 N/W. This yielded a reference area of 315 m^2, a total wing area of 80.3 m^2, and a total span of 35.7

m at an aspect ratio of 4.2. The centrebody, housing the cabin is 21.4 m long. The centrebody section uses an SC(2)-0518 airfoil profile and the outer wing an RAE 2822. Both of them are supercritical for increased drag performance. The aircraft was named Everwing to highlight its circular design philosophy. A current, to-scale model is shown on Figure 1.1.

Figure 1.1: Everwing

Propulsion

Thrust is produced by four nacelle-mounted integrated propulsion systems (IPS), each combining a low-temperature PEM fuel-cell stack, a heat exchanger, a compressor-expander module, an electric motor, and a ducted fan. That installation volume drove the engine count down from six to four, compared to the previous iteration. This also had an added benefit for fuel mass, as the more they are oversized for the requirement point, the more efficient they become at the lower demand operational point. Four units combined deliver a rated shaft power of 18,4 kW installed, at an IPS mass of 7740 kg total. Since the one engine inoperative rating oversizes the system relative to cruise, the all-engines-operating (AEO) cruise point each unit runs at roughly half throttle and the system efficiency rises to 0.43, compared to 0.36 - 0.38[1].

Aerodynamics

The clean configuration achieves a zero-lift drag coefficient of 0.00783 and an Oswald efficiency of 0.86, giving a cruise drag coefficient of 0.0122 at a cruise lift coefficient of 0.222 and a lift-to-drag ratio of 18.2. Cruise is trimmed at $0.8°$ angle of attack. As the blended wing body design is able to provide at sufficient lift in clean configuration even at low angle of attack, no high-lift devices are required, which removes a major approach-noise source and simplifies the wing layout.

Structures and materials

The airframe is built principally from carbon-fibre-reinforced PEEK (CFR-PEEK) for skin, stringers, and spar caps, with aluminium-lithium alloys for ribs and spar webs and titanium alloys at high-load fittings. These materials were chosen for their recovery routes and their specific strength. The structural assessment confirmed that the highest loads concentrate at the wing root and along the body centreline, which sets the load paths for the wing box and fuselage.

Stability, control, and actuation

Directional and longitudinal control are provided by a V-tail, which emerged from the empennage trade off as the configuration best matched to the BWB centrebody flow and aft structure. The two surfaces are inclined $20°$ from the vertical and have a combined area of 27.2 m^2, with ruddervators providing combined pitch and yaw authority. Consistent with the electric architecture, the elevons and ruddervators use electromechanical actuators and the wheel brakes are electromagnetic, removing centralised hydraulics. The undercarriage is a retractable tricycle layout on two main struts carrying four main wheels, with electric retraction.

Cabin and storage

The cabin spans the full centrebody width and seats 150 passengers across three compartments. At the sides, and aft of the cabin, liquid hydrogen is stored in three cylindrical tanks, summing to a usable volume of 59.4m^3.

1.4. Performance

The design carries the required 150 passengers over the 4000 km design range at Mach 0.80. Regarding aerodynamic efficiency, the configuration holds a cruise lift-to-drag ratio of 18.2. The mission burns about 3031 kg of liquid hydrogen, close to 5% of MTOM.

On the ground the design meets the 2100 m take-off field length requirement at MTOM under ISA conditions and is brought to rest within a conservative 508 m braking distance using electromagnetic brakes. In the climb it reaches a sea-level rate of climb of 19.6 m/s and attains FL400 in 12.1 minutes at maximum power, with a service ceiling of 14.6 km, well above the cruise altitude.

The noise requirement is to be no louder than the reference A320, set at a maximum approach level of 92.0 EPNdB, which the design is expected to meet with margin. Removing combustion eliminates core and turbine noise, the high stall angle removes the need for high-lift devices and with them a major approach-noise source. The blended wing body planform shields the engine inlet and exhaust, with scale-model tests of comparable configurations showing 20 to 25 dB of forward-sector reduction[2].

Regarding compliance, the design meets most of its top-level requirements, however, the net-zero operation could not be met. This is due to the contrail forming effect of the released water vapour.

1.5. Sustainability and End of Life

A lifecycle assessment quantified the climate change potential (CCP) across raw-material extraction, manufacturing, operations, maintenance, and end of life, with the human toxicity and acidification potentials assessed qualitatively. Over a 30-year service life of 55,500 flights the total lifecycle CCP is approximately 212,000 t CO_2-eq. Distributed across 150 passengers and the 4000 km design range, this is 6.43 g CO_2-eq per passenger-kilometre, an 87% reduction against the roughly 50 g CO_2-eq per passenger-kilometre projected for the A320neo in 2050 [3].

The aircraft itself emits zero CO_2 and zero NO_x in flight as there is no combustion, however the contrails produced by the released water vapour act as secondary greenhouse gases. As Table 1.3 shows, the dominant lifecycle burden is therefore not the aircraft but the upstream supply chain that produces its green hydrogen, which accounts for 99.1% of the total. As a result, reducing the emissions of hydrogen production would have the biggest effect on this design's environmental impact. End of life solution is a primary design driver, and its contribution to the balance is negative. Following the recovery plan, CFR-PEEK is reclaimed by solvolysis, the aluminium-lithium structure and tanks are recovered as alloy stock, and the titanium fittings are recycled, together avoiding 270.2 t CO_2-eq of virgin-material production.

Table 1.3: Lifecycle climate change potential (CCP) by phase.

Lifecycle phase	CCP (t CO_2-eq)	Share (%)
Raw material extraction	951	0.45
Manufacturing / assembly	383.3	0.18
Operations (upstream H_2)	0 (210,289.5)	0 (99.1)
Maintenance and repair	945.7	0.45
End of life	-270.2	-0.13
Total	$\approx$ **212,299.3**	**100**

1.6. Cost and return on investment

Development was estimated at 9.76 billion FY 2026 EUR, and a bottom-up estimation of the production cost is about 64.45M EUR per aircraft including a 20% margin. Against a conservative market of 47,000 narrow-body aircraft over a 2050 to 2075 production window and a 2% share, 940 units are expected to sell. Benchmarking the price against a 2026 A320neo and adding a premium for the design's sustainability advantage gives a market price of 105M EUR, which returns a 40.3% return on investment and sits well below the 150M EUR acquisition ceiling; at that ceiling the return would be 100.4%. On the operating side the direct operating cost works out to 0.030 EUR per seat-kilometre including a 20% margin, within the 0.050 EUR per seat-kilometre requirement.

2. Project Objective and User Requirements

2.1. Project Objective

The mission need statement is formatted as follows: *'Provide a sustainable medium-range aircraft entering service in 2050 with net-zero emissions and complete end-of-life upcycling capability.'* The resulting project objective statement is: *'Design a commercial 150-passenger, 4000 km range, net-zero emission aircraft for 2050 service entry with full end-of-life upcycling, in 10 weeks by 10 students.'*

2.2. User and Product Requirements

It has been opted to centralise the location of all requirements in Appendix A and reference to them during the report. Table 2.1 provides information to the types of product requirements that have been identified.

Table 2.1: Requirement Definition and Location

Requirement Type	Requirement Explanation	Requirement Location
Stakeholder Requirements	Stakeholder requirements represent the desires of the team's customers and constraints from stakeholders.	section A.1
Mission Requirements	Mission requirements represent the capabilities that the product must achieve to satisfy stakeholders.	section A.2
System Requirements	Translate mission requirements into measurable aircraft-level performance targets.	section A.3
Subsystem Requirements	Define detailed requirements for individual aircraft subsystems such as aerodynamics, structures, and propulsion.	section A.4

2.3. Market Analysis

In order to identify the market need for the EverWing mission, a market analysis will be conducted. The market for short-to-medium range aircraft is a highly competitive market driven by cost efficiency and operational flexibility. Regulators are increasingly emphasising environmental awareness and the driving demand for low-emission air travel. In response, the proposed fully recyclable, zero net-emission aircraft aims to meet future market needs while remaining economically viable. This chapter therefore evaluates stakeholders, market conditions, and external factors to support the development of design requirements.

2.3.1. The Market

As of September 2025, the Airbus A320 family has been the most sold airliner in the world, with more than 12,250 aircraft sales,[1] exceeding the Boeing 737 family, previously ranked as the best-selling commercial aircraft family. This indicates a high demand for aircraft families comparable to the A320 and Boeing 737.

These aircraft families are widely used by low-cost carriers (LCCs), such as Ryanair, Southwest, and EasyJet, as well as by legacy carriers, including Delta, American Airlines, and China Eastern.[2,3] In legacy airline operations, these aircraft are typically deployed on short- to medium-haul routes and often serve as feeder aircraft for long-haul, intercontinental networks. Seats available on an aircraft depend on the type and seat configuration. On the A320 family the range is typically from 140 to 244 seats,[4] whilst the B737 family has a range from 146 to 220 seats.[5]

The number of flights per operating day heavily depends on the routes and length flown. The operating life span of the aircraft can be over 30 years.[6] Overall, these figures provide a clear indication of the competitive and operational environment in which a new aircraft in this category must perform.

[1] URL https://simpleflying.com/a320-beats-737-best-selling-airliner/ [cited 28 April 2026]
[2] URL https://flightsmilesandpoints.com/airline-fleets/largest-airbus-a320-family-operators/ [cited 28 April 2026]
[3] URL https://simpleflying.com/5-airlines-largest-boeing-737-fleets/ [cited 28 April 2026]
[4] URL https://www.aircraft.airbus.com/en/aircraft/a320-family [cited 28 April 2026]
[5] URL https://www.boeing.com/commercial/737ng[cited 28 April 2026]
[6] URL https://simpleflying.com/up-to-36-years-the-worlds-10-oldest-active-airbus-a320s/[cited 28 April 2026]

2.3.2. Stakeholder Identification

Stakeholders need to be identified in order to accurately asses market prioritisation. The most important stakeholders are listed in Table 2.2. Each stakeholder description briefly outlines their role in either the manufacturing, regulatory or operational processes as well as the influence they have in these these areas.

Table 2.2: Stakeholder identification

Stakeholders	Description
EASA	The European Union Aviation Safety Agency is responsible for civil aviation safety in the European Union. EASA performs certification, regulation and standardisation on new aircraft. New aircraft design needs to cohere to their safety regulations in order to be approved for operations [4].
FAA	The Federal Aviation Administration is a U.S. government agency that regulates all civil aviation in the U.S. National Airspace System. New aircraft design needs to comply with FAA regulations if they are to be certified and operated in the U.S. airspace.
ICAO	The ICAO is a specialized agency of the United Nations responsible for establishing global standards for civil aviation. ICAO develops international Standards and Recommended Practices (SARPs) that define safety, security, and operational requirements for aviation. Aircraft design and operation must comply with these standards through national regulatory authorities, ensuring global harmonization of aviation safety [5].
IATA	The International Air Transport Association is the trade association representing the world's airlines. Through its IATA Operational Safety Audit (IOSA) program, it standardizes criteria for evaluating the operational management and control systems of airlines. This provides guidance for structuring airline operations in accordance with industry practices and reflects common operational requirements across the airline industry [6].
Airlines	Airlines expect any new aircraft to meet defined safety standards. They are also responsible for operational fleet planning and therefore require appropriate capacities and performance from these aircraft.
Airports	Airport infrastructure and operations define constraints on the AC size, weight and noise levels. Airports are responsible for integrating new technologies in AC design for maintenance and operations.
Passengers	Passengers want to travel from A to B and expect a certain level of comfort, which should be incorporated in the development of a new aircraft. Passengers increasingly expect new AC to be more oriented towards sustainability and environmental impact [7].
General population	While the production and operation of aircraft do not directly effects the general population, their needs have to be considered as well. Their health have to be taken into account which has an effect on allowable emissions. Furthermore a good public perception on a model can increase the extent to which airlines can employ them to their full capacity, helping to minimize utilization risk.
Aircraft leasing companies (ALCs)	The designed aircraft will be an Short to Medium Range (SMR) aircraft to be potentially used by LCC airlines such as EasyJet and AirAsia and IndiGo. ALCs are interested in the operating costs as well as the depreciation costs of aircraft, influencing their design.
Propulsion system manufacturers (PSMs)	Propulsion system manufacturers are of high interest in the design of a sustainable net-zero emissions aircraft. A design based upon zero emissions creates major demand for new propulsion technologies, giving manufacturers the opportunity to secure long-term supply contracts.
Aircraft manufacturers (AMs)	Aircraft manufacturers have a strong interest in fully recyclable aircraft designs, as a 100% recyclability design creates significant opportunities for securing long-term supply contracts.
Investors	Investors are key stakeholders in the design of a fully recyclable, net-zero emissions aircraft. They are responsible for the funding the development of the AC, whilst focusing on risk and profitability.
AM shareholders	Aircraft manufacturer shareholders have influence in the development of a fully recyclable, net-zero-emission aircraft. They are responsible for influencing the funding of the programme, while focusing on financial risk, return on investment, and overall profitability.

Tutor	The tutor commissions the project and defines the top-level requirements, providing guidance in the scope and direction of the design. The tutor's assessments and feedback at key review milestones directly influence design decisions throughout the exercise.
TU Delft Faculty of Aerospace Engineering	The Faculty of Aerospace Engineering hosts the Design Synthesis Exercise and has an interest in the technical quality of the project, as student work contributes to its academic reputation.
Energy suppliers (ES)	Fuel costs are one of the largest expenses in aircraft operations. Energy suppliers determine the fuel costs trough supply and demand, this determines the financial feasibility of the aircraft operating costs.
Material manufacturers (MM)	Material costs are of high importance during the manufacturing process. Material manufacturers determine the availability and quality, which directly affects production costs, product performance, and overall profitability of the final product.

Up to approximately two hundred stakeholders can be involved during the design process of a new aircraft model [8]. Some stakeholders have more direct influence on the design than others. Stakeholders with negligible influence are therefore omitted. A multitude of stakeholders can be represented by one organisation, for example, the ground crew and cabin crew can be represented by the airports and airlines respectively. This avoids including stakeholders that would normally have overlapping roles or limited direct influence on high-level design decisions, this keeps the stakeholder identification manageable.

Stakeholder/Interest-Influence Map

Each aforementioned stakeholder and their influence can be mapped on a Power-Interest Matrix (PIM). This map shows which stakeholders need to be satisfied, which stakeholders that need to stay informed and the key stakeholders that need to be managed closely, the PIM is shown in Figure 2.1.

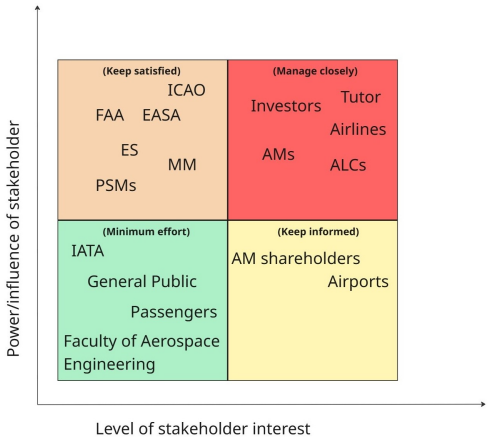

Figure 2.1: Power-Interest matrix

As illustrated by the PIM, all regulatory stakeholders, such as such as EASA, ICAO and the FAA fall within the keep satisfied category. Without complying to their regulations, the aircraft will not be granted an air-worthiness certification. Key stakeholders such as the investors, AMs and buyers (Airlines and ALCs) fall within the manage closely region. Their high level of influence determines the requirements and the overall feasibility of the project. Collaboration with AMs is in particularly necessary due to their certification, manufacturing capabilities, and access to existing aerospace supply chains.

2.3.3. SWOT Analysis

Part of the market analysis is a SWOT analysis. This provides an oversight in the market standings in which the fully recyclable and zero net emitting aircraft will be competing in. This analysis is mainly focused towards the year 2050, as this is the year in which the aircraft is intended to go into service. It evaluates the strengths and weaknesses of the concept alongside the opportunities and threats within the evolving aviation sector. This approach helps to assess the aircraft's potential competitiveness, identify risks and shows areas where strategic advantages can be developed in a future market.

SWOT Diagram

The SWOT (Strengths, Weaknesses, Opportunities, Threats) diagram in Figure 2.2 presents an evaluation of the market position of the proposed zero net-emission, fully recyclable aircraft in the projected 2050 aviation market. The analysis considers both internal factors related to the aircraft design and external factors which come from expected technological developments, future regulations and the competitive market.

From the SWOT analysis it can be concluded that the conceptual design's market strengths lie in its future-proof design. Airliners must comply with evolving regulations to obtain and maintain their Air Operator Certificate

[7] URL `https://www.faa.gov/aircraft/air_cert/aw_cert/regs_policy` [cited 24 April 2026]

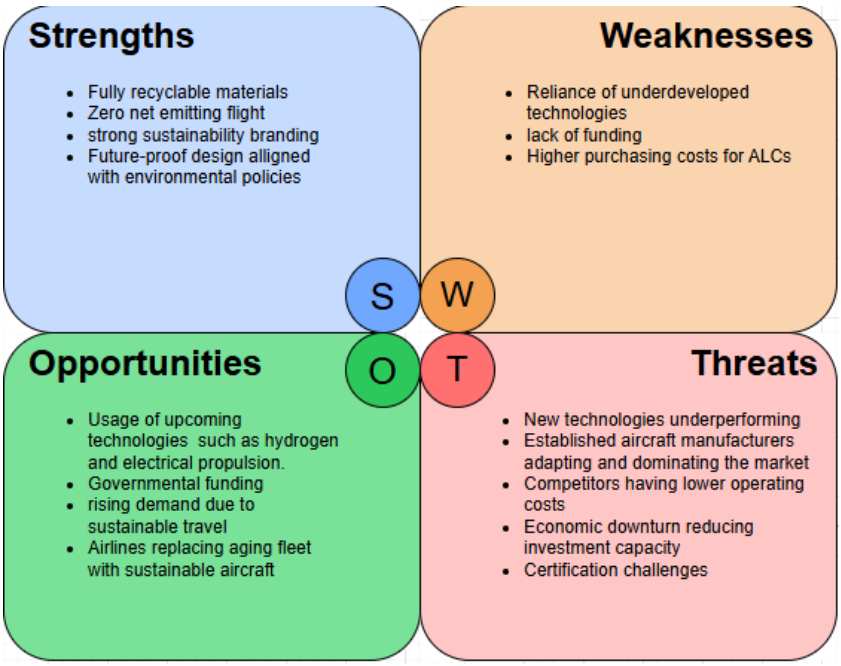

Figure 2.2: SWOT analysis of the zero net-emission, fully recyclable aircraft (2050)

(AOC). If regulators such as the FAA or EASA mandate more sustainable flight operations, designs that include recyclability, lower emissions or alternative propulsion technologies will have a significant competitive advantage. This makes the concept both compliant with current standards, but also adaptable to predicted stricter environmental regulations, which reduces the risk of costly redesigns or operational limitations.

Competitiveness of technologies

This section evaluates the proposed aircraft concepts relative to alternative technologies. An initial identification of all future aviation technologies expected to be available on the market by 2050 is shown in Table 2.3. This list can be split up into the categories propulsion, aerodynamics & structures, and materials [9].

Table 2.3: Overview of future aviation technologies expected by 2050

Aviation Technology	Description
Propulsion	**Sustainable Aviation Fuel (SAF):** SAFs are drop-in fuels compatible with existing gas turbine engines, requiring minimal aircraft modification. Although 100% SAF operation is expected by 2030 [9], the overall environmental benefit depends on the feedstock used and the production process. **Hydrogen combustion:** Hydrogen used in modified gas turbines can produce zero CO_2 emissions in flight. Challenges include cryogenic storage with a low gravimetric index and propulsion system/aircraft redesign. **Hydrogen fuel cells:** Fuel cells convert hydrogen into electricity, powering electric propulsion systems. They have a high efficiency and zero emissions, but limited by power density and thermal management requirements. **Battery-electric propulsion:** Fully electric aircraft will be enabled by improvements in battery energy density (potentially $>$350 Wh/kg by 2040). Primarily viable for short-range and regional aviation. **Ammonia Fuel Cell:** Using a Direct-Ammonia Solid Oxide Fuel Cell (DC-SOFC), converting the energy to electricity to drive an electric motor. Offers higher volumetric density than hydrogen, and easier storage at a cost of efficiency and mass energy density.
Aerodynamics & Structures	**Ultra-high aspect ratio wings:** Longer, thinner wings reduce induced drag and improve lift-to-drag ratio, increasing efficiency. **Blended Wing Body:** Integrates fuselage and wing into a single lifting surface, reducing drag and structural weight while increasing internal volume.

	Truss-braced wing: Uses structural supports to enable extremely long wings, resulting in efficiency improvements. **Multifunctional structures:** Structural components that also perform secondary functions such as fuel storage or heat management, reducing system weight.
Materials	**Advanced Aluminium alloys:** Aluminium-lithium alloys provide high strength-to-weight ratios and good fatigue resistance for aerospace applications. Aluminium alloys are highly recyclable, though with higher cost and processing complexity [10]. **Thermoplastic composites:** Thermoplastic composites are lightweight structures with high toughness and damage resistance. These properties allow for faster manufacturing and potential recyclability through remelting. Remelting does require high processing temperatures, which bring high costs [11]. **Carbon Fibre Reinforced Polymers (CRFPs):** CRFPs have a high strength to weight ratio and stiffness. They are widely used in modern aircraft to reduce weight and fuel consumption, though they face challenges in cost, damage detection, and recycling complexity. **Natural-Fibre Reinforced Composites (NFRCs):** A lightweight, renewable material class with a high strength-to-weight ratio for aerospace applications. They can reduce aircraft weight, fuel consumption, and emissions, improving efficiency, though recycling remains costly and complex [12].

Market Trend Analysis

A key consideration for the conceptual design is zero net emissions and full recyclability. Future aviation technologies of importance are therefore propulsion techniques and material selection. The upcoming technologies are therefore compared on different metrics as shown in Table 2.4 and Table 2.5.

Table 2.4 highlights the key financial and technical information needed to analyse the feasibility of different fuel choices.

Table 2.4: Propulsion comparison estimates 2050

Propulsion System	Energy Source	Price [USD/kg]	Energy Density [kWh/kg]	Price [USD/kWh]
Drop-in fuel	SAF	1.75 [13]	12.0 [14]	0.146
Hydrogen Combustion	Green Liquid H_2	4.0 [15, 16]	39.7 [17]	0.101
Hydrogen Fuel Cell	Green Gaseous H_2	2.7 [16]	39.7 [17]	0.068
Battery-Electric	Electricity	-	-	0.208 [8]
Ammonia Fuel Cell	Green Liquid NH_3	0.6-1.2 [18]	5.12 [19]	0.117

Materials are evaluated based on two metrics: the recovery percentage and the energy demand per kilogram. The recovery percentage indicates what proportion of a material can be recycled, whilst the energy demand reflects how much energy is required to recycle one kilogram of that material.

Table 2.5: Materials comparison estimates 2050

Material	Recovery % [11]	Energy Demand per kg [MJ/kg]
Aluminum alloys	98% [20]	5-10 [21]
Thermoplastic Composites	90–95% [9] [10]	15–30 [22]
CFRP	20–40% (mechanical), 90–95% (fibre) [23, 24]	40–260 [25]
NFRC	70–90% [12, 26]	10–25 [26]

[8] Bergaentzlé, C., "Introduction to Marketing 2" Technical University of Denmark, Kongens Lyngby, Denmark, 2025

[9] URL https://www.statista.com/statistics/630136/projection-of-electricity-prices-in-the-us/ [cited 24 April 2026]

[10] URL https://fip.utwente.nl/article/sixteenth-issue/sixteenth-issue-recycle-and-repair-of-thermoplastic-composite/[cited 24 April 2026]

[11] Recovery percentages for composite materials are highly dependant on the recycling method and are based on literature-reported ranges for fibre recovery, mechanical recycling efficiency, or material reprocessability.

2.3.4. Segmentation Strategies

To make an optimal entry into the market, it must understood how the market operates - what are the main forces driving it and its main threats. These will be derived with three concrete segmentation strategies: a PESTEL Analysis, which serves to scan external macro environmental factors, Porter's 5 Forces, to understand market competitiveness.[8]

PESTEL Analysis

Performing a PESTEL analysis enables identification of external macro environmental factors affecting the industry. Each letter of 'PESTEL' stands for a different category inside the factors affecting the industry (Political, Economic, Social, Technological, Environmental, Legal). A framework adapted to the aerospace industry, for a low-impact commercial aircraft, is shown in Table 2.6.

Table 2.6: PESTEL Aviation Industry

Factor	Description
Political	Strong pressure from the government to decarbonise the aviation industry. Carbon taxes from authorities & governments. Potential geopolitical issues that can affect fuel/component supply chains. Subsidies for sustainable alternatives in aviation.
Economic	Green propulsion leads to high development costs. SAF or alternative fuels have higher uncertainty in energy prices compared to traditional fossil fuels. There is a huge demand for aircraft that have low operational costs.
Social	Increasing public pressure to reduce aviation emissions — society becomes increasingly reluctant to take part in environmentally-harming transport. Passengers expect the service to be comfortable, affordable, and safe. The company shall maintain a transparent and clear image; airline accidents related to company carelessness may severely affect their business.
Technological	To maintain competitiveness and a favourable market position, companies must invest in new technology and solutions. Increased automation in the manufacturing process. Increasing use of composites complicates the recycling process.
Environmental	There is a need to improve aircraft systems and flights to decrease harmful emissions, as this poses a massive concern for the future. Push for circular economy, with increasing interest in remanufacturing. Continuous search for alternatives to fossil fuels. Long-term objective to achieve a zero-emission industry. Large amounts of aircraft materials end up at landfills or are downcycled.[12]
Legal	Most countries have their own legal basis concerning aircraft service, helping to protect the environment and ensure passenger safety. Companies must adhere to these to avoid legal proceedings. Designs must be certifiable (CS-25).

[12] URL https://www.brusselstimes.com/2112472/eu-project-targets-end-of-life-aircraft-materials-with-circular-economy-overhaul [cited 8 May 2026]

Porter's 5 Forces

The second strategy applied to visualise the market in which the product will be introduced, is Michael Porter's model. It is designed to assess the degree of competitive intensity and to help understand the underlying drivers of profitability and overall industry attractiveness. [8] The model consists of 5 'forces' which are categories that shape the competitive aspect of the industry. Figure 2.3 shows how these categories are organised. Each of these categories will be ranked in terms of its level of intensity and impact on the market (low, medium or high).

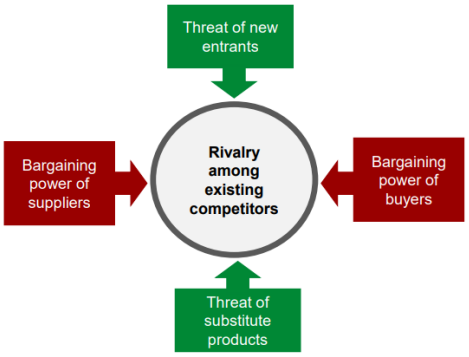

Figure 2.3: Porter's 5 Forces Schematic [**?**]

Competitive Rivalry This describes how intense the current competition in a market is. The short-range commercial aircraft market is dominated by two giants, Airbus and Boeing, plus a few other players such as COMAC or Embraer.[12] Exit barriers exist to prevent companies from ceasing operations, even when unprofitable; high sunk costs lead to aggressive and continuous pricing, together with technological and performance competition. Competitive aspects include reliability, fuel efficiency, range, and cost[27]. Future competition trends will re-direct towards net-zero emissions and circularity.The industry is thus considered **highly** competitive.

Threat of New Entry This describes what opportunities new competitors will have and how much share they will take.[8] The industry requires very high capital requirements, long development cycles and a certification process which can be significantly complex and time-consuming. Moreover, existing firms benefit from economies of scale, which new entrants can't match initially. Additionally, strong brand trust and company-consumer relationships are very hard to build [28]. All these factors contribute to inhibiting start-up creations and making the industry unattractive for new entrants. This makes the threat of similar new entry companies **low**. In the context of this project, the foreseen share will be very narrow, especially since there are few but consolidated competitors acting in the market, all of which have a great share.

Threat of Substitution Describes the risk of alternative products entering the market and fulfilling the same identical needs as the existing ones.[8] The airline industry, specifically the commercial segment, faces a non-negligible threat of substitute products or services. One of the main competitors for aircraft are long-distance, high-speed trains; they offer a more convenient and comfortable travel experience.[13] Concerning business travels, there has been a huge rise in virtual meeting technologies, which has reduced the need for face-to-face meetings, and thus the demand for business travel has declined. Nevertheless, with the existing technologies and consumer habits, aircraft travel is still the most efficient mode of transport for travelling long distances in a short period of time. In conclusion, the threat of substitute products or services is **low**. However, airlines must be aware of emerging substitutes that may impact their profitability.

Suppliers' Power Describes how much power and control suppliers have over the companies they sell to. [8] In the commercial aviation industry, limited suppliers exist for airlines. They hold dominant positions, which provide them with a significant level of power over customers.[14] Switching suppliers requires high costs and organisational complexity to customers, ultimately yielding suppliers to have a **high** bargaining power.

Buyers' Power Describes to what extent customers are able to put pressure on a company.[8] Thanks to the internet, customers have access to a wide range of options via comparison platforms, which give them power to negotiate on price an quality. This puts pressure on airlines to compete on prices and offers to attract customers and maximise profits.[15] However, as there is a low threat of substitution, customers don't have a wide range of options to chose in order to compete against aircraft industry, which results in customers often adapting to companies pricing rules. Thus, in the commercial aircraft market buyers have a **moderate** bargaining power.

2.4. Technical Risk Assessment

The technical risk assessment aims to identify, analyse and quantify potential project risks. Risks deemed unacceptable require mitigation strategies to reduce them to an acceptable level, whereas sufficiently low risks only require acknowledgement and monitoring. Since the severity of risks may change over time, continuous risk management is essential to ensure hazards are identified and addressed in time. Risks are identified through sources such as literature reviews, design trade-off analyses and project schedules.

[13] URL https://www.efinancialmodels.com/five-forces-analysis-of-airline-industry-unveiled/ [cited 22 April 2026]
[14] URL https://www.fortunebusinessinsights.com/commercial-aircraft-market-115356 [cited 22 April 2026]
[15] URL https://www.deskera.com/blog/porters-five-forces/ [cited 22 April 2026]

Each risk is assigned a consequence score and a likelihood score, the product of which yields a risk score between 1 and 25. The acceptance threshold is set at 9; risks with a score greater than 9 must be mitigated, while those scoring 9 or below are considered acceptable and may be mitigated at the project's discretion. This is due to the impossibility of mitigating all risks, risks are inherent and rather than unnecessary mitigation an approach of identification and monitoring has been identified for less critical risks. To ensure consistency across all assessments, the following rubric has been applied:

Consequence (C) Class Legend

Class	Definition	Justification
5	Severe impact	Project infeasible
4	Serious impact	Major user requirements not complied with
3	Noticeable impact	Project possible with a small change of scope
2	Manageable disruption	All user requirements complied with small project redesign
1	Minimal impact	No real impact

Likelihood (L) Class Legend

Class	Definition	Justification
5	Almost certain	$> 60\%$
4	Likely	$30-60\%$
3	Possible	$10-30\%$
2	Unexpected	$5-10\%$
1	Very unlikely	$< 5\%$

Risk (R) Class Legend

Score	Classification	Required Action
17–25	Critical	Urgent mitigation required
10–16	Unacceptable	Mitigation strategy required
5–9	Moderate	Monitor and mitigate if necessary
1–4	Low	Acceptable; acknowledgement and tracking sufficient

The risks are divided into different categories, these categories are:

- TEC - Technical risks, related to the ability to achieve the technical requirements of the mission.
- SCH - Schedule risks, related to the ability of the project to achieve its goals in time.
- COS - Cost risks, related to the cost budgeting and the ability to remain within financial budgets and economic feasibility.
- OPE - Operational risks, related to the operation and safety of the aircraft itself.

The following plots present the risk maps before and after mitigation. The subsequent table provides a description of each identified risk, whilst the final table outlines the corresponding mitigation strategies.

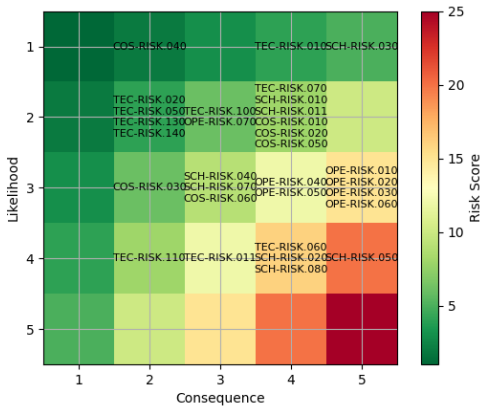

Figure 2.4: Pre-mitigation risk map

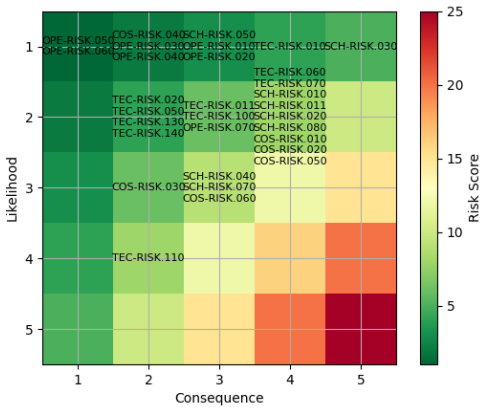

Figure 2.5: Post-mitigation risk map

Risk ID	Potential Risk	Responsible Department	C	L	R
TEC-RISK.010	The gravitropic mass of liquid hydrogen storage is too large causing the benefit of the reduced density of liquid hydrogen to be insignificant.	Energy Storage	4	1	4
TEC-RISK.011	The hydrogen power train is too heavy, the combination of fuel cell, cooling system and motors causes the aircraft mass to exceed 80,000 kg.	Propulsion	3	4	12
TEC-RISK.020	Materials that can be sourced in a more sustainable manner are heavier than their single use alternatives, leading to an aircraft mass greater than 80,000 kg	Materials	2	2	4
TEC-RISK.050	Liquid hydrogen volumetric size causes the aircraft shape that produces an excess amount of drag, reducing aerodynamic efficiency and increasing CASK.	Energy Storage	2	2	4
TEC-RISK.060	Electric propulsion systems are unable to produce the power to fly economically at required altitude and airspeed.	Propulsion	4	4	16
TEC-RISK.070	CFR-PEEK does not achieve the predicted structural material properties, requiring the use of alternative materials and resulting in an increase in aircraft mass.	Materials	4	2	8
TEC-RISK.100	Electric propulsion systems incapable of producing sufficient thrust, causing the aircraft to exceed 2100 m take off distance	Propulsion	3	2	6
TEC-RISK.110	Maturity of energy transfer technology causes a turnaround of greater than 45 minutes	Energy Storage	2	4	8
TEC-RISK.130	Storage of energy reduces usable aircraft space leading to a seating capacity less than 150 passengers	Energy Storage	2	2	4
TEC-RISK.140	Cryogenic boil-off and thermal cycling degrade hydrogen storage system performance over time, reducing operational efficiency and increasing maintenance requirements.	Hydrogen Storage	2	2	4
SCH-RISK.010	Maturity of electric propulsion technologies creates infeasibility of project completion by 2050	Propulsion	4	2	4
SCH-RISK.011	Maturity of liquid hydrogen storage technology creates infeasibility of project completion by 2050	Energy Storage	4	2	8
SCH-RISK.020	Maturity of airport infrastructure to accommodate this aircraft creates infeasibility of project completion by 2050	Energy Storage & Airframe	4	4	16
SCH-RISK.030	Maturity of certification feasibility of new energy aircraft is not ready in 2050	Certification	5	1	5
SCH-RISK.040	Delays in the development of international hydrogen handling standards postpone certification and market entry.	Certification	3	3	9
SCH-RISK.050	Electric Propulsion technology maturity limits number of cycles, causing the aircraft to be unable to run for 30 years	Propulsion	5	4	20
SCH-RISK.070	Evolving environmental regulations introduce additional design requirements, requiring redesign and delaying project completion.	Certification	3	3	9

Risk ID	Potential Risk	Department	C	L	R
SCH-RISK.080	Lack of maturity of design tools requires excessive (re)design	All	4	4	16
COS-RISK.010	Cost of acquiring manufactured materials without emissions leads to an acquisition cost greater than 150M€	Materials	4	2	8
COS-RISK.020	The price of liquid hydrogen does not decrease sufficiently to allow for CASK under 0.050€ per km	Energy Storage	4	2	8
COS-RISK.030	Limited supplier competition for fuel cells and cryogenic components leads to higher acquisition costs than anticipated.	Procurement	2	3	6
COS-RISK.040	Zero emission manufacturing practices lead to an acquisition cost greater than 150M€	Materials	2	1	2
COS-RISK.050	Cost of end of life upcycling is greater than the cost of retirement, providing no financial motivation for operators to recycle	Life cycle	4	2	8
COS-RISK.060	Fuel Cells fail to reduce cost significantly, leading to an acquisition cost greater than 150M€	Propulsion	3	3	9
OPE-RISK.010	liquid hydrogen leak and fire causing the aircraft to crash	Hydrogen Storage	5	3	15
OPE-RISK.020	Liquid hydrogen leak and fire	Hydrogen Storage	5	3	15
OPE-RISK.030	High Voltage electric short-circuit causing electrocution of souls onboard or system failure	Electronics	5	3	15
OPE-RISK.040	Back current due to wind milling causing complete system shutdown	Propulsion & Electronics	4	3	12
OPE-RISK.050	Heat exchanger failure causing a failure in the conditioning and distribution of hydrogen	Hydrogen Storage	4	3	12
OPE-RISK.060	Electric fire causing an ignition of hydrogen onboard after an uncontrolled leak	Electronics & Hydrogen Storage	5	3	15
OPE-RISK.070	Ice formation caused by cryogenic components affects surrounding systems and structural interfaces, resulting in reduced reliability.	Hydrogen Storage	3	2	6

Risk ID	Mitigation Strategy	C	L	R
TEC-RISK.011	Prioritising a lighter fuel cell at the cost of performance and therefore reducing the weight of this subsystem.	3	2	6
TEC-RISK.060	Explore novel options of achieving higher speeds, or opting to reword this requirement to allow for slower options.	4	2	8
SCH-RISK.020	Design a novel refuel system that allows for fast refuelling.	4	2	8
SCH-RISK.050	Provide modular propulsion systems that are capable of being replaced, this reduces the risk of the 30 year requirement being exceeded by allowing the airframe to continue a much longer life than the propulsion systems of which there are no circular pathways expected by 2050.	3	1	3
SCH-RISK.080	Consistently assess design performance metrics and validate models.	4	2	8
OPE-RISK.010	Design fire protection methods that accommodate for all tank load cases and protect the passengers and critical systems from the leak and fire	3	1	3
OPE-RISK.020	Design fire protection methods that accommodate for all distribution load cases and protect the passengers and critical systems from the leak and fire.	3	1	3
OPE-RISK.030	Introduce system protection systems that insulate the electric cables from the airframe, and system protection to mitigate consequences of a short circuit.	2	1	2
OPE-RISK.040	Introduce a diode to protect from motor power generation during wind-milling	2	1	2
OPE-RISK.050	Redundant heat exchanger systems	1	1	1
OPE-RISK.060	Zonal safety assessment to analyse the risk of the location of components and their interactions and mitigate problematic conditions	1	1	1

3. Budget Breakdown and Functional Analysis

3.1. Budget Breakdown

In order to ensure that the design does not stray too far from the intended path, it is important to implement some technical budgets to constrain the design process. The first budget to be considered is the preliminary mass budget. The preliminary mass budget is shown in Table 3.1. However, rather than constraining the design to the target values, the constraints were set to the spec values. This was mainly due to the fact that the mass budget was determined based on a pre-2000 conventional kerosene combustion aircraft, and as such may not be very accurate for a 2050 blended wing body hydrogen fuel cell powered aircraft.

Table 3.1: Preliminary mass budget

Subsystem	Unit	Target	Spec
Total	kg	68414	80000
Energy Supply and Storage	kg	16320	19795.8
Propulsion System	kg	5680	9155.8
Airframe	kg	18640	20957.2
Cabin Interior	kg	20606	20957.2
Avionics and Electrical	kg	4128	5286.6
Mechanical Systems	kg	3040	3619.3

Requirements on each subsystem will be made to limit mass throughout the detailed design process. The final mass breakdown is listed in Table 5.11.

A second budget considered is the design point, the W/P and W/S ratios. These values strongly constrain the design of the powertrain and lifting surfaces of the aircraft. Their values can be seen below in Equation 3.1.

$$\frac{W}{S} = 1875, \qquad \frac{W}{P} = 0.05035 \tag{3.1}$$

These budget constraints are listed among the requirements in Appendix A.

3.2. Interface Definition

Table 3.2: Interface Definition Matrix

Fuel Storage	Volume, Mass, Storage Type[1]	Storage Location,[1] Volume	Storage Location,[1] Volume	Storage Location,[2] Storage Type,[2] Volume		Storage Location[3]
Specific Energy, Energy Density, Carrier Type[1]	**Propulsion**	Propulsion Unit Location[4], fuel mass	Propulsion Unit Location[5]	Propulsion Unit Location[5], Thrust Capability[6]	Propulsion unit location (c.g.)[7], fuel mass[6]	Propulsion c.g. location[8]
Lifting Surface Volume, Structural Loads	Installation constraints[9]	**Lifting Surface**	Aerodynamic Forces, Integration Type, Structural Loads	Aerodynamic & structural efficiency[9], Available volume for storage	Geometry (sweep, dihedral, AR, etc.), Flow Interference, Surface Location	Planform, c.g. location
Structural loads	Drag generation	Aerodynamic Interference	**Housing Structure**	Volume available	Length,[10] available space	c.g. location
Volume, Storage location		Payload requirements[11]	Payload requirements[11]	**Payload Storage**		Payload requirements[11]
		Configuration,[12] Location[12]	Configuration[13]		**Control Surface**	
		Storage	Storage			**Landing Gear**

Table 3.3: N2 Explanation Key

Footnote #	Explanation
1	The choice of energy carrier influences storage integration within the aircraft structure, while storage constraints may in turn restrict carrier selection.
2	The storage type and location will affect the way you handle and distribute payload considering things like space or safety
3	If the fuel storage and landing gear compete for the same installation space, either the landing gear location must be changed or the available storage volume must be reduced.
4	If the propulsion unit is chosen to be located in the wing, aerodynamic interference will change the lift distribution of the wing, and also the structural challenges it can come with (or relief)
5	Main concern is noise level for passengers
6	Propulsion-system placement affects control, stability, and structural design through OEI behaviour, c.g. location, and local load paths; fuselage-mounted systems improve stability, while tail-mounted systems increase structural requirements.
7	The c.g. location affects the location of the LG due to tip-back, turnover & clearance constraints
8	Constraints of installation such as ground clearance, flap location or wing size may affect where the propulsion unit is located
9	How efficient aerodynamically (L/D) & structurally (W/S) and thrust (T/W) the aircraft is able to produce directly influence the amount of payload the aircraft is able to carry
10	The length of the housing structure affects the longitudinal location of the control surfaces and thus the required area/geometry needed
11	Requirements on payload capability will influence how the housing structure and the lifting surface is designed and also the type of configuration it is needed for the landing gear
12	If a canard is implemented downwash on the main lifting surface is considered
13	The configuration chosen affects how it is integrated in the housing structure, and thus loads will also change along the structure

Previously avionics has been considered a subsystem, it has been opted to remove this from this report as cockpit design and avionics extends outside the scope of this report in this design phase. Future recommendation include developing an ED-12c and ED-80 compliant hardware and software architecture, this is briefly introduced in chapter 11 however it is not considered a subsystem of the aircraft.

3.3. Functional Analysis

Functional analysis is a structured approach of recognizing, defining, and connecting the roles and operations a system needs to carry out in order to achieve its goals. The results of this analysis is shown in the form of a Functional Flow Diagram (FFD) in Figure 3.1 and a Functional Breakdown Structure (FBS) in Figure 3.2.

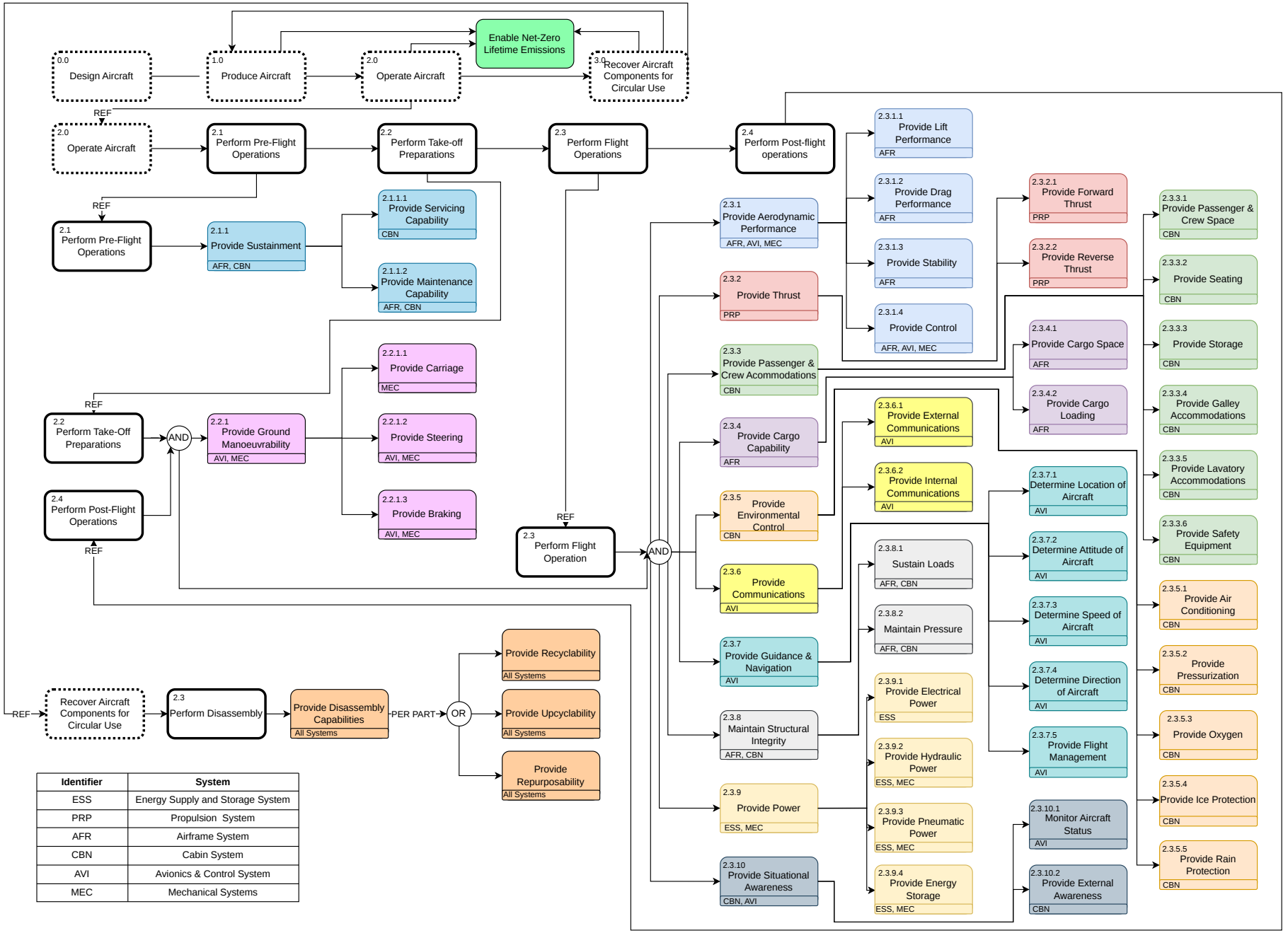

Identifier	System
ESS	Energy Supply and Storage System
PRP	Propulsion System
AFR	Airframe System
CBN	Cabin System
AVI	Avionics & Control System
MEC	Mechanical Systems

Figure 3.1: Functional Flow Diagram

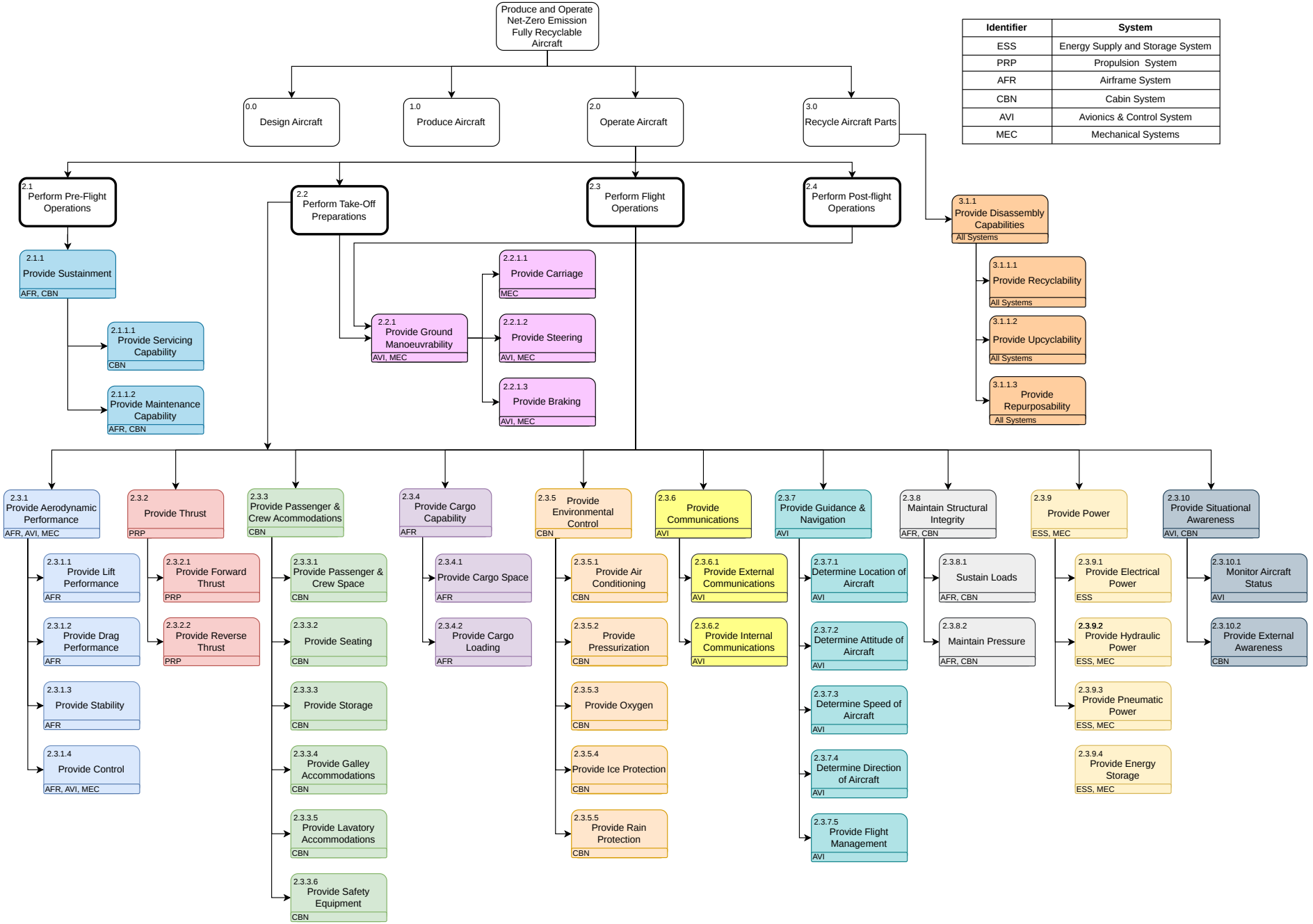

Figure 3.2: Functional Breakdown Structure

4. Initial Design

4.1. Trade-Off

Five concept designs have been taken into the design trade off, these designs arise from a design option tree assessing many potential options and reducing to 5 feasible aircraft designs with their respective propulsion type and energy storage type. Table 4.1 provides an overview of the concepts that entered into the trade-off.

Table 4.1: Overview of the detailed straw man concepts

Parameter	Box Wing	Blended Wing	Flying Wing	Dual Wing	Conventional
Energy Carrier (EGC)	Liquid Hydrogen + Supercapacitor (EGC 5.8)	Liquid hydrogen + Supercapacitor (EGC 5.8)	SAF (EGC 1.2)	SAF (EGC 1.2)	Liquid Hydrogen + Supercapacitor (EGC 5.8)
Energy Storage Location (ESL)	Fuselage + Wing (ESL 4.1)	Fuselage + Wing (ESL 4.1)	Wing tips (ESL 1.4)	Wing (ESL 1.1)	Fuselage + Wing (ESL 4.1)
Powertrain Type (PS 3)	Open fan (PS 3.6)	Ducted fan (PS 3.8)	Open fan (PS 3.6)	Turbofan (PS 3.2)	Ducted fan (PS 3.8)
Location of Powertrain (PS 2)	Fuselage mounted (PS 2.1)	Fuselage Mounted (PS 2.1)	Over-the-wing mounted (PS 2.7)	Fuselage mounted (PS 2.1)	Under-wing mounted (PS 2.2)
Tail System (TS)	V-Tail (TS-4)	No Tail (TS-1)	No Tail (TS-1)	No Tail (TS-1)	Conventional tail (TS-2)
Pitch Control (L&L 1)	Elevons (L&L 1.4)	Elevons (L&L 1.4)	Elevons (L&L 1.4)	Elevator (L&L 1.1)	Elevator (L&L 1.1)
Roll Control (L&L 2)	Elevons (L&L 2.4)	Elevons (L&L 2.4)	Elevons (L&L 2.4)	Ailerons (L&L 2.1)	Ailerons (L&L 2.1)
Yaw Control (L&L 3)	Rudder in vertical tails (L&L 3.1)	Rudder in winglets (L&L 3.1)	Rudder in winglets (L&L 3.1)	Conventional rudder (L&L 3.1)	Conventional rudder (L&L 3.1)
Fuselage Shape (FUS 1)	Cylindrical/double bubble (FUS 1.1/3)	Ovoid (FUS 1.2)	Ovoid (FUS 1.2)	Cylindrical/double bubble (FUS 1.1/3)	Cylindrical/double bubble (FUS 1.1/3)
Landing Gear Configuration (LG 1)	Tricycle (LG 1.4)	Tricycle (LG 1.4)	Tricycle (LG 1.4)	Tricycle (LG 1.4)	Tricycle (LG 1.4)
Landing Gear Placement (LG 2)	Sponson mounted (LG 2.5)	Fuselage mounted (LG 2.1)	Wing mounted (LG 2.2)	Sponson mounted (LG 2.5)	Wing mounted (LG 2.2)

The trade off is performed by assessing the performance of each concept against six criteria: re-manufacturability, mass performance, propulsive performance, cost performance, aerodynamic performance, and design schedule risk. These are a conglomerate of the most important requirements and summarised into key themes that are able to drive the design of the aircraft, Table 4.2 provides the relevant weightings, scores provided to each design option and the total scores of each option. A sensitivity analysis confirms that the blended wing body is the strongest choice for the aircraft and is therefore the driving choice for the design.

(a) Box wing **(b)** Blended Wing **(c)** Flying Wing **(d)** Dual Wing **(e)** Conventional

Figure 4.1: Artist Impression of the five strawman concepts

“

Table 4.2: Design Trade-Off Table

Design Options	Re-Manufacturability/Recyclability	Cost Performance	Aerodynamic Performance	Propulsive Performance	Mass Performance	Design Schedule Risk	Total
Weight	**20%**	**15%**	**15%**	**25%**	**15%**	**10%**	**100%**
Box Wing	Complex wing connections reduce accessibility for maintenance **(3)**	Higher manufacturing costs, but reduced operational costs **(4)**	Significantly less drag due to reduction in induced drag **(4)**	High bypass ratio open fan engines have a higher propulsive efficiency **(4)**	Higher fuel tank and wing mass compared to conventional configuration **(3)**	Only mild difference to conventional airframe, challenging wing architecture **(4)**	**3.65**
Blended Wing	Unconventional planform, modularity concerns (**3**)	Novel design, higher initial costs but amazing fuel efficiency (**4**)	Lift-producing fuselage, great L/D characteristics (**5**)	Strong environmental and acoustic benefits, sufficient thrust (**4**)	Lower necessary fuel mass, higher fuel gravimetric energy density, short fuselage (**5**)	Novel design concept, control and cabin design challenges, limited literature (**2**)	**3.90**
Flying Wing	Absence of a wing-fuselage joint makes disassembly challenging **(3)**	High development costs due to novel design and scarce research. Fuel consumption is lower than conventional counterpart **(3)**	Wetted area and non-lifting surface is minimised, very high L/D characteristics **(5)**	BLI benefit emission reduction but also lead to thrust loss and increased TSFC **(3)**	MTOW reduction, but span constraints are difficult to fulfill. Bending moments are alleviated by its payload distribution **(3)**	Challenge to develop due to scarce research and certification guidelines **(2)**	**3.20**
Dual Wing	Just as modular as conventional **(4)**	No cost gain in any way **(3)**	Increased wetted area **(2)**	High greenhouse gas emissions during operation **(3)**	Reduced bending loads result in lower mass **(4)**	Only mild difference to conventional airframe and propulsion system **(4)**	**3.30**
Conventional	Good modular design, making disassembly easier **(4)**	Cost gain in the use of hydrogen as it is cheaper, no other cost gains **(4)**	No increase in aero performance **(3)**	Decreased noise, increased efficiency, decreased emissions **(4)**	No decrease or increase in MTOW **(3)**	Most researched, large amount of sizing methods **(5)**	**3.80**

4.2. Summary of Design

After completing the trade-off between all 5 strawman concepts presented in section 4.1, the next phase was to start designing a BWB configuration, similar to Figure 4.3, that fitted into our mission characteristics and requirements. The initial design meant to establish the preliminary sizing of a hydrogen-powered BWB aircraft through a Class I weight estimation, wing and power loading analysis, configuration layout, structural assessment, stability and control positioning and environmental evaluation.

From the preliminary weight estimation, the MTOM was estimated by decomposing it into payload, energy system, and operative empty weight. The payload mass of of 16 005 kg was determined from 150 passengers and 3 cabin crew, assuming 85 kg each plus 20 kg of cargo per passenger [16]. The energy system mass fraction was computed from the hydrogen mass fraction, which was done with the modified Breguet equation following Vos et al.[17]. Additionally, it was also accounted for the weights of the hydrogen tanks and the electric motor/engines, resulting in a total energy system mass fraction of 0.157. Finally, the operating empty weight fraction of 0.53 was taken purely for reference BWB aircraft. Solving iteratively, a MTOM of 51 131 kg was obtained, which is expected to grow by 15 to 25% after Class II refinement [29].

Next, a wing and power loading diagram was produced in order to yield a point that allowed sizing the wing and the powertrain. The diagram included performance constraints such as stall speed, rate of climb, take-off field length, etc. and resulted in a design point with wing loading $\frac{W}{S} = 1875$ N/m^2 and a power loading of $\frac{W}{P} = 0.054$ N/W. From this and the MTOW obtained in the preliminary weight estimation, a reference wing area of 267 m^2, which ultimately resulted in a total wing area of 78.52 m^2 and in a total aircraft span of 33.52 m, after subtracting the fuselage planform area. Next, the NACA 0020 was applied to the fuselage cross-section, yielding a centreline fuselage length of 24.6 m.

Thirdly, the cabin was sized using a three-compartment model based on a floor area of 100 m^2, providing a cabin length of 16.55 m. Liquid hydrogen storage was allocated to two cylindrical tanks of 1.5 m diameter and 14.7 m length, providing approximately 31.7 m^3 of storage. Following, the propulsion system was sized for six units. It consists of a fuel cell stack, heat exchanger, compressor-expander module, electric motor and a ducted fan. After sizing every component and knowing their power availability, an auxiliary power budget of 192 kW was allocated with a 20% contingency margin. In terms of environmental performance, it was also found that the hydrogen fuel cell system eliminates all CO_2 and NO_x emissions during operation, and substantially reduces fine and ultra-fine particulate emissions at the airport through the removal of combustion engines. Noise levels are expected to decrease by 4 to 8 dB relative to the A320neo. However, water vapour emissions are increased but can be mitigated through operational contrail avoidance programmes.

A top-level structural analysis was performed on the structure, from which it was confirmed that the higher loads concentrate at the wing root and the fuselage centreline. Finally, wing longitudinal positioning was determined from a high-level centre of gravity estimates of the wing and fuselage groups, placing the leading edge of the mean aerodynamic chord at 12.46 m from the nose. The centre of gravity range spans from 11.99 m to 13.60 m, and twin vertical stabilisers were positioned aft of the fuselage, with a tail area of 57.69 m^2. These results establish a coherent initial design baseline from which the detailed design phase will proceed.

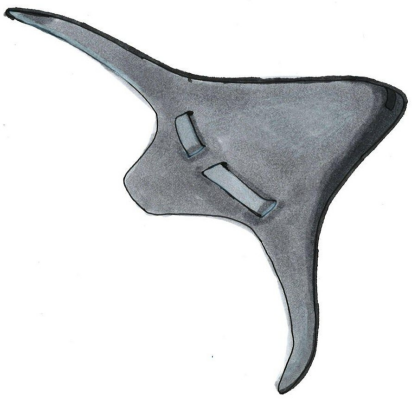

Figure 4.2: Blended-Wing-Body Concept Aircraft (ARTIST IMPRESSION)

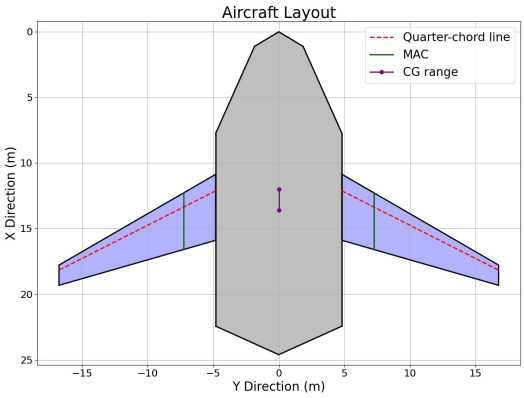

Figure 4.3: Initial Design Top View

[16] https://www.easa.europa.eu/en/the-agency/faqs/minimum-required-cabin-crew [cited 27th May 2026]

[17] Vos, R., "INTRODUCTION TO AIRPLANE DESIGN," AE1222-II Aerospace Design & Systems Engineering Elements, Delft University of Technology, Delft, Netherlands, 2024. [Cited 18 May 2026]

5. Performance Analysis

The performance of the aircraft will be evaluated and verified to comply with the design requirements in this chapter. The aerodynamic characteristics, load envelope, detailed weight estimation, climb performance and noise characteristics are analysed to assess the operational capabilities of the final aircraft configuration.

5.1. Information Dependencies

Each design chapter has an N2 chart included to illustrate the information dependencies between each chapter.

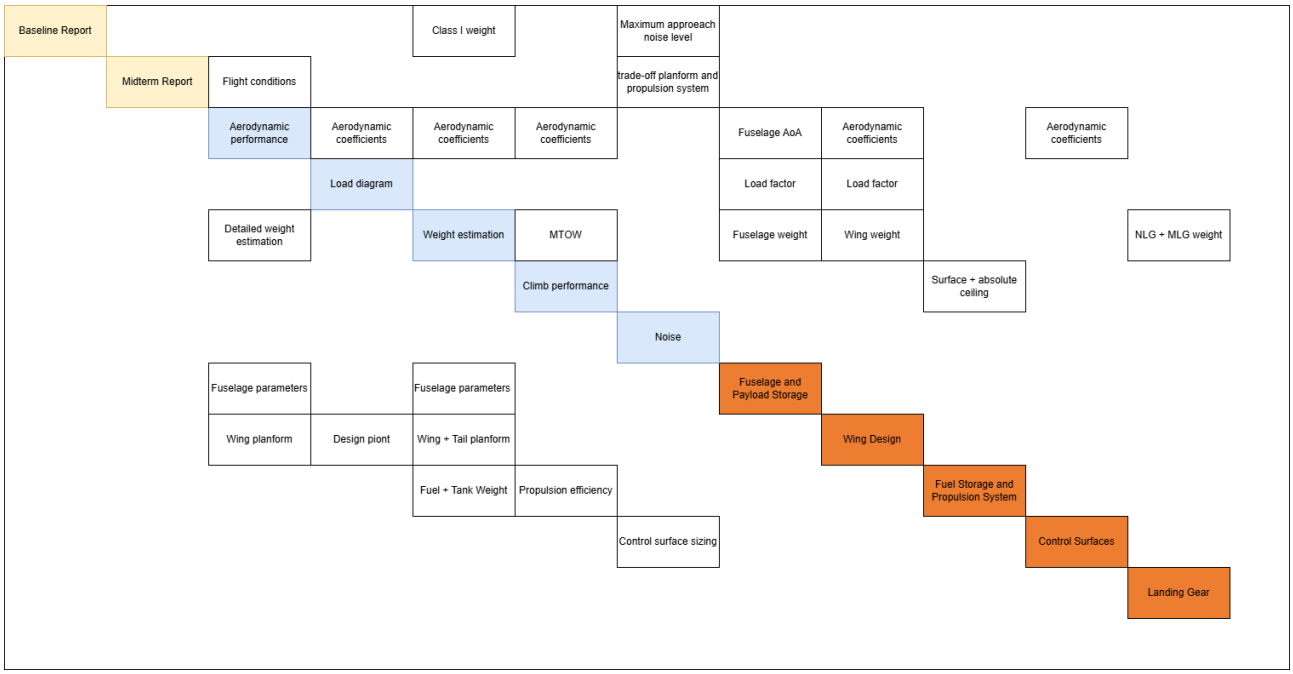

Figure 5.1: N^2 Chart indicating the flow of information within the performance analysis

5.2. Assumptions

Table 5.1: Performance Analysis assumptions

ID	Assumption	Variable(s)	Effect
PA1	The BWB is modelled as a single wing of aspect ratio $AR = 4.2$ and leading-edge sweep $\Lambda = 26.84°$ for all aerodynamic analysis, meaning that there is no distinction between the fuselage and the wing bodies aerodynamically.	C_{L_α}, L/D	Overestimates C_{L_α}, which will yield therefore a overestimate L/D.
PA2	A laminar flow fraction of 10% is assumed across all surfaces.	C_f, C_{D_0}, L/D	If a higher laminar flow fraction is found through complex analyses such as CFD, this will yield a lower C_f, decreasing the parasitic drag coefficient and thus improving the aerodynamic efficiency [30].
PA3	The dive speed V_D is assumed to be 1.25 times the cruise speed, following CS 25.335.	V_D	A ratio of 1.20 instead of 1.25 would reduce dive speed and thus the dynamic pressure at dive speed by approximately 8% and relaxes design ultimate load factor.

Continued on next page

ID	Assumption	Variable(s)	Effect
PA4	The power available from the hydrogen fuel cell electric motor system is treated as constant and independent of airspeed at each altitude.	P_a	Introducing a P_a model dependent on airspeed will turn the straight line in Figure 5.5a to a curve. This will alter the $(ROC)_{max}$ and the best rate speed, also changing slightly the time to climb results
PA5	A power lapse coefficient of $n = 0.044$ is assumed to be consistent with a power degration of 6% at cruise altitude with respect to sea level, as illustrated in [31].	n, P_a	This value controls how P_a decays with altitude and is the main contributor to the computations of ceilings. A 50% increase in n would reduce P_a at cruise altitude by approximately 3%, through Equation B.27. This would lower the service ceiling.

5.3. Methods

5.3.1. Aerodynamic Performance

Aerodynamic efficiency sets how much energy the aircraft needs to fly, making it the airframe's main influence on in-service energy use. Reducing drag lowers the shaft power the propulsion system must deliver in cruise. This is a part of why the blended wing body planform was selected: spreading lift across a single lifting surface raises the lift-to-drag ratio and reduces the energy required relative to a conventional tube-and-wing aircraft.

Airfoil Selection

Two airfoils are selected to fix the conceptual shape and to feed the later analyses: one for the body, where spatial constraints lead, and one for the wing, where aerodynamic performance leads. Only existing airfoils with published geometries were considered, all taken from the Airfoil Tools database.[1]

The body airfoil must be thick enough to house a cockpit, cabin, and storage structure, and ideally has a low C_d. The wing airfoil must above all generate to support the body. Both must have a critical Mach number above the 0.80 cruise value. Few airfoils in the database meet this, since most are NACA sections and modern airliners use proprietary designs. The selected airfoils are therefore placeholders, used to extract the aerodynamic parameters the later analyses need and to support the spatial design; a mission-specific airfoil should be designed in a more detailed design phase.

The two airfoils, both supercritical, are the SC(2)-0518 for the body and the RAE 2822 for the wing, shown in Figure 5.2 and Figure 5.3. Beyond their wave-drag behaviour, the body airfoil was chosen for its high thickness and the wing airfoil for its reliable data[19], The results of these airfoils are presented in Table 5.4.

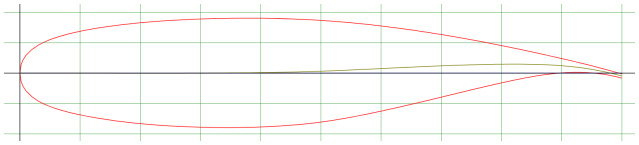

Figure 5.2: Body airfoil[20]

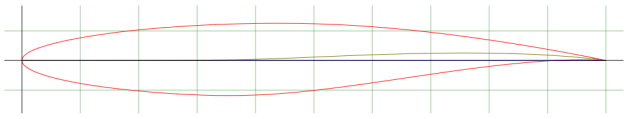

Figure 5.3: Wing airfoil[21]

Airfoil Characteristics

Each airfoil is analysed at cruise with ESDU VGK[22], a solver for viscous transonic flow over two-dimensional airfoils[23]. The airfoils were analyzed by taking the into account the reduced Mach number of the normal flow due to sweep. However Gudmundsson[32] states that in practice only half of this reduction is experienced, so the Mach numbers for the simulation were determined with the following equation:

$$M_{sim} = \frac{M_\infty + \frac{M_\infty}{cos\Lambda_{LE}}}{2} \tag{5.1}$$

[18] URL `http://airfoiltools.com/` [cited 28/05/2026]
[19] URL `https://www.sciopen.com/article/10.7638/kqdlxxb-2022.0027` [cited 29/05/2026]
[20] URL `http://airfoiltools.com/airfoil/details?airfoil=sc20518-il` [cited 05/06/2026]
[21] URL `http://airfoiltools.com/airfoil/details?airfoil=rae2822-il` [cited 29/05/2026]
[22] Recommended by Dr. F. Oliviero
[23] URL `https://www.esdu.com/cgi-bin/ps.pl?t=doc&p=esdu_vgk` [cited 15/06/2026]
[24] URL `https://www.flow5.tech/xflr5/xflr5.html` [cited 15/06/2026]

Take-off and landing are analysed in XFLR5[24], which is better suited to those conditions. The resulting characteristics are in Table 5.4.

Lift Performance

With the airfoils fixed, the three-dimensional aircraft is considered to set its lift characteristics. For the lift slope, the blended wing body is treated as a single wing of aspect ratio $AR = 4.2$ and sweep $\Lambda = 26.84°$ based on subsection 7.3.2, which simplifies the analysis. This introduces some uncertainty and probably slightly overestimates the lift slope of the fuselage part. It is acceptable for this design phase, but a more detailed analysis, including a full CFD model, is advised for future iterations. Following the AE2111-II course[25], the lift slope is

$$C_{L\alpha} = \frac{2\pi \cdot AR}{2 + \sqrt{\left(\frac{AR \cdot \beta}{\kappa}\right)^2 \left(1 + \frac{\tan^2 \Lambda}{\beta^2}\right) + 4}} \tag{5.2}$$

Where the airfoil efficiency factor $\kappa = 0.95$[25] and the Prandtl-Glauert compressibility factor $\beta = \sqrt{1 - M^2}$[32]. Since the blended wing body is treated as one wing, this is already the whole-aircraft slope and no separate fuselage value is needed.

The maximum lift coefficient follows from the airfoil sharpness parameter ΔY. From the AE2111-II course[25] the wing-to-airfoil maximum-lift ratio $C_{L_{max}}/C_{l_{max}}$ is 0.68 for the body and 0.80 for the wing. The reference-area-weighted average (7.4.2)then gives the whole-aircraft maximum lift coefficient.

The stall angle follows from the maximum lift coefficient, zero-lift angle, and lift slope[25]:

$$\alpha_s = \frac{C_{L_{max}}}{C_{L_\alpha}} + \alpha_0 + \Delta\alpha_{C_{L_{max}}} \tag{5.3}$$

Where the last term accounts for the nonlinear leading-edge vortex effects, taken as $4°$ from the AE2111-II course.[25] This gives $\alpha_s = 29.9°$. The take-off, landing, and cruise lift coefficients then follow from force equilibrium, as seen in Equation 5.4. Following Gudmundsson [32], the airfoil zero-lift angle is substituted for the wing, giving the trim angle of attack at each phase[25], as seen in Equation 5.5.

$$C_L = \frac{2W}{\rho V^2 S} \tag{5.4}$$

$$\alpha_{trim} = \frac{C_{L_{des}}}{C_{L_\alpha}} + \alpha_{0L} \tag{5.5}$$

The resulting whole-aircraft lift slope is shown in Table 5.5, the maximum lift coefficient in Table 5.6, the lift conditions and coefficients in Table 5.7, and the trim angles of attack in Table 5.8.

Drag Performance

The cruise drag sets how efficiently the aircraft flies, so it is estimated next. The analysis follows the AE2111-II course.[25] For a moderately cambered design the drag is

$$C_D = C_{D_0} + \frac{C_L^2}{e\pi(AR + \Delta AR)} \tag{5.6}$$

with C_{D_0} the zero-lift drag and e the Oswald efficiency factor, both determined below and ΔAR is the increase in aspect ratio due to the winglets, determined in Table 7.8.

The zero-lift drag uses the component build-up method:

$$C_{D_0} = \frac{1}{S_{ref}} \sum_c C_{f_c} \cdot FF_c \cdot IF_c \cdot S_{wet_c} + \sum C_{D_{misc}} \tag{5.7}$$

where for each component C_f is the skin-friction coefficient, FF the form factor, IF the interference factor, S_{wet} the wetted area, and $C_{D_{misc}}$ the miscellaneous drag, which can include for example wave drag. The skin friction is the weighted average of a laminar and a turbulent contribution; wings and tails on civil jets in classic production metals carry about 10% laminar flow[25]:

[25] Oliviero, F., "Aircraft aerodynamic analysis: Mobile surfaces of the wing", AE2111-II Aerospace Design & Systems Engineering Elements, Delft University of Technology, Delft, the Netherlands, 2022. [Cited 2 June 2026]

[26] URL `https://pure.tudelft.nl/ws/portalfiles/portal/44026770/ConferencePaper.pdf` [cited 02/06/2026]

$$C_{f_{lam}} = \frac{1.328}{\sqrt{Re}} \tag{5.8}$$

$$C_{f_{turb}} = \frac{0.455}{(\log_{10} Re)^{2.58}(1 + 0.144M^2)^{0.65}} \tag{5.9}$$

The form factor for wings and tails is

$$FF = \left[1 + \frac{0.6}{(x/c)_m}\left(\frac{t}{c}\right) + 100\left(\frac{t}{c}\right)^4\right] 1.34\, M^{0.18}(\cos\Lambda_m)^{0.28} \tag{5.10}$$

where t/c is the maximum thickness-to-chord ratio and $(x/c)_m$ and Λ_m are its chord-wise location and sweep. The interference factor is taken as 1.0 for the two wing sections[26] and 1.03 for the V-tail[25]. The wetted area is based on the exposed area; there is no unexposed wing-body junction as on a conventional aircraft, so the reference areas are used:

$$S_{wet_w} = 1.07 \times 2 \times S_{exp_w} \tag{5.11}$$

$$S_{wet_{VT}} = 1.05 \times 2 \times S_{exp_{VT}} \tag{5.12}$$

For the miscellaneous drag, the drag divergence number, above which wave drag is considered is calculated as per the following:

$$M_{DD} = \frac{k_a}{\cos\Lambda} - \frac{t/c}{\cos^2\Lambda} - \frac{C_L}{10\cos^3\Lambda} \tag{5.13}$$

with t/c (5.2) and the sweep angle known for both sections and the supercritical technology factor $k_a = 0.93$[25]. The section lift coefficients are estimated separately, since using the whole-aircraft value would be inaccurate, by converting the airfoil lift curves to three dimensions with the low-aspect-ratio (fuselage) and high-aspect-ratio (wing) relations[33] respectively:

$$C_{L_\alpha} = \frac{C_{l_\alpha}}{\sqrt{1 - M_\infty^2 + \left(\frac{C_{l_\alpha}}{\pi AR}\right)^2} + \frac{C_{l_\alpha}}{\pi AR}} \tag{5.14}$$

$$C_{L_\alpha} = \frac{C_{l_\alpha}}{\sqrt{1 - M_\infty^2} + \frac{C_{l_\alpha}}{e\pi AR}} \tag{5.15}$$

These relations are for straight wings, while the design is swept. This overestimates the slope and the lift coefficient but underestimates the drag-divergence Mach number, so it is conservative. With the lift slopes, the cruise angle of attack α_{cr} from Table 5.8, and the zero-lift angle $\alpha_{C_L=0}$ from Table 5.4, the section lift coefficient follows by definition:

$$C_L = (\alpha_{cr} - \alpha_{C_L=0})\, C_{L_\alpha} \tag{5.16}$$

There is no upsweep in the usual sense, since the fuselage has the shape of an airfoil; there are no flaps; and the propulsion drag was already accounted for as a thrust loss at sizing. The remaining miscellaneous drag, from leakage and excrescence, is taken as a conservative 5% of the zero-lift drag from the AE2111-II course. The Oswald efficiency is computed treating the aircraft as one wing, as for the lift slope, using the swept-wing relation[25]:

$$e = 4.61(1 - 0.045\, AR^{0.68})(\cos\Lambda_{LE})^{0.15} - 3.1 \tag{5.17}$$

The inputs are in Table 5.2 and the results in Table 5.9.

5.3.2. Load Diagram

The load diagram plays a critical role in the design and performance of the aircraft as it defines the limitations of the flight as well as the required loads needed to design for. The calculation of the load diagram is divided into two sections, the manoeuvrer limit loads and the gust limit loads.

Manoeuvre Loads

The manoeuvre loads are defined by defining the cruise and dive (maximum) velocities, the cruise speed of Mach 0.8 at a cruise altitude of 40000 ft results in an EAS of 236 $\frac{m}{s}$. From CS.25 an assumption of the dive speed can be made to be 1.25 times the size of the cruise speed, resulting in 295 $\frac{m}{s}$.

The next step defines the maximum loads, using CS 25.337 with an MTOW of 132555.14 lbs a maximum load can be calculated to be 2.5g and a minimum load of -1g. To finalise the manoeuvrer loads according to relevant

[25] Oliviero, F., "Aircraft aerodynamic analysis: Mobile surfaces of the wing", AE2111-II Aerospace Design & Systems Engineering Elements, Delft University of Technology, Delft, the Netherlands, 2022. [cited 02/06/2026]

Table 5.2: Inputs for the drag analysis.

Parameter	SC(2)-0518 (fuselage)	RAE 2822 (wing)
Laminar flow fraction	10%	
Interference factor IF, wing sections	1.0	
Interference factor IF, V-tail	1.03	
Wetted-area factor, wing	1.07	
Wetted-area factor, V-tail	1.05	
Wave-drag technology factor k_a	0.93	
Excrescence and leakage	5% of C_{D_0}	
Aspect ratio AR	4.2	
Winglet aspect ratio increaseAR	0.95	
Cruise Mach number Re	0.675	0.765
Cruise Reynolds number Re	5×10^6	5×10^6
Thickness-to-chord ratio t/c	18%	12%
Max thickness location $(x/c)_m$	35%	38%
Half-chord sweep Λ_m		
Airfoil lift slope C_{l_α}	$10.9\ \mathrm{rad}^{-1}$	$12.1\ \mathrm{rad}^{-1}$
Zero-lift angle $\alpha_{C_L=0}$	$-2°$	$-2°$

regulations the minimum load from V_c to V_D can be linearised, and the loads under ultimate loads during low speed can be modelled using the following equation:

$$n = \frac{qC_Lmax}{\frac{W}{S}} \tag{5.18}$$

Where q is the dynamic pressure, C_Lmax is the max lift coefficient, and $\frac{W}{S}$ is the wing loading. From here two more critical speeds can be calculated, where n=1 is the stall speed (V_s) at 58.3 $\frac{m}{s}$ and a design manoeuvre speed (V_a) at 87.5 $\frac{m}{s}$. This can be visualised in Figure 5.4 as the blue area.

Gust Loads

The gust loads are the other critical point for the load envelope of the aircraft, similarly to the manoeuvre loads an approach similar to that defined by CS 25 is used to create a certifiable aircraft. For this a limit design gust must be identified that complies with the requirements stated in CS 25.341. To do this empirical formulas of the gust alleviation factor are calculated:

$$K_g = \frac{0.88\mu_g}{5.3 + \mu_g} [34] \tag{5.19}$$

$$\mu_g = \frac{2\frac{W}{S}}{a\rho g c} [34] \tag{5.20}$$

Where $\frac{W}{S}$ is the wing loading, a is the lift curve, g is the gravitational acceleration, and c is the mean aerodynamic chord. K_g provides a number for the susceptibility of the aircraft to gusts based on input data. This can then be taken into a calculation for the load force using a non-regulatory engineering model often used as backing for certifying aircraft load envelopes (AMC 25.341):

$$\delta n = \frac{K_g \rho V a U_{de}}{2\frac{W}{S}} \tag{5.21}$$

Whilst not strictly accurate with the applicability, this can be a good assumption to calculating the ultimate loads required for CS-25 compliance. A key note is that as the altitude increases the load limits due to gusts decrease due to the decrease in air density. This means the critical load condition occurs at sea level and cruise speed, however, this is operationally impossible due to the airspeed limitations below 10000 ft. For this reason, the ultimate force is taken at 10,000 ft as here the airspeed limitations are lifted whilst still accounting for the highest

potential air density. The reference gust speed decreases linearly between cruise speed and dive speed, which results in the load force decreasing, the gust load diagram can be visualised as the green region in Figure 5.4.

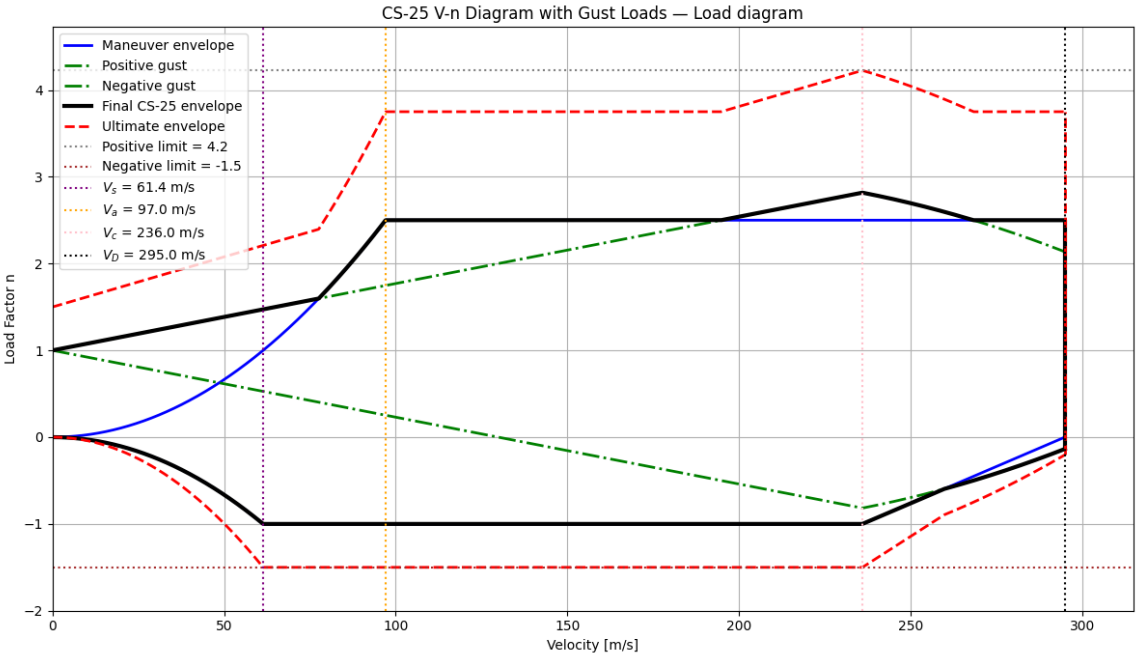

Figure 5.4: Aircraft Load Diagram

Combining the two diagrams an ultimate load of +2.8g and -1g can be identified, which carry into a design load of +4.2g and -1.5g when including the CS 25 required 1.5 safety factor. Which are used in structural calculations in chapter 7. The results are displayed in Table 5.10.

5.3.3. Detailed Weight Estimation

A detailed weight estimate is crucial for understanding how much the final concept will weigh after iterations at the subsystem level. This will enable verification of whether mass performance requirements were met. Moreover, the estimation will serve to analyse and design in depth all the subsystems of the aircraft, ultimately yielding in a fully designed configuration. As for the preliminary weight estimation done previously, an MTOM will be assumed for the first iteration loop, being 51 131 kg from the Class I weight estimation, and from it a value will be obtained. Iterations will be done until a percentage difference of less than 1% is reached in the MTOM value. The succeeding procedure consisted in following Torenbeek's method from Roskam part V [35], where relevant relations are listed in Appendix B. In a nutshell, the approach breaks down into sizing the operative empty weight components separately from each other, then sizing the fuel storage system and finally using the payload weight of 16 005 kg to obtain the MTOM of the aircraft.

Operative Empty Weight

Starting with the operative empty weight, it is important to note that it was defined slightly differently than in the previous weight estimation. In this case, the operative empty weight, W_{OEW} comprised everything except the payload and fuel (LH_2);

$$W_{OEW} = W_w + W_{emp} + W_{fus} + W_{pwt} + W_{lg} + W_{feq} + W_{tnk}$$

Firstly, the **wing** will be sized following Equation B.1, where wing geometry parameters are obtained from chapter 7, n_{ult} from Figure 5.4, t_r from subsection 5.3.1 and the maximum zero-fuel weight corresponds to $W_{MZF} = W_{MTO} - W_{LH_2}$. This procedure was done initially to go ahead with the first subsystem-level iteration, however the final wing weight was taken from the analysis in the structural department, reported in chapter 7. This procedure was done identically for the empennage.

The next component sized was the **empennage**. This was done following Equation B.2 with a slight modification; as reasoned in chapter 9 the selected empennage configuration led to a v-tail configuration with a pre-defined inclination w.r.t. the vertical axis of $\phi = 20°$, while Equation B.2 is applicable for purely vertical tails. Thus it was assumed that the weight of the v-tail scaled with the inclination angle as $W_{emp} = \frac{W_v}{cos(\phi)}$. Tail

geometry was obtained from chapter 9, the half-chord tail sweep angle from Equation B.3 and the dive speed from subsection 5.3.2. Again, the final weight of the empennage is reported in chapter 9.

Onto the **fuselage** (centre-body for the BWB), it is important to note that it was sized treating it as a pressurised tube-and-wing conventional aircraft, although differences will appear because the fuselage contributes to the lifting capabilities of the overall BWB configuration. Equation B.4 will be used, where as mentioned previously and in chapter 6, the design will include a pressurised fuselage, and the main landing gear won't be attached to the fuselage - thus $K_f = 1.08$. Fuselage geometry is taken from chapter 6; where S_{fgs} is defined as the fuselage shell (wetted) area, being $\frac{S_{wet}}{S} S_{fus} = 2.5 S_{fus}$ from Class I outputs. Finally, l_h is the distance from the wing's quarter-chord to the empennage quarter-chord, taken from chapter 7 and chapter 9. In order to quantify the suitability of the method for the BWB configuration, Howe's [36] Equation B.5 for lifting surfaces was applied, with all parameters from Equation B.5. After performing the structural analysis in the fuselage described in chapter 6, a total detailed weight was not possible to outcome due to time constraints, however based on individual components weight it was reasoned that a growth factor of 2.5 between the calculated value with Equation B.4 and the real value was a sensible estimate for BWB configurations.

Next, the **powertrain** was analysed. It has weight contributions from the nacelles, engine components and fans separately, and APSI (accessory drives, powerplant controls, starting and ignition systems). The sizing of the components followed Equation B.6 to Equation B.11, from which the velocity at take-off condition was assumed to be 1.25 times larger than the stall speed and the design power loading value from the loading diagram was used. All necessary parameters were obtained directly from chapter 8, except the sizing of the fan, in which Jason et. al. [37] provided values for the specific energy of the fans of typical turbofan engines. It is important to note that the tanks and liquid hydrogen are not included in the powertrain subsystem, as they will be sized separately in a later step in this procedure.

The **landing gear** was also considered as a separate subsystem in the analysis. Both the nose and main landing gear scaled with Equation B.12, in which K_{g_r} is a fixed constant equal to 1 for low-wing configuration and constants A_g,B_g,C_g and D_g varied depending on the landing gear type and component.

The **fixed equipment** comprises every aspect/component an aircraft has to carry for functionality purposes, but that is not considered in any other subsystem. Specifically for this design, these include flight-control systems, electrical systems, avionics, furnishings, paint etc., as described by Equation B.13, where the miscellaneous weight category was included to cover any items not specifically listed, for which a value was taken from reference aircraft. The complete process of scaling these components is explained by Equation B.14 to Equation B.20, plus the cargo handling equipment which was taken from chapter 6. Cabin geometry was also computed in chapter 6, the ferry range and the wetted area were computed in the Class I weight estimation, being $R_{ferry} = 6129km$ and $S_{wet} = 668.8m^2$. Finally, an areal density of 0.6 kg/m^2 from Roskam [35].

Fuel System Weight

The final step before obtaining a detailed weight distribution of the design embodies calculating the weight of the fuel system, consisting of the hydrogen tanks and the liquid hydrogen. As all existing sizing approaches, such as Roskam, Raymer or Torenbeek, do not consider novel energy configurations such as liquid hydrogen, it is not possible to size the fuel system through these methods in an accurate manner. For these reasons, both the tanks and the fuel were sized through a more detailed approach that combines numerical and literature-based relations, discussed deeply in chapter 6 and chapter 8.

After subsystem-level iterations between all departments, the results of the detailed weight estimation are presented in Table 5.11.

5.3.4. Climb Performance

A climb performance study serves to identify the behaviour of the aircraft and its optimal climb state to maximise different parameters such as the rate of climb, range, endurance, etc. It also explains how the performance of the aircraft varies with altitude, and whether the pre-defined design cruise altitude is feasible based of power availability. The procedure followed Ruijgrok's "Elements of Airplane Performance" [38] framework for steady, symmetric flight and all formulas and derivations were taken from it. The analysis takes as inputs; the MTOM from subsection 5.3.3, wing's reference area, aircraft's parasitic drag coefficient and maximum lift coefficient from subsection 5.3.1 and the take-off power from the constraint loading diagram. From these, the rate of climb, best-climb speed, service and absolute ceilings, and time to climb to the cruise altitude of FL400 are determined, assuming a constant power output of the hydrogen fuel-cell and electric motor system.

Performance Diagram

The performance diagram describes how power varies with airspeed at sea-level. The power available at sea-level, $P_{a_{SL}}$, will be treated as constant and independent of velocity for hydrogen fuel cells, and assumed that it

is equal to the power at take-off times the fan efficiency;

$$P_{a_{SL}} = \eta_{fan} P_{TO} = \eta_{fan} \frac{MTOW}{(W/P)}$$

and the power required $Pr = D \cdot V$. First, the velocity and the total drag coefficient of the aircraft is calculated for different values of C_L up to the maximum lift-coefficient with Equation B.21 and Equation B.24, and then drag is computed from Equation B.22. With all these information, the plot can be constructed, and the performance velocity points identified. For that, Table 5.3 shows how to obtain each point, together with its physical meaning.

Table 5.3: Description of Performance Points

Symbol (m/s)	Meaning	Formula(s)
V_{min}	Velocity at maximum lift coefficient	Equation B.21 with C_L = $C_{L_{max}}$
$V_{Pr_{min}}$	Velocity at min. Pr, max. endurance and max. ROC	Equation B.25, then Equation B.21
$V_{D_{min}}$	Velocity at min. D and max. range	Equation B.23, then Equation B.21
V_{max}	Maximum velocity, where $Pr = P_{a_{SL}}$	-

Climb Ceilings and Effect of Altitude

The next step is quantify the performance degradation with increasing altitude. This is done by calculating the rate of climb of the aircraft at different altitudes, with Equation B.26, where the power available scales with Equation B.27, using the lapse coefficient as n = 0.044, which corresponds to a 6% power degradation at FL400. Densities are calculated using standard ISA relations [27]. The rate of climb is plotted against airspeed for a set of altitudes, from where maximum value $(ROC)_{max}$ and its corresponding airspeed V_y, defined as the best rate speed, can be spotted for each altitude. Following, the maximum rate of climb is plotted against the altitude, from where the service and absolute ceilings can be identified. By definition, the service ceiling correspond where the maximum rate of climb is 0.5 m/s, while the absolute ceiling relates to a zero rate of climb. However, from the detailed structural analysis performed in section 6.5 it was concluded that going beyond an altitude of 14 780 m will impose severe structural concerns. Thus, due to performance and safety issues, although the propulsion system is capable of climbing and sustaining cruise at the altitude represented by Figure 5.5c, the absolute ceiling constrained by structures will be taken. The percentage difference between the absolute and service ceilings calculated following the aforementioned process will be used to calculate the new service ceiling. Table 5.12 shows the final ceiling values.

Time to Climb

Finally, the aircraft is assessed by the minimum time it takes to climb to its cruise altitude, t_{cl}, with the help of Equation B.28, where $(ROC)_{max}$ varies for each altitude. As a sanity check, the obtained value will be compared to its conventional counterpart to confirm calculation correctness.

5.3.5. Noise Analysis

The aircraft is required to be no louder than the reference A320, formalised as a maximum approach noise level of 92.0 EPNdB. Approach is typically the most constraining for this class, as it usually produces the highest effective perceived noise levels on the ground. No aeroacoustic solver is run at this stage, so noise is treated qualitatively: the dominant sources of a conventional turbofan aircraft are identified, and the effect of the fuel cell propulsion and blended wing body integration on each is assessed.

For a turbofan aircraft the noise budget is dominated by the propulsion system, the main contributors being combustion and core noise, fan noise, and jet mixing noise, with airframe noise from the landing gear and high-lift devices becoming significant on approach. The fuel cell propulsion system replaces the gas turbine core with a fuel cell stack driving an electric motor and ducted fan [1, 31]. Combustion and turbine noise vanish entirely, as the architecture has no combustor and no turbine. The compressor-expander module (CEM) introduces new core turbomachinery noise, but it processes only the small core mass flow and is integrated in the core duct behind the stack, so its contribution is expected to be minor. Fan noise can be reduced, as the electrically driven fan is decoupled from the cycle constraints of a gas turbine and can be tuned for acoustics through lower pressure ratio, lower tip speed, and nacelle liners [39]. Jet mixing noise is not a benefit of the architecture. The bypass stream exits at approximately 287 m/s at take-off against a freestream of 112 m/s, a velocity ratio of about 2.5. This is comparable to the take-off jet velocity of a modern high-bypass turbofan, driven by the same low fan pressure ratio. The waste heat rejected into the bypass duct raises the exit temperature and therefore

[27] URL `https://www.aviationhunt.com/standard-atmosphere-calculator/` [cited 10/06/2026]
[28] URL: https://community.infiniteflight.com/t/a320-family-climb-thrust-profiles/883105 [Cited 16/06/2026]

the exit velocity slightly, a small adverse effect on jet noise. Jet mixing noise is thus treated as neutral and is a candidate for mitigation through nozzle shaping in the detailed design.

The blended wing body integration provides the clearest gains. The aft-placed engines are shielded by the airframe planform: scale-model BWB tests measured 20 to 25 dB of forward-sector reduction in the full-scale 2000 to 4000 Hz band, decreasing to 10 dB or less at lower frequencies. The absence of slats and flaps eliminates high-lift device noise entirely, removing a major airframe source on approach [2].

Landing gear noise is the residual concern. A NASA study found that a fully clean airframe is only about 8 dB quieter on approach than one with gear and high-lift devices deployed, so the gear remains a meaningful contributor even after the high-lift devices are removed. Detailed gear fairing and shaping is therefore deferred to the detailed design phase. The combined reduction from eliminating combustion and core noise, shielding the inlet and exhaust behind the planform, and removing the high-lift devices is large enough that the approach target is expected to be met with margin even before the gear is addressed.

The aircraft is therefore expected to satisfy the requirement and to be no louder than the A320. These conclusions rest on comparison with reference data rather than direct analysis, so aeroacoustic modelling is required to confirm them, with final verification by ground-based measurement during the flight-test campaign.

Low noise emission also contributes directly to the project's ultra-low-impact objective. Noise pollution is a dominant local environmental impact of aviation, causing sleep disturbance and health effects near airports and constraining operations through curfews and noise-based charges. An aircraft no louder than the A320, and quieter on approach, therefore extends the low-impact goal to the community scale. These reductions are a benefit of the architecture chosen for climate and efficiency reasons rather than a separate measure: the fuel cell powertrain that removes combustion emissions also removes combustion and turbine noise, and the blended wing body planform selected for aerodynamic efficiency combined with the body mounted propulsion system shields the ground from engine noise.

5.4. Results

5.4.1. Airfoil Selection

Table 5.4: Airfoil data at the design points.

Parameter	SC(2)-0518 (fuselage)	RAE 2822 (wing)
Take-off Mach number M_{TO}	0.2	0.2
Take-off Reynolds number Re_{TO}	8×10^7	2×10^7
Cruise Mach number M_{cr}	0.68	0.78
Cruise Reynolds number Re_{cr}	5×10^6	5×10^6
Zero-lift angle $\alpha_{C_l=0}$	$-2°$	$-2°$
Cruise lift slope C_{l_α}	$10.9\ \mathrm{rad}^{-1}$	$12.1\ \mathrm{rad}^{-1}$
Take-off maximum lift coefficient $C_{l_{max}}$	2.74	1.8
Moment coefficient C_m	-0.160	-0.165
Sharpness parameter ΔY	0.048	0.025

5.4.2. Lift and Drag Performance

Table 5.5: Whole-aircraft lift slope.

Flight phase	Mach number	Lift slope
Take-off / landing	0.2	$0.065\ \mathrm{deg}^{-1}$
Cruise	0.8	$0.079\ \mathrm{deg}^{-1}$

Table 5.6: Maximum lift coefficient during take-off and landing.

Fuselage	Wing	Aircraft
1.86	1.45	1.74

Table 5.7: Lift conditions for take-off, landing, and cruise.

Flight phase	Air density	Mass	Airspeed	Lift coefficient
Take-off	$1.23\ \mathrm{kg/m^3}$	MTOW	$73.2\ \mathrm{m/s}$	0.571
Landing	$1.23\ \mathrm{kg/m^3}$	$0.955\,\mathrm{MTOW}$	$72.0\ \mathrm{m/s}$	0.564
Cruise	$0.303\ \mathrm{kg/m^3}$	MTOW	$236\ \mathrm{m/s}$	0.222

Table 5.8: Angle of attack at each flight phase

Flight phase	Lift coefficient	Angle of attack
Take-off	0.571	6.8°
Maximum take-off lift	1.0	13.4°
Cruise	0.222	0.8°
Landing	0.564	6.7°
Maximum landing lift	1.2	16.5

The required coefficients stay below the aircraft maximum lift coefficient (Table 5.6), and for normal take-off and landing the angle of attack stays under the $12°$ scrape angle, so the design does not include high-lift devices.

Table 5.9: Drag results.

Component	C_f	FF	IF	S_{wet} [m^2]
Centrebody (SC(2)-0518) 0.00196	1.60	1	485	
Outer wing (RAE 2822)	0.00247	1.51	1	164
V-tail	0.00251	1.53	1.03	53.4
Drag Divergence Number	Fuselage: 0.82		Wing: 0.83	
Zero-lift drag C_{D_0}	0.00783			
Oswald efficiency e	0.86			
Cruise drag coefficient C_D	0.0122			
Aerodynamic efficiency $\frac{L}{D}$	18.2			

5.4.3. Aircraft Loading

Table 5.10: Load envelope results

Parameter	Units	Value
Manoeuvre Speed (V_a)	$\frac{m}{s}$	97 EAS
Dive Speed (V_d)	$\frac{m}{s}$	295 EAS
Ultimate positive load	g	2.8
Design ultimate positive load	g	4.2
Ultimate negative load	g	-1.0
Design ultimate negative load	g	-1.5

5.4.4. Weight Results

The output MTOM was obtained using an input of 60 127 kg, which was the number used in all subsystem analyses and was the result of the previous iteration. This results in approximately a 20% increase with respect to the preliminary weight calculations. The main growth area was the operative empty weight, where the fuselage and powertrain weight resulted being much heavier than expected initially.

5.4.5. Climb Performance

Figure 5.5 shows all the plots regarding the performance of the aircraft during climb and at sea level, while Table 5.12 contains all the relevant parameters obtained through the methods above. The main finding is the time the aircraft takes to climb up to its cruise altitude (FL400). The A320 class and B737 take roughly 15-20 minutes to climb to FL350-FL390 [40], based on a sea level ROC of $\approx$ 13 m/s [28]. It is important to mention that these values are not at maximum throttle power, but at nominal service power. Thus, a fair comparison is not guaranteed, but based on the ROC at sea level, a performance improvement can be concluded with respect to similar aircraft. This improvement is acknowledged mainly due to the considerable weight reduction of the BWB compared to its conventional counterpart.

Table 5.11: Detailed Weight Estimation Results

Component	Weight (tons)
Wing, W_w	1.190
Empennage, W_{emp}	0.375
Fuselage, W_{fus}	11.779
Powertrain, W_{pwt}	10.600
Landing Gear, W_{lg}	2.361
Fixed Equipment, W_{feq}	8.425
Tanks, W_{tnk}	6.866
OEM	41.596
Payload	16.005
Fuel (H_2)	3.789
MTOM	**61.390**

Table 5.12: Climb Performance Result Parameters

Variable	Value	Explanation
		Sea-Level Performance
V_{min}	42 m/s	See Table 5.3
$V_{Pr_{min}}$	77 m/s	See Table 5.3
$V_{D_{min}}$	102 m/s	See Table 5.3
V_{max}	205 m/s	See Table 5.3
ROC_{max}	19.64 m/s	Maximum rate of climb at sea-level
		Climb Parameters
Service Ceiling	14.6 km	-
Absolute Ceiling	14.8 km	A320 absolute ceiling FL398 (12.1 km) [285]
t_{cl}	12.1 min	Minimum time to climb at cruise altitude with maximum power

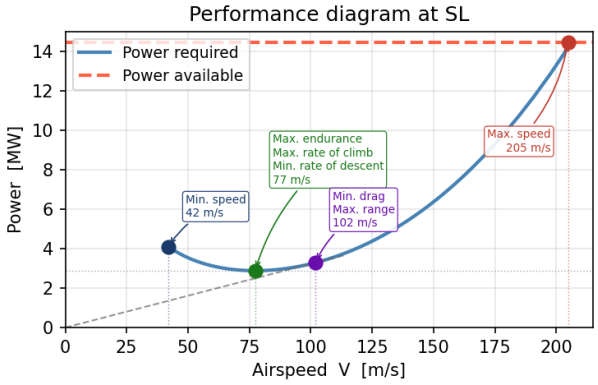

(a) Power against velocity

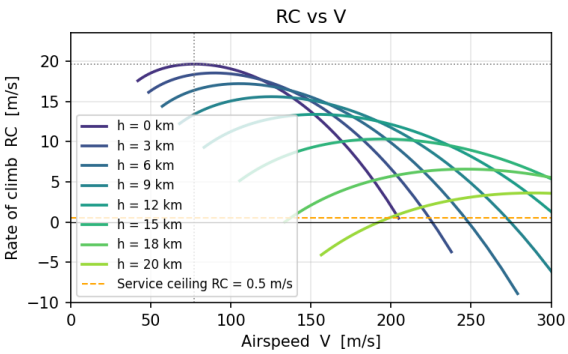

(b) ROC against velocity

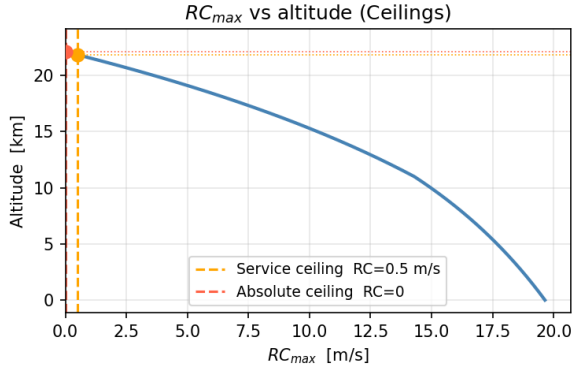

(c) Altitude against maximum ROC

Figure 5.5: Climb and ROC Performance

6. Fuselage Design and Payload Storage

The design of the fuselage and payload storage system of the BWB is presented in this chapter. First, multiple packaging concepts are evaluated to determine the optimal arrangement of the passenger cabin, cargo compartment and liquid hydrogen storage tanks. The selected configuration is then used to size the cabin, cross-sectional geometry and overall fuselage dimensions. Cockpit visibility requirements are subsequently assessed after which the primary fuselage structure is analysed and sized to withstand cabin pressurisation, operational, and landing loads. Lastly the resulting dimensions and storage capacities are presented.

6.1. Information Dependencies

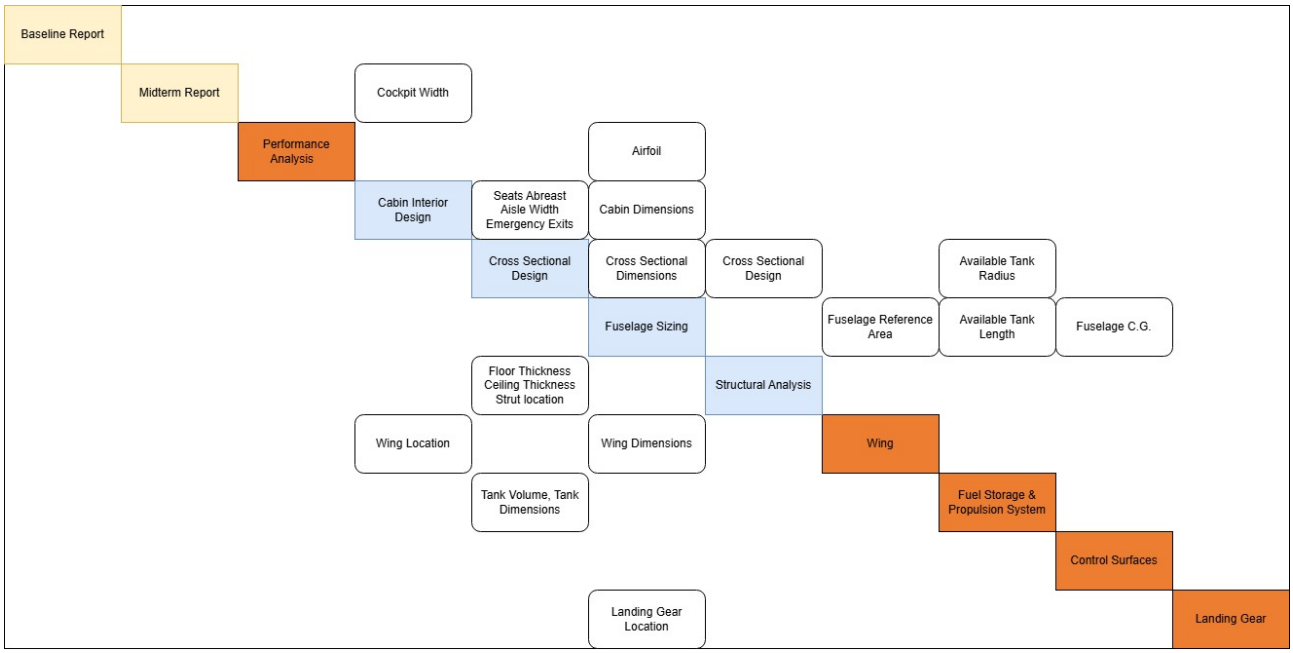

Figure 6.1: N^2 Chart indicating the flow of information within the design of the fuselage payload storage components

6.2. Assumptions

Table 6.1: Model assumptions

ID	Assumption	Variable(s)	Effect
FU1	Height, width and cross section of the fuselage was assumed to be constant along the length of the fuselage	I, σ	Overestimation of area moment of inertia of the cross section contributes to an underestimation of bending stress
FU2	Internal bending moment was assumed to be constant along the length of the fuselage	M, σ	Overestimation of internal bending moment contributes to an underestimation of bending stress
FU3	Fuselage skin was assumed to be a flat plate for the pressurisation calculations	Skin thickness	Uncertainty in required skin thickness
FU4	Airframes are assumed to be squares, whereas I-beams are implemented	Airframe mass	I-beams have lower mass when equal stiffness is provided. Mass of the airframes is overestimated by 5-10~%

Continued on next page

ID	Assumption	Variable(s)	Effect
FU5	No cutouts and cutout reinforcements for holes in the aircraft are considered	Fuselage mass	Fuselage mass is underestimated by 1-2~%
FU6	For the moment calculations the fuselage was idealised with skin and stringers		
FU7	Deformation of the skin was assumed to be linear	v, t	Deformation is underestimated, Required skin thickness is underestimated
FU8	Where applicable, thin walled assumptions were used for the second moment of inertia calculations	I	Area moment of inertia underestimated by 0.1~%
FU9	All calculated thicknesses are assumed to be constant throughout the cross section	Fuselage mass	Overestimation of fuselage mass
FU10	Beams in the floor/ceiling structure were assumed to be clamped		

6.3. Fuselage Design

6.3.1. Packaging

In order to obtain outer dimensions of the fuselage, the size of the cabin, fuel storage system and cargo space are constraining factors. In order to store liquid hydrogen, a cylindrical or circular tank shape is chosen, with spherical caps on each side. For this, four layout possibilities are considered. Each considered option is based on an ovoid cross section, as follows from Table 4.1. The possibility to make use of existing or custom designed unit load devices (ULD's) or to omit these is considered after a trade off is performed. Four packaging options, depicted in Figure 6.2 are subjected to a trade off, which is presented in Table 6.2.

The first option, 'bottom tanks' (Figure 6.2a) is characterised by a main cargo compartment in the rear of the aircraft, behind the cabin. The cabin is located in the middle. Multiple, smaller sized tanks are placed in longitudinal direction underneath the cabin floor, in the bottom of the fuselage.

The second option 'side and rear tanks' (Figure 6.2b) considers three or four tanks. Here, the passenger cabin is placed in the middle of the fuselage. Two hydrogen tanks are placed longitudinally on each side, in the sides of the pressurised area. One or two additional cylindrical hydrogen tanks are placed in the rear of the fuselage, laterally. The Cargo space is located in the belly of the aircraft, underneath the passenger cabin.

The third option 'centre tank' (Figure 6.2c) is characterised by a single cylindrical fuel tank. The tank is located in the centre of the aircraft, where the tank diameter governs the fuselage height. The cabin is split into two compartments, each located on one side of the hydrogen tank. This design features three cargo compartments. One cargo compartment is placed behind the fuselage and fuel tank, whereas the remaining two compartments are located underneath the floor of each cabin compartment.

Lastly, the fourth layout configuration 'rear tanks' (Figure 6.2d) include the hydrogen storage tanks in the rear of the fuselage. The cabin is located in front of the fuel tanks, and spans the complete width of the fuselage. This configuration features a single cargo compartment, located underneath the cabin.

Table 6.2 demonstrates a trade off between the four layout options, for which five criteria are established. 'Space usage' considers the degree to which all available volume in the fuselage is utilized, in order to minimize material use and weight of the aircraft. For the aircraft to be economically feasible, it should provide an acceptable environment for passengers. Therefore, the degree of to which the environment is provides comfortable travel is assessed with 'passenger experience'. 'Safety' entails the likelihood and severity of injury or fatal accidents in case of a system failure. Through 'Operations', consequences of layout for airport operations, as well as in flight operations are taken into account. Lastly, with 'Feasibility of design' implications for other aircraft subsystems is considered. This includes, i.a. impact on stability and structural elements of the aircraft.

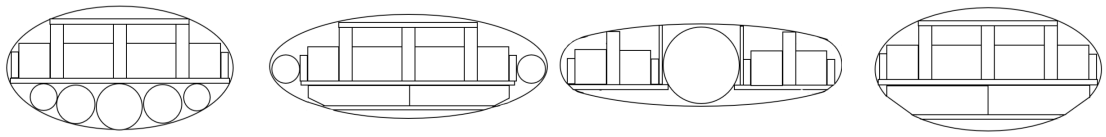

(a) Bottom tanks **(b)** Side and rear tanks **(c)** Centre tank **(d)** Rear tank

Figure 6.2: Cross sectional view of the four packaging options

Table 6.2: Trade off for packaging options

Packaging Option	Space Usage	Passenger Experience	Safety	Operations	Feasibility of Design	Total
Weight	**20%**	**15%**	**30%**	**10%**	**25%**	**100%**
Bottom Tanks	Underutilised space between tanks, tall cross section (3)	possibility for windows, singular cabin (5)	Hydrogen tanks carry impact during belly landing (1)	Unconvenient tank location for refueling (2)	Large tank mass to fuel ratio (2)	2.35
Side and Rear Tanks	Side tanks fit to oval shape, underutilised space below and above side tanks (4)	No windows, singular cabins (3)	Tanks located close to cabin, cargo carries impact during belly landing (3)	Multiple refueling locations needed, yet easily accesible (4)	Requires double bubble pressure shell (3)	3.3
Centre tank	Least tall cross section, underutilised space underneath cabins (5)	Possibility for windows, seperate cabin (3)	Each cabin can be evacuated on one side only, tanks close to cabin, Hydrogen tank carries impact during belly landing (1)	Single tank to be refilled, minimal connection between cabins hampers cabin crew operations (3)	Low tank mass to fuel ratio, requires double bubble pressurisation or two pressurised areas, connected at the cockpit(4)	3.05
Rear tanks	Circular/ Cylindrical tanks don't fit rear fuselage shape, tall cross section (1)	Possibility for windows, singular cabin (5)	Tanks far away from cabin, cargo carries impact during belly landing (5)	Multiple tanks to be refueled, convenient refueling location (3)	Centre of gravity moves severely aft, little space for structural attachment of engines and vertical tail (1)	3

Based on the final scores, the packaging option characterised by two side tanks and a tank in the rear of the fuselage is used to develop the internal layout of the aircraft. First, the cabin is designed internally, in order to obtain outer dimensions of the cabin. This is then combined with the required volume of cargo and fuel tanks and the cockpit, to perform cross sectional and longitudinal sizing of the fuselage simultaneously.

6.3.2. Cabin Design

Before designing the interior of the cabin, a set of constraints is to be defined. Given REQ-OPE-1.1.10-19, (Table A.3), volumetric restrictions are given on aisle width, number of seats abreast, and presence and accessibility of emergency exits. Besides, the aircraft is designed for short to medium range, seat dimensions of economy class are opted for. Thus, a seat pitch and width of 83 cm and 43 cm respectively are used, with an armrest width of 5 cm. [17] Aisle width is constraint to 51 cm in width (REQ-OPE-1.1.14). Cross aisles leading to an exit have a width equal to the width of the exit it leads to, such that the cross-aisles are unobstructed (REQ-OPE-1.1.15). Given the aircraft has 150 passengers, at least two exits type C or larger and one exit type II or larger is required per side of the cabin. Furthermore, there must be floor-level exits at the rear and front of the cabin (REQ-OPE-1.1.19). Moreover, the aisles need to accommodate for a smooth flow of passengers during boarding and deboarding, in accordance with REQ-OPE-2.2.10. Lastly, galleys and lavatories need to be accounted for.

6.3.3. Cross Sectional Design

Given the width of the cabin, a cross sectional design of the fuselage can be made. As the fuselage outer shape is determined by an airfoil, the aircraft does not have a constant cross section throughout its length. Thus, multiple diagrams for the cross section are produced. For the aircraft, four critical cross sectional views

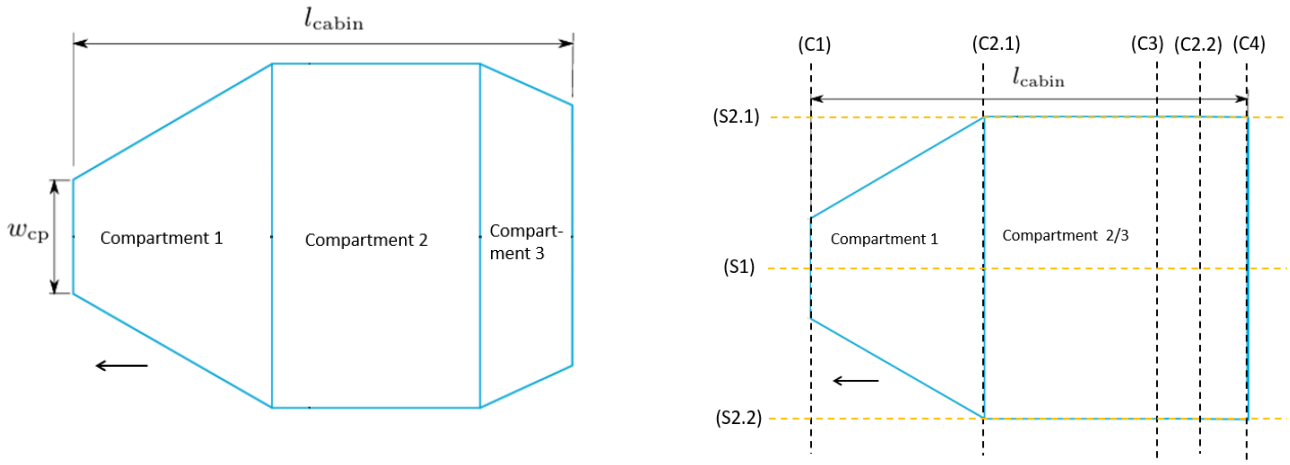

(a) General cabin shape for a blended wing body (top-down view)[41]

(b) Opted cabin shape

Figure 6.3: Cabin shapes for the blended wing body design

along the length are produced, for which the location along the cabin, accompanied by an identification number (C1-C4) is presented in Figure 6.3b. Cross sections C2.1 and C2.2 are identical, and appear twice in cabin compartment 2/3. C2.1 is located at the first seat row of 3x4x4x3 seats abreast, and C2.2 is located at the last seat row.

The first cross sectional views to be produced are C2.1 and C2.2. The reason for this, is that the dimensions of the interior at this locations C2.1 and C2.2 constrain the size of the airfoil to be fitted around the aircraft interior in subsection 6.3.4. The size of the ovoid at this location is constrained by the cabin width, cabin height, and the size of the tanks on the side of the aircraft. Here, the height of the cabin is governed by the aisle height, set at 2m. Furthermore, shoulder height and armrest height of the seats are specified, based on existing aircraft[17]. The height of the ovoid at cross sections C2.1 and C2.2, both in the middle as well as at the side wall of the cabin is then used as an input to size the length of the aircraft.

After the height of the fuselage at all locations along its length is known, as follows from the procedure described in subsection 6.3.4, cross sections C1, C3 and C4 are produced. The fixed heights of the ovoid in the middle of the cabin, as well as at the cabin side walls, are used to find the shape of the ovoid. The remaining cross sectional views are then created by fitting the tanks, cabin and cargo space in the given ovoid.

6.3.4. Length Sizing

The sizing the fuselage length is performed by producing a side view of the aircraft. For this, the airfoil of the body of the aircraft is fit around the cabin and cargo storage. Furthermore, space for the cockpit, landing gear and rear fuel tank is accounted for when fitting the airfoil. The smallest airfoil which can be fit around the interior of the aircraft is then used to determine the length of the aircraft.

This procedure is performed twice, and thus, two side views are produced. The first side view is produced along the centreline of the fuselage (S1). The second side view is produced at either sides of the cabin (S2.1 and S2.2). In Figure 6.3b, green lines indicate the location of these side views.

6.3.5. Cockpit Visibility

As the body of a blended wing aircraft is wider than a conventional tube and wing configuration, the cockpit visibility needs to be assessed. The minimum lateral viewing angle towards each side of the cockpit is 120°(REQ-OPE-1.1.22). Furthermore, a minimum downward visibility of 17°, and upward visibility of 21°is required (REQ-OPE-1.1.20/21). Given the angle of attack at approach equals 7.9°, downward visibility for the pilots shall be at least 24.9°.

6.4. Results

As an initial cabin shape, a shape as presented in Figure 6.3a is used [41]. Due to fuel tanks being present on each side of the cabin, no taper is implemented in compartment 3, leaving a tapered compartment in the front of the cabin, connected to an extended compartment 2, as indicated in Figure 6.3b. Here, compartment 1 houses two of the required exits per side. The third exit is located on the side wall, aft in compartment 2/3, yielding exits both forward and aft in the fuselage. Each exit is accessible through cross-aisles, connecting exits on the left and right side of the cabin. Three aisles are implemented in the cabin, in order prevent congestion during

boarding and deboarding. Based on the number of aisles, a seat configuration of 3x4x4x3 is opted for. The width of the seats, aisles and space to account for structural struts in the cabin which determines the width of the cabin. The length of the cabin is then determined by placing 150 seats, lavatories, galleys, and cross-aisles in the cabin. Iterations of the cabin layout are governed by dimensions of the cockpit, as well as locations of struts after structural analysis.

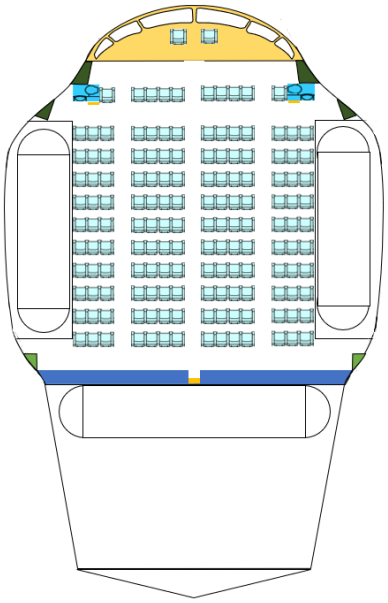

Figure 6.4: Top view of the aircraft including cabin, cockpit and tanks

Figure 6.4 presents a top view of the aircraft, including 150 seats, three fuel tanks, two lavatories, 4 type C exits in the front of the cabin, and two type II emergency exits at the rear of the fuselage. Furthermore, three jump seats, depicted in yellow, are included for flight crew during take off and landing. Exits on either side of the cabin are connected with an unobstructed cross aisle.

In Figure 6.5, the cross sectional view C3 is depicted.

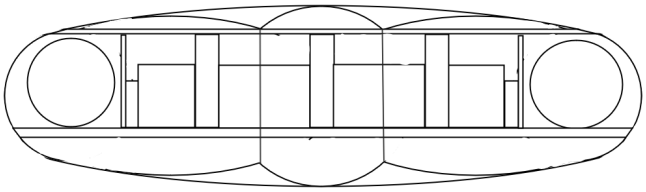

Figure 6.5: Cross section C2

In the cabin, aisles, shoulder height of the seats, and the height of the armrest of the outer seats are depicted. A cross section of the tanks is visible on each side of the cabin. The hydrogen tank is separated from the cabin by a wall. The triple bubble structure has connection points in the middle of the seat blocks with four seats abreast. In between these seats, there is available space for a strut. The dimensions of the cabin, tanks, as well as the outer dimensions of C1, C2.1, C2.2, C3 and C4 are indicated in Table 6.3.

Cargo can be stored in the area enclosed between the pressure shells and cabin floor. The cargo volume is 7.7 m in length (Figure 6.6, and varies in with between 12.3 and 13.0 m. It has a variable height up to 1.1 m. It has an estimated volume of 44 m^2.

The tanks have buffer with the passengers in this image, this is due to the schematic highlighting the largest cross section, however in the shorter sections the tank and bulkhead wall are flush.

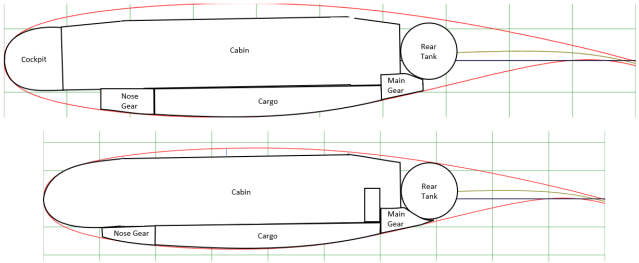

Figure 6.6: Side views S1 and S2

In Figure 6.6, sideviews S1 and S2 are depicted. The fuselage airfoil (Figure 5.2) is fitted around the interior of the aircraft. Here, the cabin, cockpit, rear cylindrical tank and the storage area for the landing gears are depicted. The cabin is tilted downward with 1^o, for an optimised fit of the airfoil. The volume on top of the cabin contains structural elements for pressurisation, and allows for wiring. The volume behind the rear tank contains structural elements for connection of the wing and engines. As S1 is located at the centreline of the aircraft, and S2 at the outer side of the cabin, the airfoil of S1 has a larger chord length. The chord length of S1 determines the length of the fuselage, of 21.4 m. The chord length of section S2 equals 19.0 m

Cockpit Visibility

Figure 6.7 presents the lateral visibility on the right side of the aircraft, from the seat of the first officer. Here, a direct viewing angle of 120 ^{o} is obstructed by the width of the body. Therefore, a mirror is included in the cockpit, of which the position is indicated in red in Figure 6.7. The body of the aircraft is shaped such that the pilot's view through the mirror is unobstructed in the same field of view as an unobstructed 120°viewing angle would provide. In a similar manner, a second mirror is located at the same location. This mirror provides downward visibility of 27°between the lateral viewing angle of 70°and 95°.

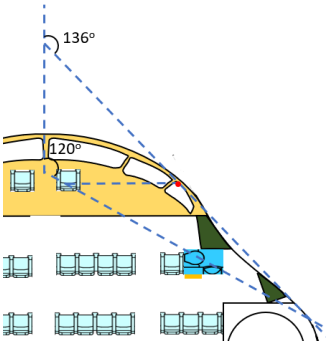

Figure 6.7: Lateral cockpit visibility

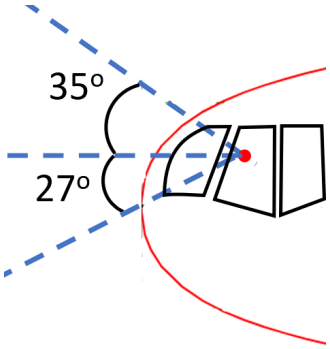

Figure 6.8: Upward and downward cockpit visibility

Figure 6.8 Presents the upward and downward visibility of the aircraft. A forward visibility of 35^o upward is provided, as well as a 27^o downward visibility angle. Here, the pilot's eye is located 0.7 m ahead of the back of the cockpit, and 1.5 m above the cockpit floor.

A final description of dimensions of the aircraft is provided in Table 6.3. Dimensions of the cross sections, fuel tanks, cabin and location of the landing gear is elaborated on. Based on the final dimensions, the surface area of the body of the aircraft was determined to be 234 m^2, which is used for sizing of the wing.

Table 6.3: Dimensions and volumes of the cabin, fuel tanks, cargo space, landing gear location and fuselage

Variable	Value	Explanation
		Fuselage/Pressurised area
$l_{fus_{centre}}$	21.4 m	Length of the fuselage at the centreline of the cabin
$l_{fus_{side}}$	19.0 m	Length of the fuselage at the side of the cabin, 4.25 m to the side of the centreline
$w_{fus_{C1}}$	7.9 m	Cross sectional width of the fuselage, at cross section C1
$h_{fus_{C1}}$	2.7 m	Cross sectional height of the fuselage, at cross section C1
$w_{fus_{C2.1}}$	13.2 m	Cross sectional width of the fuselage, at cross section C2.1

Continued on next page

Continued from previous page

Variable	Value	Explanation
$h_{fus_{C2.1}}$	3.5 m	Cross sectional width of the fuselage, at cross section C2.1
$w_{fus_{max}}$	13.8 m	Maximimum Cross Sectional width of the fuselage, located 7.75 m (longitudinally) from the nose tip, at cross section C3
$h_{fus_{max}}$	3.9 m	Maximimum Cross Sectional height of the fuselage, located 7.75 m (longitudinally) from the nose tip, at cross section C3
$w_{fus_{C2.2}}$	13.2 m	Cross sectional width of the fuselage, at at cross section C2.2
$h_{fus_{C2.2}}$	3.3 m	Cross sectional height of the fuselage, at at cross section C2.2
$w_{fus_{C4}}$	10.9 m	Cross sectional width of the fuselage, at cross section C4
$h_{fus_{C4}}$	2.8 m	Cross sectional height of the fuselage, at cross section C4
S_{fus}	234 m^2	Surface area of the fuselage
		Fuel tanks
r_{tank_s}	0.95 m	Radius of the hydrogen fuel tank located at the side of the fuselage, including tank thickness and insulation
l_{tank_s}	7.5 m	Length of the hydrogen fuel tank located at the side of the fuselage, including tank thickness and insulation
V_{tank_s}	17.83 m^3	Available storage volume in the tank located at the side of the fuselage
r_{tank_a}	0.95 m	Radius of the aft hydrogen fuel tank, including tank thickness and insulation
l_{tank_a}	10.0 m	Length of the aft hydrogen fuel tank, including tank thickness and insulation
V_{tank_a}	23.76 m^3	Available storage volume in the tank located aft in the fuselage
V_{total}	59.42 m^3	Total available volume for hydrogen storage
		Cabin and cargo
V_{cargo}	44 m^2	Available Cargo Volume
$h_{cab_{max}}$	2.3 m	Maximum cabin height (including floor and ceiling thickness)
$h_{cab_{min}}$	2.1 m	Minimum cabin height
$w_{cab_{max}}$	8.5 m	Maximum cabin width
$w_{cab_{min}}$	13.2 m	Minimum cabin width
t_{floor}	20 cm	Floor thickness
$t_{ceiling}$	12 cm	Ceiling thickness
l_{seat}	83 cm	Seat pitch
w_{seat}	43 cm	Seat width
w_{arm}	5 cm	Armrest width
h_{arm}	100 cm	Armrest height
$h_{shoulder}$	135 cm	Shoulder height
h_{aisle}	200 cm	Aisle height
		Landing gear
x_{mlg}	13.4 m	Longitudinal position of the nose landing gear
x_{nlg}	1.47 m	Longitudinal position of the main landing gear
b_{mlg}	8.9 m	Gear span of the of the main landing gear (Distance between outside edges of the outer wheels)

6.5. Structural Analysis

The structural design of a non-circular fuselage presents challenges that differ significantly from those of a conventional circular configuration. While circular fuselages efficiently carry cabin pressurisation through hoop stresses, non-circular geometries introduce substantial bending stresses within the skin and supporting structure. As a result, careful selection and sizing of the primary structural members is required to achieve an efficient balance between structural integrity and weight.

The fuselage structure consists of skin panels, stringers, struts, frames, and floor and ceiling beams, each

performing a distinct role in transferring and resisting loads experienced in flight and on the ground.

The fuselage skin is divided into two parts: the pressure vessel skin and the aerodynamic outer skin. The pressure vessel skin carries cabin pressurisation loads and shear forces, while the outer skin primarily defines the aerodynamic shape.

Stringers are longitudinal stiffeners running between frames and attached to the skin. Their main function is to carry axial loads arising from fuselage bending moments, while also increasing skin stiffness by reducing unsupported panel sizes and delaying local buckling.

Struts are vertical stiffening members spanning between intersections in the multi-bubble structure. They primarily carry axial loads induced by cabin pressurisation.

Frames are transverse structural elements positioned at regular intervals along the fuselage. They maintain the cross-sectional shape and support the skin against pressure-induced deformation. Unlike circular fuselages, where pressurisation is resisted mainly by hoop stresses, frames in non-circular fuselages are subject to significant bending moments due to outward deflection of flat surfaces.

The floor structure consists of crossbeams spanning between opposite sides of the fuselage, supporting cabin and cargo loads while also contributing to resistance against pressure-induced deformation. The ceiling structure is similar but primarily carries axial loads induced by cabin pressurisation.

6.5.1. Structural Analysis Methodology

Frame Sizing

The frames, together with the fuselage skin, maintain the fuselage cross-sectional shape. Two primary loading cases were analysed to determine the required structural capacity, from which an initial airframe mass was subsequently derived.

The first case considers the lateral moment generated when the aircraft rests on its main landing gear. As shown in **??**, the main landing gear are modelled as point loads acting on either side of the fuselage, while the aircraft weight is represented as a point load acting through the centre of the cross-section. The resulting moment is multiplied by a safety factor of 1.5 to account for modelling simplifications.

The second case considers mid-flight loading conditions, shown in **??**. In this case, wing lift is assumed to act at a discrete fuselage attachment point, while fuselage lift and aircraft weight are again modelled as central point loads. The resulting moment is multiplied by the ultimate load factor to satisfy certification requirements. Both loading cases represent simplified 3D loading conditions, as not all forces act at the same longitudinal position, as illustrated in **??** and **??**. The mid-flight case results in the larger bending moment and therefore governs the frame design.

The frames are assumed to be equally spaced at 40 cm intervals, based on reference aircraft. Frame sizing is carried out by defining a required area moment of inertia, allowing flexibility in the cross-sectional geometry. Several simplifying assumptions are made: the frames are uniformly spaced at 40 cm, consistent with industry practice, and the normal stress is assumed to reach the yield stress of Aluminium-Lithium 2050. Using Equation 6.1, the required area moment of inertia is determined.

$$\sigma = \frac{Mz}{I} \Rightarrow I = \frac{M_x z_{max}}{\sigma_y} \tag{6.1}$$

Stringer Sizing

The stringers run longitudinally along the fuselage and support the skin under longitudinal bending, while also delaying local skin buckling. Two global bending cases were considered: a ground case, where only component weights and landing gear reaction forces act on the airframe, and an in-flight case, where lift, weight, aerodynamic moments, and thrust-induced moments act on the structure. The in-flight case, shown in Figure 6.9, produces the largest bending moment and therefore governs the design.

Stringer sizing is based on boom theory, which idealises the fuselage cross-section by lumping the effective skin area into discrete booms located at the stringer positions. An assumed number of stringers is first selected, from which the circumferential spacing is defined. The first stringer is placed at the top centre of the oval cross-section, and all subsequent stringers are distributed symmetrically with equal arc length spacing, as shown in Figure 6.10.

Using Equation 6.1 and Equation 6.2, the required boom area distribution is determined. Due to the symmetric placement of stringers and the assumption of equal stringer area, the boom area contribution can be simplified by taking a constant stringer area outside the summation, leading to a direct expression for the required stringer cross-sectional area A$_s t$

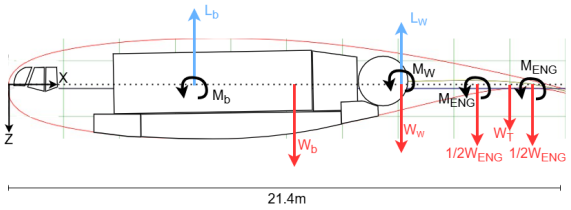

Figure 6.9: Body Longitudinal Loading In Air

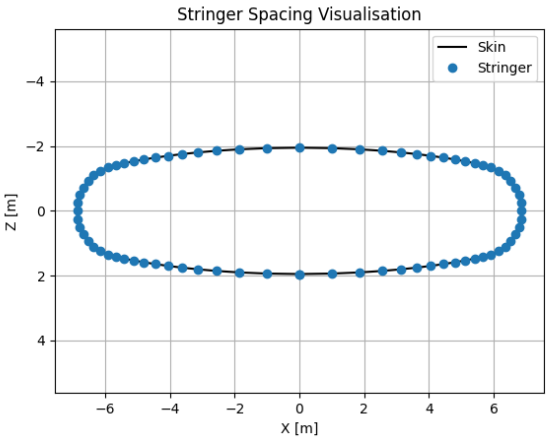

Figure 6.10: Stringer Spacing Example, Using 76 Stringers

$$I_z = \sum_{i=0}^{n_{st}} B_i z_i^2 \tag{6.2}$$

$$B_i = A_{st} + \frac{t_{skin} b}{6} \tag{6.3}$$

Pressurised Cabin Structure

Cabin pressurisation is one of the primary structural design drivers for the proposed non-circular fuselage configuration. Unlike conventional circular fuselages, where pressure loads are primarily carried through membrane stresses, the relatively flat panels in this geometry deform outward under pressure, introducing significant bending stresses in the skin. This necessitates careful structural sizing of both the skin and the supporting stiffening system.

The cabin is pressurised to provide passenger comfort equivalent to a cabin altitude of approximately 6,000 ft, consistent with modern transport aircraft such as the Boeing 787 Dreamliner and Airbus A350.[29] This corresponds to a cabin pressure of

$$p_{\text{cabin}} = 81.2 \text{ kPa}, \tag{6.4}$$

and an ambient cruise pressure of

$$p_\infty = 18.8 \text{ kPa}. \tag{6.5}$$

The resulting design pressure differential is therefore

$$\Delta p = p_{\text{cabin}} - p_\infty = 62.4 \text{ kPa}. \tag{6.6}$$

The fuselage skin and stringers are assumed to be manufactured from Carbon Fibre Reinforced Polyether Ether Ketone (CFR-PEEK), selected for its high specific stiffness, high specific strength, and excellent fatigue and environmental resistance. The low density of this material also contributes to reducing overall structural weight. The material properties used in this analysis are

$$\rho = 1530 \text{ kg m}^{-3}, \tag{6.7}$$

$$E = 146 \text{ GPa}, \tag{6.8}$$

$$\nu = 0.324. \tag{6.9}$$

To evaluate the structural response of the fuselage skin, each panel is modelled as a slender rectangular plate spanning between adjacent frames. The plate dimensions are taken as

$$a = 0.4 \text{ m}, \qquad b = 14 \text{ m}, \tag{6.10}$$

corresponding to the frame spacing and fuselage width respectively. Two limiting boundary conditions are considered: fully simply supported and fully clamped edges. The actual behaviour is expected to lie between these cases due to partial restraint provided by the surrounding structure.

The structural response is analysed using Kirchhoff–Love thin plate theory. Given the large aspect ratio

$$\frac{b}{a} = 35, \tag{6.11}$$

[29] URL `https://flysafe.zone/blog/cabin-altitude-of-6-000-feet-how-the-airbus-a350-manages-cabin-pressure` [Cited 21/05/2026]

the panel exhibits beam-like behaviour. The maximum central deflection is approximated by using **??**. Where α depends on boundary conditions and D is the flexural rigidity of the plate, defined by Equation 6.13.

$$v = \alpha \frac{\Delta p a^4}{D} \tag{6.12}$$

$$D = \frac{Et^3}{12(1-\nu^2)} \tag{6.13}$$

For the limiting cases,

$$\alpha_{cccc} = \frac{1}{384}, \tag{6.14}$$

$$\alpha_{ssss} = \frac{5}{384}. \tag{6.15}$$

To account for stiffening, the skin is reinforced with longitudinal stringers, increasing the effective flexural rigidity given to Equation 6.16. Where I_{str} is the second moment of area of a single stringer and s_s is the stringer pitch. A hat-stringer configuration is adopted, with the second moment of area approximated by Equation 6.17.

$$D_{\text{eq}} = \frac{Et^3}{12(1-\nu^2)} + \frac{EI_{\text{str}}}{s_s} \tag{6.16}$$

$$I_{\text{str}} = \frac{2t_{\text{str}}h^3}{3} + bt_{\text{str}}h^2 \tag{6.17}$$

where t_{str}, h, and b are the stringer thickness, height, and cap width respectively. Based on reference aircraft data, a stringer pitch s_s of 0.15 m was selected, resulting in approximately 126 stringers across the fuselage width [42]. The adopted stringer dimensions are

$$t_{\text{str}} = 0.002 \text{ m}, \tag{6.18}$$

$$h = 0.045 \text{ m}, \tag{6.19}$$

$$b = 0.030 \text{ m}. \tag{6.20}$$

Strut Sizing

The triple-bubble fuselage configuration requires additional structural reinforcement at the intersection points between the individual lobes in order to limit excessive deformation caused by cabin pressurisation [43]. Due to the non-circular geometry, significant loads develop at these intersection regions as the pressure forces acting on the adjacent shell sections are not self-equilibrating. To react these loads, a system of discrete struts is introduced.

The struts act as tension members, transferring pressure-induced forces from the intersection regions into the surrounding fuselage structure. The proposed arrangement is shown in Figure 6.11.

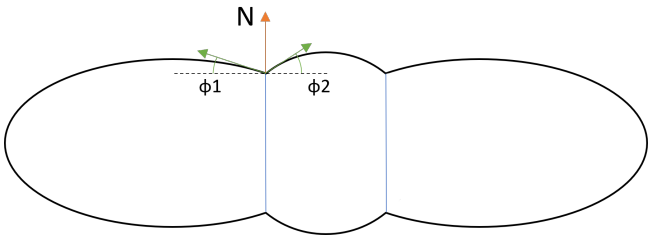

Figure 6.11: Triple-bubble fuselage strut layout.

The struts are attached at regular intervals along the fuselage length, with the strut pitch chosen as an integer multiple of the frame spacing of 0.4 m. This ensures compatibility with the primary fuselage structure and allows the strut loads to be introduced directly into the frames.

The axial load carried by each strut is determined from the pressure forces acting on the adjacent shell sections and is given by

$$N = (R_1 \cdot \Delta p \cdot \sin(\phi_1) + R_2 \cdot \Delta p \cdot \sin(\phi_2)) \cdot l, \tag{6.21}$$

where $R_1 = 3.97$ m and $R_2 = 1.97$ m are the radii of curvature of the two elliptical shell sections at the intersection point, $\phi_1 = 23.8°$ and $\phi_2 = 45.5°$ are the corresponding tangent angles, and l is the strut pitch.

Substituting the design pressure differential yields

$$N = 281360\, l \quad \text{N}. \tag{6.22}$$

The struts are therefore designed as discrete load paths between the lobe intersections and the surrounding fuselage frames, ensuring compatibility with the global pressurised structure.

Ceiling Structure

The ceiling represents a unique structural component of the proposed fuselage configuration, as conventional transport aircraft do not typically incorporate a dedicated load-bearing ceiling structure. Functionally, the ceiling is similar to a standard aircraft floor and consists of transverse crossbeams attached to the fuselage frames, interconnected by longitudinal spacers that provide lateral support and load redistribution.

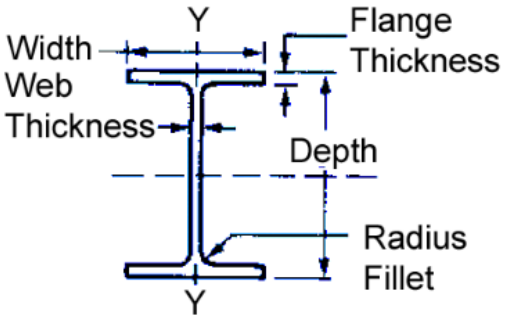

Figure 6.12: Measurements of an I-beam

The crossbeams are assumed to be commercially available I-beams, with the geometry shown in Figure 6.12, manufactured from an aluminium-lithium alloy with density $\rho = 2700\ \text{kg}\,\text{m}^{-3}$ and Young's modulus $E = 77 \times 10^9\ \text{Pa}$. The beams are spaced at the frame pitch of $0.4\ \text{m}$ and are primarily subjected to axial compression due to cabin pressurisation.

The compressive force acting on each crossbeam is determined from the pressure forces generated by the two intersecting fuselage shell segments and is given by

$$N = (R_1 \cdot \Delta p \cdot \cos(\phi_1) - R_2 \cdot \Delta p \cdot \cos(\phi_2)) \cdot l, \tag{6.23}$$

where $R_1 = 12.65\ \text{m}$ and $R_2 = 1.5\ \text{m}$ are the radii of curvature of the fuselage sections at the intersection, $\phi_1 = 13.84°$ and $\phi_2 = 25.84°$ are the corresponding tangent angles, and $l = 0.4\ \text{m}$ is the frame spacing.

Since the crossbeams are predominantly loaded in compression, buckling is expected to govern the design. The critical buckling load is evaluated using Euler buckling theory:

$$P_{cr} = C\frac{\pi^2 E I_{yy}}{L_e^2}, \tag{6.24}$$

where $C = 4$ corresponds to clamped–clamped boundary conditions, I_{yy} is the second moment of area about the weak axis, and L_e is the effective buckling length. An I-beam cross-section is selected, with buckling assumed to occur about the weak axis due to its lower stiffness.

The effective buckling length is reduced through longitudinal spacers positioned between adjacent crossbeams. These spacers act as lateral supports, increasing overall buckling resistance. A trade-off therefore exists between increasing crossbeam stiffness and reducing effective length through additional supports, with the optimal design minimising total mass while satisfying buckling constraints.

For the preliminary sizing, the spacers are assumed to behave as rigid members with a constant cross-sectional area of

$$A_{str} = 2 \times 10^{-4}\ \text{m}^2. \tag{6.25}$$

Floor Structure

The floor structure consists of a set of transverse crossbeams supported by four longitudinal beams located at 3.2 m, 5.4 m, 7.9 m, and 10.1 m from the left reference edge. The longitudinal beams primarily serve to reduce the effective buckling length of the crossbeams and provide mounting points for the passenger seats. Due to time constraints, their detailed structural sizing is not included in this analysis and is deferred to future work.

The crossbeams are subjected to a combined loading scenario consisting of a distributed passenger load, an axial compressive load due to cabin pressurisation, and discrete point loads representing the hydrogen tanks as can be seen in Figure 6.13. This results in a combined bending, axial, and shear loading state governing the structural response.

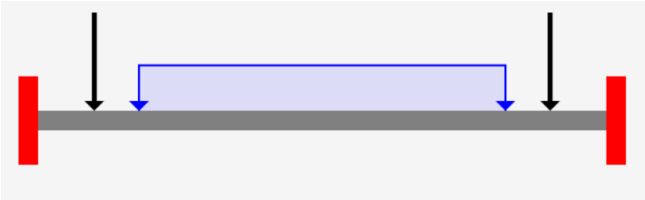

Figure 6.13: Forces on the floorbeam

The crossbeams were modelled as symmetric I-sections defined by the design variables flange width b, flange thickness t_f, web thickness t_w, and overall height h. A constrained optimisation routine was implemented in Python using the SciPy SLSQP solver to determine the minimum feasible section satisfying all structural requirements.

The axial and bending interaction was evaluated using superposition of stresses, where the maximum normal stress is given by

$$\sigma_{\max} = \frac{N}{A} + \frac{M_{\max} c}{I_{xx}}, \tag{6.26}$$

with I_{xx} representing the strong-axis second moment of area.

Global stability was assessed using Euler buckling about the weak axis, with the critical load given by Equation 6.24, where I_{yy} governs the weak-axis stiffness of the section.

Shear resistance was evaluated using the web shear capacity, where the average shear stress is approximated by

$$\tau = \frac{V_{\max}}{A_w}, \qquad A_w = t_w(h - 2t_f). \tag{6.27}$$

The optimisation was carried out under geometric bounds to ensure manufacturability and numerical stability. The solver converged to a feasible minimum section at the lower bound of the design space.

6.5.2. Structural Analysis Results

Frame Sizing

To estimate the mass of a single frame, the cross-sectional area and fuselage circumference were used. As a first-order approximation, the frames were modelled as rectangular sections, providing a conservative and computationally simple estimate.

Each frame is assumed to have a thickness of 40 mm, with the required width determined from the bending requirements. Based on these assumptions, the required width of one frame is 73.4 mm, resulting in a mass of approximately 150 kg per frame.

With a total of 54 frames spaced at approximately 40 cm intervals along the fuselage, the total frame mass is estimated to be 8121 kg. This represents a significant contribution to the overall structural mass, and future work should investigate the inclusion of cut-outs and more efficient cross-sectional optimisation to reduce weight.

Stringer Sizing

For the current loading conditions, the resulting solution for the required stringer area yields a negative value. While this is not physically meaningful, it indicates that the skin alone is sufficient to carry the applied longitudinal bending loads in this simplified analysis.

Despite this result, stringers remain an important part of the structural concept, as their primary function may shift towards improving skin stability and reducing susceptibility to buckling rather than carrying primary bending loads. This outcome also highlights the sensitivity of the result to the current modelling assumptions, and suggests that higher-fidelity loading cases should be used in future analysis to confirm the structural requirements and validate the necessity and sizing of the stringers.

Strut Sizing

Since the members are loaded exclusively in tension, CFR-PEEK is selected as the preferred material due to its high specific strength and stiffness, combined with excellent fatigue and environmental resistance. This makes it well suited for carrying pressure-induced tensile loads within the fuselage structure.

As the struts are located within the pressurised cabin volume, a protective outer casing is required to prevent accidental impact damage from passengers, cargo, or maintenance activities. This casing is assumed to be non-structural and does not contribute to the load-carrying capability of the strut system.

The interaction between the struts, the surrounding fuselage structure, and local skin deformation was not fully resolved within the scope of this study. As such, the sizing presented here should be considered a preliminary estimate. A higher-fidelity finite element analysis is recommended in future work to accurately capture the coupled structural behaviour and optimise the strut arrangement.

Pressurised Cabin Structure

A parametric study was conducted for skin thicknesses between 1.5 mm and 2.5 mm to assess deformation under the design pressure loading. For a skin thickness of 2.5 mm and 126 stringers, the predicted maximum deflection lies in the range

$$0.0025\ \mathrm{m} \leq v \leq 0.012\ \mathrm{m}, \tag{6.28}$$

depending on whether simply supported or clamped boundary conditions are assumed.

While stiffening via stringers significantly reduces deformation, the resulting deflections remain non-negligible, indicating that pressurisation is a dominant design driver for the non-circular fuselage concept.

Using CFR-PEEK for both skin and stringers, the total estimated mass of the pressurised cabin structure is

$$m = 3390\ \mathrm{kg}. \tag{6.29}$$

These results are highly sensitive to boundary condition assumptions and the simplified analytical model. A higher-fidelity finite element analysis is therefore recommended in future work to validate the structural response and refine the stiffening layout.

Ceiling Structure

Using the required critical buckling load, the minimum second moment of area was determined and used to select a commercially available aluminium I-beam section.[31] The selected beam dimensions are

$$\text{Depth} = 0.10\ \mathrm{m} \qquad \text{Width} = 0.08\ \mathrm{m} \tag{6.30}$$

$$\text{Flange thickness} = 0.007\ \mathrm{m} \qquad \text{Web thickness} = 0.004\ \mathrm{m} \tag{6.31}$$

One crossbeam is located at each frame, and ten equally spaced longitudinal spacers are incorporated along the beam span. Based on this arrangement, the total mass of the ceiling support structure is estimated to be

$$m = 2530\ \mathrm{kg}. \tag{6.32}$$

This value includes both the transverse crossbeams and the longitudinal spacers required to achieve the desired buckling resistance.

Floor Structure

The optimisation resulted in an I-section with dimensions: $b = 0.050$ m, $t_f = 0.005$ m, $t_w = 0.003$ m, and $h = 0.100$ m.

The corresponding section properties were:

$$I_{xx} = 1.31 \times 10^{-6}\ \mathrm{m}^4, \tag{6.33}$$

$$I_{yy} = 1.04 \times 10^{-7}\ \mathrm{m}^4, \tag{6.34}$$

$$A = 7.70 \times 10^{-4}\ \mathrm{m}^2. \tag{6.35}$$

The structural mass of the beam was estimated using an aluminium-lithium alloy density of $\rho = 2700\ \mathrm{kg/m^3}$. The mass per beam is given by

$$m' = \rho A = 2600 \cdot 7.70 \times 10^{-4} \cdot 13.8 = 28.7\ \mathrm{kg}. \tag{6.36}$$

The floor consists of 54 crossbeams and 4 transverse beams. Assuming the transverse beams have the same cross section as the crossbeams, results in a mass of

$$m = 1675\ \mathrm{kg}. \tag{6.37}$$

[31] https://www.engineersedge.com/Ibeamsaluminum.htm [cited 17-06-2026]

6.5.3. Total Mass Estimate

Summing the individual component masses yields an estimated total fuselage structural mass of $15{,}715\ \mathrm{kg}$. This value represents a preliminary first-order approximation and is associated with a significant level of uncertainty. Several structural elements have not yet been fully sized at this stage of the design process; for these components, mass estimates have been derived by analogy with already-sized structural members and representative aircraft data.

The current mass estimate does not include the contribution of the fuselage struts, which will be incorporated once their final sizing is completed. Furthermore, additional refinement is expected once cut-outs, local reinforcements, and other geometric discontinuities are explicitly accounted for in the structural model.

Despite these limitations, the obtained total fuselage mass provides a useful first-order estimate and is subsequently used in the centre of gravity calculations presented in the following section.

7. Wing Subsystem

The design and analysis of the wing subsystem will be presented in this chapter. First, a loading diagram is developed to determine the design wing and power loading. These values are subsequently used to size the wing and v-tail planforms. A longitudinal stability analysis is then performed to determine the optimal wing position. Finally, the structural design of the wing and tail boxes is addressed through a mass-optimisation procedure, including load calculations, structural sizing, material selection, and mass estimation. The resulting designs are evaluated against strength, stiffness, stability, and sustainability requirements.

7.1. Information Dependencies

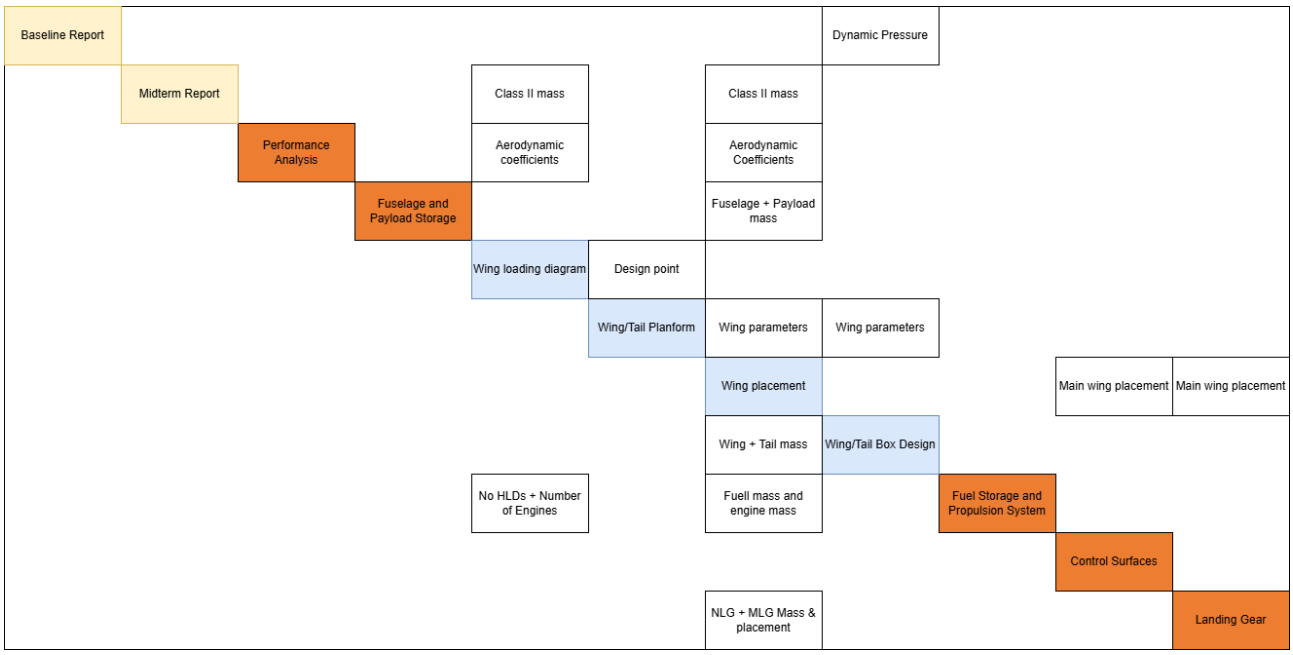

Figure 7.1: N^2 Chart indicating the flow of information within the design of the Wing subsystem

7.2. Assumptions

Table 7.1: Wing subsystem assumptions

ID	Assumption	Variable(s)	Effect
WS1	For sizing wings, the separated wings are assumed to have the same properties as a continuous wing	b, AR	Local effects due wing separation are neglected
WS2	Tail operates in clean flow	V_t	neglects fuselage and wing downwash effects on tail airflow
WS3	Wing properties stay the same after adding winglets except for lower wing fortex generation	C_{D0}	Only induced drag changes, all other changes are neglected
WS5	Thin-walled box structure	skin thickness	Local 3D stress concentrations not captured
WS6	Boom Idealisation	B_i	Simplified local skin-stringer load sharing

Continued on next page

ID	Assumption	Variable(s)	Effect
WS7	Linear elastic material behaviour	Material properties	No plasticity, progressive damage, or post-buckling reserve strength. Gives conservative estimate instead.
WS8	Schrenk wing loading	$c_l(y)$	Detailed CFD and aeroelastic effects not included
WS9	Drag moment neglection	M_{res}	Overestimates the resulting nose-up moment that is acting around the c.g.
WS9	Aircraft is rigid	Cl_α	Overestimates the resulting Cl_α, since wing deflection negates some of the lift that is generated

7.3. Methods

The methodology used to design and analyse the wing subsystem will be shown in this section. First a loading diagram will be made, to determine the wing and power loading. With the wing loading the wing and tail planform can be designed. Finally a longitudinal stability analysis will be performed to find the optimal wing position for sufficient aircraft stability.

7.3.1. Loading Diagram

The wing and the propulsion system can be designed following the design point of the loading diagram. In this diagram multiple constraint lines are plotted. When all these lines are drawn, a feasible design space is being formed. In the design space a point can be chosen, which gives a wing loading [W/S] and a power loading [W/P]. The six constraint requirements that are used to plot the loading diagram will be shortly discussed and are shown below [17]:

1. Stall speed (V_s)
2. Landing field length ($\mathcal{L}_{LFL}$)
3. Cruise speed (V_{cr})
4. Climb rate (c)
5. Climb gradient (G)
6. Take-off field length ($\mathcal{L}_{TO}$)

Stall Speed

The stall speed of the aircraft is the lowest speed the aircraft can attain at its maximum lift coefficient. When decreasing below the stall speed, the aircraft stalls and loses lift. Following CS/-FAR 25.125 for jet aircraft, the approach speed of the aircraft should be 1.23 times the stall speed of the aircraft.[17] This requirement results in the stall speed requirement given by Equation 7.1.[17] An approach speed should be chosen and the mass fraction during landing should be determined.[17]

$$\frac{W_{TO}}{S_w} < \frac{1}{\beta}\frac{\rho}{2}\left(\frac{V_{app}}{1.23}\right)^2 C_{L_{max}} \tag{7.1}$$

Landing Field Length

By definition, the landing field length starts when the airplane flies over an obstacle with a height of 15 m and ends when the aircraft has come to a standstill.[17] The landing field length can be calculated using Equation 7.2.[17] Here, C_{LFL} is the landing field length coefficient and has a value of 0.45 s^2/m for CS/FAR-25 aircraft. V_{S0} is the stall speed of the aircraft during landing conditions. The equation for the requirement is given by Equation 7.3.[17] Furthermore the mass fraction during landing is used.

$$\mathcal{L}_{LFL} = C_{LFL} \cdot V_{S0}^2 \tag{7.2}$$

$$\frac{W_{TO}}{S_w} < \frac{1}{\beta}\frac{\mathcal{L}_{LFL}}{C_{LFL}}\frac{\rho C_{L_{\max}}}{2} \tag{7.3}$$

Cruise Speed

The cruise speed is the speed the aircraft flies at its cruising altitude. The cruise altitude has to be chosen. The speed that needs to be flown is given by REQ-OPE-2.2.1 section A.3, and has a value of Mach 0.8. With increasing altitude, the power delivered by the propulsion unit decreases this is described by the power lapse. The equation for the cruise speed requirement is given in Equation 7.4.[17]

[17] Vos, R., "INTRODUCTION TO AIRPLANE DESIGN," AE1222-II Aerospace Design & Systems Engineering Elements, Delft University of Technology, Delft, Netherlands, 2024. [Cited 18 May 2026]

$$\frac{W_{\mathrm{TO}}}{P_{\mathrm{TO}}} < \eta_p \frac{\alpha_p}{\beta} \left(\frac{C_{D_0} \frac{1}{2} \rho V_{\mathrm{CR}}^3}{\beta \, W_{\mathrm{TO}}/S_w} + \frac{\beta W_{\mathrm{TO}}/S_w}{\pi A R e \frac{1}{2} \rho V_{\mathrm{CR}}} \right)^{-1} \tag{7.4}$$

Rate of Climb

The rate of climb is the vertical speed of the aircraft. The service ceiling of an aircraft is also expressed in terms of this rate of climb. Typically, for transport aircraft the service ceiling is defined as the altitude at which the maximum rate of climb is equal to 100 ft/min, or 0.5 m/s.[17] Equation 7.5 shows the rate of climb relation. In this case, the mass fraction during cruise is assumed to be equal to the mass fraction during take-off.[17] This ensures the most constraining value is used, resulting in a β of 1. The density is. taken at the cruising altitude using ISA relations. The rate of climb constraint is performed for the normal operations as well as the one engine inoperative condition which is determined Equation 7.6.[17]

$$\frac{W_{\mathrm{TO}}}{P_{\mathrm{TO}}} < \eta_p \frac{\alpha_p}{\beta} \left(c + \frac{4 C_{D_0}^{1/4}}{(3\pi A R e)^{3/4}} \sqrt{\beta \frac{W_{\mathrm{TO}}}{S_w} \frac{2}{\rho}} \right)^{-1} \tag{7.5}$$

The rate of climb constraint is performed for both the normal operations and the one engine inoperative as determined by Equation 7.6.[27]

$$\frac{W_{\mathrm{TO}}}{P_{\mathrm{TO}}} < \frac{N_e - 1}{N_e} \eta_p \frac{\alpha_p}{\beta} \left(c + \frac{4 C_{D_0}^{1/4}}{(3\pi A R e)^{3/4}} \sqrt{\beta \frac{W_{\mathrm{TO}}}{S_w} \frac{2}{\rho}} \right)^{-1} \tag{7.6}$$

Climb Gradient

The climb gradient is the ratio between the vertically climbed distance and the horizontally flown distance. The climb gradient must be determined for different operating conditions, following CS/FAR-25 regulations, and are summarised in Table 7.2.[30]

Table 7.2: CS/FAR-25 category and configurations [30]

CS/FAR-25 category	Climb gradient c/V	Configuration	Gear configuration
25.119	0.032	Landing	down
25.121(a)	0.007	Take-off	down
25.121(b)	0.036	Take-off	up
25.121(c)	0.020	Clean	up
25.121(d)	0.033	Landing	up

When flaps will be used during landing and take-off, the Oswald efficiency and the zero-lift drag coefficient will change. This is shown by Equation 7.7 and Equation 7.8 respectively. The extension of the landing gear only influences the zero-lift drag coefficient by a value between 0.01 and 0.025. For this aircraft a value of 0.02 is assumed.[17]

$$\Delta f_e \approx 0.0046 \cdot \delta_f \tag{7.7}$$

$$\Delta_f C_{D_0} \approx 0.0013 \cdot \delta_f \tag{7.8}$$

The required power loading can be found by filling the obtained values into Equation 7.9.[17] Here, $\mathrm{C_L}$ is the value for the clean, take-off, or landing configuration.

In Equation 7.10 the same concept as Equation 7.9 is used, adjusted for a 1-engine inoperative constraint.[17]

$$\frac{W_{\mathrm{TO}}}{P_{\mathrm{TO}}} < \eta_p \frac{\beta}{\alpha_p} \left(\frac{1}{c/V + C_D/C_L} \right) \sqrt{\frac{\rho}{2} \frac{C_L}{\beta W_{\mathrm{TO}}/S_w}} \tag{7.9}$$

In Equation 7.10 the same concept as Equation 7.9 is used, adjusted for a 1-engine inoperative constraint.[17]

$$\frac{W_{\mathrm{TO}}}{P_{\mathrm{TO}}} < \frac{N_e - 1}{N_e} \eta_p \frac{\beta}{\alpha_p} \left(\frac{1}{c/V + C_D/C_L} \right) \sqrt{\frac{\rho}{2} \frac{C_L}{\beta W_{\mathrm{TO}}/S_w}} \tag{7.10}$$

[30] URL https://www.easa.europa.eu/en/document-library/easy-access-rules/online-publications/easy-access-rules-large-aeroplanes-cs-25?page=6#_DxCrossRefBm548991139 [Cited 19th May 2026]

Take-Off Field Length

The take-off field length is the distance measured between the standstill location and the location where the aircraft clears an obstacle of height h_2.[17] In order to determine the constraint posed by the required take-off field length, C_{L_2} needs to be determined using Equation 7.11.[17]

$$C_{L_2} = \left(\frac{V_{S1}}{V_2}\right)^2 C_{L_{\max}} \tag{7.11}$$

After C_{L_2} is determined, the curve can be calculated based on Equation 7.12.[17] The take-off length $\mathcal{L}_{TO}$ is set to be 2,100 m as per REQ-AIR-2.1.3, which can be found in section A.3. This includes both the ground roll and the air distance until a clearance height of 35m. k_T relates the thrust at V_2 to the average acceleration force and is assumed to be equal to 0.85.[17] The obstacle clearance height h_2 is equal to 11 m for CS/FAR-25 aircraft.[17] Finally, the one engine inoperative case for the take-off field length is plotted using Equation 7.13.

$$\frac{W_{\mathrm{TO}}}{P_{\mathrm{TO}}} < \alpha_p \left(1.15\sqrt{\frac{W_{\mathrm{TO}}/S_w}{\mathcal{L}_{TO} k_T \rho g \pi A R e}} + \frac{4h_2}{\mathcal{L}_{TO}}\right)^{-1} \sqrt{\frac{C_{L_2}}{W_{\mathrm{TO}}/S_w}\frac{\rho}{2}} \tag{7.12}$$

$$\frac{W_{\mathrm{TO}}}{P_{\mathrm{TO}}} < \alpha_p \left(1.15\sqrt{\frac{N_e}{N_e-1}\frac{W_{\mathrm{TO}}/S_w}{\mathcal{L}_{TO} k_T \rho g \pi A R e}} + \frac{N_e}{N_e-1}\frac{4h_2}{\mathcal{L}_{TO}}\right)^{-1} \sqrt{\frac{C_{L_2}}{W_{\mathrm{TO}}/S_w}\frac{\rho}{2}} \tag{7.13}$$

7.3.2. Wing Planform Design

With the wing loading from the loading diagram in given subsection 7.4.1, the wing area can be determined using Equation 7.14 where S_f is the fuselage area and S_w is the area of a half part of the wing [41]. The span of the aircraft can be determined using Equation 7.15. The span of the wings separately can be determined by subtracting the width of the fuselage from the total aircraft span. This gives the span for two wings that are connected at their roots. Later further in the design, the two wings will be split apart and moved to the side of the fuselage.

$$S_{ref} = S_f + 2 \cdot S_w \tag{7.14}$$

$$b = \sqrt{AR \cdot S_{ref}} \tag{7.15}$$

To size the wing, the formulas from the AE1222-II course [17] were used. With the number for the design cruise speed, the minimum required quarter chord sweep angle can be calculated, using Equation 7.16. The taper ratio can then be estimated using the value found for the quarter chord sweep angle with Equation 7.17.

$$\Lambda_{1/4} = \arccos\left(\frac{1.16}{M_{CR} + 0.5}\right) \tag{7.16}$$

$$\lambda = 0.2 \cdot \left(2 - \Lambda_{1/4} \cdot \frac{\pi}{180}\right) \tag{7.17}$$

After calculating the taper ratio, the root and tip chord can be calculated using Equation 7.18 and Equation 7.19 respectively. Where b is the span of both wings together.

$$C_r = \frac{2 \cdot S_w}{(1+\lambda) \cdot b} \tag{7.18}$$

$$C_t = \lambda \cdot C_r \tag{7.19}$$

Finally the mean aerodynamic chord can be calculated via Equation 7.20.

$$MAC = \left(\frac{2}{3}\right) \cdot C_r \cdot \left(\frac{1 + \lambda + \lambda^2}{1+\lambda}\right) \tag{7.20}$$

7.3.3. Tail Design

Following the sizing of the wing comes the sizing of the tail. For the tail a trade-off is needed to be performed, to find out what the best empennage system will be. Previously, the wing tip rudders were chosen, yet a type of vertical stabiliser can be implemented for additional controllability[44]. Therefore a trade-off was performed between four options: Winglet tails, Two vertical tails, horizontal tail and vertical tail and finally a v-tail. The trade-off can be seen in Table 7.3. Following the trade-off the best option is the v-tail with a score of 4.6. Therefore the v-tail will be chosen to provide pitch and yaw control. Additionally wing elevators will be added to provide additional pitch control. Finally the sizing process of the v-tail will be discussed below.

Table 7.3: Trade-off for yaw control surface options

Empennage	Surface area	Moment arm	Space occupation	Pitch & yaw control	Total
Weight	**25%**	**25%**	**15%**	**35%**	**100%**
Winglet tail	Surface area needed too large for the wing tips (3)	Not maximized due to wing position (3)	Space available at the wing tips (4)	Can only provide yaw control (3)	3.15
Two vertical tails	Can provide enough area needed (5)	Moment arm can be maximized (5)	Can be placed everywhere (5)	Can only provide yaw control (3)	4.3
Horizontal tail and vertical tail	Extra surface area required (2)	Moment arm can be maximized (5)	Gets in the way of the engine locations (2)	Does provide both pitch and yaw control (5)	2.275
V-tail	Slightly increased surface area (4)	Moment arm can be maximized (5)	Takes more space due to the dihedral angle (4)	Can provide both pitch and yaw control (5)	4.6

The area needed for the vertical tail can be determined by using the volume coefficient method [45]. The equation for the coefficient method is given by Equation 7.21. The area of a single vertical tail can be found by dividing the total tail area by two.

$$S_{vertical} = \frac{c_v \cdot S_{ref} \cdot b_{total}}{x_{tail} - x_{cg,aft}} \tag{7.21}$$

For a v-tail the tail is tilted by a certain dihedral angle. The area of the straight vertical tail needs to be transformed to that for a v-tail with Equation 7.22. This equation gives the area of one v-tail.

$$S_{V,tail} = \frac{S_{vertical}}{\sin^2(\Gamma)} \tag{7.22}$$

After finding the area, the same formulas for the wing sizing from subsection 7.3.2 can be used to size the tail. The quarter chord sweep angle of the tail is a free parameter to change.

7.3.4. Winglet Design

To decrease the induced drag of the aircraft, a winglet can be installed at the wing tips of the aircraft. These winglets decrease the wing tip vortices, which results in an decrease in the induced drag. By using Equation 7.23 the extra aspect ratio that is caused by the winglet can be calculated [24]. The ΔAR is added to the existing wing aspect ratio and gives a new effective aspect ratio for the wing. Here b is the span of the wings of the aircraft and AR the corresponding aspect ratio. Inserting a value for the height h of the winglet, gives a corresponding ΔAR. The taper ratio can be chosen freely. The root chord of the winglet can be set equal to the tip chord of the aircraft wing. The tip chord can than be calculated using Equation 7.19. The dihedral angle of the winglet, shows how much the winglet is tilted and is a free design parameter. Increasing the dihedral, causes the height of the winglet to be lowered, unless the winglets span is increased. Finally the sweep should be close to that of the aircraft's main wings [46].

$$\Delta AR = 1.9 \cdot (\frac{h}{b}) * AR \tag{7.23}$$

7.3.5. Longitudinal Stability

Longitudinal stability of the aircraft can be analysed by using Figure 7.2. The wing, fuselage, elevons and elevators are the main lift-generating components. In addition to producing lift, the wing generates an aerodynamic moment ($M_{ac,w}$) about its aerodynamic centre. Since the fuselage is also modelled as a wing, it likewise produces an aerodynamic moment ($M_{ac,f}$) about its own aerodynamic centre. The elevons and elevators generate aerodynamic forces only, which contribute to the pitching moment about the aircraft's centre of gravity. Lastly,

[24] Oliviero, F., AE2111-II Aerospace Design System Engineering Elements Lecture 2, Delft University of Technology, Delft, Netherlands, 2025

the thrust generated by the four engines is significant enough that its associated pitching moment cannot be neglected and is therefore included in the longitudinal stability analysis.

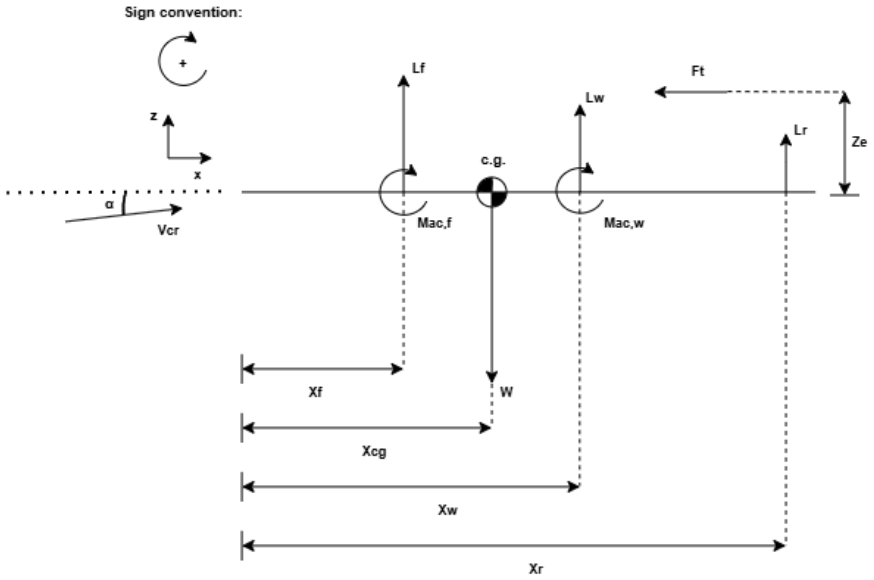

Figure 7.2: Free-body diagram in cruise condition

From the FBD, the longitudinal moment equilibrium about the centre of gravity is obtained by summing the individual moment contributions, resulting in Equation B.29. This expression is subsequently non-dimensionalised to derive the total moment coefficient C_m, which is expanded in terms of the relevant aerodynamic coefficients and corresponding angles of attack, which results in Equation B.30.

The pitch stability derivative of the complete aircraft is obtained by differentiating Equation B.30 with respect to α, resulting in Equation B.31. This expression is evaluated for a range of wing positions, after which different loading configurations are considered to assess their effect on the C_{m_α} slope. Based on the neutral point location, which is computed using Equation B.34, a wing position is selected that provides longitudinal stability over all the operational loading configurations.

7.4. Results

After all the methods are discussed, the process can be followed to form a complete wing and tail planform. These two planforms will result in the optimal wing position on the aircraft.

7.4.1. Design Point Selection Results

Filling the values from Table 7.4 in the process explained in subsection 7.3.1, results in the constraint lines. In the initial design a number of 6 engines was used. As explained in subsection 8.3.3, the six engines are not feasible due to space constraints. Therefore the choice is made to use 4 engines. Therefore the Rate of Climb, Climb Gradient and the Take-off field Length constraint lines changes, with respect to the loading diagram made for the initial design. As explained in subsection 5.3.1 there is also no need for HLD's. This has influence on the Stall Speed, Landing-field Length and the Climb Gradient constraints. Due to these changes in design constraints, the optimal design point shifted.

Table 7.4: Loading diagram parameters

Parameter	Value	Parameter	Value	Parameter	Value
M_{cr}	0.80	V_{cr}	234.7 m/s	V_{app}	72 m/s
V_{stall}	58.55 m/s	$C_{L_{\max,\text{TO}}}$	1.0	$C_{L_{\max,\text{land}}}$	1.2
C_{D_0}	0.007	e	0.9186	AR	4
h_{cr}	12192 m	ρ_{cr}	0.303 kg/m^3	ρ_{land}	1.225 kg/m^3
β_{land}	0.96	α_p	0.94	η_p	0.43

The new loading diagram can be seen in Figure 7.3. To keep the implementation of this change easy, the wing loading was kept constant and only the power loading changed. The new values are given in Figure 7.5.

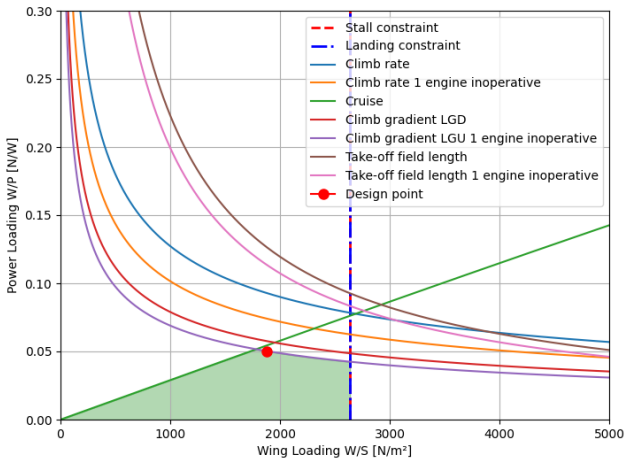

Figure 7.3: Loading diagram

Table 7.5: Comparison of initial and final design parameters

Parameter	Initial Design	Final Design
Wing Loading W/S	1875 N/m^2	1875 N/m^2
Power Loading W/P	0.054271 N/W	0.05035 N/W

7.4.2. Wing Sizing Results

With the wing loading found in subsection 7.3.1 and the MTOW of 60126.97 · 9.81 N as found in subsection 5.4.4, the total reference area of the aircraft can be determined and was found to be 314.58 m^2. Substituting the value for the reference area in Equation 7.14 results in a total wing area of 80.58 m^2. Completing the process described in subsection 7.3.2 gives all the parameters needed for the wing sizing. The results are shown in Figure 7.6. A plot of the wing planform is shown in Figure 7.4. Here the wing root does start at and offset of 6.6 m, which is half of the fuselage width in the y-direction, since the wing will be attached to the side of the fuselage.

Table 7.6: Wing size parameters

Parameter	**Symbol [unit]**	**Value**
Wing span (complete aircraft)	b [m]	35.47
Half wing area	S_w [m^2]	40.292
Wing span (half)	b_w [m]	22.273
Wing aspect ratio	AR_w [-]	6.15
Quarter chord sweep	$\Lambda_{1/4}$ [deg]	27
Leading edge sweep	Λ_{LE} [deg]	30.8
Dihedral angle	Γ [deg]	5
Taper ratio	λ [-]	0.3
Root chord	C_r [m]	5.54
Tip chord	C_t [m]	1.69
Mean aerodynamic chord	MAC [m]	3.96

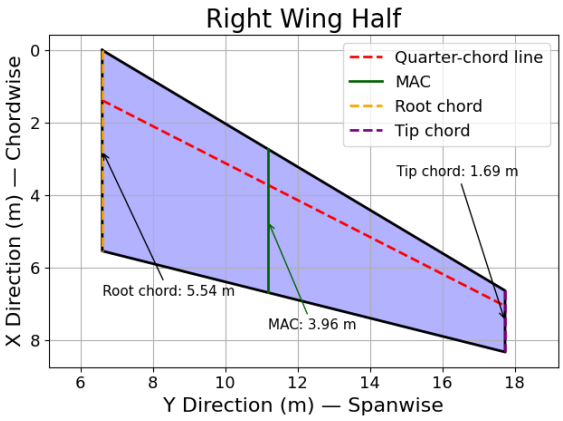

Figure 7.4: Wing planform

7.4.3. Tail Sizing Results

Filling in the reference area found, results in a total tail area of 27.24 m^2. Therefore each tail part will have an area of 13.618 m^2. For the tail a quarter chord sweep of 34 degrees has been chosen, together with an tail aspect ratio of 1.5. The dihedral angle of the tail was set to be 70 degrees, to be able to keep enough space available to mount the aircraft engines and to make sure the rudder does not lose to much effectiveness. Filling in these values results in the v-tail parameters shown in Figure 7.7. Figure 7.5 shows the v-tail, when looking perpendicular onto the surface of one of the v-tails. The location of the v-tail is set to be as far aft as possible. The cg loacation of the tail will therefore be at 20.7 m seen from the nose of the aircraft.

Table 7.7: Tail size parameters

Parameter	Symbol [unit]	Value
Tail area	S_t [m^2]	13.618
Tail span	b_t [m]	4.52
Dihedral angle	Γ [deg]	70
Quarter chord sweep	$\Lambda_{t_{1/4}}$ [deg]	34
Aspect ratio	AR$_t$ [-]	1.5
Taper ratio	λ [-]	0.3
Root chord	C_r [m]	5.54
Tip chord	C_t [m]	1.69
Mean aerodynamic chord	MAC [m]	3.2

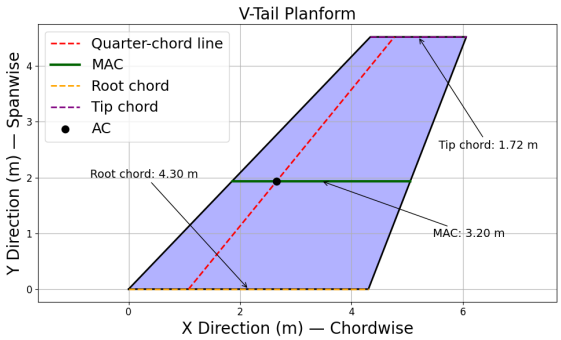

Figure 7.5: Tail planform

The position of the tail was set to the maximum value possible. This resulted in the root of the tail starting at the distance of 17.5 m from the nose of the aircraft. This causes the cg of the tail at a distance of 20.64 m. Finally the tail root will start at 4 m away from the centreline of the aircraft. The position on the fuselage can be seen in Figure 7.6. The side view shown is taken from the point where the root of the wing will touch the fuselage. Since the fuselage has sweep, the middle of the fuselage will be longer. Therefore the fuselage shape shown does not represent the actual aircraft length. The red part in the figure shows a structural member that is added to the bottom of the tail, to make sure that the tail can stay in a upright position and does not have to be tilted to be mounted. Also it causes the rudder to be partially outside of the fuselage boundary layer.

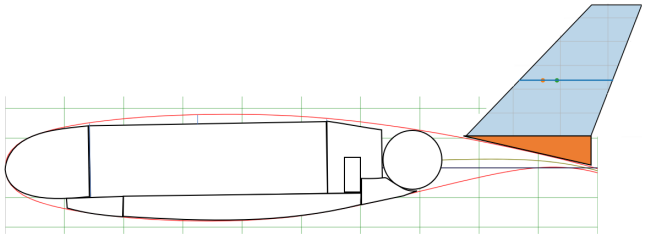

Figure 7.6: Tail location on the side of the fuselage

7.4.4. Winglet Results

In Equation 7.23 a value of 1.8 m for the height of the winglet has been filled in. This results in a ΔAR of 0.95. The root chord of the winglet is the same as the tip chord of the wing, which is given in Figure 7.6. The taper ratio of the winglet is chosen to be 0.5. This results in a tip chord of the winglet of 0.85 m. The sweep of the winglet is set to be 30 degrees. Therefore no Mach waves occur during the cruise velocities achieved, since this is a higher value than the minimum sweep needed, given by Equation 7.16. At the root of the wing, the winglet goes straight up. This is done, such that the plane can still fit in the 36 m. Therefore the winglet span is the same as the winglet height. The winglet parameters can be seen in Table 7.8.

Table 7.8: Winglet size parameters

Parameter	Symbol [unit]	Value	Parameter	Symbol [unit]	Value
Quarter chord sweep	$\Lambda_{t_{1/4}}$ [deg]	30	Tip chord	C_t [m]	0.85
Taper ratio	λ [-]	0.5	Winglet Height	h [m]	1.8
Root chord	C_r [m]	1.69	Extra Aspect Ratio	ΔAR [-]	0.95

7.4.5. Stability Results

Plotting the C_{m_α} slope for a range of different wing positions results in Figure 7.7a. It can be seen that C_{m_α} varies for different loading conditions at a given wing position (X_{LEMAC}). From Figure 7.7a, it is evident that as the centre of gravity moves further aft, the aircraft becomes progressively less stable. It is therefore desirable for the aircraft to remain inherently stable ($C_{m_\alpha} < 0$) regardless of the loading configuration considered. The loading configurations included in the analysis are summarised in Table 7.9.

Table 7.9: Aircraft CG for all considered loading in cruise

Configuration	$\mathbf{X_{cg}}$ [m]	Loading description
Forward CG	10.69	Payload and only fuel in both forward tanks.
Aft CG	12.19	No payload, only fuel in the aft tank.
MTOW CG	10.94	payload and fuel load.
Forward tanks drained first CG	11.05	Full payload with only aft tank still having fuel load.
No payload CG	11.98	No payload, full fuel load.
No fuel CG	10.95	Full payload, no fuel load.
OEW CG	12.10	No payload, no fuel load

The wing position can be exactly pinpointed in Figure 7.7a by looking at where the blue line crosses the dashed green line, as this is the X_{LEMAC} location where the neutral point exceeds both the most forward and the most aft centre of gravity location, making the aircraft inherently stable for all loading configurations. This crossing point however is not the final X_{LEMAC} location, since a small amount of contingency is required. This contingency is accounted for by adding 5% of the MAC of the wing ($\bar{c}_w = 3.95$ [m]), giving a final longitudinal wing position of $X_{LEMAC} + 0.05 \cdot \bar{c}_w[m]$. From the graphs it can be seen that this crossing point happens at $X_{LEMAC} = 13.4$ [m], adding the contingency results in a final wing position of 13.6 [m].

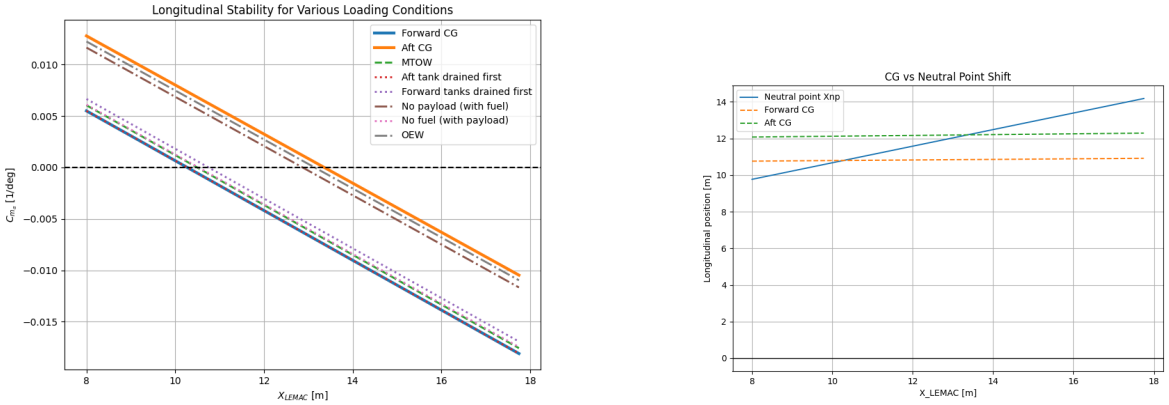

(a) C_{m_α} against X_{LEMAC}

(b) X_n location against X_{LEMAC}

Figure 7.7: Longitudinal stability

The loading of the aircraft can be visualised by a potato plot, this diagram shows the cg shift when different components are loaded at different times. This plot looks rather unconventional due to the majority of the payload loading in front of the centre of gravity location. Also the neutral point and limit for controllability have been added to show the stability of the aircraft during all loading conditions.

With the horizontal position of the wing determined, its vertical position can now be established. In figure Figure 7.9 it can be seen that the emergency exit (shown in red) is placed at the back of the aircraft. Therefore the wing cannot be placed in the middle of the fuselage. Placing the window at the bottom of the fuselage, would cause part of the airfoil shape to fall outside of the fuselage. Therefore spars can not be connected and extra surface area would have to be added, which would in crease the drag. A figure of the aircraft wing position can be seen in Figure 7.9, where the airfoil is coloured in blue.

7.5. Wing Box Design: Wing and Tail

The wing box design is driven by two primary objectives: structural integrity and minimum mass. To determine the optimal layout and dimensions, an optimisation routine was developed that minimises structural mass while satisfying all strength and stiffness requirements.

The wing box is modelled as a three-cell thin-walled structure comprising front and rear spars, upper and lower skins, discrete stringers, spar caps and spanwise ribs. Structural analysis is performed using boom idealisation for bending and a multi-cell shear flow method for torsion and transverse shear loads.

The optimisation routine directly varies the stringer spacing and geometry, spar-cap area and rib spacing. A design is considered valid when the maximum boom stress remains below 85% of the material yield strength,

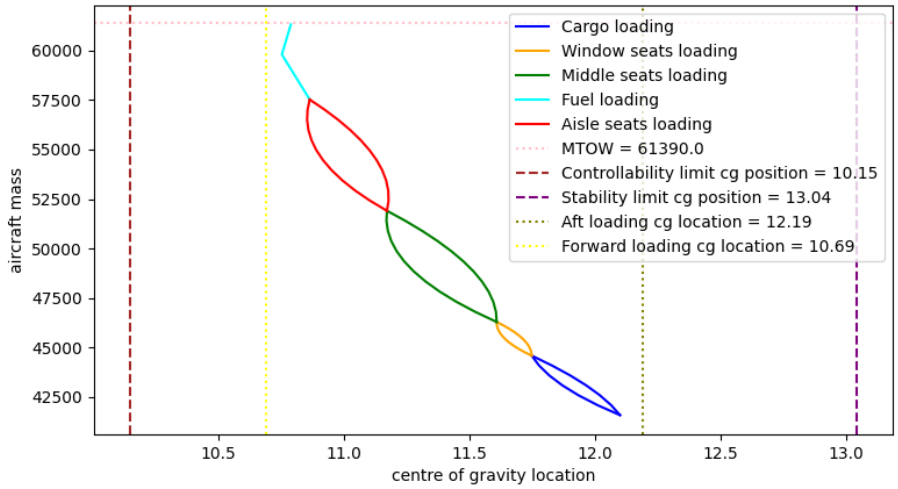

Figure 7.8: Loading Potato Plot

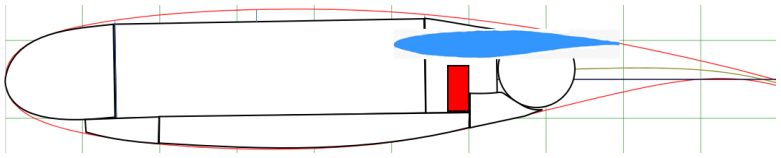

Figure 7.9: Wing position on the fuselage side

the wing-tip deflection and twist do not exceed $1.5\,\mathrm{m}$ and 1.5° respectively, stringer column buckling remains below 85% of the critical stress and all component dimensions remain within predefined manufacturing limits.

For the final design, the code outputs the skin and spar-web thickness distributions, stringer geometry and spacing, spar-cap area distribution and a component-wise mass breakdown including the total mass of a single wing.

7.5.1. Load Calculation

The airfoil geometry is determined using an airfoil coordinate file, and the wing is discretized to a number of spanwise stations at which sizing is calculated. The chord length is calculated at each station through:

$$c(y) = c_r + \frac{c_t - c_r}{b/2} y \tag{7.24}$$

where c_r and c_t represent the root and tip chords respectively. The front and rear spars are located at $0.15c$ and $0.60c$, creating three structural cells.

To calculate lift, the Schrenk approximation is used for the lift distribution and then scaled to the limit load factor of 4.2 (including safety factor).

$$c_e(y) = c_{e0}\sqrt{1 - \left(\frac{y}{b/2}\right)^2} \qquad c_s(y) = \frac{c(y) + c_e(y)}{2} \tag{7.25}$$

$$w_L(y) = L_{\text{design}} \frac{c_s(y)}{\int c_s(y)\, dy} \qquad L_{\text{design}} = nW \tag{7.26}$$

The wing weight was distributed proportional to local chord, and the net load at each station was calculated:

$$w_W(y) = W_{wing} \frac{c(y)}{\int c(y) dy}, \qquad w(y) = w_L(y) - w_W(y) \tag{7.27}$$

To calculate shear force and bending moment, the net load is integrated twice:

$$V(y) = \int_y^{b/2} w(\eta)\, d\eta, \qquad M(y) = \int_y^{b/2} V(\eta)\, d\eta \tag{7.28}$$

These are the primary loads used for sizing. To calculate torque, the aerodynamic pitching moment and lift-induced torque are considered with airfoil aerodynamic center at $x_{ac} = 0.25c$. The shear center is determined, and then torsion is calculated through:

$$T'(y) = w_L(y)[x_{sc} - x_{ac}]c(y) + \frac{1}{2}\rho v^2 c(y)^2 C_m, \qquad T(y) = \int_y^{b/2} T'(\eta)d\eta \tag{7.29}$$

The structure was then idealised into booms, with:

$$B_i = A_{structural,i} + A_{skin,i}, \qquad A_{eff} = \frac{ts}{6}(2 + \frac{\sigma_L}{\sigma_i}) + \frac{ts}{6}(2 + \frac{\sigma_R}{\sigma_i}) \tag{7.30}$$

where t and s represent skin thickness and stringer spacing respectively. The next analysis is on bending, where the neutral axis and second moment of inertia are calculated through:

$$\bar{z} = \frac{\Sigma B_i z_i}{\Sigma B_i}, \qquad I_{xx} = \Sigma B_i (z_i - \bar{z})^2 \tag{7.31}$$

Skin Sizing

In order to size the skin, shear flow and panel buckling loads are considered. Required skin thickness due to shear yield is calculated through:

$$t_{shear} = \frac{|q|}{\tau_{allow}} \tag{7.32}$$

And panel buckling skin thickness is calculate by rearranging the standard plate buckling equation for t:

$$t_{buckling} = b\sqrt{\frac{\sigma_{cr}}{(k_c \pi^2 E)/(12(1-v^2))}} \tag{7.33}$$

After calculating both sizes, the larger of the two is taken as the skin thickness for the given station.

Spar Web Sizing

To size the spar web, shear yield and shear buckling are considered. They are calculated through:

$$t_{shear} = \frac{|q|}{\tau_{allow}}, \qquad t_{buckling} = b\sqrt{\frac{12(1-\nu^2)\tau_{cr}}{k_s \pi^2 E}} \tag{7.34}$$

Wing twist is calculated based on the twist rate $d\theta/dy$ determined in the multi-cell shear flow analysis:

$$\frac{d\theta}{dy} = \frac{1}{2AG}\oint \frac{q}{t} ds, \qquad \theta(y) = \int_0^y \frac{d\theta}{dy} dy \tag{7.35}$$

For compatibility, all cells share the same twist rate. This calculated twist must satisfy:

$$|\theta| \leq 1.5^\circ \tag{7.36}$$

Stringer Sizing

Originally, T-stringers were used for the optimiser, but large compression loads caused column buckling issues. As such, the team opted for hat stringers instead due to larger weak axis moment of inertia for similar area. The sizing was performed by iterating through a set of predetermined stringer geometries defined by:

- h = hat height
- b_{top} = top width
- b_{base} = base width
- t = wall thickness

For each option, stringer area and weak axis moment of inertia are calculated, and a final geometry and size are chosen based on stress and column buckling requirements.

For bending stress, the stringers fail if the maximum boom bending stress exceeds 85% of the material yield strength, i.e. utilisation rate ≥ 0.85:

$$\sigma_i = \frac{M(z_i - \bar{z})}{I_{xx}}, \qquad U_i = \frac{|\sigma_i|}{\sigma_{allow}} \tag{7.37}$$

Euler column buckling is then calculated by testing compression between ribs and calculating the critical load, where K is the Euler effective length factor:

$$P = \sigma A, \qquad P_{cr} = \frac{\pi^2 EI}{KL^2} \tag{7.38}$$

And the utilization is calculated through:

$$U_b = \frac{P}{P_{cr}} \tag{7.39}$$

where $U_b \leq 0.85$.

Spar Cap Sizing

Spar caps are represented as concentrated booms at the upper and lower ends of the spars. The required spar cap area is obtained from the boom stress sizing loop, and the selected spar cap area must satisfy:

$$A_{cap,req} \leq A_{cap} \tag{7.40}$$

They contribute strongly to I_{xx} due to their locations near the largest $|z|$ values, and were sized to reduce bending stress and deflection.

Rib Modelling

In the optimiser, ribs are included primarily as buckling supports. Rib spacing effects the skin and spar web panel aspect ratios, as well as the stringer buckling length.

Bending Deflection

The final check for the optimizer is based on maximum wing bending deflection. The spanwise flexural rigidity is calculated through an equivalent transformed-section stiffness, calculating the modular ratios between materials and scaling the geometry based on the result. The curvature was calculated as:

$$\kappa = \frac{M(y)}{EI(y)} \tag{7.41}$$

With the bending slope and deflection calculated through:

$$\phi(y) = \int_0^y \kappa(\eta) d\eta, \qquad w(y) = \int_0^y \phi(\eta) d\eta \tag{7.42}$$

The final design must satisfy $w_{tip} \leq w_{allow}$.

V-Tail Modifications

This optimiser is also configurable to size the v-tail of the aircraft, mainly by making changes to the loading. The aerodynamic normal force on one v-tail panel is calculated through:

$$F_{panel} = nq_\infty S_{panel} * C_{L_h} \tag{7.43}$$

and distributed spanwise in proportion to local chord:

$$w_N(y) = F_{panel} \frac{c(y)}{\int_0^L c(y) dy} \tag{7.44}$$

The panel normal force is then resolved into vertical and side-force components based on the tail dihedral angle, with:

$$w_z(y) = w_N(y) \cos(\gamma), \qquad w_x(y) = w_N(y) \sin(\gamma) \tag{7.45}$$

After which the vertical and lateral bending moments are calculated separately and then combined into a resulting bending moment:

$$M(y) = \sqrt{M_z(y)^2 + M_x(y)^2} \tag{7.46}$$

The rest of the calculations are the same as for the wing, just using the tail geometry and loads.

7.5.2. Material Selection and Mass Calculation

The material selection process was performed based on analysis of load types on the different components and the results provided by the optimizer. The considered materials were Al-Li 2050 and continuous carbon fiber reinforced polyether ether ketone (CFR-PEEK). Other potentially super sustainable materials were considered, such as mass timber. However, in practice, bio-based materials like this are simply not yet advanced enough to be feasibly used in a structure like a wing box for a large aircraft. Strength-to-volume ratio is the main issue, as for its standard use in construction there is much more volumetric space that can be allocated to the material. Flammability is also a concern, as for a hydrogen aircraft any flammability risks must be mitigated. For components like the skin, stringers, and spar caps, composites work well due to the geometry allowing for long, uninterrupted fibers. However, for spar webs, due to the multiple load types present, they are more likely to experience out-of-plane stresses and transverse shear loads. As such, for the spar webs, a material such as Al-Li 2050 that exhibits isotropic material properties is preferable. This is the same for ribs, as they will have many cutouts which compromises the strength of composites due to limitations in fiber length. For both v-tail and wing, CFR-PEEK was selected for stringers, skin, and spar caps, with Al-Li 2050 for ribs and spar webs.

The mass per component is calculated based on the thicknesses and areas determined by the optimizer. They are listed below:

$$m'_{skin} = \rho_{skin}[(L_{1,u} + L_{1,l})t_1 + (L_{2,u} + L_{2,l})t_2 + (L_{3,u} + L_{3,l})t_3] \tag{7.47}$$

$$m'_{spar} = \rho_{spar}[h_f t_f + h_r t_r] \tag{7.48}$$

$$m'_{stringer} = \rho_{stringer} N_s A_s \tag{7.49}$$

$$m'_{cap} = \rho_{cap} N_c A_c \tag{7.50}$$

$$\tag{7.51}$$

where N_s and N_c represent the number of stringers and spar caps respectively. The rib mass is based on a predetermined geometry and a material fraction that considers the fraction of the total rib area with material in it. The total mass of the wing is calculated by integrating the component mass per unit span along the entire span. The optimiser finds a design through the following process:

1. Geometry and load generation (aerodynamic loads, weight loads, shear, moment, torque)
2. Boom idealisation and bending analysis
3. Stringer and spar-cap sizing
4. Buckling verification
5. Multicell shear-flow analysis
6. Skin and spar-web sizing for shear, buckling, and twist
7. Twist and deflection calculation
8. Mass calculation and self-weight update
9. Constraint verification and storage of valid designs
10. Selection of the minimum-mass valid design

7.5.3. Fuselage Connection

Generally, aircraft wing boxes extend through the fuselage to connect both wings and create continuous load paths. However, due to the positioning of hydrogen tanks in the cabin, this is not possible. As such, it becomes much more difficult to connect the wing to the fuselage. In order to keep the load paths as continuous as possible, the front and rear spars will continue through the fuselage and into the wing on the other side. Based on the position of the wing, there is some space that must be filled in order for the root chord to smoothly connect to the fuselage. This is treated as part of the fuselage, and is not included in the wing box sizing calculation due to time constraints. However, a conservative estimate for the total mass including the blended section and spar continuation was taken by multiplying the wing mass by 1.2.

For the V-tail, lug fittings will be used to attach the spars and distribute the loads into the fuselage, as is standard for empennage attachment in large commercial aircraft. In order to estimate this mass, the calculated mass will be multiplied by 1.15. In addition to this, the aircraft uses electromechanical actuators for elevons and ruddervators rather than hydraulics. A conservative estimate for the mass of one of these actuators for an aircraft the size of the A320neo is around 20kg[47]. Using two of each per wing for redundancy as is standard adds a mass of approximately 40kg per wing, and 40kg per V-tail panel.

7.5.4. Results

After setting values and determining geometry, the mass and sizing results for the wing and v tail are determined. For the wing, the spanwise loading, internal shear, bending moment, and torque were calculated, and the resulting sizing for each component is shown in Figure 7.10. The constraints are then checked in Figure 7.11. Finally, the mass distribution per component is plotted in Figure 7.12. The optimised design ends up with a total per-wing mass of 462.403 kg, which is then increased to 1189.767 kg for both wings including the blended area, spar continuation, and actuators.

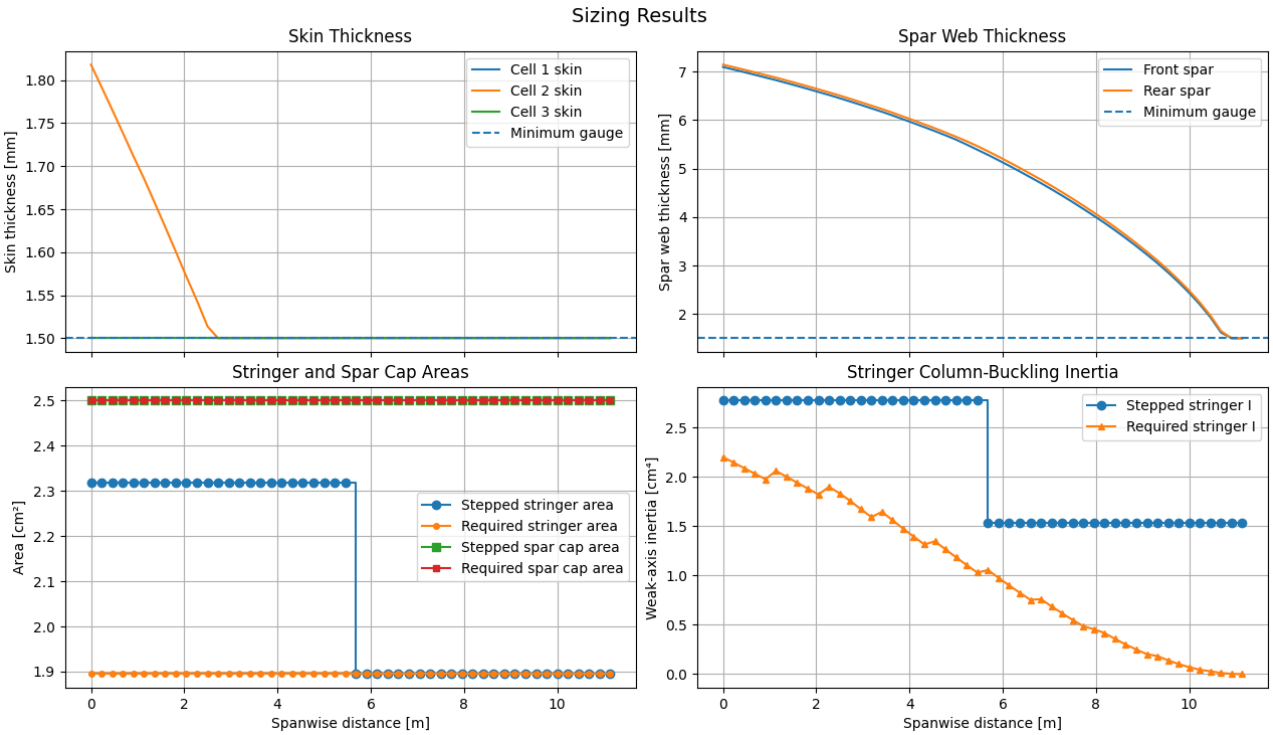

Figure 7.10: Spanwise sizing per wing component

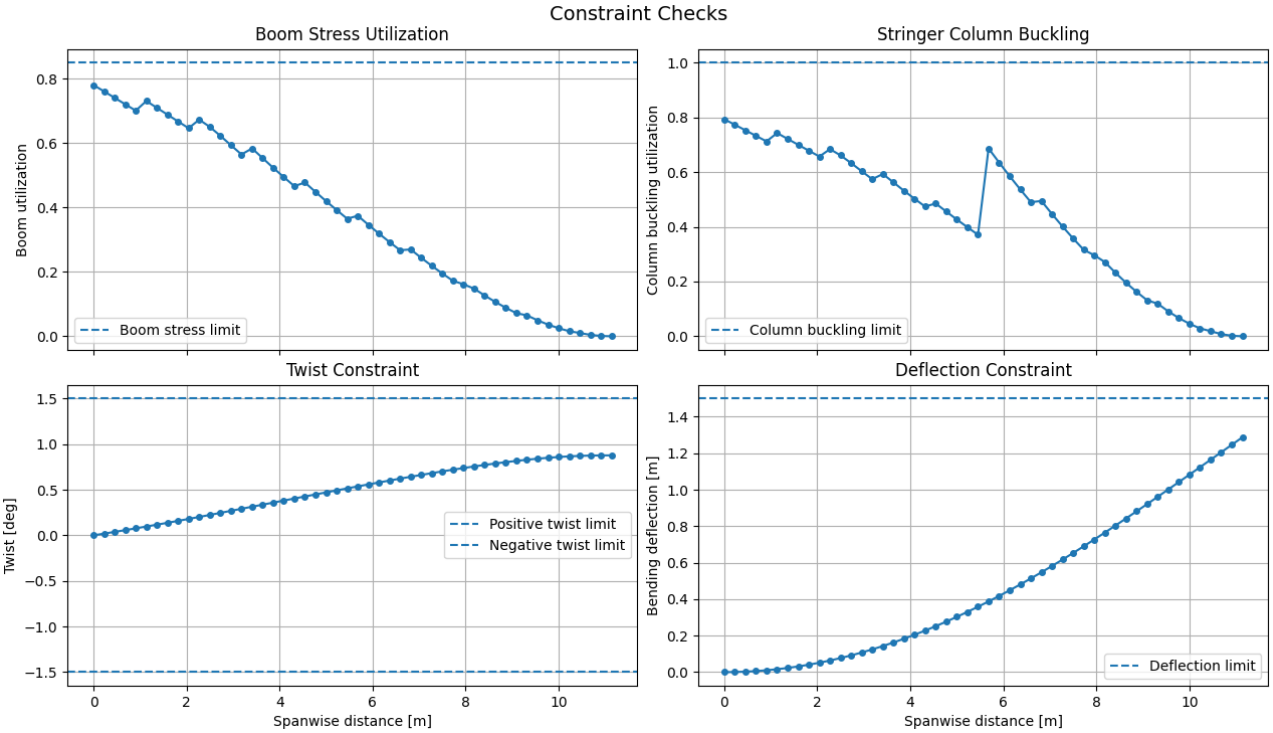

Figure 7.11: Wing constraints for valid design

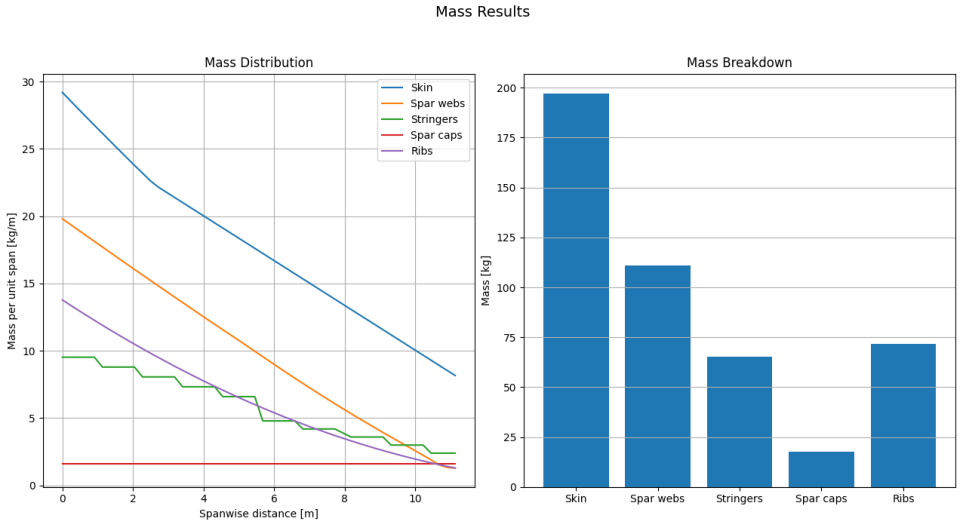

Figure 7.12: Wing optimised mass distribution

For the v-tail, weights and sizing are calculated through the same optimiser. The material distribution is the same as for the wing, but due to the much smaller loads on the structure, most of the sizing is controlled by manufacturability limits. The final one-panel v-tail mass is 128.259 kg, and the full tail with actuators and fuselage connection estimate included is 374.995 kg.

Table 7.10: Wing and tail component materials and masses

Component	Material	Main wing (kg)	V-tail (kg)
Skin	CFR-PEEK	197.205	65.807
Spar web	Al-Li 2050	110.849	24.228
Stringers	CFR-PEEK	65.176	19.050
Spar caps	CFR-PEEK	17.596	7.141
Ribs	Al-Li 2050	71.576	12.032
Total		**462.403**	**128.259**
Two-surface total with connections and EMAs		**1189.767**	**374.995**

8. Fuel Storage and Propulsion Subsystem

Everything related with how the BWB is going to be powered and how the energy carrier is going to be stored is collected in this chapter. First, the liquid hydrogen storage system is developed, which includes tank sizing, insulation design and operational considerations. Subsequently, the hydrogen distribution network is sized to safely transport fuel throughout the aircraft. Finally, the fuel cell based propulsion system is designed and analysed to satisfy the aircraft's power and performance requirements.

8.1. Information Dependencies

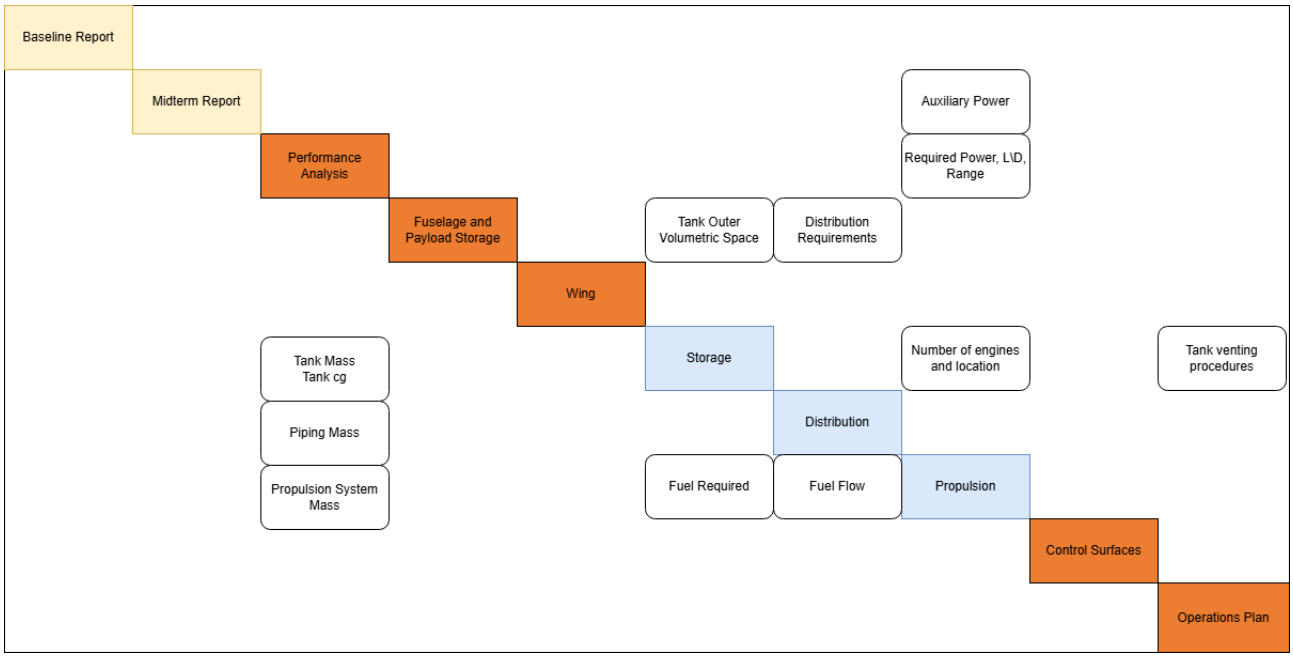

Figure 8.1: N^2 Chart indicating the flow of information within the design of the fuel storage and propulsion subsystem

8.2. Assumptions

Table 8.1: Model assumptions

ID	Assumption	Variable(s)	Effect
FSP1	The insulation layer of the LH_2 tank provides no structural support to the tank structure	t_i	-
FSP2	The structural layers provide no thermal insulation for the LH_2 tanks	t_{inner}, t_{outer}	-
FSP3	All conduction is through the insulation material	t_i	Potentially significant. The internal structure and hydrogen fuelling/defuelling mechanism may cause a significant amount of heat influx; however, detailed analysis is impossible without detailed internal structures and complex heat-flow analysis.
FSP4	Convection can be assumed negligible due to the implementation of the vacuum insulation.	t_i	Negligible

Continued on next page

Table 8.1 – continued from previous page

ID	Assumption	Variable(s)	Effect
FSP5	The temperature in the tank is considered constant and equal.	Q	Potentially significant. Stratification causes large changes in temperature within the structure, resulting in varying heat-flow behaviour. This was excluded from the models used by reference papers due to its complexity.
FSP6	The properties of the rounded ends of the tanks are assumed identical to those of the cylindrical section.	t	Limited
FSP7	All hydrogen distribution pipes are considered straight.	m_p	Bends require thicker pipes to accommodate momentum changes in the hydrogen and the associated degradation. Since bends are limited and sparsely distributed, the mass increase is considered negligible.
FSP8	Aircraft weight at top of climb and in cruise is taken equal to MTOW; the outer MTOW feedback loop is not closed.	F_{req}, P_{shaft}, m_{IPS}	Conservative. Mission fuel is about $5\,\%$ of MTOW, so cruise weight is up to that much lower; required thrust, shaft power and IPS mass are overestimated by a comparable margin.
FSP9	All stack, CEM, HEX and electrical parameters are taken at the 2035 LT-PEM end-of-life technology level rather than the 2050 entry-into-service forecast.	η_{FC}, SP_i, m_{IPS}	Conservative. While these are only estimates, the 2050 enter into service allows for reaching as good of values as the 2035 predicted ones
FSP10	HEX entrance Mach ($M_{\text{HEX}} = 0.22$) and air-channel length ($L_{\text{air}} = 9.25\,\text{cm}$) are reused as fixed inputs from the reference 2D thermal optimisation; the 2D solve is not re-run and the stagnation pressure ratio is held at $\pi_x = 0.984$.	π_x, A_{HEX}, $u_{e,x}$, F_{net}	Potentially significant. While in the study, for 2035 technology, they were independent of aircraft size, cruise altitude or speed, this specific condition shall be modelled in the future.
FSP11	End-of-life degradation is modelled as a uniform cell-voltage drop $\Delta E_{\text{deg}} = 0.0313\,\text{V}$ across all current densities, with sizing performed at EOL.	E_{cell}, η_{FC}, P_{gross}	Conservative. Real degradation varies with current density; the flat EOL penalty oversizes the stack relative to beginning of life.
FSP13	The auxiliary electrical load is fixed at $P_{\text{aux}} = 192\,\text{kW}$, drawn directly off the stack bus and split across the surviving engines.	P_{gross}	Linear on gross stack power; the stack is under- or oversized in proportion to any error in the true systems load.
FSP14	Nacelle external drag is captured by a single coefficient $C_{D,\text{nac}} = 0.03$ on frontal area.	F_{net}	Small. A fixed coefficient ignores the Reynolds- and Mach-dependence of nacelle drag.

8.3. Methods

8.3.1. Hydrogen Storage

Material Choice

There is one key decision to be made for the liquid hydrogen tank which is its structure. To complete this decision a small trade off has been made to opt between a selection of standard industry used cryogenic hydrogen storage solutions. [48] highlights the modern options available and industry standard for cryogenic liquid hydrogen storage and provides backed information for 4 structural materials, aluminium and aluminium alloys, stainless steal, composites, and polymers. Composite and polymer options are immediately removed due to the lack of circular material pathways, stainless steal is removed due to its large mass resulting in the only material for the structure of the aircraft being aluminium, notably the same aluminium as that used on the cryogenic tanks of the space shuttle, aluminium–copper–lithium alloy 2195. This is a highly optimised alloy and therefore is difficult to return to its constituent elements that would be needed for large scale material recycling, however, this alloy has a very high demand, with an increasing demand in the future due to the rising implementation of cryogenic hydrogen in various industries. Therefore, the material can be returned into the

material stream as an alloy rather than as its constituent elements [48].

The next characteristic is the insulation layer, [48] also highlights different insulation materials used in aerospace, the most favourable for this application is aerogel. This material when sourced organically is the only option that has circular material pathways and sufficient material properties to supply these needs. Organic aerogels are expected to have a technical TRL level of 8-9 by 2040 and therefore can be assumed as viable for this project [49].

Sizing

To size the tank first the maximum allowable pressure must be determined, typical values for this are approximately 3 bar, to accommodate for extreme conditions a design maximum pressure of 5 bar is defined, including an industry standard safety factor of 2 the design internal pressure is 10 bar. The tank consists of 2 layers, with a design internal pressure of 10 bar, a partial vacuum ($\approx$ 0 bar) in between, and an external pressure of 1 bar, 1.25 bar to account for variations in outside pressure and extreme conditions. To size the inner layer of the tank the following equation for hoop stress is used, given by Equation 8.1. To size the outer layer the Zoelly approximation [50] for buckling of shells is used to provide an equation to preliminarily size a shell under external pressure. This can be done with help of Equation 8.2.

$$t = \frac{\Delta P * r}{\sigma_{yield}} \tag{8.1}$$

$$t = R\left(\frac{\Delta P\sqrt{3(1-\nu^2)}}{2E}\right)^{\frac{1}{3}} \tag{8.2}$$

This provides the thickness of the structural layers of the tank, next the insulation layer can be estimated by setting a mass flow rate of hydrogen boil off as constant, calculating the required heat influx and then an insulator thickness required sized to accommodate for this heat influx. The value taken is 0.005 kg per second per tank or 0.015 kg per second of H_2, this was taken due to its optimisation between 'time to vent' for ground operations, a usable amount of hydrogen and a heat transfer acceptable to maintain the cabin environment. The heat influx required to provide this hydrogen can be calculated using Equation 8.3. To model the heat influx calculation an approach as used by [51]. Heat transfer can be divided into three categories, conduction, convection, and radiation. Conduction through the aerogel insulation material can be calculated using Equation 8.4.

$$Q = \dot{m}\Delta h_{vap} \tag{8.3}$$

$$Q_{cond} = kA\frac{\Delta T}{L} \tag{8.4}$$

Convection is assumed negligible due to the evacuation of the aerogel, by removing all gas from between the aerogel spacing convection can be removed to almost 0. Vacuum decay is a property of all vacuums, that over time the pressure in the tank starts to increase, however if the vacuum is pulled after every flight or every day, then the decay is reduced to negligible levels. Lastly, radiation is prevalent between the two structural layer, the reason for applying the aerogel insulation is to mitigate the effects of this radiation as the reflective material of aerogel disrupts the passage of radiation energy. By assuming there are two plates this conservative estimate of the heat transfer. [51] Provides a method for calculating this heat transfer.

$$Q_{rad} = \epsilon S B_{21}\sigma(T_e^4 - T_i^4) \tag{8.5}$$

$$B_{21} = \frac{F_{21}\epsilon}{1-(1-\epsilon)^2F_{21}F_{12}-(1-\epsilon)F_{22}} \tag{8.6}$$

$$F_{11} = 0, F_{12} = 1, F_{21} = \frac{S_e}{S_i}F_{12}, F_{22} = 1 - F_{21} \tag{8.7}$$

By combining these the total heat transfer can be calculated and solved for an optimal insulation thickness capable of the functionality of this tank.

Operations

To supply the propulsion units with hydrogen, gaseous hydrogen is extracted through a regulator placed on the top of the tank. This is done through a liquid/gas separator to ensure that only gas will enter the regulator, this is unlikely due to heat rising. During operations the top of the tank will be noticeably warmer than the liquid due to this principle, this will mean that any liquid hydrogen that ends up in this section will quickly evaporate. During manoeuvring the liquid separator plays a key role in ensuring that the liquid hydrogen remains in the tank. The hydrogen passes through the regulator and is then combined with the flow from another tank before being sent to the aft of the aircraft to be used by the propulsion system. There are 3 regulators per tank, this is to provide independent hydrogen to each motor such to mitigate part failures higher up the fuel supply path.

Secondly, each tank section contains a vent stack capable of venting the hydrogen to the wing of the aircraft in case an overpressure situation occurs. This is most likely during taxi and landing as the hydrogen usage by the aircraft is low, meaning less hydrogen is being extracted from the tank whilst heat continues to enter the system, resulting in a potential over-pressure and vent. It is opted to use the wing tip of the aircraft as the location for the venting as this moves it out of potential danger zones of the engines on the aft of the aircraft. If the venting occurs in flight the force is small due to the light mass and low pressure, however an audio warning can be made for the pilots and memory items for a corresponding control input to correct due to the large moment arm. To protect ground workers the outlet is on a mechanical axis, when force is detected on the main gear the vent arm rotates to a vertical position rather than the horizontal position during flight. The tanks are designed to resist 10 bar, venting occurs at 5 bar, venting is performed through an automatic regulator that engages when a pressure of 5 bar is detected. To avoid sloshing causing stability problems in the aircraft, spacers shall be installed that withstand this load and any frequencies that may occur due to the movement of the liquid in such a large tank.

There are electric heaters installed under the tanks, these electric heaters allow the pilots to artificially increase hydrogen mass flow rate by increasing the energy entering the system. These are sized to allow the maximum potential mass flow rate with a safety margin of 1.5, this is calculated by calculating the required heat influx, removing the natural heat influx and sizing the heaters as the difference. This is taken off the auxiliary power budget. Future development of the tank includes the design of a potential jettisoning system where the liquid hydrogen is ejected out of the aircraft in a dangerous situation.

Crash safety can be assured through the usage of steel springs, these springs are laid longitudinally between the outer and inner tanks in a crossing pattern. The structural supports of the tank are designed to fail at the edge of the operational envelope, should this be exceeded the energy of a crash is absorbed by these springs as the inner tank is able to slide within the outer shell. Above a certain load the tank edges will touch causing a catastrophic failure, this should be designed to occur only after the loads at which a survivable crash can be deemed unfeasible.

Self Pressurisation

The aircraft is susceptible to over pressure when left dormant, [51] provides a model to predict the internal pressure of the tank when left dormant such as waiting at the gate, or on the taxiway. To ensure safety of ground personnel and limit loss of hydrogen due to venting, Figure 8.2 model the pressure in the tank pressure when left dormant.

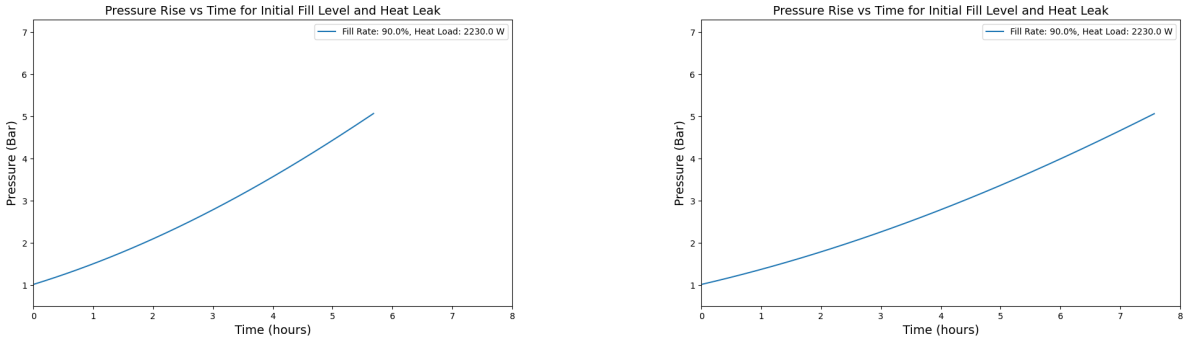

(a) Side tank self pressurisation plot

(b) Aft tank self pressurisation plot

Figure 8.2: Self Pressurisation Plots

These plots show the progression of over pressure towards the 5 bar vent value, the expected time till over pressure is much greater than any realistic operational dormancy period, and therefore the criticality of this system is reduced, aircraft venting during operation can be seen as a rarity.

8.3.2. Hydrogen Distribution

The hydrogen must be distributed through pipes, the pipes responsible for venting must be rated for the maximum 10 bar flow, to accommodate for over pressure situations a safety factor of 1.5 bar shall be taken. For the propulsion lines the pressure should never be greater than 2 bar in operations due to the the regulator reducing the pressure out of the tank. To accommodate for a potential regulator failure the distribution lines are also rated for 15 bar to ensure that any failure of the hydrogen system occurs within an identified and controlled zone, the tank.

Sizing of hydrogen pipes can be difficult due to the difficulty in modelling thermal and flow fluctuations, therefore

conservative assumptions shall be made to ensure functionality. The first step is to define the material used, ASME-B31.12 [52] fines a large amount of materials that are accepted for hydrogen piping applications Table 8.2 highlights the key groups, their properties and the trade-off.

Table 8.2: Material trade off for hydrogen distribution piping

Material	**Recyclability**	**Density**	**Yield Strength**	**Cost**	**Maintain-ability**
-	30%	25%	25%	10%	10%
Steel	5	2 (7850 $\frac{kg}{m^3}$)	3 (210 MPa)	4 (2-5.5€)	5 [32]
Copper	5	1 (8960 $\frac{kg}{m^3}$)	4 (320 MPa)	2 (9€)	2 [33]
Aluminium	5	4 (2700 $\frac{kg}{m^3}$)	4 (200-500 MPa)	3 (3.5-15€)	4 [34]

The results put aluminium (4.2), above steel (3.65) above copper (3.15). A clear advantage for using aerospace grad aluminium alloys for these pipes. The next step is to calculate the diameter of the pipe and the thickness of the pipe. The main factors to include are mass, compliance with standards, and pressure loss. First the flow velocity must be assumed, traditionally natural gas pipelines use a maximum flow velocity of 20 $\frac{m}{s}$, this would be too low for this application. Hydrogen required in fuel cells is incredibly clean, reducing erosion and allowing a higher flow velocity. The negatives of this include a higher pressure loss and increased noise inside the cabin due to turbulence in the cabin. Whilst higher velocity could be feasible an initial value of 80 $\frac{m}{s}$ has been taken.

$$A = \frac{\dot{m}}{V\rho} \tag{8.8}$$

To be conservative the pressure and density is assumed to be the combination that causes the highest possible H_2 density, notably 10 bar and 100°C, resulting in 0.9748 $\frac{kg}{m^3}$. The highest potential required mass flow is 0.225$\frac{kg}{s}$, whilst this is total mass flow, it is operationally beneficial to be able to use tanks independently, for this reason the mass flow will be taken from each tank rather than averaged across all 3 sources. This results in a pipe diameter of 60 mm. The next step is determining if the pressure loss of this pipe is acceptable, to calculate this the Darcy–Weisbach equation can be used as shown in Equation 8.9. Where f is the friction factor, and L is the length of pipe. The longest pipe extends from the most forward outlet of the side tanks to the aft most engine, at 10.4 m, the friction factor is a function of the Reynolds number, which can be calculated with Equation 8.10.

$$\Delta P = f\frac{L\rho V^2}{2D} \tag{8.9}$$

$$Re = \frac{\rho V D}{\mu} \tag{8.10}$$

μ is the absolute viscosity, information on this at low temperatures is difficult to identify, however with the earlier conservative numbers it is safe to use the value at 0°C of $0.84e-5$. This results in a Reynolds number of $5.63e6$. Using a Moody diagram an equivalent friction factor for an aluminium pipe with relative roughness of 0.001 is 0.02. This results in a pressure drop of 10705 Pa, or 0.1 bar, this is significant but not limiting and therefore this diameter can be accepted.

To identify the thickness, the ASME-B31.12 is consulted to provide standard requirements on the manufacturing of hydrogen pipelines. With help of Equation 8.11. P is the internal design gage pressure, D is the outside diameter of the pipe, S is the stress value of the chosen material, E the quality factor, M_f is the material performance factor, Y is a material coefficient between 0 and 1. The ASMe document provides standard information for aluminium pipes. S = 73.7 MPa, E = 1, M_f = 1 (not prevalent in Appendix IX, defaults to 1) Y = 0.4 (not prevalent, used worst case value stated for stainless steel). This results in an allowable thickness of 0.62 mm, to allow for manufacturing and structural stiffness this number is increased to 1mm. An important parameter to carry through is the mass per unit meter, which is calculated with Equation 8.12.

$$t = \frac{PD}{2(SEM_f + PY)} \tag{8.11}$$

$$m = \pi\rho(Dt + t^2) \tag{8.12}$$

[32] Corrosion resistant, standard instrutial practices
[33] High corrosion under high flow velocity
[34] low maintainability and easy inspection, increased corriosn than stainless steel

8.3.3. Propulsion System

The propulsion system is the largest single contributor to the aircraft's in-service footprint, so apart from reaching the required thrust, its architectural choices are influenced by the low-impact requirements(REQREG 1.1.4, REQREG 1.1.8). The main result from this is electrochemical rather than thermal conversion: the LT-PEM stack oxidises hydrogen to water without combustion, emitting no CO_2, NO_x, hydrocarbons, soot, or ultra-fine particulates, and removing the local air-quality burden combustion places on airports. On green hydrogen the in-service climate impact from these is zero; only water vapour leaves the nozzle, so the residual climate effect reduces to the contrail term.

Efficiency is the other attribute where environmental impact is reduced. The fuel-cell powertrain converts hydrogen to thrust at a cruise overall efficiency of 0.43, above the $0.36 - 0.38$ of conventional single-aisle turbofans (the B737-800 and A220-100) [1], resulting in less energy required. Going with four engines instead of the six proposed earlier leaves all four at 54% throttle in cruise. At this part load the stacks run at higher cell voltage raising the overall efficiency from 0.33 at the design point to 0.43 in cruise and cutting mission fuel accordingly.

Propulsion System Sizing Methodology

The aircraft uses four nacelle-mounted integrated propulsion systems (IPS), as defined by Shah and Ansell [1, 31]. Each IPS is a ducted fan driven by an electric motor, a low-temperature proton exchange membrane (LT-PEM) fuel cell stack, a compressor expander module (CEM), an inclined annular heat exchanger (HEX) in the bypass duct, and a nacelle. The sizing follows the stack, CEM, and mass models of [1] and the flowpath, HEX, and thrust models of [31], run in a Python tool at the 2035 LT-PEM end-of-life (EOL) level for the FL400, Mach 0.80 cruise condition.

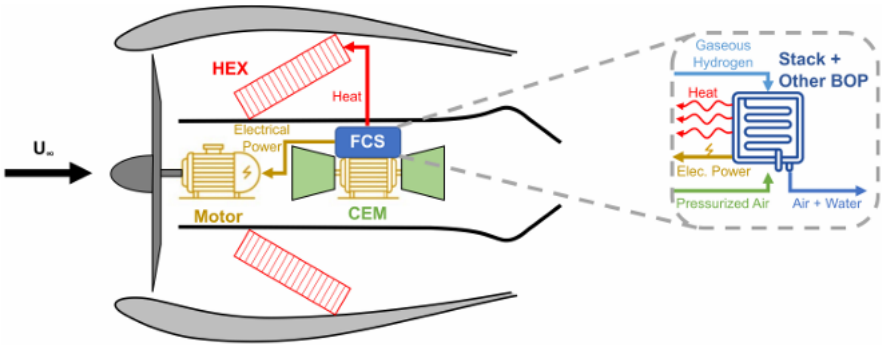

Figure 8.3: Schematic showing the IPS internal layout [1]

IPS Architecture and Sizing Philosophy

The engines are sized for the one-engine-inoperative (OEI) case: if one fails, the other $N - 1$ must still cover the propulsive power set by the thrust-power loading W/P from the design point. The per-engine thrust target is

$$F_{req} = \frac{\mathrm{MTOW}\, g}{(W/P)\, V\, (N-1)} \tag{8.13}$$

where W/P is the thrust-power loading and is based on Figure 7.3, V the cruise speed, and N = 4 the engine count. With MTOW the total propulsive power is $\mathrm{MTOW}\, g/(W/P) = 10.87$ MW, and Equation 8.13 gives $F_{req} = 15.35$ kN per engine.

Four engines were chosen ($N = 4$) rather than the six [1] finds optimal: six do not fit the available installation volume, and sizing each for OEI with the factor $N/(N-1) = 4/3$ leaves all four oversized in normal all-engines-operating (AEO) cruise, so the stacks run lower on the polarization curve at higher cell voltage and better efficiency.

The sizer converges on thrust, not power. A plain estimate that converts the thrust power to shaft power by dividing by the fan efficiency ignores the HEX pressure loss and nacelle drag, so it falls short on thrust. The full sizing chain is run for a trial shaft power, the net thrust is checked against Equation 8.13, and the shaft power is rescaled by F_{req}/F_{net} until the error drops below 10^{-4}. With π_f and the HEX geometry fixed, thrust is very nearly linear in shaft power, so a single rescaling almost closes the loop and it converges in three passes.

LT-PEM Stack Model

The stack performance is the polarization curve, the cell voltage E_{cell} against current density i [1]:

$$E_{cell} = E_{OCV} - \Delta E_{act} - \Delta E_{ohm} - \Delta E_{conc} - \Delta E_{deg} \tag{8.14}$$

where E_{OCV} is the Nernst open-circuit voltage and the four loss terms are the activation, ohmic, concentration, and end-of-life degradation losses. E_{OCV} is corrected for stack temperature and the oxygen and hydrogen partial pressures, which fall with current density as the reactants deplete. The loss parameters come from [1], with a flat degradation penalty $\Delta E_{deg} = 0.0313\ \mathrm{V}$. The stack runs at $p_{stack} = 2.10\ \mathrm{bar}$ and $T_{stack} = 353\ \mathrm{K}$ with the 2035 limiting-current factor of 1.25; these and the other operating values can be found in [1].

The stack is sized at the peak of the gross power density $P''_{gross} = i\,E_{cell}$, which fixes the rated point (i_{op}, E_{op}) and minimises the membrane area. The membrane area and stack mass are

$$A_{mem} = \frac{P_{gross}}{i_{op}\,E_{op}}, \qquad m_{FC} = ASM_{FC}\,A_{mem} \tag{8.15}$$

with the area-specific stack mass $ASM_{FC} = 2.4\ \mathrm{kg/m^2}$. The cell efficiency is $\eta_{FC} = E_{cell}/E_{th}$ with the thermoneutral voltage $E_{th} = 1.253\ \mathrm{V}$, and the cell count follows from a $460\ \mathrm{cm^2}$ cell area.

CEM and Balance-of-Plant Power Chain

The CEM compresses the core air from the post-fan pressure $p_{t,core}$ up to the cathode pressure, then expands the stack exhaust back down to recover part of the work [1]. Because the cathode flow is proportional to stack current, the CEM draw is written as a fraction of gross power, $f_{CEM} = P_{CEM}/P_{gross}$, and the rest of the balance of plant as $\zeta_{BOP} = 0.03$ of gross power. Inverting the chain from the shaft power through the electrical efficiency $\eta_{elec} = 0.9556$, and adding this engine's share $P_{aux,eng}$ of the auxiliary electrical load, gives the gross stack power Equation 8.16. The auxiliary load is a fixed $192\ \mathrm{kW}$ drawn directly off the stack, so $P_{aux,eng} = P_{aux}/(N-1)$ across the surviving engines at OEI and P_{aux}/N at AEO. The CEM and motor masses follow from their specific powers given by Equation 8.17 and Equation 8.18 respectively. With $SP_{CEM} = 1.63\ \mathrm{kW/kg}$ and $SP_{motor} = 20.4\ \mathrm{kW/kg}$ [1].

$$P_{gross} = \frac{P_{shaft}/\eta_{elec} + P_{aux,eng}}{1 - \zeta_{BOP} - f_{CEM}} \tag{8.16}$$

$$m_{CEM} = \frac{P_{CEM}}{SP_{CEM}} \tag{8.17}$$

$$m_{motor} = \frac{P_{shaft}}{SP_{motor}} \tag{8.18}$$

Thermal Management and HEX Sizing

The waste heat is the total electrochemical loss at the operating point given by Equation 8.19 and is rejected to the bypass stream through an annular crossflow HEX set at $\delta = 70°$ to the engine axis [1]. The HEX frontal area follows from bypass continuity at the entrance Mach number shown by Equation 8.20. This is evaluated at $M_{HEX} = 0.22$. The $70°$ inclination spreads this area over a larger annular ring calculated with Equation 8.21.

$$Q_{waste} = i_{op}\,\Delta E_{loss}\,A_{mem} \tag{8.19}$$

$$A_{HEX} = \frac{\dot{m}_{HEX}}{\rho_{HEX}\,V_{HEX}} \tag{8.20}$$

$$A_{ring} = \frac{A_{HEX}}{\sin\delta} \tag{8.21}$$

Whose inner edge is the core wall and whose outer radius sets the smallest nacelle the HEX allows; the nacelle diameter is the larger of the fan tip and HEX outer diameter [31]. The HEX mass follows from the heat load and the 2035 forecast specific power by usin Equation 8.22, with $SP_{HEX} = 10.0\ \mathrm{kW/kg}$ [53].[35]

$$m_{HEX} = \frac{Q_{waste}}{SP_{HEX}} \tag{8.22}$$

The entrance Mach number $M_{HEX} = 0.22$ and channel length $L_{air} = 9.25\ \mathrm{cm}$ are reused as fixed inputs from the 2D thermal solve in [1]. These numbers were deemed to be optimal as in the study, for 2035 technology, they were independent of aircraft size, cruise altitude or speed.

[35] HEX mass and geometry are sized independently and not cross-checked, following [1].

Fan and Flowpath Geometry

The fan mass flow follows from the shaft-power balance across the fan:

$$\dot{m}_{fan} = \frac{P_{shaft}\,\eta_{fan}}{c_p\,T_{t,2}\left(\pi_f^{(\gamma-1)/\gamma} - 1\right)} \tag{8.23}$$

at a fan pressure ratio $\pi_f = 1.45$ and efficiency $\eta_{fan} = 0.89$ [31]. The flow then splits into a core stream into the CEM, set by the stack air demand ($\beta = 1.8$ excess air), and the bypass stream through the HEX. The duct areas come from continuity at $M = 0.60$ at the fan face and $M = 0.30$ in the core duct; the core radius is the fan hub and HEX inner radius, and the fan tip radius follows from the annular fan area.

Thrust Model

Net thrust comes from the two exit streams [31]. Both nozzles expand isentropically to ambient pressure, with the exit velocities set by the exit stagnation states: the core carries only diffuser, fan, and nozzle losses, since the CEM returns the flow to roughly fan-exit pressure, while the bypass adds the HEX stagnation pressure ratio π_x and the heat-driven temperature rise. The per-engine net thrust is

$$F_{net} = \dot{m}_{core}\,u_{e,c} + \dot{m}_{HEX}\,u_{e,x} - \dot{m}_{fan}\,u_0 - C_{D,nac}\,q_\infty\,\tfrac{\pi}{4}D_{nac}^2 \tag{8.24}$$

where $u_{e,c}$ and $u_{e,x}$ are the core and bypass exit velocities, u_0 the flight speed, and $C_{D,nac} = 0.03$ the nacelle drag coefficient on frontal area. The HEX stagnation pressure ratio π_x is taken directly from the full 2D compressible HEX solve of [31], which integrates the coupled friction and heat-addition losses along the channels and gives $\pi_x = 0.984$ at the 70° inclination.

Off-Design Operation and Mission Fuel

The engine is sized at OEI power, but fuel is evaluated at the AEO cruise throttle, where thrust balances drag, $F_{cruise} = \mathrm{MTOW}\,g/(L/D)$ with $L/D = 17.8$, split over four engines. Using $F_{net} \propto P_{shaft}$ from the design point, this sets the AEO shaft power at about 54% of rated. The off-design point is found by holding the membrane area at its OEI value and moving down the polarization curve until the fixed stack delivers that power through Equation 8.16, with f_{CEM} recomputed each step. The engine then runs at lower current and higher voltage, which is what lifts η_{FC}. The cruise hydrogen flow per engine follows from Faraday's law:

$$\dot{m}_{H_2} = i_{AEO}\,A_{mem}\,\frac{MM_{H_2}}{2F} \tag{8.25}$$

where i_{AEO} is the cruise current density, MM_{H_2} the molar mass of hydrogen, and F Faraday's constant. Mission fuel is this constant cruise flow integrated over an equivalent cruise time, with climb and acceleration modelled in as a lost-range term on the nominal range $R_{nom} = 4000$ km:

$$R_{lost} = \frac{1}{\eta_{sys}}\,\frac{L}{D}\left(h_{CR} + \frac{V^2}{2g}\right), \qquad m_{fuel} = \frac{1.05\,(R_{nom} + R_{lost})}{V}\,\dot{m}_{H_2,total} \tag{8.26}$$

where 1.05 is a contingency margin and $\dot{m}_{H_2,total}$ the four-engine cruise flow. Because the flow is taken at fixed MTOW it never drops as fuel burns, so this is conservative against a weight-tracking integration.

8.4. Results

8.4.1. Hydrogen Storage

Information is provided in chapter 6 on the available locations and sizes of the liquid hydrogen tanks, notable two on the left and right side of the cabin, and one aft of the aft galley. All tanks have the same diameter of 1.9 m, the front tanks a length of 7.5 m and the aft tank with a length of 10 m. Table 8.3 provides the relevant material information to perform the analysis. These materials used in combination with the method described in subsection 8.3.1 provide sizing of the tank its results are shown in Table 8.4.

Table 8.3: Material Properties of materials selected for the LH_2 tank

Property	Unit	Aluminium 2195	Organic Aerogel
E (Youngs Modulus)	GPa	69	-
σ_y (Yield Stress)	MPa	530	-
ν (Poisson's Ratio)	-	0.3	-
ϵ (Radiation Emissivity)	-	0.05	-
k (Thermal Conductivity)	$\frac{W}{mK}$	-	0.003

Table 8.4: Sizing of the LH_2 tank including two structural layers and one insulation layer

Property	Unit	Side Tank	Aft Tank
Outer Shell Thickness	mm	10.91	10.91
Inner Shell Thickness	mm	2.00	2.00
Insulation Layer Thickness	mm	24.63	35.34
Tank Mass	kg	2062	2742
Hydrogen Storage Mass	kg	1137	1515
Hydrogen Storage Volume	m^3	16.05	21.38

Key notes in this sizing include that the mass includes a 10% contingency, this is to accommodate for the implementation of additional tools such as the refuelling infrastructure, spacers to prevent sloshing, electric heaters, pressure sensors, crash safety devices, and other potential sources of additional mass which would make this calculation an underestimate. Another note is that the hydrogen storage volume accounts for 10% ullage space to account for gas expansion as is industry standard [54]

8.4.2. Hydrogen Distribution

With aluminium having a density of 2800 $\frac{kg}{m^3}$ this results in a unit mass of 0.5419 kg. For the 106.64 m network of hydrogen this results in a total system mass of 57.79 kg. Figure 8.4 shows a schematic of this network, the blue lines show the propulsion lines transporting hydrogen to the propulsion units and the orange lines show the vent paths to the wing tips.

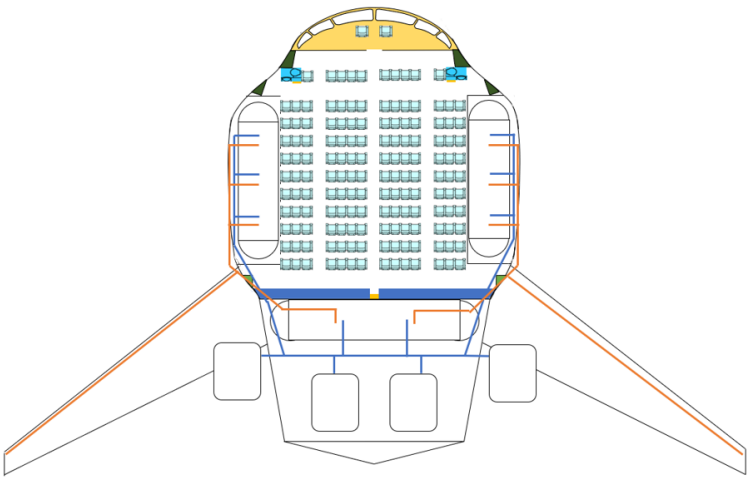

Figure 8.4: Hydrogen Distribution Schematics

Parameter	Symbol [unit]	Result
Length of pipes	[m]	106.64
Pipe thickness	[mm]	1
Total System Mass	[kg]	57.79

Table 8.5: Results of the hydrogen distribution section

8.4.3. Propulsion System Results

The loop reaches $F_{req} = 15.35$ kN per engine in three passes. The open-loop estimate of 4134.6 kW falls 10.2% short on thrust, confirming the HEX loss and nacelle drag matter, and the loop closes at a converged shaft power of 4606.9 kW per engine. Table 8.6 gives the converged design and Table 8.7 the OEI and AEO operating points, Figure 8.5 and Figure 8.6 show the curves and mass breakdown.

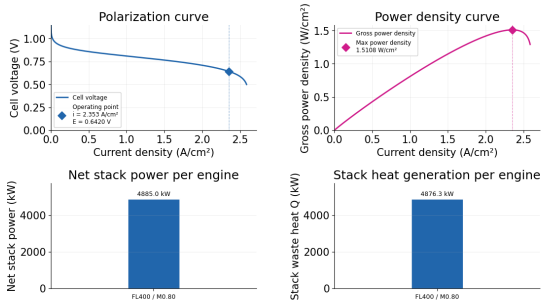

Figure 8.5: Engine Characteristics

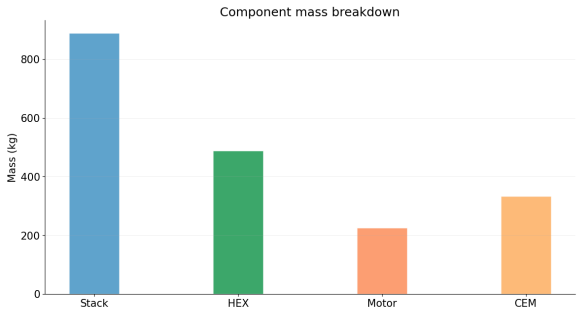

Figure 8.6: Mass breakdown

Table 8.6: Converged IPS sizing summary at FL400, Mach 0.80, 2035 LT-PEM EOL ($N = 4$, OEI design point).

Parameter	Symbol [unit]	Per engine	Total ($\times 4$)
Shaft power (OEI rated)	P_{shaft} [kW]	4606.9	18,428
Net stack power	P_{net} [kW]	4885.0	19,540
Gross stack power	P_{gross} [kW]	5594.9	22,380
CEM power	P_{CEM} [kW]	542.1	2168.3
Balance of plant	P_{BOP} [kW]	167.8	671.4
Waste heat	Q_{waste} [MW]	4.876	19.51
Stack mass	m_{FC} [kg]	888.8	3555.2
HEX mass	m_{HEX} [kg]	487.6	1950.4
CEM mass	m_{CEM} [kg]	332.6	1330.4
Motor mass	m_{motor} [kg]	225.8	903.2
IPS mass	m_{IPS} [kg]	1934.8	7739.2
Membrane area	A_{mem} [m^2]	370.3	1481.3
Cell count	n_{cells} [–]	8051	32,204
Fan mass flow	$\dot{m} * fan$ [kg/s]	149.1	–
Core / HEX mass flow	$\dot{m} * core / \dot{m} * HEX$ [kg/s]	5.58 / 143.5	–
Fan diameter	$D * fan$ [m]	1.79	–
Core duct diameter	D_{core} [m]	0.379	–
Nacelle diameter (HEX)	D_{nac} [m]	2.32	–

The IPS specific power is $2.52\ \mathrm{kW/kg}$ of net stack power, matching the 2035 LT-PEM figure in [1] and serving as a check on the implementation. The stack is the heaviest part at 45.9% of IPS mass, then the HEX at 25.2%, the CEM at 17.2%, and the motor at 11.7%. The $2.32\ \mathrm{m}$ nacelle is set by the HEX, not the $1.79\ \mathrm{m}$ fan: the 70° tilt spreads the $3.87\ \mathrm{m^2}$ frontal area over a $4.11\ \mathrm{m^2}$ ring whose outer radius ($1.16\ \mathrm{m}$) beats the fan tip ($0.90\ \mathrm{m}$). The HEX therefore drives the nacelle size, which pushed the engine count down from six to four.

Parameter	Symbol [unit]	OEI rated	AEO cruise
Throttle (fraction of rated)	[–]	1.00	0.54
Shaft power per engine	P_{shaft} [kW]	4606.9	2485.9
Current density	i [A/cm^2]	2.353	0.988
Cell voltage	E_{cell} [V]	0.642	0.811
Fuel cell efficiency	η_{FC} [–]	0.512	0.647
System efficiency	η_{sys} [–]	0.332	0.428
H_2 mass flow per engine	$\dot{m}_{H_2}$ [g/s]	90.32	37.91

Table 8.7: Fuel cell operating point and efficiencies at the OEI rated condition and at AEO cruise (fixed stack area). System efficiency is $P_{shaft}/(\dot{m}_{H_2}\,\mathrm{LHV})$.

At the OEI rating the cells sit near peak power density, giving a module efficiency of 0.447 that matches the 0.48 in [1], the small gap from the higher compression ratio at FL400. In cruise the throttle correction drops the point to $i = 0.988\ \mathrm{A/cm^2}$, lifting the cell voltage from 0.642 to $0.811\ \mathrm{V}$ and the system efficiency from 0.3332 to 0.428, a 29% gain purely from OEI oversizing.

In the thrust budget the bypass dominates: of the $16.41\ \mathrm{kN}$ internal force, the HEX stream gives $49.9\ \mathrm{kN}$ of gross momentum against $35.2\ \mathrm{kN}$ of ram drag and $1.7\ \mathrm{kN}$ from the core. The HEX loss is modest ($\pi_x = 0.984$) and its heat adds $33.8\ \mathrm{K}$ to the bypass exit, recovering part of it. Nacelle drag is $1.07\ \mathrm{kN}$ (6.5% of the internal force), leaving $F_{net} = 15.35\ \mathrm{kN}$. The OEI fleet thrust of $46.0\ \mathrm{kN}$ sits 39% above the $33.1\ \mathrm{kN}$ cruise drag, which is the margin left for climb at top of climb.

With the four-engine cruise flow of $151.7\ \mathrm{g/s}$, Equation 8.26 gives a mission fuel mass of $3031\ \mathrm{kg}$, or 5.0% of MTOW. This backs up the open-loop assumption: at about 5% of MTOW, leaving the MTOW loop open shifts the thrust target by at most a few percent, well inside the conservatism already built in by holding MTOW high through the cruise.

9. Control Surface Subsystem

The empennage of the BWB will be designed in this chapter. The ailerons, wing elevators and ruddervators are analysed to ensure adequate control in roll, pitch and yaw. Critical operating conditions such as engine inoperative flight, crosswind operation and Dutch roll damping are evaluated to verify compliance with handling and stability requirements. Finally, the trim characteristics of the aircraft are assessed to determine the optimal cruise control surface configuration.

9.1. Information Dependencies

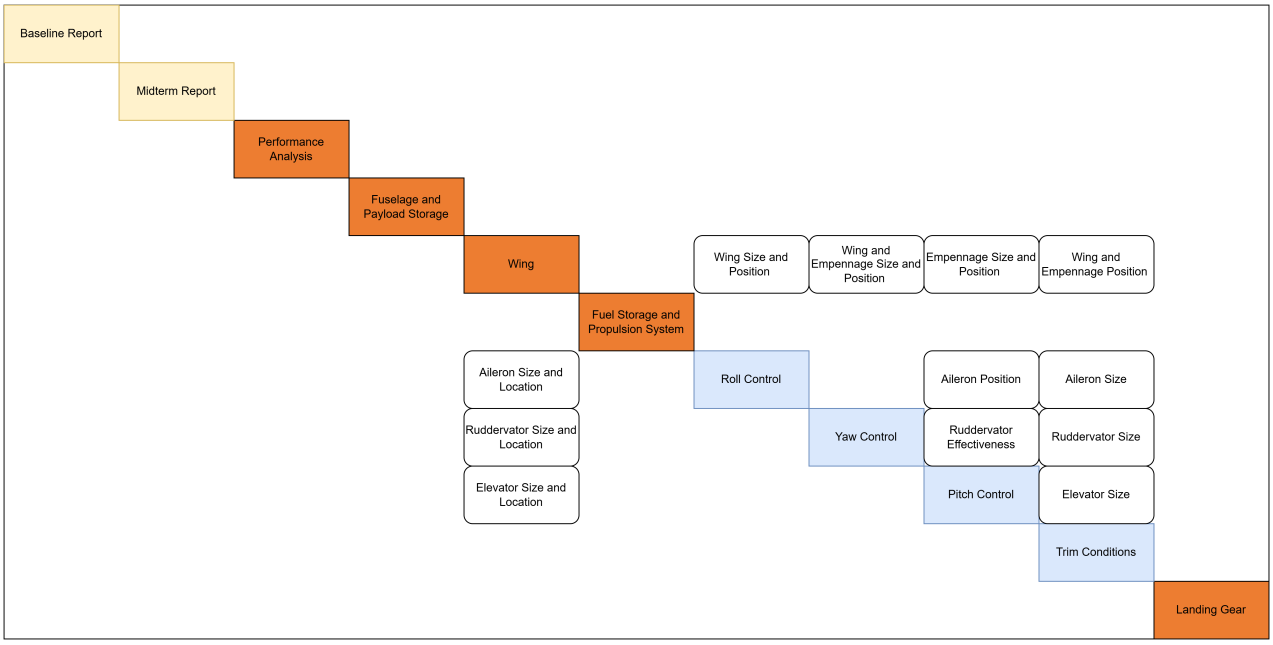

Figure 9.1: N^2 Chart Control Surface Design

9.2. Assumptions

Table 9.1: Model assumptions

ID	Assumption	Variable(s)	Effect
CS1	The dihedral of the wing is neglected for the determination of the stability and controllability derivatives.	$C_{l_{\delta_a}}$,$C_{m_{\delta_e}}$,C_{l_p}	Small. The wing only has a dihedral angle of 5 degrees and therefore effects on the derivatives are small.
CS2	The sweep angle of the v-tail is neglected in the determination of the stability and controllability derivatives.	$C_{n_{\delta_{rv}}}$,$C_{Y_{\delta_{rv}}}$,$C_{m_{\delta_{rv}}}$	Moderate. Since the v-tails have a sweep angle of over 30 degrees, the effects on the derivatives could be significant.
CS3	It is assumed that the effectiveness coefficient of the control surfaces stays constants with spanwise position.	τ_a,τ_e,$\tau_{rv,r}$,$\tau_{rv,e}$	Small. Since the elevator and the aileron only span a small part of the wing and are both relatively far outboard of the wing, the effectiveness coefficient can safely be assumed to be constant. For the ruddervators, since the v-tail is connected to the fuselage by means of a blended structure, it is put higher above the fuselage and therefore is located (mostly) outside of the boundary layer.

Continued on next page

ID	Assumption	Variable(s)	Effect
CS4	For the calculation of the mass moment of inertia, the aircraft components are simplified to point masses.	I_{zz},I_{yy}	Moderate. Large components such as wings have a highly distributed mass affecting the mass moment of inertia.
CS5	For the trim drag of the trim tab, the angle of attack during cruise is assumed to be zero.	$C_{L,r,tot}$,$C_{L,w,tot}$	Small. Angle of attack during cruise is limited.
CS6	The downwash of the main wing affecting the v-tail is neglected.	$C_{L,r,tot}$,$C_{L,w,tot}$	Small. V-tail is not directly behind the wing but partly above the fuselage.
CS7	The velocity of the v-tail is assumed equal to that of the wing.	V_r	Potentially significant. Depending on engine interference with engines and size of boundary layer of fuselage affecting v-tails, the velocity difference could be significant, however this remains unquantifiable at this stage.
CS8	Steady, straight flight is assumed for the critical design cases.	Equation 9.12	Potentially significant. Depending on the flight conditions and flight phase.

9.3. Methods

The control surfaces can be sized and analysed based on the wing and v-tail design presented in chapter 7, as shown in the N^2 Chart in Figure 9.1. Given the configuration of the wing and empennage, it was decided to implement ruddervators, together with ailerons and elevators on the wings. The following subsections explain the method applied for the sizing and placement of these control surfaces. Furthermore, the trimmed conditions during cruise are analysed.

9.3.1. Aileron

An aircraft provides roll control using ailerons on the wings. These need to comply with set requirements by EASA, which are shown in Table 9.2 [4]. These requirements take into account the velocity in the flight phase, the gear configuration, and the flap position. Since no high lift devices will be used on the aircraft, these will not be taken into account.

Table 9.2: Roll Rate Requirements

Configuration	Gear position	Requirement	Required roll rate [deg/sec]
Take-off	Up	$60°$ in 11 sec	5.45
Landing	Gear down	$60°$ in 7 sec	8.57
Cruise	Gear up	$60°$ in 7 sec	8.57

The rolling moment coefficient due to an aileron deflection angle $C_{l_{\delta_a}}$ is calculated using Equation 9.1.[36] In this equation, $C_{l_{\alpha_w}}$ is the lift curve slope of the airfoil of the wing, c_w the chord of the wing at spanwise location y from the centre of gravity, and τ_a the aileron effectiveness obtained from Figure 9.2 using the assumed chord-to-chord ratio of the aileron and wing. The integral will be performed only on the part of the wing that fits the aileron, where a_1 is the start of the aileron and a_2 the end.

Following the value for the roll damping, C_{l_p} of the aircraft needs to be calculated. Since the fuselage also has the shape of an airfoil, it also provides roll damping. The damping is calculated using Equation 9.2. Here, the equation is integrated over the fuselage width and the span of the wing separately. C_{d_0} is the zero lift drag coefficient.

$$C_{l_p} = -\frac{4}{S_{ref} \cdot b^2} \left((C_{l_{\alpha_{fus}}} + C_{d_{0_{fus}}}) \int_0^{b_{fus}/2} c_{fus}(y) \cdot y^2 dy \; + (C_{l_{\alpha_w}} + C_{d_{0_w}}) \int_{b_{fus}/2}^{b/2} c_w(y) \cdot y^2 dy \right) \tag{9.2}$$

[36] Oliviero, F., AE2111-II Aerospace Design System Engineering Elements Lecture 3, Delft University of Technology, Delft, Netherlands, 2025

$$C_{l_{\delta_a}} = \frac{2 \cdot C_{l_{\alpha_w}} \cdot \tau_a}{S_{ref} \cdot b} \int_{a_1}^{a_2} c_w(y) \cdot y \, dy \qquad (9.1)$$

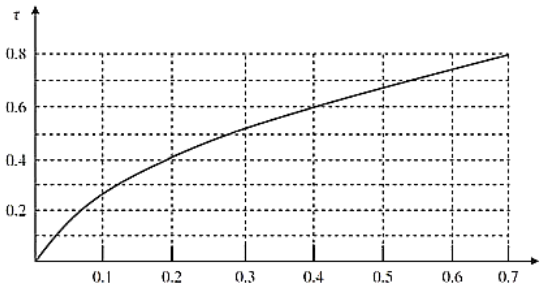

Figure 9.2: Control Surface Effectiveness given Chord-to-Chord Ratio [55]

Finally after finding the $C_{l_{\delta_a}}$ and the C_{l_p}, the steady state roll rate of the aircraft can be determined with Equation 9.3. Here δ_a is set to the maximum deflection angle of the aileron, which is determined to be +/- 25 degrees.

$$P = -\frac{C_{l_{\delta_a}}}{C_{l_p}} \delta_a \frac{2 \cdot V}{b} \qquad (9.3)$$

9.3.2. Elevator

The moment created per elevator deflection angle is calculated using Equation 9.4. This equation has been derived from Equation 9.1 for the ailerons by converting it to get the equivalent relation for the elevator. By multiplying this coefficient with the elevator deflection angle, the additional moment from the elevator deflection can be obtained. It was decided that the maximum elevator deflection angle would be +/- 25 degrees [56].

$$C_{m_{\delta_e}} = \frac{2 \cdot C_{l_{\alpha_w}} \cdot \tau_e}{S_{ref} \cdot \bar{c}} \int_{e_1}^{e_2} c_w(y) \cdot (x(y) - x_{cg}) \, dy \qquad (9.4)$$

Using the moment coefficient calculated from the above equation, the total moment around rotation point of the main landing gear on the runway surface during take-off can be obtained for a given elevator deflection angle. The total moment includes the lift force generated by the fuselage and wing, the weight force of the aircraft, the thrust force during take-off, and the additional elevator lift force. Equation 9.5 [56] shows the relation, which involves the mass moment of inertia around the take-off rotation axis $I_{yy,MLG}$, and the angular pitching acceleration $\ddot{\theta}$. The mass moment of inertia was calculated using Equation 9.6. The elevator is sized by means of trial and error by assuming an elevator chord-to-chord ratio of the wing and a spanwise length and location. This resulted in the angular acceleration for a given deflection angle. For medium sized transport aircraft, a pitch acceleration of approximately 8 deg/s^2 is desired [56].

$$\Sigma M_{MLG} = I_{yy,MLG} \cdot \ddot{\theta} \qquad (9.5) \qquad I_{yy} = \Sigma(m \cdot x^2) + \Sigma(m \cdot z^2) \qquad (9.6)$$

9.3.3. Ruddervator

The ruddervator control surfaces combine the functions of the rudder and elevator for yaw and pitch. Given the dihedral of the v-tails, the aerodynamic forces obtained from a given deflection angle of the ruddervator can be separated into a side force and lift force. The side force Y generates a yawing moment n, while the lift force L generates a pitching moment m.

By converting Equation 9.1 to the yawing counterpart, Equation 9.7 was obtained. Given the inclination angle of the v-tail, the rudder effectiveness will scale according to the sine of this angle as shown by Equation 9.8 [57]. A visual representation of these angles can be found in Figure 9.3.

$$C_{n_{\delta_{rv}}} = -\frac{2\, C_{y_{\beta_{tail}}} \tau_{rv,r}}{S_{ref}\, b} \int_0^{b_{tail}} c_{tail}(b) \, (x_{ac,tail}(b) - x_{cg}) \, db \qquad (9.7) \qquad \tau_{rv,r} = \tau_r \sin(\Gamma_{tail}) \qquad (9.8)$$

In addition, given that the airfoil of the v-tail is taken to be symmetric, the following assumption is made.

$$C_{y_{\beta_{tail}}} \approx C_{l_{\alpha_{tail}}} = 2\pi \frac{1}{rad}$$

Similarly to the yawing moment, the side force generated due to a ruddervator deflection is calculated using Equation 9.9. In this case, however, the moment arm inside the integral is omitted given that this is a force as opposed to a moment.

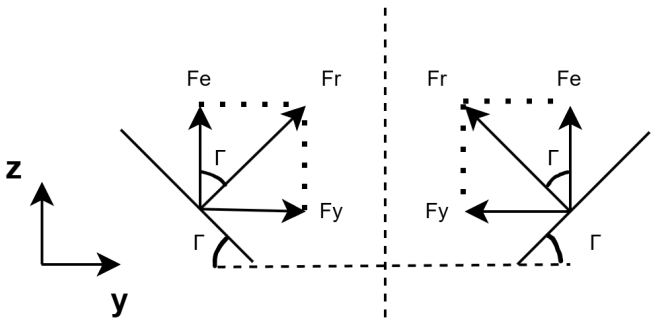

Figure 9.3: Ruddervator Angles

$$C_{Y_{\delta_{rv}}} = \frac{2 \cdot C_{y_{\beta_{tail}}} \cdot \tau_{rv,r}}{S_{ref}} \int_0^{b_{tail}} c_{tail}(b) db \tag{9.9}$$

The remaining aerodynamic moment component generated by a ruddervator deflection is the pitching moment. Equation 9.10 shows the corresponding contribution specifically generated by the tail surfaces. In contrast to the yawing component, the pitching component is scaled by the cosine of the dihedral angle as shown in Equation 9.11 [57].

$$C_{m_{\delta_{rv}}} = -\frac{2\, C_{l_{\alpha_{tail}}}\, \tau_{rv,e}}{S_{ref}\, \bar{c}} \int_0^{b_{tail}} c_{tail}(b)\, (x_{ac,tail}(b) - x_{cg})\, db \tag{9.10}$$

$$\tau_{rv,e} = \tau_e \cos(\Gamma_{\text{tail}}) \tag{9.11}$$

9.3.4. Critical Design Cases

In order to size the control surfaces such that they are sufficiently effective in the most demanding conditions, the engine inoperative, crosswind, and the Dutch roll damping are analysed.

Engine Inoperative

The first potential constraining required rudder deflection is in the case of an engine inoperative. Given that the aircraft has four engines, the analysis includes the assumption of two engine failures on the same side of the aircraft at the same time for extra redundancy. The matrix equation in Equation 9.12[37] shows the relation for stationary flight with asymmetric power.

$$\begin{bmatrix} C_L & C_{Y_\beta} & 0 & C_{Y_{\delta_{rv}}} \\ 0 & C_{l_\beta} & C_{l_{\delta_a}} & 0 \\ 0 & C_{n_\beta} & 0 & C_{n_{\delta_{rv}}} \end{bmatrix} \begin{bmatrix} \varphi \\ \beta \\ \delta_a \\ \delta_{rv} \end{bmatrix} = - \begin{bmatrix} 0 \\ C_{l_e} \\ C_{n_e} \end{bmatrix} \tag{9.12}$$

This matrix equation can be used to determine the rudder and/or aileron deflection for an engine out situation. Given that the engines are not positioned on an incline, the rolling moment due to an engine failure C_{l_e} is neglected. The engine inoperative yawing coefficient is calculated using Equation 9.13.[37] In this equation, ΔT_p indicates the thrust loss from an engine at spanwise location y_e.

$$C_{n_e} = \frac{\Delta T_p y_e}{\frac{1}{2}\rho V^2 S_{ref} b} \tag{9.13}$$

The required rudder deflection angle can be calculated for a zero sideslip angle corresponding to the engine inoperative case, resulting in Equation 9.14. The same is done for the aileron deflection in Equation 9.15. In addition, the corresponding roll angle is calculated with Equation 9.16. In this equation, C_L is simply the lift coefficient of the aircraft.

$$\delta_{rv,EIO,\beta=0} = -\frac{C_{n_e}}{C_{n_{\delta_{rv}}}} \tag{9.14}$$

$$\delta_{a,EIO,\beta=0} = -\frac{C_{l_e}}{C_{l_{\delta_a}}} \approx 0 \tag{9.15}$$

$$\varphi_{EIO,\beta=0} = \frac{C_{Y_{\delta_{rv}}}\, C_{n_e}}{C_L\, C_{n_{\delta_{rv}}}} \tag{9.16}$$

[37] in 't Veld, A., 'Part 3: Static stabililty, Lateral Stability and Control in Steady Flight,' AE3212-I Aerospace Flight Dynamics & Simulation, Delft University of Technology, Delft, The Netherlands, 2026

By using the previously obtained equations for the moment coefficient derivative with respect to a control surface deflection angle, the C_{n_β} derivative can similarly be calculated as shown in Equation 9.17. In this case, since this derivative does not include a control surface deflection, the control surface effectiveness τ is omitted from the equation. Furthermore, the equations should be scaled with the corresponding trigonometric relations of the dihedral angle to separate the individual contributions of the inclined tail surfaces, as shown in Figure 9.4 for a positive sideslip angle.

$$C_{n_\beta} = \frac{2 \cdot C_{y_{\beta_{tail}}} \cdot \sin^2(\Gamma)}{S_{ref} \cdot b} \int_0^{b_{tail}} c_{tail}(b) \cdot (x_{ac,tail}(b) - x_{cg})\, db \tag{9.17}$$

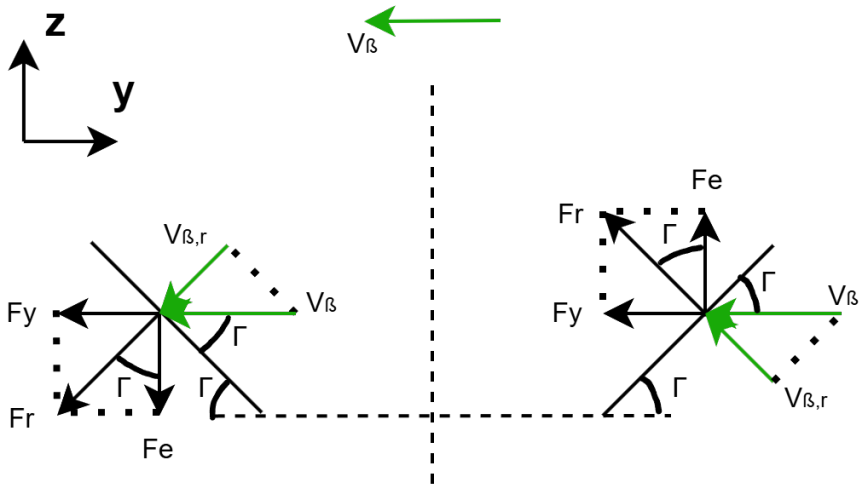

Figure 9.4: Ruddervator Angles with Sideslip Velocity

The produced side force due to a sideslip angle C_{Y_β} can be calculated by using Equation 9.18.

$$C_{Y_\beta} = -\frac{2 \cdot C_{y_{\beta_{tail}}} \cdot \sin^2(\Gamma)}{S_{ref}} \int_0^{b_{tail}} c_{tail}(b) db \tag{9.18}$$

Crosswind

The second potential constraining conditions for the required elevator deflection are during a strong crosswind, described by Equation 9.19.

$$\begin{bmatrix} C_L & C_{Y_\beta} & 0 & C_{Y_{\delta_{rv}}} \\ 0 & C_{l_\beta} & C_{l_{\delta_a}} & 0 \\ 0 & C_{n_\beta} & 0 & C_{n_{\delta_{rv}}} \end{bmatrix} \begin{bmatrix} \varphi \\ \beta \\ \delta_a \\ \delta_{rv} \end{bmatrix} = \begin{bmatrix} 0 \\ 0 \\ 0 \end{bmatrix} \tag{9.19}$$

The corresponding sideslip angle can be calculated using Equation 9.20. Consequently, the ruddervator deflection angle for yawing during crosswind with given magnitude can be calculated using Equation 9.21. Furthermore, the aileron deflection angle for this situation is given by Equation 9.22.

$$\beta_{crosswind} = \arctan\left(\frac{V_{crosswind}}{V_{TO}}\right) \tag{9.20}$$

$$\delta_{rv,crosswind} = -\frac{C_{n_\beta}\, \beta_{crosswind}}{C_{n_{\delta_{rv}}}} \tag{9.21}$$

$$\delta_{a,crosswind} = -\frac{C_{l_\beta}\, \beta_{crosswind}}{C_{l_{\delta_a}}} \tag{9.22}$$

The rolling moment due to a sideslip angle C_{l_β} is obtained through the following relations, which takes into account the v-tail contribution and the dihedral of the wing of the aircraft.

$$C_{l_\beta} = C_{l_{\beta_{\Lambda,w}}} + C_{l_{\beta_{tail}}} \tag{9.23}$$

$$C_{l_{\beta_{\Lambda,w}}} = -\frac{C_L}{b\,\sin(\Lambda_{1/4})\,y_{mac}} \tag{9.24}$$

$$C_{l_{\beta_{tail}}} = -\frac{2 \cdot C_{l_{\alpha_{tail}}} \cdot \sin(\Gamma)\cos(\Gamma)}{S_{ref} \cdot b} \int_0^{b_{tail}} c_{tail}(y) \cdot (y\sin(\Gamma_{tail}) + y_{root,tail})dy \tag{9.25}$$

Dutch Roll Damping

Given that the v-tail sizing was mainly based on the required stability and control characteristics of the aircraft as discussed in chapter 7, the Dutch roll damping is an important parameter to analyse for the design of the tail. This damping coefficient can be determined through a series of equations as shown in Equations 9.26 - 9.34 [56].

In Equation 9.26 and Equation 9.27, the yawing moment due to a yaw rate coefficient C_{n_r} and the side force due to a yaw rate coefficient C_{Y_r} is calculated using the previously computed value of C_{Y_β}.

$$C_{n_r} = 2\left(\frac{x_{ac,tail} - x_{cg,fwd}}{b}\right)^2 C_{Y_\beta} \tag{9.26}$$

$$C_{Y_r} = -2\left(\frac{x_{ac,tail} - x_{cg,fwd}}{b}\right) C_{Y_\beta} \tag{9.27}$$

Equations 9.28–9.31 calculate the forces and moments due to yaw rate and sideslip. In these equations, the mass moment of inertia I_{zz} is taken about the centre of gravity and is estimated using Equation 9.32. The velocity U is the steady-state flight speed and is taken as the cruise speed, while m is the aircraft mass.

$$N_r = \frac{C_{n_r}\, q\, S_{ref}\, b^2}{2\, I_{zz}\, U} \tag{9.28}$$

$$Y_r = \frac{C_{Y_r}\, q\, S_{ref}\, b}{2\, m\, U} \tag{9.29}$$

$$N_\beta = \frac{C_{n_\beta}\, q\, S_{ref}\, b}{I_{zz}} \tag{9.30}$$

$$Y_\beta = \frac{C_{Y_\beta}\, q\, S_{ref}}{m} \tag{9.31}$$

$$I_{zz} = \Sigma(mx^2) + \Sigma(my^2) \tag{9.32}$$

Using the above relations, the undamped natural frequency ω_n and consequently the Dutch roll damping coefficient ζ can be calculated from Equation 9.33 and Equation 9.34, respectively.

$$\omega_n = \sqrt{\frac{Y_\beta N_r + N_\beta(U - Y_r)}{U}} \tag{9.33}$$

$$\zeta = -\frac{N_r + \frac{Y_\beta}{U}}{2\,\omega_n} \tag{9.34}$$

The desired Dutch roll damping coefficient is between 0.2 and 0.3.[38] In case an insufficient damping value is calculated from Equation 9.34, a yaw damper can be implemented into the aircraft. Using Equation 9.35, the new C_{n_r} can be calculated using a chosen gain K_r. This new value of C_{n_r} can be used to obtain a new Dutch roll damping coefficient. Through trial and error, a desired gain value can be determined.

$$C_{n_r} = C_{n_r} + K_r \cdot C_{n_{\delta_r}} \tag{9.35}$$

9.3.5. Trim Conditions

The optimal trim configuration of the ruddervator and wing elevator is determined using Equation B.35, which is obtained from Equation B.30 by imposing the trim condition and solving for the required ruddervator deflection angle, (δ_r). For the selected wing position, the wing elevator and ruddervator deflections are evaluated over a range of wing elevator values to establish the relationship between the two control surfaces and to identify the optimum trim configuration.

The optimum configuration is determined by computing the total trim drag associated with each combination of wing elevator and ruddervator deflections. The combination of (δ_e) and (δ_r) that yields the minimum trim drag is selected as the optimal trim configuration. Minimising the trim drag is desirable, as it reduces the aerodynamic penalty associated with maintaining longitudinal equilibrium during cruise. The total trim drag can be computed using Equation 9.36:

$$D_{\text{trim}} = \frac{1}{2}\rho V_{cr}^2 S_w \frac{C_{L,w,\text{tot}}^2}{\pi A_w e_w} + \frac{1}{2}\rho V_r^2 S_r \frac{C_{L,r,\text{tot}}^2}{\pi A_r e_r}, \tag{9.36}$$

[38] URL `https://mil-spec.tpub.com/MIL-F/MIL-F-8785C/MIL-F-8785C00022.htm` [cited 16/06/2026]

Where $C_{L,w,\text{tot}}$ and $C_{L,r,\text{tot}}$ can be expressed as:

$$C_{L,w,\text{tot}} = C_{L_{\alpha,w}}(\alpha - \alpha_{0,w}) + C_{L_{\delta_e}}\delta_e \quad (9.37) \qquad C_{L,r,\text{tot}} = C_{L_{\alpha,r}}\left[\alpha\left(1 - \frac{d\varepsilon}{d\alpha}\right) - \alpha_{0,r} + \alpha_i\right] + C_{L_{\delta_r}}\delta_r \quad (9.38)$$

In this analysis however, the aircraft angle of attack, zero-lift angles and ruddervator incidence angle are fixed. Therefore, only the additional lift generated by the control surface deflections is considered in the trim drag optimisation. The relevant lifting areas are taken as the wing elevator area, S_{δ_e}, and the ruddervator control surface area, S_{δ_r}, rather than the full wing and ruddervator areas. This reduces Equation 9.36 to:

$$D_{\text{trim}} = \frac{1}{2}\rho V_{cr}^2 S_{\delta_e}\frac{\left(C_{L_{\delta_e}}\delta_e\right)^2}{\pi A_{\delta_e} e_{\delta_e}} + \frac{1}{2}\rho V_r^2 S_{\delta_r}\frac{\left(C_{L_{\delta_r}}\delta_r\right)^2}{\pi A_{\delta_r} e_{\delta_r}}. \quad (9.39)$$

9.4. Results

The results obtained from the methods presented in section 9.3 are presented in this section. First, the control surface results are shown and consequently the trim conditions.

9.4.1. Aileron Results

The design process started with the sizing of the ailerons on the wing. The ailerons were placed at the tip of the wings to maximise the lateral moment arm and thus its effectiveness. It was decided to use a chord-to-chord ratio of 0.25 for the aileron, resulting in an aileron effectiveness τ_a of 0.475 using Figure 9.2. This allows to calculate the achievable roll rate by first assuming a spanwise length of the aileron. The spanwise start of the aileron is a_1 and the spanwise end is a_2. These values are expressed as a fraction of the half-wing span, starting from the root chord of the wing. a_2 was fixed at 0.92, meaning only a_1 is iterated to obtain a sufficient roll rate, while minimising the space occupied by the aileron. Table 9.3 summarises the obtained aileron results and size.

It can be seen that all roll rates during take-off, landing and cruise are higher than the required roll rates. Therefore the ailerons are sufficient to provide roll control in all flight configurations. The values of the roll rates are slightly higher than the required values as can be seen in Table 9.2, such that the ailerons do not require the maximum deflection to provide the roll rate. The cruise roll rate is significantly higher, because of a significantly higher velocity compared to the other cases. Therefore, only very small deflection angles are needed. In further designs steps, ailerons can be added near the fuselage to provide lower roll rates during cruise.

Table 9.3: Aileron Results

Parameter	Value	Unit	Parameter	Value	Unit
$\frac{c_a}{c_w}$	0.25	-	τ_a	0.475	-
a_1	0.7 $\frac{b_w}{2}$	m	a_2	0.92 $\frac{b_w}{2}$	m
$C_{l_{\delta_a}}$	0.095	$\frac{1}{rad}$	δa_{max}	+/- 25	deg
C_{l_p}	-0.800	$\frac{1}{\text{rad}}$	P_{cr}	39.7	$\frac{\text{deg}}{\text{s}}$
P_{to}	11.1	$\frac{\text{deg}}{\text{s}}$	P_{land}	12.1	$\frac{\text{deg}}{\text{s}}$

9.4.2. Ruddervator Results

Now that the aileron location and size is known, the elevators on the wings can be designed. However, since the elevator effectiveness at this location relative to the main landing gear is limited, it was decided to first evaluate the ruddervators on the v-tail and subsequently provide any remaining required pitch control using elevators on the wing to limit the control surface area on the wing.

Following the previously presented method for the sizing of the ruddervator, the control and stability derivatives can be calculated to obtain the required ruddervator deflection angle for yawing in case of an engine inoperative, during crosswind, as well as to test the Dutch roll damping performance. The ruddervator span is taken equal to the span of the v-tail, such that the entire surface can be efficiently used for lateral and longitudinal control. The chord-to-chord ratio of the ruddervator on the v-tail was chosen to be 0.4, resulting in a control surface effectiveness of 0.6. The final results can be found in Table 9.4. Prior to this, the required deflection angles were fed back into the empennage design to optimize its size.

Table 9.4: Control/Stability Derivative Results

Parameter	Value [1/rad]	Parameter	Value [1/rad]
C_{l_e}	0	C_{n_e}	0.007
$C_{n_{\delta_{rv}}}$	-0.066	C_{n_β}	0.103
$C_{Y_{\delta_{rv}}}$	0.307	C_{Y_β}	-0.480
$C_{m_{\delta_{rv}}}$	-0.149	C_{l_β}	-0.070
C_{n_r}	-0.311	C_{Y_r}	0.214

These obtained result can be used to calculate the forces and moments needed to obtain the desired Dutch roll damping, as well as the deflection angles for the critical design cases. The obtained values are summarised in Table 9.5. Table 9.5 shows that the maximum required deflection required of the ruddervator for one of the critical design cases is 14.1 degrees, which is well below the maximum ruddervator deflection angle of 25 degrees. However, the damping ratio is too low for proper Dutch roll damping. Therefore, it was decided to implement a yaw damper. The gain of the yaw damper K_r was determined using trial and error to obtain the desired damping ratio of 0.2-0.3. From Table 9.6, it was concluded that a gain of 4 would be optimal for yaw damping. However, note that given the positive Dutch roll damping coefficient without yaw damper, the aircraft will still be damped in case the yaw damper fails. It will simply be less than ideal for passenger comfort given the increased time to damp out the motion.

Table 9.5: Critical Design Cases Results

Parameter	Value	Unit	Parameter	Value	Unit
$\delta_{rv,EIO,\beta=0}$	6.0	deg	$\beta_{crosswind}$	9.0	deg
$\delta_{a,EIO,\beta=0}$	0	deg	$\delta_{rv,crosswind}$	14.1	deg
$\varphi_{EIO,\beta=0}$	-2.6	deg	$\delta_{a,crosswind}$	8.2	deg
ω_n	2.18	$\frac{\text{rad}}{\text{s}}$	ζ	0.059	-

Table 9.6: Yaw Damper Gain Results

K_r	C_{n_r}	ζ
0	-0.048	0.059
1	-0.114	0.111
2	-0.180	0.163
3	-0.245	0.214
4	-0.311	0.266
5	-0.377	0.317

Now that the yaw component of the ruddervator is sized, the elevator contribution can be analysed to determine the additional required elevator size on the wing to adhere to the angular acceleration requirement. Using the result of $C_{m_{\delta_{rv}}}$ from Table 9.4, the total moment during take-off rotation at the main landing gear can be calculated to determine the resulting acceleration, as described in Equation 9.5. The final ruddervator design still resulted in a pitching down acceleration during full deflection. Therefore, additional elevators on the wing were required for take-off.

9.4.3. Elevator Results

Given the method presented in subsection 9.3.2, the elevator spanwise length on the wing is iterated to obtain a sufficient angular acceleration during take-off rotation. As specified, the required rotational acceleration is at least 8 $\frac{\text{deg}}{\text{s}^2}$. Given that the start of the aileron is located at 0.7 $\frac{b_w}{2}$, the spanwise end position of the elevator e_2 is determined to be at 0.65 $\frac{b_w}{2}$ to maximise the longitudinal moment arm, while providing sufficient spacing between the two control surfaces. The chord-to-chord ratio of the elevator will be equal to that of the aileron, which is 0.25. Table 9.7 shows the final results including the elevator size.

Table 9.7: Elevator Results

Parameter	Value	Unit	Parameter	Value	Unit
$\frac{c_e}{c_w}$	0.25	-	τ_a	0.475	-
$C_{m_{\delta_e}}$	-1.78	$\frac{1}{\text{rad}}$	$\delta_{e,max}$	+/- 25	deg
e_1	0.5 $\frac{b_w}{2}$	m	e_2	0.65 $\frac{b_w}{2}$	m
$\ddot{\theta}_{to}$	20.1	$\frac{\text{deg}}{\text{s}^2}$			

The combination of ruddervator and elevator allows for a certain extent of redundancy in case large deflections of both rudder and elevator at the same time are needed. Furthermore, from Table 9.5 it can be seen that full

deflections of the ruddervator are not needed in any of the critical cases, leaving sufficient room for combined rudder/elevator input. The same applies to the elevator, where the achievable angular acceleration as shown in Table 9.7 is significantly larger than the minimum required value for take-off rotation. Figure 9.5 shows the integration of the aileron and elevator on the wing of the aircraft.

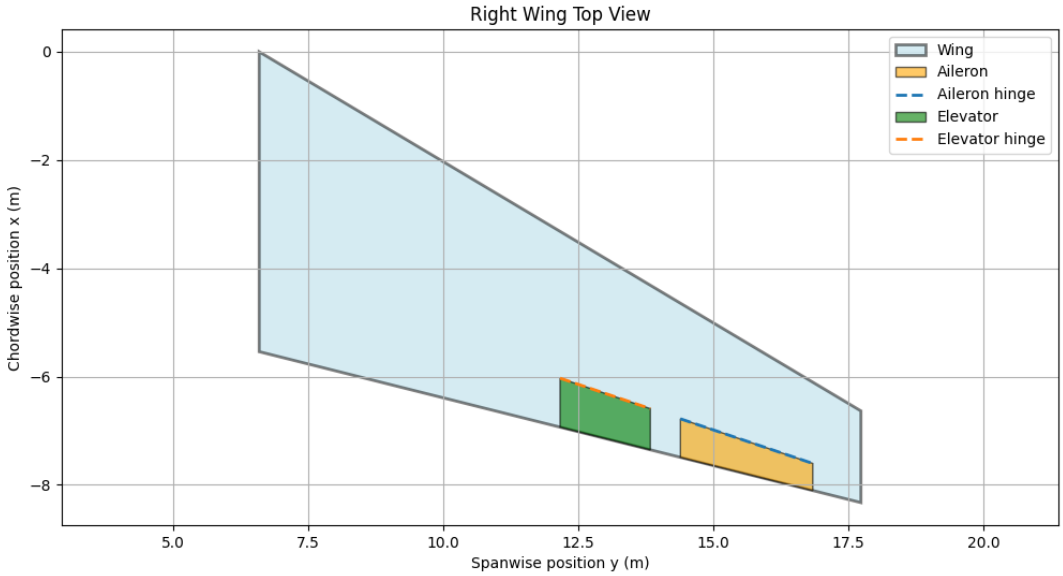

Figure 9.5: Wing Planform with Control Surfaces

9.4.4. Trim Conditions

With the wing location and empennage size determined, the cruise trim conditions can be evaluated. The combinations of elevator deflection, δ_e, and rudder deflection, δ_r, that satisfy the trim condition in cruise are shown in Figure 9.6a. The corresponding trim drag values are presented in Figure 9.6b. For both the most forward and most aft centre-of-gravity positions, a distinct minimum in trim drag can be identified, representing the most favourable trim condition for each case. As the centre of gravity shifts aft during flight, the required trim setting moves gradually between these minima. For the current design the most forward CG position was selected as the design trim condition, as it represents the worst-case loading scenario in terms of stability requirements. At this condition, the minimum trim drag occurs at a wing elevator deflection of $-3°$ [deg], corresponding to a rudder deflection of $-0.62°$ [deg].

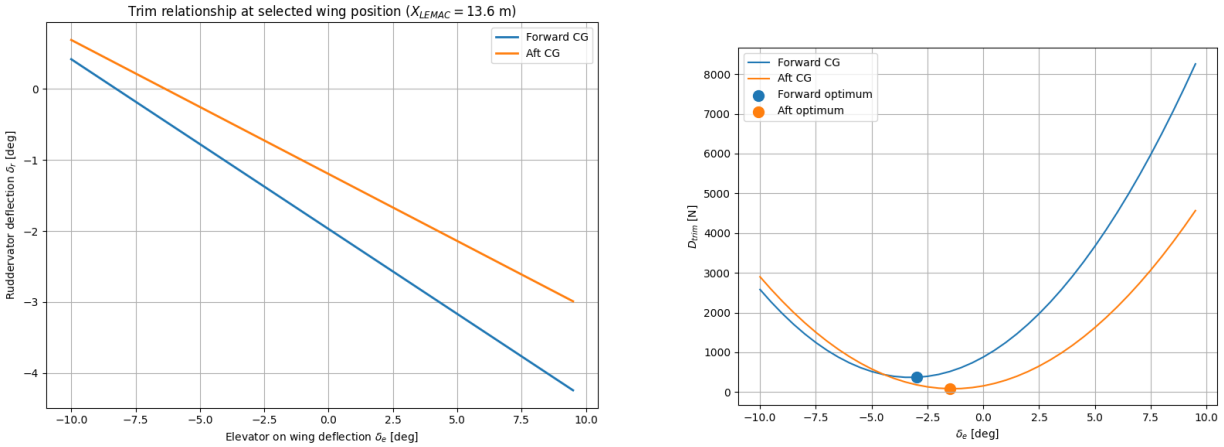

(a) δ_e against δ_r

(b) D_{trim} location against δ_e

Figure 9.6: Trim configuration

10. Landing Gear Subsystem

The procedure on how all components concerning the landing gear will be described in this chapter. The landing gear is responsible for supporting the aircraft during ground operations, absorbing landing and taxiing loads, providing steering and braking capability, protecting the runway surface, and facilitating towing. To fulfil these functions, the wheel, shock absorber, braking, positioning, struts and retraction systems are designed and evaluated against the operational requirements of the aircraft.

10.1. Information Dependencies

Figure 10.1 illustrates the design dependencies of the landing gear system within the complete aircraft design. It can be seen that the main aspects treated are the design of the subsystem are; gear design, which consists in a force calculation, wheel and shock absorber design, brakes design, motor sizing, positioning the gears and designing the retraction mechanism. Gear Design receives inputs from nearly all upstream subsystems, including aircraft weight, CG location, fuselage and engine geometry and available stowage space, reflecting its highly coupled nature. Its outputs: wheel dimensions, allowable loads, and strut dimensions feed directly into Brakes Design and Motor Sizing. The chain finishes with Positioning and Retraction Mechanism design, which depend on all preceding outputs. This structure highlights that landing gear design cannot be finalised in isolation, but requires convergence of structural, geometric, and performance inputs from across the aircraft design.

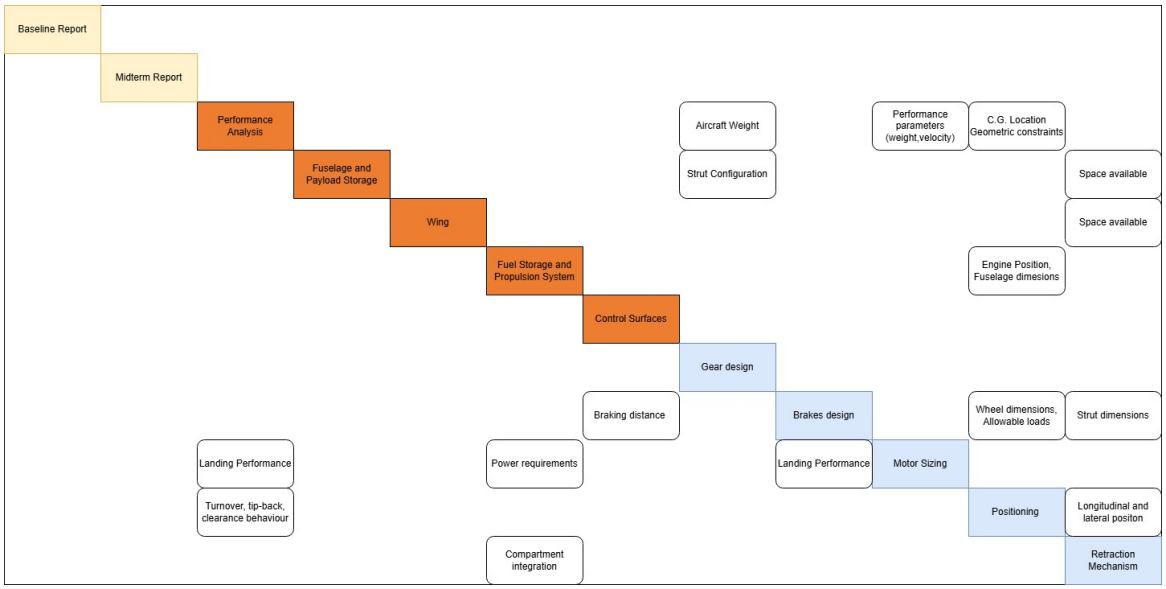

Figure 10.1: N^2 Chart indicating the flow of information within the design of the landing gear subsystem

10.2. Assumptions

Table 10.1: Landing Gear assumptions

ID	Assumption	Variable(s)	Effect
LG1	Number of nose wheels are assumed to be 2 because it is the current state of art	N_{NW}	New configurations could arise by 2050, which can offer an increase in performance compared to current technologies and will therefore be chosen for the BWB.

Continued on next page

ID	Assumption	Variable(s)	Effect
LG2	A main/nose gear loads split is assumed to be 90%/10% respectively	P_M, P_N	A change in the load distribution in the gears will change the tire selection process, and thus the strut configuration and the shock absorber. A 10% decrease in the main gear load will decrease the shock absorber diameter by 1.85%.
LG3	Carbon-fiber anti-skid brakes are assumed to be the best choice from [35] without a proper trade-off	μ_{brake}	If conventional brakes are chosen above carbon-fibre, μ_{brake} would decrease to 0.3, and thus the braking distance would increase by 62.5%
LG4	Breaking distance procedure is performed with several top-level assumptions that simplify considerably the analysis. Lift and drag during braking are assumed to be equal to zero	L, D	If lift is not assumed to be completely destroyed it will increase the distance, while if the effect of drag is included it will decrease the braking distance by 10% , taking a drag coefficient similar to approach conditions.
LG5	Crosswind bank angle is comparable to that of a conventional aircraft	bank angle	Difficult to quanifty without complex aerdynamic and flight control simultions.

10.3. Methods

10.3.1. Force Calculation

The first step in designing the landing gear for an aircraft is determining the expected loads on each strut and each tire. To do this, first the number of nose and main gear struts and tires must be determined. To do this an approach determined in ADSEE 3 was used:

$$N_{MW} = f\frac{W_{MTO}}{210000} \tag{10.1}$$

The weighting 'f' is equal to 4 for this sized aircraft, W_{MTO} is 112685 lbs. The number obtained from Equation 10.1 must be rounded up to the nearest multiple of 4. The number of nose wheels is common for this category of aircraft. If the total number of main gear wheels is less than 12, two main gear struts will be used, otherwise higher number of struts will be needed. Next the static forces on the tires and struts must be determined, to this the approach used by Roskam in Airplane Design Part IV, the load on the main and nose struts can be written as:

$$P_M = \frac{W_{MTOW} * g * 1.01 * 1.07 * 0.9 * 1.25}{num_{maingear}} \tag{10.2}$$

$$P_N = \frac{W_{MTOW} * g * 1.01 * 1.07 * 0.1 * 1.25}{num_{nosegear}} \tag{10.3}$$

Each number in this equation represents a different correction, W_{MTOW} is the take off weight, g is the gravitational acceleration, 1.01 corrects for the ramp weight being higher than the take off weight, 1.07 is required as per CS 25, 0.9/0.1 accounts for the ratio of weight between main and nose gear, 1.25 is a correction to allows for a growth in aircraft weight. Lastly, to identify the static forces on each tire the force on each strut must be divided by the amount of tires on each strut determined earlier.

The nose gear is also subjected to dynamic loads due to steering, these are included in the tire selection by standard 1.5 corrections. The equation to determine the dynamic forces on the nose gear consists as follows:

$$P_{n_{dyn_t}} = MTOW\frac{l_m + \frac{a_x}{g} * h_c g}{F_{Nt}(l_m + l_n)} \tag{10.4}$$

l_m is the distance of the centre of gravity to the main gear, l_n is the distance from the nose gear to the centre of gravity, a_x is the deceleration force, $h_c g$ is the distance from the ground to the centre of gravity. This equation

provided numbers lower than the static load, allowing the design to take the static load as the design point.

10.3.2. Wheel Design

To determine the tire the input force must be taken into a table comparing tyre types and selecting a tire which has the best properties, for the main gear it has been chosen to use a 44x16 inch tire, weighing 168 lbs and a nose gear of 15.00 due to its light mass off 55lbs. These were chosen as they are low weight and their ability to comply with the requirements.

10.3.3. Shock absorber

Roskam also provides information for the sizing of the shock absorber, the following equation provides information to the size of the main gear shock absorber:

$$s_s = \frac{0.5 MTOW w_t^2}{2 P_M N_g} \tag{10.5}$$

w_t is the touchdown rate as defined by CS 25.723 of 12 feet per second, N_g is the landing gear load fraction as supplied by Table 2.18 in Roskam. Similarly a shock absorber diameter can be determined empirically by the following equation:

$$d_s = 0.041 + 0.0025\sqrt{P_M} \tag{10.6}$$

10.3.4. Brakes design

The braking system plays a crucial role in the capabilities and performance that the landing gear delivers. Brakes help stop the aircraft, hold it when parked, control speed when taxiing, and even help steer the aircraft by differential braking action. The selection and design of the brakes and the brake actuation system were done according to Roskam [35], unless specified otherwise.

The principle of reducing the aircraft's speed during braking is the rolling friction between the tires and the runway surface while applying the braking action. The rolling friction coefficient is related to the so-called slip ratio, defined by Equation 10.7.

$$\text{Slip ratio} = 1 - \frac{RPM_{\text{braking}}}{RPM_{\text{no braking}}} \tag{10.7}$$

When the slip ratio is zero, the friction coefficient is purely due to the runway characteristics, as the brakes have not reduced the wheel's rpm. On the other side, at a slip ratio equal to 1, the wheels are locked by brakes, and the tire starts to wear out, potentially causing tire blow-out if this condition is maintained, called the skidding condition. This is the reason why modern aircraft use disc-type, anti-skid brakes. The best-suited brakes for the design are carbon fiber, anti-skid, composite brakes because they offer a significant improvement on the aircraft decceleration and they are about 40% lighter than conventional brakes, with the trade-off being that their manufacturing process is very time-demanding, producing a single carbon disc involves high-temperature processing such as chemical vapour infiltration, which can take up to 100 hours [39], doubling the cost w.r.t. conventional. Additionally, carbon fiber brakes are proven to cut maintenance time by 40% [40], as Safran Landing Systems' new generation of lightweight carbon brake discs aim at saving fuel and cutting CO_2 emissions [41]. Specifically, Sepcarb X, which has 20% improved wear resistance and is being tested on Airbus A350 and Boeing 787 fleets. Thus, Safran's Sepcarb X will be integrated into the design.

Brake actuation system

The brake actuation system describes how the braking procedure is carried out and serves to explain which components participate and how they interact with each other. As the main landing gear was decided to have two struts, the system will consist of two independent sub-systems with respect to electrical sources, and metering and anti-skid valves. As a reference, Figure 10.2 serves to illustrate a schematic of the brake system of a commercial aircraft, but the design will differ from it.

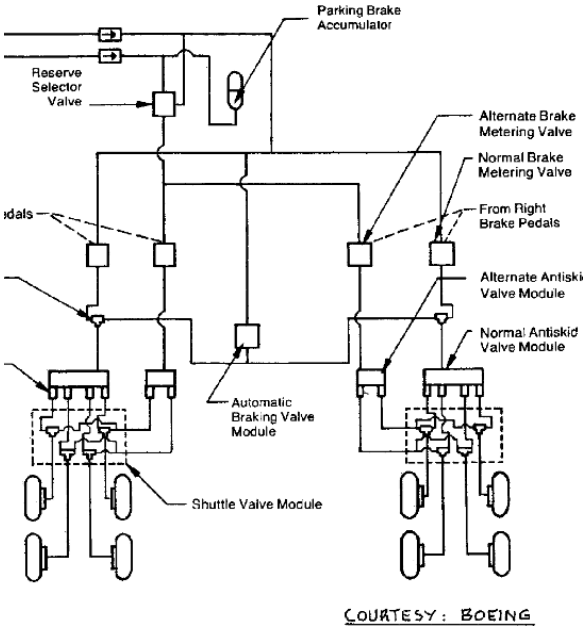

The brake actuation system will include the following components:

- **Heat shields:** To prevent overheating of the tire from the inside.
- **Brake discs**
- **Brake pedals:** Located in the cockpit to control the system during flight. When a pilot presses the brake pedals, hydraulic pressure is applied to the discs.
- **Anti-skid system**
- **Hydraulic systems/Brake control units:** Controls the discs and ensures that the necessary pressure is applied to them.
- **Emergency brakes:** In case of system failure.

Figure 10.2: Boeing 767 Main Gear Braking System [35]

Landing Capability

The design needs to be able to land safely an in a relatively short distance to satisfy with runway constraints. REQ-OPE-2.2.15 sets the maximum allowable runway distance the aircraft needs to operate within. During landing, braking is one of the main contributors to the total distance covered. For this analysis, the braking procedure was modelled as a constant-decelerating motion, thus the braking distance, s_{brake} is defined as;

$$s_{brake} = \frac{V_{TD}^2}{2a_{brake}}$$

where V_{TD} is the touchdown speed, assumed to be equal to the approach speed V_{app} and the braking deceleration is defined as;

$$a_{brake} = \frac{g(\mu_{brake} + \mu_{roll})(W - L) + D - T_{idle}}{W}$$

Where μ_{brake} and μ_{roll} are the dynamic friction coefficients of the brakes and of the runway surface respectively, which from Roskam μ_{brake} = 0.5 for carbon-fiber, anti-skid brakes in dry conditions and for commercial aircraft on a dry concrete/asphalt runway, $\mu_{roll} \approx 0.02$. L is the lift, D drag and T_{idle} is the idle thrust during braking. It is defined as the residual thrust produced by the engines when they are in idle position, which is 0 for electric motors driven by hydrogen fuel cells [58]. Setting $L \approx 0$ (lift destroyed after touchdown) and D = 0, using the MTOW from subsection 5.3.3, the braking distance is sized. It is important to note that this is a conservative estimate as it ignores aerodynamic drag during braking, which in reality would add effective deceleration, thus the real braking distance will be shorter.

10.3.5. Motor Sizing

To reduce airport particulate emissions a focus is given to reducing the tire wear, and brakepad usage, as these are known to cause particulate emissions. This is done by attempting to use electromagnetic plates in combination with conventional brakes on the main gear, and using this energy to turn the gear before touchdown, reducing the wear when they come into contact with the runway.

The original intention for sizing this motor assumed it being used as a generator and collecting an equivalent amount of energy as current brake-pads do on conventional aircraft, the original sizing gave information that this system would need to absorb approximately 20.2k Wh. Which is equivalent of modern large batteries. However, the landing roll only lasts approximately 60 seconds. This transfer of 72 MJ of energy in such a short period of time is equivalent to 1.3 MW generator. A motor being sized this large would be incredibly large and heavy, providing large negative contributions when brining, therefore it has been opted to use conventional carbon

[39] URL https://www.marketgrowthreports.com/market-reports/aircraft-carbon-brake-disc-market-103570 [cited 08/06/2026]

[40] URL https://www.alliedmarketresearch.com/airplane-carbon-brake-disc-market-A10103 [cited 08/06/2026]

[41] URL https://www.safran-group.com/companies/safran-landing-systems [cited 08/06/2026]

breaks as the UFP emissions are comparably low from this source compared to a conventional jet engine and APU, allowing the requirement to be validated without utalising this aditional system.

10.3.6. Undercarriage Positioning

Longitudinal

To determine the landing gear position a potato plot for the loading of the aircraft was produced, including a 5% contingency from this the most aft and forward cg position during loading can be identified.

From the most aft cg position can be determined for landing gear sizing. For longitudinal stability it is a balance between tip back angle, required rotation moment, and scrape angle. To determine the longitudinal position a scrape back angle of 12°was taken, this is comparable to that of the A320. A line can be drawn from the tail of the aircraft at 12°and a first requirement can be drawn, the compressed landing gear must be below this line. This line can be seen on. A second line can be drawn as the tip back angle, if the cg ever occurs further aft than the cg the wheels the aircraft will tip over backwards causing a tail strike. The TU Delft Aerospace Engineering bachelor program provides a value of 15°as a safe margin to accommodate for take off and landing conditions [42]. Therefore another line can be drawn through the aft most cg location determined in the potato plots, the landing gear centre line must be aft of this line. Now to minimise the moment required to rotate the aircraft the landing gear are placed as far into the intersection as possible, the most forward stable position is chosen.

The nose gear of the aircraft require a minimal normal force of 0.08 MTOW [42] due to requiring sufficient force to provide directional stability. By taking the ground moments about the center of gravity the nose gear position can be calculated.

$$(x_{cg} - x_{ng})0.08MTOW = (x_{mg} - x_{cg})0.92MTOW \tag{10.8}$$

Lateral

After having already positioned the undercarriage longitudinally, the lateral position can be determined. For the NLG, it is straight-forward as because of only having one strut, it will be positioned in the centre line of the body, which by convention is considered as having zero lateral displacement, $y_{NLG} = 0m$. The procedure to position the main landing gear is more complex; two constraints need to be taken into account, ground clearance and turnover security. Due to the chosen engine location discussed in chapter 8 the engines won't reduce the clearance of the aircraft during ground procedures, thus ground clearance won't constrain the design. Figure 10.3 provides an schematic and formulas of how the turnover constraint is derived, using a maximum turnover angle of $\Psi = 55°$. The longitudinal position of the NLG w.r.t the most aft c.g. and the MLG together with the vertical position of the c.g. can be derived from Figure 10.4, yielding a minimum lateral position of the MLG of $y_{MLG} = 3.37m$ w.r.t. the centre line of the body. To ease retraction procedures, which will be discussed in the next stage, the lateral positioning of the MLG was determined to be $y_{MLG} = 3.75m$. This value is expected to be conservative considering that the bank angle required during cross-wind of the BWB is going to be lower than for a tube-and-wing layout. This is mainly due to the shape of the fuselage; the BWB has a much flatter fuselage, which reduces considerably the lateral profile area, and thus the sideforce generating during cross-wind situations, allowing for a lower bank angle. From Figure 10.6a, this means that the main landing gear span yields 8.9 m, classifying the design in Class C [59]. Moreover, this position will allow easier retraction procedures, as will be seen later in this section. A final reason why the main landing gear was chosen to be located at 3.75 metres from the centreline of the body is due to the fuselage design; the method that was used to derive the constraint is based on conventional configurations. Tube-and-wing fuselages are narrow and lighter compared to BWB fuselages, which require a much wider MLG configuration for correct weight distribution and to prevent turnover.

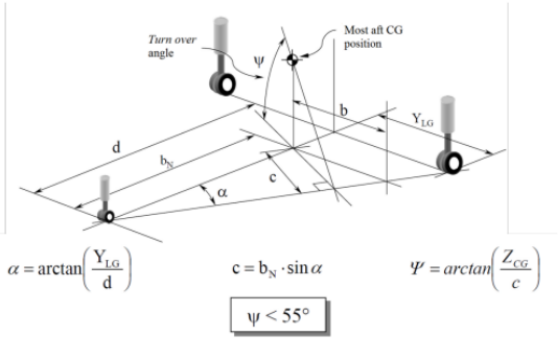

Figure 10.3: Turnover angle [42]

Combination of stability conditions

The last consideration due to the aft location of the wing tips is to analyse the potential of a maximum scrape angle and bank angle. This can occur during a crosswind take off or landing. To analyse this the aircraft was assumed to be at a roll position corresponding with a wing strike (10°), calculating the position of the lowest component of the wing during this manoeuvrer and taking that point into a longitudinal position analysis. Once the longitudinal position and strut length is identified there can be another bank angle analysis to ensure that no requirements on the lateral positioning are not complied with.

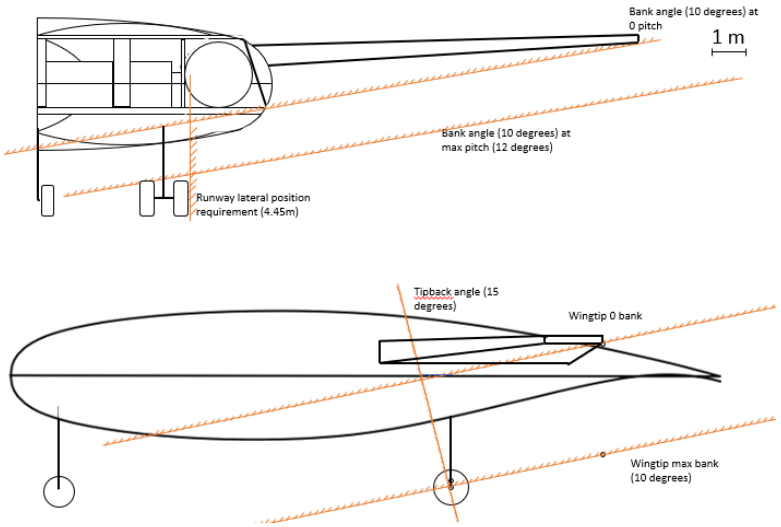

Figure 10.4: Determination of lateral and longitudinal gear position

This results in a main gear has an x position of 13.09 meter from the nose of the aircraft, and a distance from airfoil centre line to tire centre of 3.33 meter. Using Equation 10.8 the nose gear can be placed at 1.465 meter from the nose of the aircraft. The length of the strut being 0.05 meter longer than that of the main gear to accomodate for the slightly smaller tire diameter.

10.3.7. Retraction Procedure

Once the position of the undercarriage has been determined, the way it is retracted needs to be studied. The retraction procedure is as important as the position, as it constrains space distribution, influences the overall performance of the aircraft and can introduce structural challenges. Designing this mechanism includes (for both NLG and MLG); designing the strut to know the dimensions needed for the storing space, describing the retracting procedure and designing the retraction mechanism. The NLG will be sized first, followed by the MLG.

Nose Landing Gear

Starting with the tire dimensions, they were already obtained from subsection 10.3.2 and the total height of the system was taken from Figure 10.4. The width from tire centrelines was taken from Airbus' A319 datasheet [60]

[42] Oliviero, F., "INTRODUCTION TO AIRPLANE DESIGN," AE3212-I Systems Engineering & Aerospace Design, Delft University of Technology, Delft, Netherlands, 2026. [Cited 08 June 2026]

and the maximum strut diameter from the internet [43]. Figure 10.5a represents the simplified strut design, with all the relevant dimensions included. To ensure spacing availability and to satisfy volume constraints, the NLG was decided to be retracted backwards (away from the nose) into the fuselage. With this retraction direction, the storing compartment will be constrained in length by the total gear system length, in height by the tire diameter and in width by the tire-to-tire width. Thus, the space shall have a length of more than 2.55 metres, a minimum height of more than 0.9 metres and a minimum width of more than 0.88 metres. The specific space allocated for the NLG from the fuselage top view can be seen in Figure 10.5b. Contingency was taken in the available space of the compartment to ensure supporting structure and mechanisms fit.

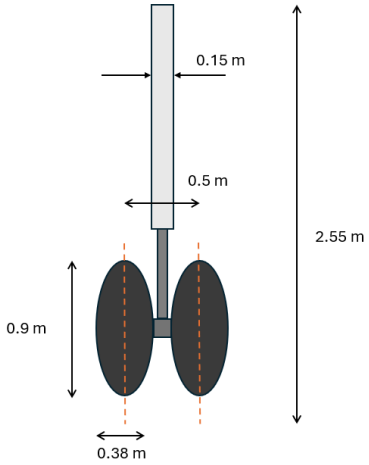

(a) NLG Strut Configuration

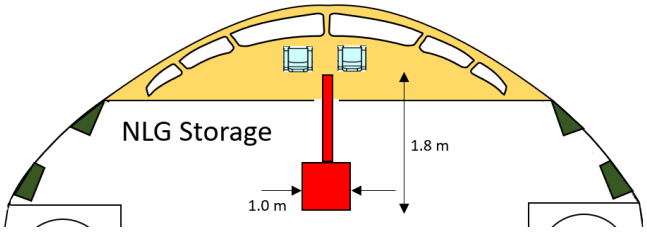

(b) NLG Storage

Figure 10.5: NLG Strut Design

Main Landing Gear

The procedure for designing the strut of the main landing gear was identical to the nose landing gear; from the schematic of the strut in Figure 10.6a, the dimension were derived in the same manner. In this case, the MLG was decided to be retracted into the fuselage towards the tail (in an aft direction). Due to the space unavailability of the fuselage, a fairing structure will be added to the back of the fuselage. For simplicity and time purposes, the aerodynamic and performance analyses were performed with the original shape of the fuselage, without the fairing. Thus, the compartment will be constrained in length by the total strut length (2.6 m), in height/thickness by the tire diameter (1.0 m) and in width by the tire-to-tire width (1.4 m). The compartment location and its dimensions can be seen from Figure 10.6b. As for the NLG, contingency was taken into account to fit the actuator system and other mechanisms.

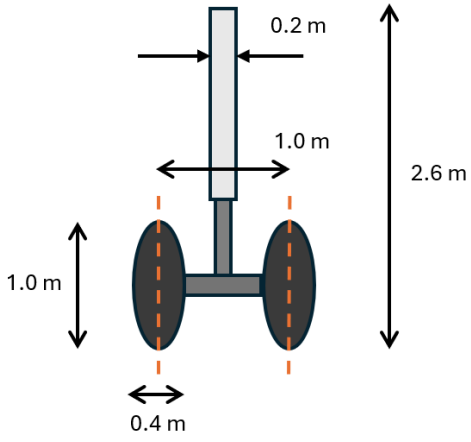

(a) MLG Strut Configuration

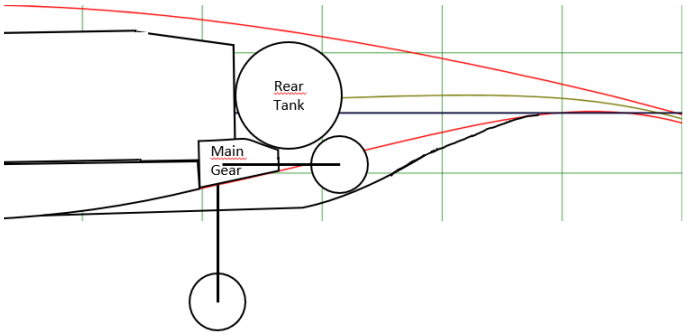

(b) MLG Storage

Figure 10.6: MLG Strut Design

[43] URL `https://an.aero/landing-gear-system/` [cited 08/06/2026]

Mechanism Design

The final step is to design the retraction mechanism, for which the actuator technology will be selected through a trade-off. At first glance, the options brought to the table were;

1. **Centralised Hydraulic Servo (CHS):** Uses a single hydraulic power unit shared across the entire aircraft to supply pressurised fluid [44].
2. **Electro-Hydrostatic Actuator (EHA):** Combines an electric motor, a hydraulic pump, and a cylinder into a single, compact unit [45].
3. **Electro-Mechanical Actuator (EMA):** Converts electrical energy into mechanical movement using an electric motor, a gear train, and a motion converter [46].

These design options will be assessed against the following six criteria, derived from the project requirements and linked to the trade-off done to select the aircraft concept in section 4.1. The weights allocated are intended to match the scope of the design process and emphasise sustainability and remanufacturability, alongside with performance efficiency. Among others, the compatibility of the technology with the fuel-cell architecture is also graded, which will favour EHA and EMA over CHS. The complete trade-off procedure, together with an explanation for each assigned weight, can be seen in Table 10.2. As for convention, scores are between 1-5, being 5 a major benefit, 3 average performance and 1 a critical issue.

Table 10.2: Retraction Technology Trade-Off

Design Options	Sustainability & Emissions	Re-Manufacturability	Energy Efficiency	Powertrain Integration	System Mass & Complexity	TRL by 2050	Total
Weight	**25%**	**20%**	**20%**	**15%**	**10%**	**10%**	**100%**
Hydraulic (CHS)	Hydraulic fluid cannot be recycled or reconditioned and leaks and regular servicing generate chemical waste at the airport [47]. **(1)**	Valves and sealing components get contaminated by fluid during operations, so they need to be decontaminated, making the remanufacturing process way harder. **(2)**	Require continuous pump operation to maintain pressure, causing 30 to 50% losses [48]. **(2)**	The aircraft is purely fuel-cell powered, thus integration an additional electric motor and a hydraulic pump, leading to conversion losses [61]. **(1)**	High system mass required and routing is complex [62]. Although, they offer a high power-to-weight ratio **(2)**	Proven in all commercial aircraft. **(5)**	**1.90**
Electro-Hydrostatic (EHA)	Smaller fluid volume than SHA, so less contamination and disposal concerns [45]. **(3)**	Can be removed as a whole unit, but the hydraulic cylinder makes disassembly still complex,**(3)**	The EHA pump only activates when the actuator is moving, but hydraulic conversion losses are still present [63]. **(3)**	Direct electrical interface to the fuel cell architecture, but still hydraulic fluid present. **(4)**	≈50% heavier than SHA at system level [63] . **(3)**	In service on A380 and A350, not on SMR aircraft. **(4)**	**3.25**
Electro-Mechanical (EMA)	Requires no fluid, thus no waste and no emissions. [46]. **(5)**	Consists of three independent component; the motor is rewindable the gearbox rebuildable and the electronics reconditionable [49]. **(5)**	Zero standby losses; ≈85–90% efficiency vs. 30–50% for hydraulic [63] [64] . **(5)**	Completely direct coupling with the fuel-cell powertrain. **(5)**	Low complexity due to the absence of hydraulic lines. **(4)**	Expected TRL 9 by 2050, but not proven currently. [62] **(3)**	**4.70**

As seen from Table 10.2, EMA is undisputedly the best design option for the purpose of the requirements. It is the only option meeting the zero-emission requirement, plus it offers higher efficiency and integration feasibility than the rest of the options, with the sole drawback of not being proven in commercial aviation. Therefore, the retraction mechanism will be designed as an electro-mechanical actuator system.

The retraction mechanism also needs to satisfy certain requirements; first, from Roskam [35], the retracted actuator length can't be less than one-half of the extended actuator length. Secondly, the gear must be retracted before the aircraft reaches 75% gear placard speed V_{LO} at maximum forward acceleration, which is the maximum airspeed at which it is permitted to operate the landing gear. This rule serves to prevent structural

[44] URL https://www.firgelliauto.com/blogs/mechanisms/hydraulic-servo [cited 11/06/2026]
[45] URL https://www.moog.com/products/actuators-servoactuators/actuation-technologies/electrohydrostatic.html [cited 11/06/2026]
[46] URL https://repositories.lib.utexas.edu/items/e777e211-0ee2-49ff-b4ef-791c7def25c3 [cited 11/06/2026]
[47] URL https://stauff.com/en/blog/worldwide/skydrol-the-high-performance-hydraulic-fluid [cited 11/06/2026]
[48] URL https://eureka.patsnap.com/report-electric-actuators-vs-hydraulic-systems-evaluating-energy-loss [cited 11/06/2026]
[49] URL https://goinfinitum.com/remanufacturing-electric-motors/ [cited 11/06/2026]

damage on the gear from aerodynamic loads. Figure 10.7 illustrates the retraction mechanism for both the NLG and the MLG. For the NLG, the drawing shows the side view, while for the MLG it is the view from the tail of the mechanism. Taking V_{LO} = 222 kts from [35] and a liftoff speed of V_{LOF} = 142 kts, the aircraft reaches 0.75V_{LO} = 150 kts, the available time for retraction and the lift-off acceleration are computed with Equation 10.9 and Equation 10.10. Thrust loading and aerodynamic efficiency conditions at take-off were taken from chapter 5. With these results, it will be confirmed whether the retraction mechanism is expected to satisfy the $t_{retr} \leq t_{avail}$ requirement, knowing that current mechanisms complete full gear retraction in $t_{retr} \approx$ 10-12 s, from reference current retraction times for commercial aircraft systems [65]. Proper force modelling and energy usage for retraction will be studied in latter stages of the design.

$$a_{LOF} \approx g \cdot ((\frac{T}{W})_{TO} - \frac{1}{(L/D)_{TO}}) \tag{10.9}$$

$$t_{avail} = \frac{0.75V_{LO} - V_{LOF}}{a_{LOF}} \tag{10.10}$$

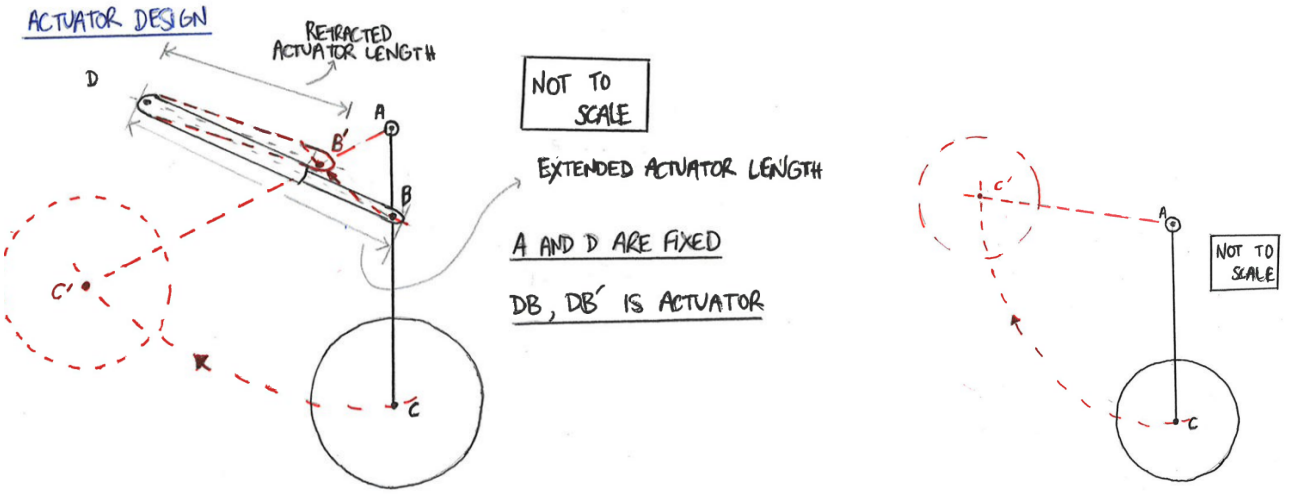

(a) Retraction Mechanism Operating

(b) Final Position

Figure 10.7: Retraction Mechanism Design

10.4. Results

Table 10.3: Results of the Landing Gear design

Variable	Value	Explanation
		Gears Design
N_{MW}	4	Number of main landing gear wheels
N_{NW}	2	Number of nose landing gear wheels
$N_{M_{struts}}$	2	Number of main landing gear struts
y_{MLG}	3.75 m	Lateral positioning of the main landing gear
x_{NLG}	1.47 m	Longitudinal positioning of the nose landing gear
x_{MLG}	13.09 m	Longitudinal positioning of the main landing gear
h_{NLG}	2.55 m	Height of nose landing gear (strut-to-floor)
h_{MLG}	2.6 m	Height of main landing gear (strut-to-floor)
		Brake Design
Brake type	-	Disc-type, carbon fiber anti-skid composite brakes (Sepcarb X)
s_{brake}	508 m	Braking distance
		Retraction Mechanism

Continued on next page

Continued from previous page

Variable	Value	Explanation
Type of mechanism	-	Electro-mechanical actuator (EMA)
retraction$_{NLG}$	Aft, towards tail	Retraction procedure of the nose landing gear
retraction$_{MLG}$	Aft, towards tail	Retraction procedure of the main landing gear
a_{LOF}	0.98 m/s^2	Lift-off acceleration
t_{avail}	12.6 s	Available time for retraction. Satisfies $t_{retr} \leq t_{avail}$

11. Detailed Aircraft Description

An integrated overview of the final aircraft design is provided in this chapter. The hardware, software, electrical and data handling architectures are presented to illustrate the interaction between the major aircraft subsystems and their supporting infrastructure.

11.1. Final Design

Figure 11.1: Final Design Render

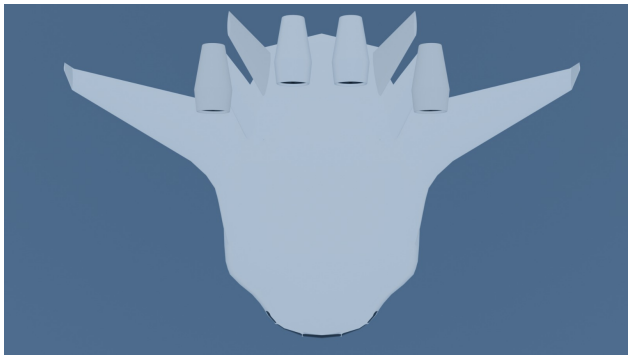

Figure 11.2: Render Top View

11.2. Design Configuration Diagrams

11.2.1. Hardware / Software Diagram

The hardware and software interact through a series of independent controllers governed by a supervising Aircraft Information Management System (AIMS). This distributed information architecture is more common in modern aviation, this is due to the reduced reliance on any one individual system which can be susceptible to faults, but rather operate each system independently and ensure consistent data types, input command, and display faults through a centred system. Another applicability is for certifiability within the ED-12c (DO-178) certification framework where focus is laid on partitioning and reduction in software dependency where possible. Another gain is the reduction of usage in bus bar bandwidth due to the more directional communication, allowing controllers to control individual systems and communicate with each other over the bus reduces the amount of data required on that bus. All these lead to the conclusion that a distributed control system is better than that of an integrated control system.

Power Control Unit (PCU)

Figure 11.3 Shows the PCU communicating with the central data bus, here it communicates with the remaining controllers to determine how to control the powertrain. As well as receiving information from the powertrain such as constant sensor data which can be displayed to the pilots, fault messages to be dealt with, and providing response to inputs for the flight deck. The system is powered by 48 V whilst the corresponding propulsion subsystem provides its own power internally through the fuel cell. There are two independent controllers in each propulsion unit, which actively compare data for fault analysis.

H2 Control Unit (HCU)

The H2 control unit manages the tanks, distribution of hydrogen, and controlling the evaporation of liquid hydrogen. This controller is powered by 48V and the energy storage system is powered by 540 V. The hydrogen is able to vent during over pressure by an independent mechanical system such that this does not pose any dangerous situations even without aircraft power.

Flight Control Unit (FCU)

The flight control unit governs the remaining aircraft systems, including the landing gear (braking and ground handling), aircraft fuselage (fault monitoring, hull pressurisation), wing and control surface subsystems. The controller uses 48 V, the corrosponding subsystems use a combination of 540 V and 48 V.

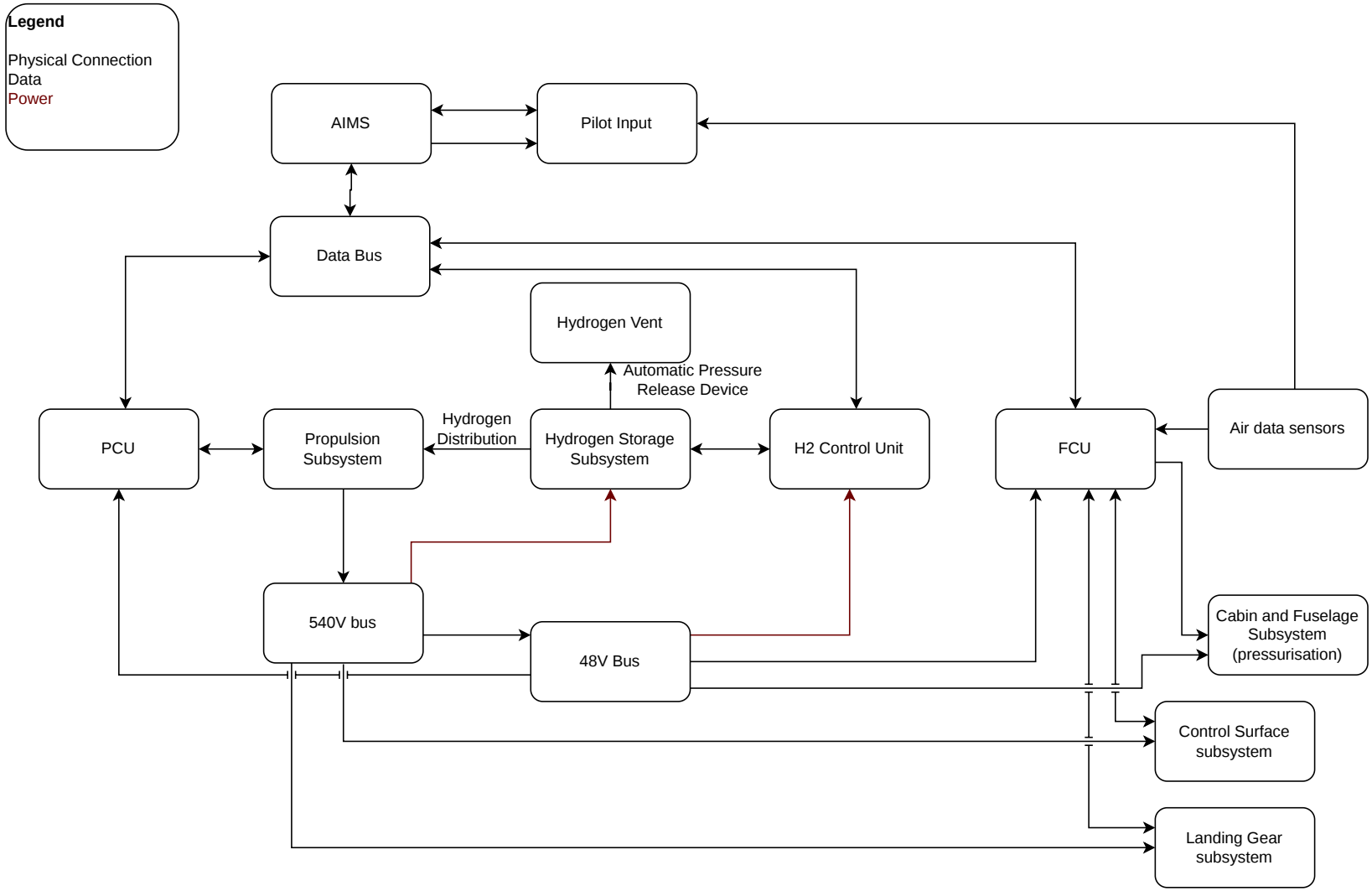

Figure 11.3: SW/HW diagram

11.2.2. Electrical and Data Handling Block Diagram

The electrical structure of the aircraft can be divided into three sections, a high, medium, and low voltage section. This has been opted for to categorise the components requiring electrical power into these categories to size and install large infrastructure based on that corresponding voltage.

High Voltage

The high voltage section is an isolated system within the IPU. This section provides all of the non emergency power. The power is produced, stabilised at 7000V (chosen due to its relative value to the output voltage and favourable wire sizing), separated to supply auxiliary power, and then used by the electric motor. The stable 7kV DC power is beneficial for sizing of the inverter. There are industry standards on the input voltage of large industrial motors, an output of 6600V was chosen as it is similar to input (increasing system cohesion and maintainability) whilst aligning with these industry standards.

Medium Voltage

The medium voltage section utilises three bus bars, bus A is the main choice and standard utilised bar, bus B provides redundancy for faults in the bus A component. Bus E is the emergency bus which only supply systems critical for flying the aircraft and is engaged by a RAT (RAM Air Turbine) rather than the fuel cell power. This section powers all major electrical components onboard including the hydrogen tank heaters, control surface actuators, on board climate control, and landing gear systems. The section uses 540 V, this is because of this being an industry standard value taken for central power systems, allowing this aircraft to use a larger arrangement of components that are rated to this voltage, increasing the maintainability of the aircraft and therefore reducing the climate impact.

Low Voltage

The low voltage uses a similar principle as the medium voltage and opted for 48V, which aligns with the standard voltage rating of a large amount of standard avionics. This section also includes a bus A, B, and E for redundancy, the power is regulated to this voltage through 3 independent DCDC converters, increasing the redundancy as the power always has at least 2 paths to reach its intended component.

Electrical Protection

Conventional aircraft use a large array of relays and circuit breaks to ensure electrical protection. For this reason all low voltage components come with a simple circuit breaker. The high voltage components cannot directly use a circuit breaker due to the relative high power, for this reason a solid state power controllers were opted due to their reduced mass and increased reliability while performing the functions of traditional circuit breaker and electromagnet relays.

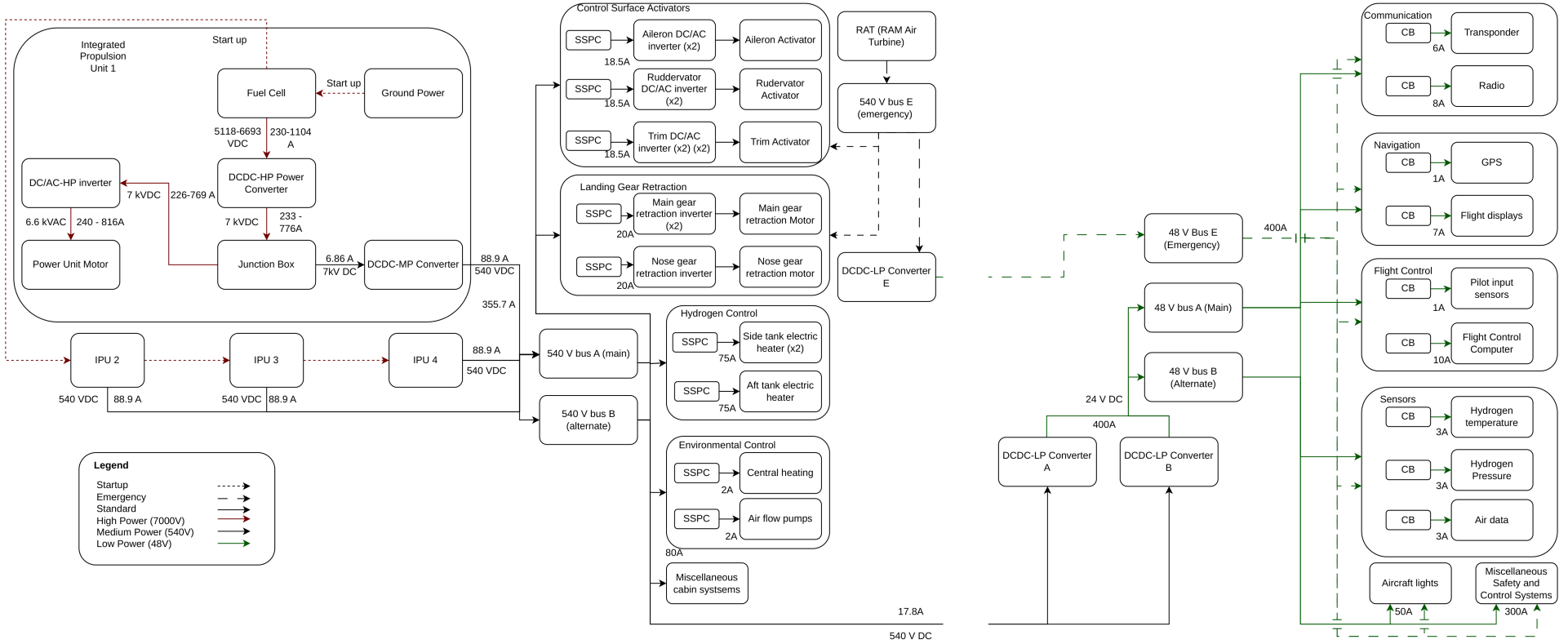

Figure 11.4: Electrical Block Diagram

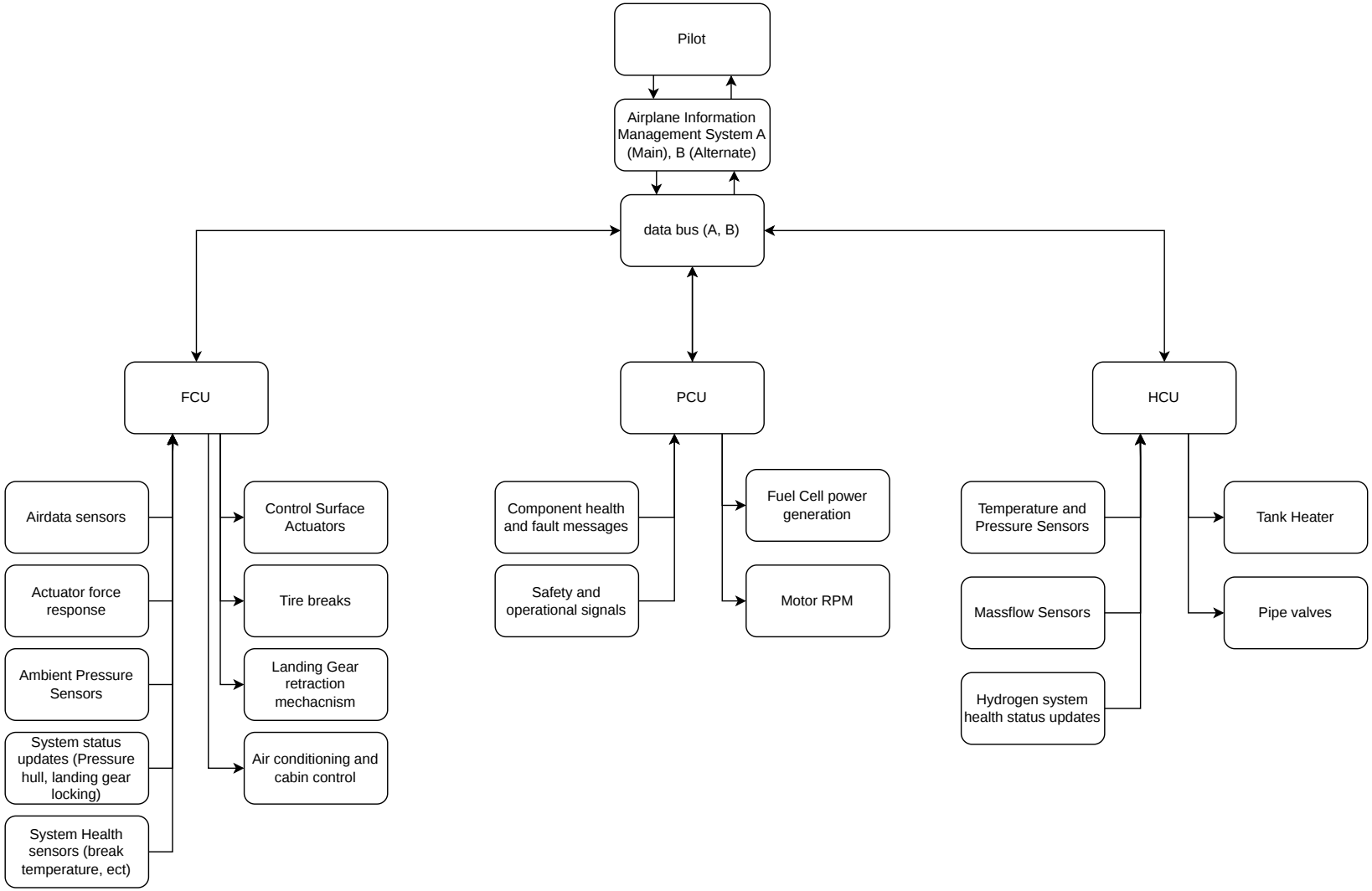

Figure 11.5: Data Handling Block Diagram

12. Operations Concept

The operations concept covers how the aircraft is serviced on the ground and flown, and the liquid-hydrogen logistics that support both. These procedures are shaped by the powertrain they serve: the aircraft produces no combustion emissions in service, so its only in-flight climate effect comes from contrails (subsection 8.3.3). The concept targets this directly through contrail-avoidance routing, where the detection system identifies ice-supersaturated air ahead and the aircraft reroutes around it in coordination with ATC.

12.1. Operations and Logistics Concept Description

12.1.1. Ground Operations

Ground operations are defined as all operations of the aircraft until the aircraft enters and exits the runway. This is because the operational conditions require for take-off and landing align closer with flight operations than that of ground operations.

Passenger Embark and Disembark

Passengers enter in through the front left door, as is standard for aircraft operations. These passengers enter either through a jet bridge or conventional aircraft stairs. The floor of the cabin is at 1.6 m from the ground, falling within the ranges of standard jet bridges and jet stairs.
There is a reduction of embarking and disembarking time by at least 50% due to the multiple galleys and the ability to divide passengers into passengers seated on the 'left' (seats A through to G) and passengers seated on the 'right' (seats H through to N) at the entrance. This allows seats to be filled similarly to conventional aircraft whilst being half as long.
Reducing embarking and disembarking time by 50% can therefore be achieved without any change in airport infrastructure. The wingspan being lower than 36 m allows usage of ICAO Code C rated terminal gates, which are used by current A320 aircraft.

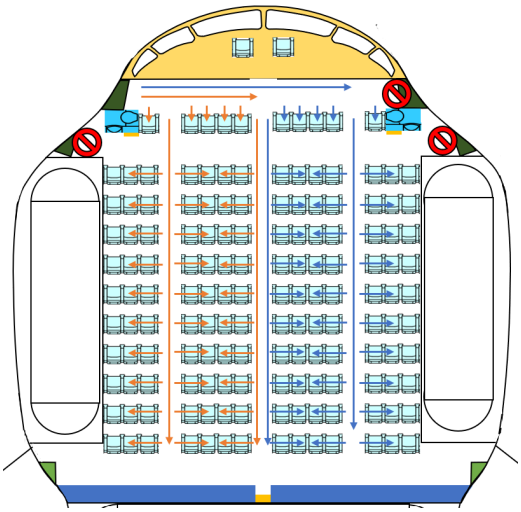

Figure 12.1: Boarding Procedure Schematic, flow of passengers is split into blue and orange at the entrance

Disembarking is the opposite procedure, however inevitably more chaotic. The increased galley space allows for more passengers to access their luggage at any one time, increasing the rate of passenger flow. an assumed boarding time of 15 minutes is taken, and a disembark of 10 minutes. It will be probable that the boarding and deboarding will be less than that of the A320 due to the higher aisles, however simulation analysis would have to be used to validate this.

Refuelling

The largest change to airport infrastructure arises through the implementation and distribution of liquid hydrogen. This fuel type needs to be stored under pressurised cryogenic conditions. This can be performed with large industrial, well insulated liquid hydrogen tanks underground, fed via pipeline from hydrogen production centres. The liquid hydrogen is fuelled into the aircraft through initially purging the lines with an inert gas, cooling the lines with progressive cooler hydrogen, and ultimately filling the tank with liquid hydrogen as the gaseous hydrogen is removed from the space. This results in a large amount of boil-off and gas leakage due to the cycling of gases through the system. To minimise losses the vent lines can be reconnected into a gaseous hydrogen system to be re circulated into the airport infrastructure, notably to power ground vehicles, to be sold to other customer, or to be sent to an on-site plant to return the hydrogen to liquid for aviation application. This is possible due to line purging to remove contaminants, often with nitrogen, meaning that the recycled H_2 is still of a sufficient purity to be reused. Figure 12.2 provides a concept for liquid hydrogen refuelling, where different checks and purge gases are include to ensure operational safety. A refuel time of less than 6 minutes can be assumed [66], to account for connection and system safety checks this phase can be considered 10 minutes.

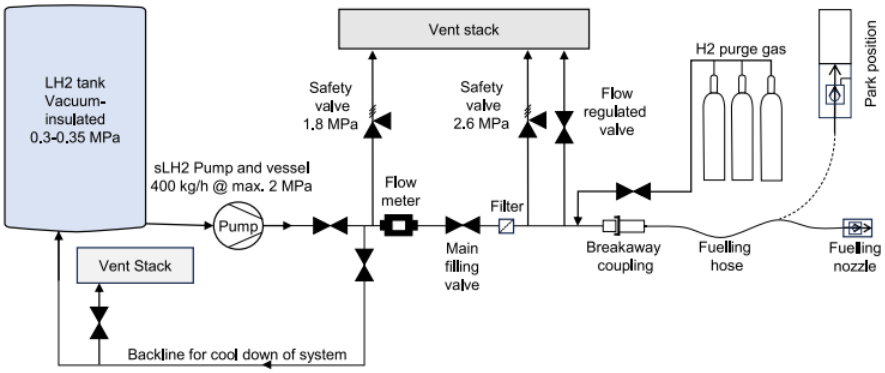

Figure 12.2: Concept liquid hydrogen refuelling system [67]

LH_2 refuelling is a comparatively new technology compared with conventional jet fuel, therefore the lack of industry experience and the large amount of hydrogen flow and use of venting lines; it has been opted to fuel the aircraft before boarding passengers. This is also compliant with current industry practice where possible for conventional aircraft as refuelling presents the highest danger state for the fuel.

The fuel level can be measured with tank temperature sensors, a theoretical model can be created by measuring the tank temperature gradient and from there an estimate for the level of H_2 in tank. Due to the low mass flow this is sufficient accuracy for operations.

Baggage Handling

The vertical space at the highest point for the baggage area is 1.06 m, with the accommodation for a wire box this can be assumed as approximately 1 m which is less than the A 320 at 1.22 m, however this still falls within an acceptable range for a baggage handler. The entrance to the the cargo hold is 0.6 m from the ground, allowing usage of standard baggage handling infrastructure at airports.

Pushback and Taxi

Pushback is performed by electric or hydrogen electric ground vehicles which will be common practice by 2050, the ground vehicles will also be equipped with a power source capable of startup of one fuel cell stack, approximately 7000 VDC, 1 MW supercapicitor. This is because the aircraft does not use an APU and therefore requires ground power to start up. The ground car will provide the power for one unit startup once they have left the gate, then during the taxi the power drawn from that fuel cell will be used for start up on the remaining four units.

Post-flight

Figure 12.3 shows two options for the aircraft after disembarking, if it is required for the aircraft to turnaround and leave again the aircraft returns to flight planning and refuelling, if the aircraft will spend an extended period of time at the airport the aircraft will de-fuel back into the airport storage system, purge lines of hydrogen and enter into storage.

Additional Remarks

Hydrogen in a commercial airport setting could lead to some safety concerns, the venting of hydrogen under widespread operations is inevitable. Whilst harmless to ground crew under normal operations due to hydrogen's low density, zones above the airport where hydrogen concentrations are high could lead to dangerous situations, therefore careful airport planning, hydrogen flow analysis, and extended prohibited zones above terminals could be a requirement. This results in alterations in flight planning and emergency procedures to avoid flying into these zones.

Additional marked no go zones and additional ground crew training is required

12.1.2. Flight Operations

Take off operations consists of all standard operations for the aircraft once the take off role is started until the landing roll has been completed. This section does not include emergency situations, and focuses on operations that are different to the standard.

The take-off and climb out can be considered similar to that of conventional aircraft, once the aircraft is at cruise altitude the contrail detection system will be active, providing the pilots with live information on the outside conditions and the current production of harmful contrails. When this system is engaged, the route is updated, this is communicated to surrounding aircraft and ATC, the aircraft is then able to alter heading and altitude to avoid the contrail formation zone.

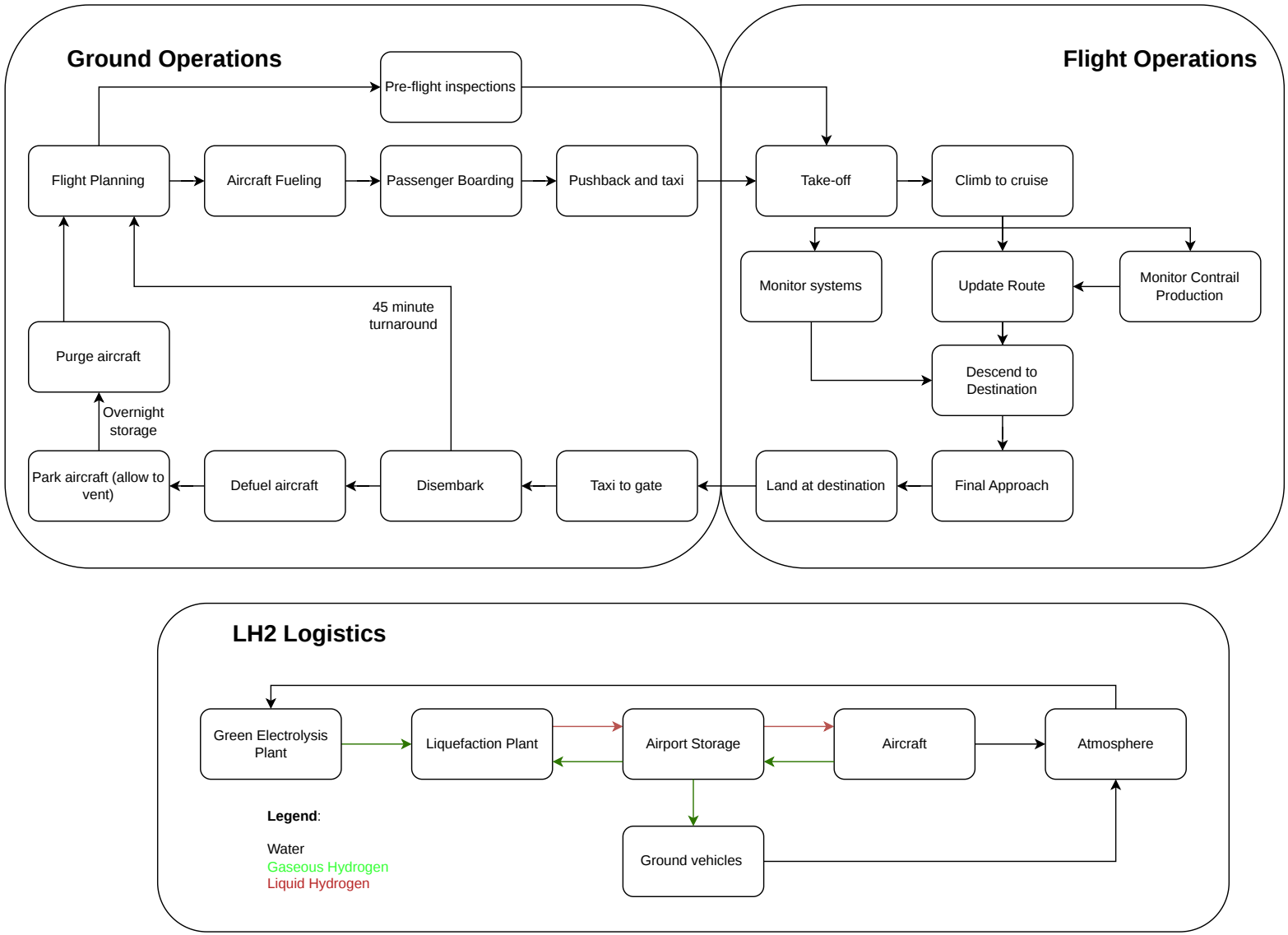

Figure 12.3: Aircraft Operations Concept (top), Airport LH_2 infrastructure concept (bottom)

13. Production Plan and Remanufacturing

The production plan for the aircraft and the re manufacturing process used to recover it at the end of its life cycle are described in this chapter. Production follows a standard subsystem and final assembly line route, but it is at end of life where the closed-loop material requirement shapes the design directly. Rather than retiring to a boneyard, the aircraft is returned to the final assembly line and disassembled, which drives, for example how the major joints are connected: bolting lets components come apart without cutting and keeps waste low. Furthermore, both Aluminium alloys and CFR-PEEK fibres are re-entering production alongside virgin materials. This makes end of life lifecycle phase a negative emissions balance (15.4), avoiding around 270 tons of CO_2 equivalent pollution and partly offsetting the emissions from manufacturing.

13.1. Production Plan

The production of this aircraft follows a similar philosophy to that of Airbus in terms of component and subsystem manufacturing and then being assembled on a final assembly line (FAL). The key difference is the manufacturing of the pressure bulkhead into two sections, split in the largest cross section. This is due to the accessibility into the aircraft for installation of the large internal systems such as tanks and hydrogen distribution components.

13.1.1. Material Acquisition

Materials are sourced from different locations, from end of life aircraft where the parts are inspected for airworthiness and are reused, or reduced to recyclate and fed into the raw material stream. Another source is from the market, either raw or recycled material. The preference is to reuse materials as high up the economic diagram as specified by the Ellen-McArthur foundation to reduce wasting energy. However, to remain competitive with competing aircraft it may also be required to use raw material streams if the price is substantially more favourable. The materials are acquired and processed in material processing plants. The main materials used in the aircraft are CFRP-PEEK, and aluminium (various alloys).

13.1.2. Part Manufacturing

Parts are manufactured at respective manufacturing facilities such that facilities are able to specialise in a certain manufacturing practice rather than attempt to integrate all into one facility. The parts are constructed and assembled into the sub-assemblies described in Figure 13.1. These sub-assemblies are moved to the final assembly line (FAL), for operational reasons it is opted for these facilities to be close together to minimise cost and environmental impact of transporting large amounts of aircraft parts.

The aircraft fuselage is formed unconventionally, while the pressure bulkhead is formed through automated fibre placement (AFP) using a variable degree of freedom robotic arm for the unconventional shape. The machine is also capable of applying variable thickness by altering the deployment of fibres depending on the required local thickness. The pressure bulkhead is formed up until the thickest point of the fuselage, this is to allow the installation of the large internal systems such as the hydrogen tanks, the distribution networks, flight computers, bus bars, etc. The nose of the aircraft is also manufactured in a similar method, however is only mechanically joined after the internal systems have been integrated.

13.1.3. Final Assembly

The subsystem are transported to the final assembly line where the internal cabin, cockpit and avionics, and final wire harness is installed as well as painting the aircraft and achieving the final airworthiness approvals required to achieve a type rating. The aircraft is then shipped to the client.

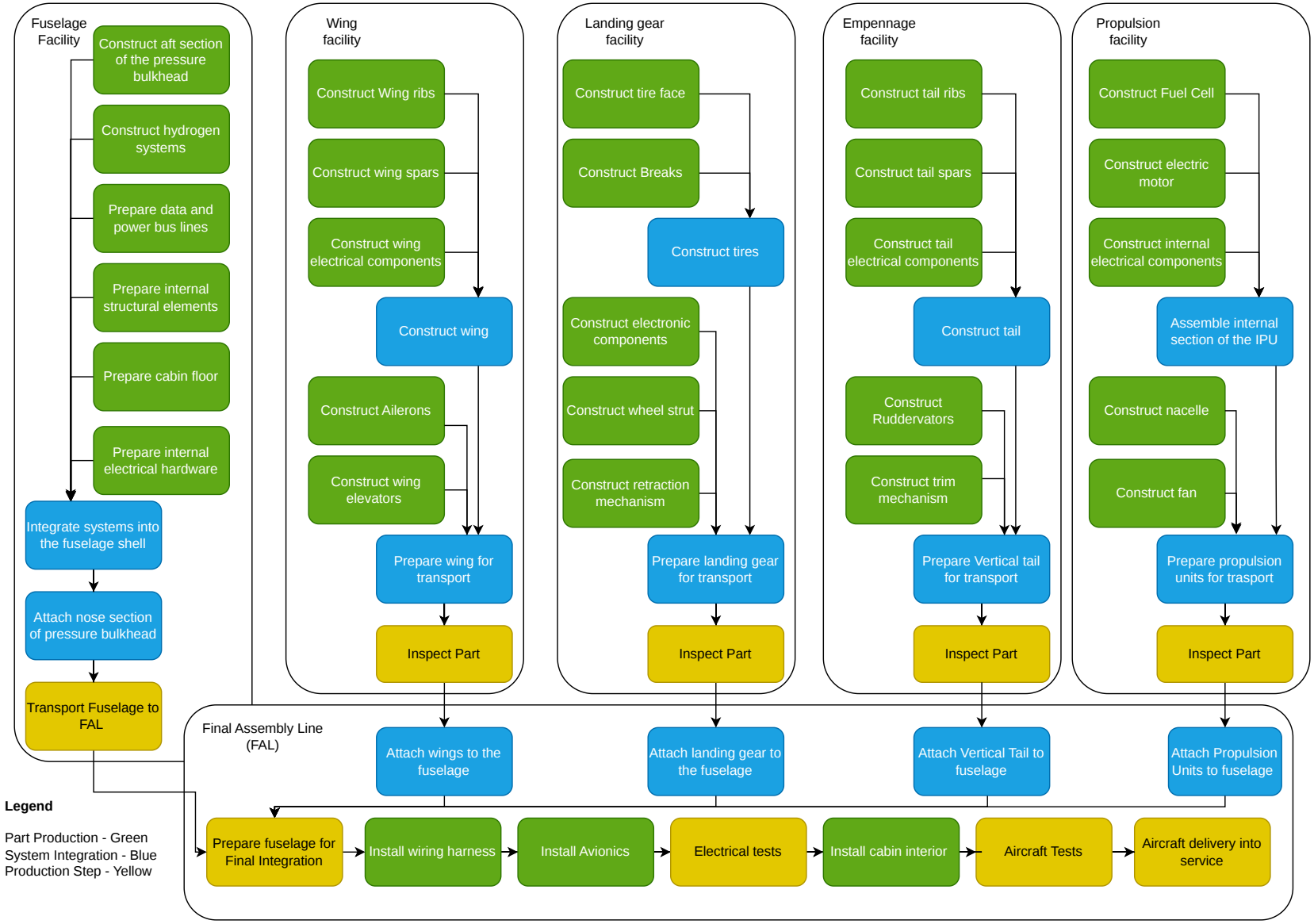

Figure 13.1: Production Plan

13.2. Recycling and Re-manufacturing Plan

To reduce the impact of this aircraft a re-manufacturing process must be identified to ensure that the materials return back into the stream. This is done by returning the aircraft to the manufacturer at end of life, rather than a bone yard. Figure 13.2 highlights the process that the aircraft goes through when returning to the FAL facility. The aircraft is disassembled, inspected, and returned to the material stream at as many locations as possible. By using metals such as aluminium alloys a material recycleability of 100% can be expected. Whilst materials such as CFRP-PEEK are reused whilst experiencing a drop in material properties, meaning ultimately it will leave the cycle.

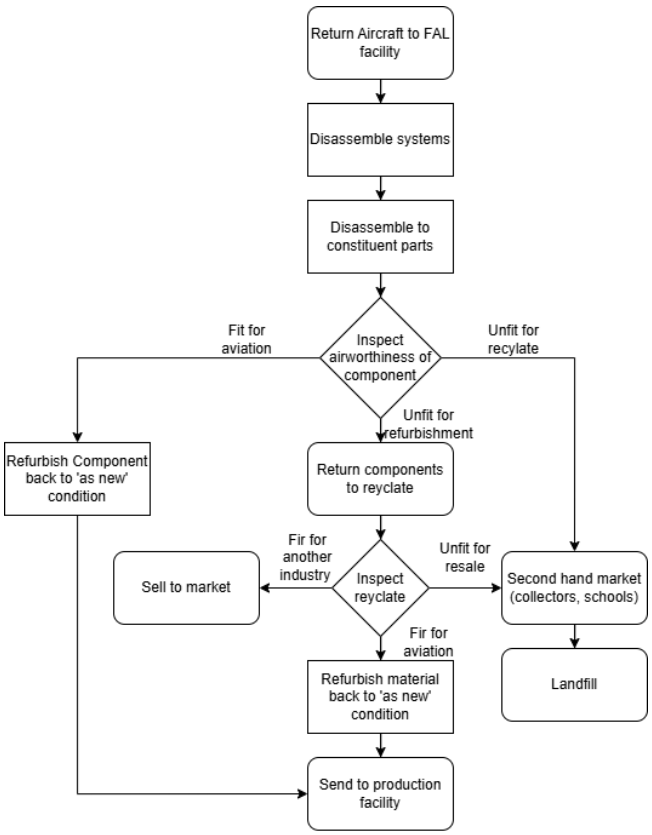

Figure 13.2: Flow chart highlighting the material stream after the aircraft has been returned to the manufacturer

13.2.1. Aircraft Disassembly

The large aircraft components are attached to the fuselage through bolts, allowing the disassembly of the major components to be quick when using the right equipment. The parts are largely connected through bolts for the same reason, where welds or other forms of permanent joints are required these can be disassembled through destructive methods. Due to the design for disassembly methods implemented, in later design phases, returning the aircraft to its constituent parts is possible with minimal costs above machinery, which is already required for the manufacturing of the aircraft.

13.2.2. Inspection of Parts

Inspection of aluminium parts can be performed through Ultrasonic testing, Active Infrared Thermal Imaging, [68], or multi-frequency eddy current inspection [69]. These methods allow a non-destructive quick and potentially cheap inspection of the nano-structure of aluminium alloys, they allow the quantification of potential damages such that it can be credibly stated if the component is fit for further aviation applications. CFR-PEEK also has a range of acceptable non destructive test methods to be used to inspect component health, such as ultrasonic, radiographic [70], or eddy current methods [71]. With these methods, faults in the structures can be identified and a decision can be made on whether a component is capable of returning to the air.

13.2.3. Re-manufacturing of Parts

Parts that are able to return into service in another aircraft after re-manufacturing, the part needs to return to a state that is equal to that of the original part. To do this for aluminium current practices include cleaning, polishing, and welding cracks in the atomic structure of the metal. Whilst this is still unconventional in current practice, the aircraft shall enter service in 2050 and then enter its intended 30 year life span. This means that

it is not expected that this aircraft shall return for disassembly until 2080, where potentially new methods for EOL of metal nanostructures have been developed where more direct influence on the properties of the part can be used. Practices are similar for CFR-PEEK, often limited to cleaning and polishing with minor structural improvements without removing the matrix.

13.2.4. Recycling of Material

When re-manufacturing of the component is not feasible the option is to recycle it, for CFRP-PEEK this consists of placing the material in a solution that removes the matrix exposing the underlying carbon fibres, these fibres can be inspected and re-introduced back into the manufacturing process directly [72]. This comes at a slight degradation of performance, and as such the first generation aircraft has been designed with excessive structural safety margins such that at least two cycles can be performed directly without a loss in aircraft performance. After these cycles, the fibres can be introduced in a different airframe with different load requirements, increasing the lifetime further until ultimately the material cannot continue.

Aluminium has almost 100% retention when being recycled, the European Aluminium Association provides a schematic showing the process of conventionally recycling aluminium and aluminium alloys Figure 13.3.

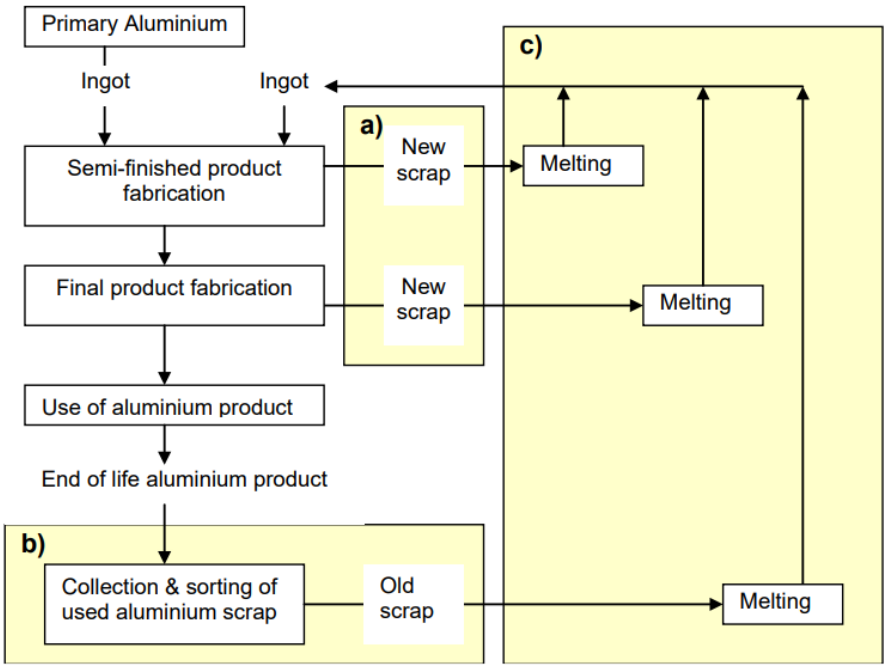

Figure 13.3: Life Cycle Schematic of aluminium [73] Version: September 201 European Aluminium Association

Using this process a circular material economy can be assumed where materials enter life, are used, and are returned back into the aviation sector through a centralised aircraft manufacturer rather than relying on boneyards and material economics.

13.2.5. Second Hand Market

There is the last potential attempt to sell at a very low price the remaining material to schools, and private collectors who may be interested in working with these material. This will generate limited to no revenue but provides an opportunity to avoid scrapping material.

14. Reliability, Availability, Maintainability, and Safety Analysis

The Reliability, Availability, Maintainability, and Safety (RAMS) analyses cover four key metrics of the aircraft's operational performance. The Safety analysis results in a list of safety critical functions, and the redundancy policies applied. The Maintainability analysis lists predicted maintenance activities and their timelines, which serves as input into the Availability analysis, which relates the aircraft up-time and down-time. The reliability analysis finally shows the expected failure rate of one aircraft.

14.1. Safety Analysis

As a first assessment on the product safety, a safety analysis was conducted. A Functional Hazard Assessment (FHA)[74] was chosen as preferred methodology, in which the effect of the loss of functions, as listed in Figure 3.2, was categorised. These failures were defined by the following parameters: Condition Type (Total Loss or Partial Loss), Crew Awareness (Annunciated or Unannunciated), and Flight Phase (Take-Off, Cruise, Landing, On-Ground, or a combination). The failures are then assessed based on their effect on the aircraft, the crew, and the passengers, and finally given a Consequence Class (No Safety Effect, Minor, Major, Hazardous, and Catastrophic), as shown in Table 14.1. First, the lowest level of requirements were assessed. The higher levels of requirements were based on the results of their respective lower levels. The result of this analysis is shown in Table 14.2 and Table 14.3, where the worst-case failure classification is listed.

Table 14.1: Consequence Class Characteristics [75]

Class	Crew Workload	Passenger Injury	Aircraft Effect
Catastrophic	High Workload/Physical Distress	Death	Aircraft Unusable/Destroyed
Hazardous	High Workload/Physical Distress	Serious Injury	Significant Damage
Major	Significant Increase in Workload	Injury	Repairable Damage
Minor	Slight Increase in Workload	No Injury	Operating Limitations
No Safety Effect	No Increase in Workload	No Injury	Aircraft Usable

The FHA is conducted at two levels of depth; "low level", regarding system functionalities, and "high level", regarding aircraft/product functionalities. The system-level analysis is performed first, aiming to find design- or component-specific safety concerns. In order to do so, the functions found in Figure 3.2 have been further refined, to obtain an appropriate amount of detail regarding the design concept.

Table 14.2: Functions and Failure Categories, Aircraft Level

ID	Description	Worst-Case Failure Category
0	Design Aircraft	Analysis only considers operational use of product
1	Manufacture Aircraft	Analysis only considers operational use of product
2	Perform Operational Procedures	
2.1	Perform Pre-Flight Operations	Minor
2.2	Perform Take-Off Preparations	Catastrophic
2.3	Perform Flight Operations	Catastrophic
2.4	Perform Post-Flight Operations	Minor
3	Recycle Aircraft Parts	Analysis only considers operational use of product

Table 14.3: Functions and Failure Categories, System Level

ID	Description	Worst-Case Failure Category
	ESS FUNCTIONS	
FUN-2.3.9	Provide Power	
FUN-2.3.9.1	Provide Electrical Power	Catastrophic
FUN-2.3.9.1.1	Provide Fuel Cell(s) with Hydrogen	Catastrophic
FUN-2.3.9.1.2	Provide Fuel Cell(s) with Oxygen	Catastrophic
FUN-2.3.9.1.3	Provide Fuel Cell(s) with Cooling Capabilities	Catastrophic
FUN-2.3.9.1.4	Transport Electrical Power	Catastrophic
FUN-2.3.9.1.5	Provide Startup and Reserve Power	Major
FUN-2.3.9.4	Provide Energy Storage	
FUN-2.3.9.4.1	Refuel Fuel Tank	Minor
FUN-2.3.9.4.2	Provide Fuel Tank with Venting Infrastructure	Catastrophic
FUN-2.3.9.4.3	Manage Fuel Tank Thermal Metrics	Catastrophic
	PRP FUNCTIONS	
FUN-2.3.2	Provide Thrust	
FUN-2.3.2.1	Provide Forward Thrust	Catastrophic
FUN-2.3.2.1.1	Power Propeller	Catastrophic
FUN-2.3.2.1.2	Compress Air	Catastrophic
FUN-2.3.2.2	Provide Reverse Thrust	Catastrophic
	AFR FUNCTIONS	
FUN-2.1.1	Provide Sustainment	
FUN-2.1.1.2	Provide Maintenance Capability	Minor
FUN-2.3.1	Provide Aerodynamic Performance	
FUN-2.3.1.1	Provide Lift Performance	Catastrophic
FUN-2.3.1.2	Provide Drag Performance	Major
FUN-2.3.1.3	Provide Stability	Catastrophic
FUN-2.3.1.6	Provide Pitch Control	Catastrophic
FUN-2.3.1.7	Provide Roll Control	Hazardous
FUN-2.3.1.8	Provide Yaw Control	Catastrophic
FUN-2.3.1.9	Provide Landing Gear Control	Catastrophic
FUN-2.3.4	Provide Cargo Capability	
FUN-2.3.4.1	Provide Cargo Space	Minor
FUN-2.3.4.2	Provide Cargo Loading	Minor
FUN-2.3.8	Maintain Structural Integrity	
FUN-2.3.8.1	Sustain Loads	Catastrophic
FUN-2.3.8.2	Maintain Pressure	Major
FUN-2.3.8.3	Provide Mounting Opportunities for Equipment	Catastrophic
	CBN FUNCTIONS	
FUN-2.1.1	Provide Sustainment	
FUN-2.1.1.1	Provide Servicing Capability	Minor
FUN-2.1.1.2	Provide Maintenance Capability	Minor
FUN-2.3.3	Provide Passenger and Crew Accommodations	
FUN-2.3.3.1	Provide Passenger and Crew Space	Minor
FUN-2.3.3.2	Provide Seating	Minor
FUN-2.3.3.3	Provide Storage	Minor

Continued on next page

ID	Description	Worst-Case Failure Category
FUN-2.3.3.4	Provide Galley Accommodations	Minor
FUN-2.3.3.5	Provide Lavatory Accommodations	Minor
FUN-2.3.3.6	Provide Safety Equipment	Catastrophic
FUN-2.3.5	Provide Environmental Control	
FUN-2.3.5.1	Provide Air Conditioning	Major
FUN-2.3.5.2	Provide Pressurization	Major
FUN-2.3.5.3	Provide Oxygen	Catastrophic
FUN-2.3.5.4	Provide Ice Protection	Hazardous
FUN-2.3.5.5	Provide Rain Protection	Major
FUN-2.3.10	Provide Situational Awareness	Catastrophic
FUN-2.3.10.2	Provide External Awareness	Catastrophic
	AVI FUNCTIONS	
FUN-2.2.1	Provide Ground Manoeuvrability	
FUN-2.2.1.4	Transmit Landing Gear Actuation Commands	Hazardous
FUN-2.2.1.5	Transmit Ground Steering Commands	Hazardous
FUN-2.2.1.6	Transmit Ground Braking Commands	Catastrophic
FUN-2.3.1.4	Provide Control	
FUN-2.3.1.4.1	Receive Pilot Input	Catastrophic
FUN-2.3.1.4.2	Transmit Control Surface Actuation Commands	Catastrophic
FUN-2.3.1.4.3	Transmit Thrust Control Commands	Hazardous
FUN-2.3.6	Provide Communications	
FUN-2.3.6.1	Provide External Communications	Catastrophic
FUN-2.3.6.2	Provide Internal Communications	Minor
FUN-2.3.7	Provide Guidance and Navigation	
FUN-2.3.7.1	Determine Location of Aircraft	Hazardous
FUN-2.3.7.2	Determine Attitude of Aircraft	Major
FUN-2.3.7.3	Determine Speed of Aircraft	Major
FUN-2.3.7.5	Provide Flight Management	Hazardous
FUN-2.3.7.6	Determine Altitude of Aircraft	Hazardous
FUN-2.3.10	Provide Situational Awareness	Catastrophic
FUN-2.3.10.1	Monitor Aircraft Status	Catastrophic
FUN-2.3.9.1.5	Divide electrical power over systems	Catastrophic

Any functions listed in Table 14.2 with classification Major, Hazardous, or Catastrophic must be designed with significant redundancy policies and fail-safe philosophies. For any aviation-wide safety critical function (i.e., those applicable to all aircraft, and not specific to innovations associated with the EverWing), these redundancies are covered by existing design methodologies and certification standards. For functions specific to the Blended Wing Body, fuelled by hydrogen, the following points have been considered:

FUN-2.3.9.1.1 & FUN-2.3.9.1.2: Each fuel cell stack will cease power generation and may sustain damage without an appropriate supply of hydrogen and oxygen. Each propulsion unit already includes redundancy by being independent from one another, and each has their own air intake to provide oxygen. The hydrogen distribution network receives hydrogen from all tanks, includes multiple cut-off valves, and each fuel cell stack can receive hydrogen from two separate lines.

FUN-2.3.9.1.3: Cooling failure will result in the loss of a fuel cell stack. In the current stage of design, the only redundancy is included in the fact that there are multiple individual propulsion units. Further detailed design should include further analysis into this matter.

FUN-2.3.9.1.4: The power distribution network contains two of any critical component.

FUN-2.3.9.1.5: The aircraft runs solely on electricity generated by the fuel cell stacks, and includes a RAM Air Turbine to provide additional power generation in the worst-case scenario in which all motors have suffered

total failures.

FUN-2.3.9.4.2: Each tank has access to venting lines leading to the aircraft wing tips, with numerous pipelines being available.

FUN-2.3.9.4.3: The hydrogen tank is not actively cooled, and multiple independent heaters are installed to allow for extracting gaseous hydrogen. Further detailed design should include further analysis into the cooling performances of the passive insulation.

FUN-2.3.1.6 & FUN-2.3.1.8: Although pitch and yaw control are common to all aircraft, this design specifically employs ruddervators, which couple the two functionalities. Pitch control can be aided by the additional elevators on the wing, and whereas yaw control can be provide by a singular ruddervator, albeit with significant performance loss.

14.2. Maintainability Analysis

The aircraft, in its lifetime, will go through various phases of maintenance and checks, often referred to as Maintenance, Repair, and Overhaul (MRO). These can be categorised into scheduled and non-scheduled activities, all of which affect the aircraft's availability. Based on Rahn et al.'s analysis of the A320[76], details of the high-level standardised maintenance checks have been written up in Table 14.4, where the duration of each activity is given in hours and the intervals are given in days, Flight Hours (FH), or years. The APU shop has been omitted as the aircraft in design does not include one. The engine shop is used as a high-level estimation, as the aircraft's propulsion system diverges from conventional.

A-, C-, and D-checks are overall aircraft checks of various levels of depth. The checks require specific tools and special facilities. Most industry-standard tools should be usable, but certain design features require additional procedures, tools, and facilities to be made available. Aside from the general aviation activities, the aircraft design will require the additional procedures, listed below.

The systems requiring additional maintenance are the propulsion (PRP) and energy supply & storage (ESS) systems, and the airframe (AFR) may need revised procedures due to the novel configuration.

Table 14.4: Maintenance Check Durations and Intervals[76]

Check	Duration	Margin	Interval
Daily	2h	2.7h	1 day
Weekly	3h	4.05h	7 days
A-Check	10h	13.5h	450 FH
C-Check	168h	226.8h	5000FH
D-Check	672h	907.2h	6 years
Engine Shop	672h	907.2h	9000FH
Landing Gear Shop	1009h	1362.15h	10 years

The aircraft's engines require less direct maintenance due to the decrease in moving parts and high operating temperatures, but the fuel cell stacks within a propulsion unit requires existing MRO organisations to expand their business and gain experience in fuel cell MRO operations. Maintenance and repair on the fuel cells would require the entire propulsion unit to be removed from the aircraft due to its aft placement, limiting its accessibility. Overall, despite the introduced novelties, it is possible to implement effective fuel cell MRO [77].

The hydrogen distribution system introduces new complexities, due to the usage of hydrogen as fuel. Inspection operations may be similar to that of aircraft using jet fuel, such as checking for leaks and piping degradation. However, additional care must be taken to inspect the tanks, their venting lines, and the quality of the valves, considering the small molecular size of hydrogen. As found by Meissner et. al. [78], substituting a conventional APU for one fuelled by liquid hydrogen would increase maintenance efforts by 22% - 32%, for the hydrogen distribution system alone. The EverWing design utilises a hydrogen distribution system of increased size, and thus the upper bound is considered.

Due to the uncertainty of required maintenance hours for the novel systems, a conservative 35% margin was added to all hours. This will affect the availability analysis covered in section 14.3, and it is thus highly recommended to analyse the novel systems and their maintenance requirements. Unscheduled activities refer to repair, often found through the checks listed above. A first estimate, based on A320 numbers, would result in 33% of all maintenance hours being caused by unscheduled activities.[50]

14.3. Availability Analysis

As stated by REQ-OPE-2.2.10 and REQ-OPE-2.2.11 (section A.3), the aircraft must have quick turnaround time (45 minutes), and a high utilisation rate. The availability of an aircraft, the up- and down-time compared to a total time frame of reference, is thus of high importance.

[50] Weiss, O. "Maintenance of Tomorrow: The AHM path from Airbus' Perspective, 5th Paperless Aircraft Operations and RFID Conference, Cranfield, United Kingdom. [Cited 17 June 2026]

Considering one year in operation, the aircraft undergoes 985.5 hours of daily inspections, and 210.6 hours of weekly inspections. Most A320 aircraft operate for about 2800 to 3500 FH per year.[79] Using the upper bound as estimate, the aircraft would undergo an additional 97.2 hours of A-checks (and would be due soon for another). A brand-new aircraft would not require any additional checks, but any aircraft in service for 2 or more years could require a C-check, D-check, and a shop visit. This would result in a best-case scenario (brand-new) in 1291 planned maintenance hours, and in a worst-case (10 year old aircraft, requiring an Engine and Landing Gear Shop visit) 3560 planned maintenance hours. Taking the hydrogen-related margins and unscheduled maintenance into account would result in 1717 to 4735 maintenance hours, over the span of one year. The worst-case estimate is larger than the most-used estimate for flight hours, and would thus negatively impact the aircraft availability rates. Maintenance can be performed largely at night, when flights aren't normally scheduled, but the overall maintenance schedule should be analysed in depth to optimise activities and ensure no activity is missed. Since the aircraft would require additional checks, specific to the aircraft itself, the availability is calculated using a worst-case estimate for both flight hours and maintenance time. Thus, the estimated aircraft availability would be $4735/(2800 + 4735) = 0.63$.

14.4. Reliability Analysis

According to REQ-OPE-2.2.9, as seen in section A.3, the aircraft must have a dispatch reliability of at least 99.5%. This means that only 1 in 200 flight departures can be delayed by more than 15 minutes solely due to technical faults and unscheduled maintenance. It is very difficult to predict this for the aircraft due to the novelty of design, as well as the extended time until service, increasing uncertainty towards figures later in life.

14.4.1. Methods

Two methods were considered to estimate the aircraft's dispatch reliability. The first is a technical bottom-up approach using a Fault Tree Analysis (FTA), in which component- and function-level failures are combined through logic gates to trace how lower-level faults accumulate into major or catastrophic aircraft failures, with individual failure rates quantified through research and testing. The second method assumes that systems with functionalities comparable to conventional, well-researched aircraft inherit their failure rates, while the novel systems are assessed conceptually. The FTA is favourable, as its deeper analysis yields more accurate and traceable results, but due to time constraints and the lack of relevant research on the novel systems, the second method better fit the project scope.

14.4.2. Results

Conventional aircraft, such as the A320, have dispatch reliabilities above 99%, and often near to 99.7% [80]. This comparison for conventional aircraft can be used as a basis for the conceptual aircraft. The A320 reliability is driven by the powertrain as the engines require more frequent and more inconsistent maintenance than the airframe, largely due to the high speeds, large amounts of moving parts, and temperature changes approaching the limits for the used materials. By utilising a fuel cell powertrain, extreme operating temperatures are avoided and the number of moving parts is reduced. Resulting in an assumed increase in mean time between failure (MTBF). For theoretical fuel cell aircraft using a fuel cell APU, four times lower scheduled maintenance than with kerosene is expected [78]. From this, the assumption was made that a scaled up system would utilise a similar reduction. The hydrogen powertrain is more complex, with more valves, sensors, and regulators than a conventional kerosene fuel supply system. However, the architecture has been formatted in such a way that no individual failure can jeopardize flight safety and operations, often with multiple layers of redundancy such that even in the case of a system fault, the aircraft should still be able to dispatch on time allowing operators time to plan maintenance. This would be formalised within the MEL (minimum equipment list), such that partial faults in the hydrogen distribution network are acceptable for departure, given sufficient redundancy. With these assumptions the dispatch reliability can be assumed equal to or greater than that of the A320 [**?**], which currently has a dispatch reliability of approximately 99.5%. Future recommendation include constructing a detailed system Fault Tree Analysis and comprehensive component testing such that a more concrete value can be identified, and critical failure paths can be mitigate through redundant pathways.

14.5. Future Recommendations

Throughout the RAMS analyses, certain simplifications were made or certain data was not available. Therefore, some recommendations are made for future design phases, to improve the level of detail and accuracy of these analyses. For safety, further analysis must be done for safety-critical, novel systems, such as the propulsion units and hydrogen storage. For the maintenance plan and availability analysis, the level of detail of the scheduled activities should be analysed. The reliability analysis would benefit from design-specific failure rates, given by extensive testing. In turn, these failure rates could improve the accuracy of predicting scheduled versus unscheduled maintenance activity durations.

15. Sustainability Development Strategy

15.1. Sustainability Framework

The sustainability strategy for the BWB rests on the three pillars of sustainable development, planet, people and profit, and on a circular-economy approach to the materials it is built from. The pillars set the objectives that shaped the design; the circular approach governs how those objectives are met at the material level. The framework is not separate from the design: each pillar maps onto specific choices made elsewhere in the report, and the ex-ante life-cycle assessment that follows measures how far those choices reach the net-zero target.

The planet pillar targets the lifecycle emissions of the aircraft and the resources it consumes, and it drove the largest design choices in the report. The hydrogen fuel-cell powertrain removes combustion at the aircraft, leaving water and contrails as the only in-flight effects, as set out in the propulsion and operations chapters. The blended wing body raises the lift-to-drag ratio and lowers the energy required per passenger-kilometre, reducing both the hydrogen burned and the renewable electricity needed to produce it. The same weight-driven sizing minimises material demand, and the material that is used is selected to re-enter the supply chain rather than be lost at end of life.

The people pillar concerns the effect of the aircraft on those around it. With combustion removed, the aircraft emits no NO_X and no fine or ultra-fine particles in flight, lowering the health burden on communities near airports and on ground crews, while noise is held to no more than the A320 class. Hydrogen handling introduces new ground-safety considerations, which are addressed in the operations concept.

The profit pillar keeps the design commercially viable, since an aircraft that is not purchased by airlines can deliver no environmental benefit. Sustainability and cost are treated as aligned rather than opposed: lower energy per passenger-kilometre reduces fuel cost over the 30-year life, and returning materials to the manufacturer creates a second supply stream alongside virgin feedstock.

The framework is verified quantitatively by the ex-ante life-cycle assessment that follows. The assessment shows the design does not reach net-zero, with the residual dominated by the upstream production of hydrogen, but it reduces the lifecycle climate impact well below the A320-class benchmark. Net-zero is therefore treated as the direction the design is built toward, and the LCA as the measure of what can be achieved, with the carbon intensity of the hydrogen supply chain identified as the main emission source.

15.2. Ex-ante Life Cycle Assessment

The sustainability performance of the BWB design concept was evaluated using an ex-ante life-cycle assessment (LCA), which provides a study on products and technologies that have not been proven yet in the industry or that they do not even exist during the analysis, as they are still conceptual or in development. This section serves to address the expected emissions of the aircraft during all its life phases for a set of selected Environmental Impact Indicators (EII).

15.2.1. Goal & Scope

The Life Cycle Assessment goal, which defines the purpose, audience and type of the assessment, is to evaluate and quantify the environmental impacts of EverWing based on the designed specifications, such as material choice and propulsion type. The main purpose of the assessment is to validate the chosen design concepts by proving that it is capable of achieving a lower environmental impact than A320-class aircraft. Moreover, it also intends to identify the phase and processes which contribute most significantly to each EII, thereby guiding future design iterations and allocating burdens to mitigate emissions.

A prospective, ex-ante LCA will be conducted, where each database used will suit the timeframe of every phase of the aircraft.[51] For the manufacturing and operations phases 2047-2050 data will be used, and for the end-of-life the 2080 database will be taken, as the aircraft is expected to have a lifetime of 30 years, following from REQ-OPE-2.4. Data will be extracted from public databases and literature. The results are intended to be reviewed by operator stakeholders or any regulatory entity checking compliance with the net-zero target by 2050.

Study Coverage

It is essential to define the coverage of the study before starting the actual analysis because it reduces uncertainty and avoids misinterpretation of the results. Coverage is divided into three sub-categories: life coverage, temporal coverage and geographical coverage. First, in terms of life coverage this study will assess the aircraft in all its flight phases, ”cradle-to-grave” [81].This include the following phases;

1. **Raw Material Extraction**: Covers the extraction and processing of the main materials used in the BWB. The main materials used in the design are; CFR-PEEK and Aluminium-Lithium (Al-Li) alloys for the main airframe structure and other structural elements as discussed in chapter 6 and chapter 7, Aluminium-Lithium-Copper (Al-Li-Cu) alloys for the hydrogen tanks, as mentioned in subsection 8.3.1, Titanium (Ti) Alloys and Polymer Electrolyte Membrane (PEM) materials [82] for the hydrogen fuel cell stacks. It is important to note that liquid hydrogen won't be included in this phase as it is consumed during the operations phase and thus it from ISO standards [52] it should be included in that phase.
2. **Manufacturing/Assembly**: Includes the processing of all the previously mentioned materials and their integration into the aircraft. It also includes the transport of the manufactured parts
3. **Operations + H_2 Sourcing**: Covers all activities during the 30 years of the use-phase of the aircraft plus the upstream hydrogen production.
4. **Maintenance and Repair**: Covers all the expected and not expected maintenance procedures throughout the operational phase, such as replacement of components such as stack replacement, refurbishment etc.
5. **End-of-life**: Following from chapter 13, and REQ-REG-1.2, which is one of the most important requirements of the design, this phase includes, disassembly of aircraft, remanufacturing of parts, recycling and waste streams for selected components (powertrain).

Table 15.1 specifies the temporal and geographical coverage for each of the life phases of the aircraft.

Table 15.1: Temporal and Geographical coverage for each life phase of the BWB

Phase	Temporal Coverage (Year)	Geographical Coverage
Raw Material Extraction	2047-2050	Global
Manufacturing/Assembly	2047-2050	Europe
Operations + H_2 Sourcing	2050	Global (SMR based on the A320-class)
Maintenance and Repair	2050-2080	Europe
End-of-life	2080	Europe

Assumptions

During the assessment, the following assumptions and simplifications will be done to simplify the process and make the gathering viable.

- Green hydrogen is assumed to be used, which is produced using 100% renewable electricity [53].
- Based on REQ-REG-1.2, powertrain components will be excluded from the remanufacturing cycle.
- As briefly mentioned earlier, unavailable data will be substituted with literature values.

Other assumptions used during the investigation process will be explained when mentioned in the following sections.

15.2.2. Life Cycle Inventory

The previously mentioned life cycle phases can be assessed on their environmental impact through the use of Environmental Impact Indicators (EIIs). The EIIs used to assess each lifecycle phase are listed and explained in Table 15.2. From the detailed weight estimation explained in subsection 5.3.3, it was obtained an operative empty weight of the BWB of 34 538.22 kg, not including tanks. From chapter 8 it is known that the hydrogen tanks, which for simplicity assumed they are fully made of Al-Li-Cu 2195, have a total mass of 6 866 kg and that the PEM fuel cell stacks weight in total 3 555.2 kg. Thus, without taking into account heat exchangers, compressor-expander modules and electric motors, we have as a result a structural airframe weight of 26 799 kg . As already discussed, the airframe of the design is composed principally of CFR-PEEK, aluminium-lithium

[51] Dransfeld, C., “ADVANCED CONCEPTS IN LCA” AE3211-II Production of Aerospace Systems, Delft University of Technology, Delft, Netherlands, 2026. [Cited 12 June 2026]

[52] URL: https://ecochain.com/blog/life-cycle-assessment-lca-guide [Cited 13 June 2026]

[53] URL: https://www.iberdrola.com/sustainability/green-hydrogen [Cited 13 June 2026]

alloys and titanium alloys. Based on the material breakdown of the wing subsystem and of the tail subsystem from chapter 7 and chapter 9 they exhibited a CFR-PEEK/Al-Li division of 60%/40% and 67%/33%, respectively. For the purposes of this LCA, a uniform division across the airframe will be assumed between CFR-PEEK, Al-Li alloys and Ti alloys of 60%/35%/5%, respectively. This division is consistent with the explanation in chapter 6. Apart from the fuselage, wing and tail this division applies for fairings, pylons and other components regarding the airframe of the BWB. The uncertainty regarding this split will be treated in subsection 15.2.4.

Table 15.2: Environmental impact indicators used for each lifecycle phase

Environmental impact indicator	Description	Metric
Climate Change Potential (CCP)	Measures the contribution of carbon emissions to global warming throughout the life cycle.	CO_2 [kg-eq]
Human Toxicity Potential (HTP)	Represents the potential harmful effects of emitted substances on human health during the life cycle.	1.4-DCB [kg-eq] [54]
Acidification Potential (AP)	Quantifies the potential of emissions such as NO_x and SO_x to acidify soils and water bodies during each lifecycle phase.	SO_2 [kg-eq]

Raw Material Extraction

Table 15.3 show the CCP emission factors for all materials considered during this study, together with the quantified CCP will be quantified for every flight phase of the BWB. HTP and AP will be assessed in subsection 15.2.3, because specific values for 1.4-DCB and SO_2 can't be reliably quantified from open literature. The climate change potential follows from; CCP $=$ Mass $\times$ Emission Factor. In conclusion, raw material extractions carries a total CCP burden of 951 tons CO_2-eq. PEM are the dominant contributor to the raw material extraction phase, representing 49.7% of the total burden.

Table 15.3: Quantified CCP for every material

Material	Mass (kg)	Emission factor(kg CO_2-eq/kg)	CCP (tons CO_2-eq)
CFR-PEEK	9 379.7	26.4 [55]	247.6
Al-Li alloys	22 945.5	8 [73]	183.6
Ti-alloys	1 340.0	35 [83]	46.9
PEM fuel-cell stacks	3 555.2 (19 540 kW)	24.2 per kW [84]	472.9

Manufacturing/Assembly

Again, precise values are not available from the public databases, thus it will be scaled with respect to the A320-class. From Howe et al. [85], manufacturing an A320-class aircraft is equivalent to approximately 6.5 days of its operational emissions. Assuming a average utilisation rate of 1850 flights/year, from [79] and emissions of 53 tons of CO_2-eq per flight [56] result in 1 746 tons CO_2-eq for A320neo manufacturing. Scaling to the BWB by the OEW mass ratio it results of ;

$$1\,746 \times \frac{OEW_{BWB_{\text{no tanks}}}}{OEW_{320}} = 1\,746 \times \frac{34.5t}{44t} = 1\,369.1\text{tons } CO_2\text{-eq}$$

Adjusting for the 2050 European electricity grid, emissions are expected to be reduced by $\approx$ 72% [57], thus the manufacturing contribution in 2050 is expected to be $1\,369.1 \times 0.28 = 383.3$tons CO_2-eq

Operations + H_2 Sourcing

Before presenting the results of this phase, it is important to note that the CCP attributed this phase of the BWB does not represent the aircraft emissions, it represent the upstream carbon released during the supply chain of producing green hydrogen used to power the BWB. This includes the industrial processes tied with wind turbines, solar panels, electrolysers etc., which are not expected to be fully carbon free by 2050. Therefore, the aircraft itself emits zero CO_2 and zero NO_x during flight, as there is no combustion and no direct emissions [53]. According to Ajeeb et al. [86], the emission factor of green hydrogen taking into account its supply chain yield 1.0 kg CO_2-eq per kg H_2. Assuming utilisation rates similar to A320-class, from [79] it results of a total of 55 500 flights during the 30 years of operations. Taking 3 789 kg of hydrogen per flight, as calculated in chapter 8 and multiply everything by the associated emission factor it yields a CCP of;

$$55\,500\,\text{flights} \times 3\,789\text{kg } H_2\text{/flight} \times 1.0\text{kg } CO_2\text{-eq/kg } H_2 = 210\,289.5\text{t } CO_2\text{-eq over 30 years}$$

To put this into perspective, the A320neo currently emits 20 000 tons CO_2 per year of operational lifetime [87]. Thus, the BWB offers a 68% of the total burden, and a 100% reduction purely from operations, without including hydrogen's supply chain.

Maintenance and Repair

The main contribution during this phase is considered to be the replacements of the PEM stacks. The US Department of Energy [58] states that by 2050 PEM fuel cell systems target to operate for 30 000 hours for heavy duty road transportation. Aviation is more demanding, thus 30 000 hours is an optimistic estimate for the operating life in aircraft applications. Recalling the assumed utilisation rate of 55 500 flights and assuming an average usage time of 5 hours per flight, it is required minimum 2 scheduled replacement activities. Table 15.3 gives an emission factor of 24.2 kg CO_2-eq/kW, so using the number of fuel stacks used in the BWB and their shaft power from chapter 8, it yields a CCP of $2 \times 4 \times 4\,885 \times 24.2 = 945.7$t CO_2-eq. To this number other scheduled maintenance needs to be added to obtain the total burden for the maintenance phase, which are not available from the public database and thus for the purpose of this study won't be included.

End-of-life

Following chapter 13, the main structural materials of the aircraft will be remanufactured, generating negative CCP contributions. Based on their CCP stated in Table 15.3 and recovery efficiency from literature, Table 15.4 show all the avoided CCP for every material. The 90% recovery efficiency of Al-Li alloys reflect the fact that the tanks can be returned as another alloy rather than broken into constituent elements, as noted in subsection 8.3.1.

Table 15.4: CCP at end-of-life

Material	Mass (kg)	Recovery	CCP
CFR-PEEK	9379.7	80%	-198.1
Al-Li alloys	22945.5	90%	-165.24
Ti-alloys	1340	80%	-37.52
Processing energy	–	–	6.9

CFR-PEEK is recycled via glass transition assisted mechanical delamination, which retained over 80% of the original laminate's flexural strength, flexural modulus, and interlaminar shear strength according to Xing et al.. The CCP accounting for the disassembly of aluminium-lithium alloys was calculating knowing that recycling aluminium via meltless technology emits 0.3 kg CO_2-eq/kg [88], together with the total mass of aluminium-lithium alloys used in the aircraft. Summing all the contributions, it results in a net avoided CCP burden of -393.94 tons CO_2-eq.

15.2.3. Impact Assessment Results

After gathering all the data, the results of the analysis will be presented for each EII. Together, a hot-spot analysis will be derived from the results and they will be compared with the A320neo published data.

Climate Change Potential (CCP)

Table 15.5 adds all the CCP contributions of all the phases, resulting in a total burden of 212 299.3 t CO_2eq. The biggest contributor by far is the operations + H_2 sourcing phase, although it is purely from the upstream hydrogen production, while during operations there is no burden at all, as reasoned before. The other phases are negligible in comparison to the hydrogen upstream contribution. From [3] the emissions the A320neo is expected to have by 2050 are $\approx$ 50 grams CO_2-eq/pax-km. Using again the utilisation rate of 55 500 flights during the whole BWB lifetime and the design requirements of 150 pax and 4 000 km design range, it results in emissions of (212 299.3 t CO_2eq $\times$ 1 000 000) / (55 500 $\times$ 150 $\times$ 4 000) $=$ **6.37 grams CO_2-eq/pax-km**. This represents a 87% reduction in the total CCP emissions.

Human Toxicity Potential (HTP)

As briefed earlier, quantitative HTP is not available from public databases and therefore the results will be presented as a discussion, based on literature information. The dominant HTP hotspot across the full lifecycle of the BWB is platinum mining for the PEM fuel-cell stacks [89]. They release heavy metals such as nickel or palladium into local soils and drinkable water streams. Moreover, Chung et al. [90] notes that acrylonitrile is a precursor of CFR-PEEK during its production, and it's classified by the IARC as a Group 1 human carcinogenic [59]. Comparing these results with the A320neo, the BWB results in higher HTP during the first two phases due to the use of hydrogen as energy carrier and carbon-fibre composites for the airframe. The third important finding is that during operations the design significantly reduces its HTP score compared to the A320neo, as fine and ultra-fine particulate emissions are only reduced to the landing procedures (zero NO_x emissions). In

[54] 1.4-Dichlorobenzene, 10 kg-eq indicates the emissions had the same effect as 10 kg of dichlorobenzene

[55] URL: https://journals.stmjournals.com/article/article=2026/view=245976 [Cited 14 June 2026]

[56] URL: https://theicct.org/publication/co2-emissions-from-commercial-aviation-2013-2018-and-2019/ [Cited 14 June 2026]

[57] URL: https://www.enerdata.net/research/forecast-enerfuture.html [Cited 14 June 2026]

[58] URL: https://www.energy.gov/cmei/fuels/doe-technical-targets-fuel-cell-systems-and-stacks-transportation-applications [Cited 14 June 2026]

Table 15.5: CCP Results

Lifecycle Phase	CCP (t CO_2eq)	% of total
Raw Material Extraction	951	0.45
Manufacturing/Assembly	383.3	0.18
Operations (H_2 Sourcing)	0 (210 289.5)	0 (99.1)
Maintenance and Repair	945.7	0.45
End of Life	-393.94	-0.19
Lifecycle Total	**≈212 175.6**	**100%**

summary, the BWB increases HTP during raw material extraction and the manufacturing phases, but reduces it significantly during operations compared to its conventional counterpart.

Acidification Potential (AP)

For the same reasons as HTP, quantitative analysis on acidification potential is not computed at this stage. Similarly as HTP, platinum smelting during PGM mining for fuel cells is one of the main hotspots of acidification potential [83]. Secondly, aluminium-lithium smelting contributes to the AP burden through SO_2 emissions from anode bake ovens [60]. Concerning the use of green hydrogen, Ajeeb et al. [86] mentions that the contribution to AP from the upstream production is negligible. Comparing these with its conventional counterpart, the BWB lowers the AP burden by eliminating the primary source of aviation's acidification, which is NO_x and SO_2 emissions during operations, while A320neo have high AP burden due to these emissions [91].

15.2.4. Limitations & Uncertainties

The study was performed making several assumptions, which will carry uncertainty with them and impose limitations in the accuracy of the results, mainly governed by the scarce availability of data for certain parameters. First, all quantitative results were based on the weights obtained from the detailed estimation in subsection 5.3.3, which over-simplifies certain aspects of the aircraft and does not represent the real weight of the BWB with full accuracy, and thus the burden is not fully accurate. Next, as an accurate material investigation into the airframe is not available, a material split was assumed to estimate the masses of each material in the BWB. Although it is consistent with the explanation in chapter 6, it was done from the known divisions in the wing and empennage, but the fuselage distribution will be different due to the different loads and magnitudes it has to carry.

Moreover, the utilisation rate and the lifetime of the fuel cells were estimated. For the utilisation rate, the assumption was accurate as it take in consideration the rate of the current A320, although these value could increase by 2050. Regarding the fuel cells, the lifetime was a very top-level estimate and will carry significant uncertainty. However, the number of scheduled maintenance is a conservative estimate and thus the real-life burden during maintenance is not expected to be higher.

Finally, apart from the major limitation of not being able to quantify the HTP and AP due to resource availability problems, the last uncertainty is linked with the CCP projection of green hydrogen by 2050. Ajeeb et al. mentions values ranging from 0.5 kg CO_2-eq/kg H_2 for wind-only to 3.66 kg CO_2-eq/kg H_2 for solar PV under current conditions. As the upstream hydrogen production is by far the main contributor of the total CCP burden of the aircraft, a slight change in this value will highly influence the results.

15.2.5. Interpretation & Design recommendations

With the results and limitations in hand, the first and highest priority recommendation is to make sure that the hydrogen supply chain is dominated by wind. As mentioned in the limitations, this will reduce the green hydrogen emission factor and have a significant effect on the total burden of the aircraft, as this is by far the dominant contribution. A wind-only electrolysis will reduce the emission factor to 0.5 kg CO_2-eq/kg H_2, halving the burden of green hydrogen supply chain, also roughly halving the total burden of the aircraft. Moreover, another recommendation is to recover as much material as possible during end-of-life.

[59] URL: https://monographs.iarc.who.int/news-events/volume-136-talc-and-acrylonitrile/ [Cited 15 June 2026]
[60] URL: https://www.nrdc.org/bio/ian-wells/role-inert-anodes-aluminum-decarbonization [Cited 15 June 2026]

16. Future Product Development

16.1. Cost Breakdown Structure

Once the design has been finalised, it becomes possible to calculate all the costs needed to get the aircraft into service. The development costs have been estimated in section 16.3. Next to consider are per-unit production costs, direct operating costs, and re-manufacturing/recycling costs at end of life.

16.1.1. Production Costs

For production costs, the costs per subsystem were calculated and summed. For material-based costs, five materials were considered: CFR-PEEK, Al-Li 2050, Al-Li 2099, Al 2195, and aerogel. A buy-to-fly (B2F) ratio was assigned to each, which is an estimate of how much mass is lost during manufacturing between the raw material and finished product. For CFR-PEEK, a ratio of 1.1 was assigned as automated fiber placement (AFP) is a very efficient method to manufacture parts. For the Al alloys, a ratio of 1.25 was assigned, as subtractive manufacturing is much more common for metals. A material cost per kg was then assigned to each, with the Al alloys being assigned a cost of 25 USD FY26 per kg based on standard pricing with a slight reduction for bulk purchase. The CFR-PEEK is much more expensive, with prices ranging from 100-300 USD per kg. As such, a median estimate of 200 USD per kg was assigned. For the aerogel, the price was determined based on a sales price for an aerogel layer of certain dimensions and mass,[61] scaled up to a price per kg of 620.99 USD. In order to find the full production price of the fuselage components, the manufacturing cost must be considered. For the Al alloys, a conservative multiplier of 2.4 is assigned [92]. For CFR-PEEK, a multiplier of 3.5 was assigned based on AFP costs [62]

Table 16.1: Material properties and manufacturing assumptions

Material	Material Cost ($ FY26/kg)	Buy-to-Fly Ratio	Manufacturing Multiplier
CFR–PEEK	200	1.10	3.5
Al–Li 2050	25	1.25	2.4
Al–Li 2099	25	1.25	2.4
Al 2195	2.5	1.25	2.4
Aerogel	620.99	1.0	1.0

Next, the masses and materials used for all components of the fuselage, wings, and tail were calculated and defined based on the structural analysis results, and the total fuselage manufacturing cost was determined in Table 16.2.

Table 16.2: Airframe component mass and manufacturing cost breakdown

Component	Material	Mass (kg)	Material Sourcing Cost ($ FY26)	Manufacturing Cost ($ FY26)
Wing	61% CFR–PEEK, 39% Al–Li 2050	1,109.77	147,828	550,235
Tail	72% CFR–PEEK, 28% Al–Li 2050	294.99	46,551	169,184
Beams	Al–Li 2099	2,355.84	73,620	176,688
Bulkhead	Al–Li 2099	706.75	22,086	53,007
Skin	CFR–PEEK	3,769.35	829,257	2,902,400
Struts	CFR–PEEK	1,177.92	235,584	824,546
Longerons	CFR–PEEK	1,884.68	376,935	1,319,272
Airframes	Al–Li 2099	1,884.68	58,896	141,351
Total		**13,183.98**	**1,790,757**	**6,136,683**

The tanks each use Al 2195 shells with an inner insulating aerogel layer. Based on buy-to-fly ratios and manufacturing multipliers, the total tank price was calculated as USD 741037.

The landing gear package was estimated as USD 1.8M, based on the A320 landing gear configuration and price.[75] The electromechanical actuators were estimated as USD 2500 per item, and assuming two actuators

[61] URL `https://www.buyaerogel.com/product/cryogel-z/`

[62] URL `https://www.strategicmarketresearch.com/market-report/automated-fiber-placement-market`

per control surface and landing gear for redundancy, 14 are needed. The environmental control system price was estimated based on that of the A320 as USD 150 k. For the cabin and avionics, the cost was based off standard fractions of a full aircraft production cost. Based on reports of A320 sales up to 50% discounted from the standard USD 110M,[64] the production cost of an A320 was estimated as around USD 50M. The full avionics and electrical systems package was estimated as 25% of the full production cost,[65,66] while the cabin was estimated as 7.5%.[67]

The propulsion system was difficult to price due to its extremely novel design, both in terms of energy supply and engine configuration. The fuel cells were conservatively priced at USD 800/kWh, and based on the per engine energy requirement of 5600 kWh, a price per fuel cell of USD 4.48M was estimated. The other parts of the engine were simply estimated as a fraction of the fuel cell cost. The ducted fan and nacelle were estimated as 50% of the fuel cell cost, while the heat exchangers and piping were estimated as 40% and 10%, respectively. The inverter was priced based on its required kWh. This resulted in a total price per engine of USD 9.52M, and a total propulsion system price of USD 38.08M. The final combined costs of all parts of the aircraft have been listed in Table 16.3. The final cost has been converted into EUR FY26 to match the acquisition cost requirement. A 20% margin has also been added to the acquisition cost to account for uncertainties associated with estimating several novel components.

Table 16.3: Production cost breakdown

Component	Cost ($ FY26)
Propulsion system	38,080,000
EMA actuators (14)	35,000
Landing gear package	1,800,000
Environmental control package	150,000
Cabin	3,750,000
Avionics & electrical package	12,500,000
Airframe	6,136,683
Total Production Cost (USD)	**62,451,683**
Conversion to Euro (0.86 EUR/USD)	53,708,447
Total + 20% Margin (EUR FY26)	**64,450,137**

16.1.2. Recycling and Re-manufacturing Costs

Once the acquisition costs have been determined, it is possible to calculate the recycling costs for the aircraft. These costs will only be calculated based on recycling of the airframe, as the cabin interior and in flight systems are assumed to be switched out when needed throughout the aircraft's service life. For CFR-PEEK, the cost to recycle per kg is estimated conservatively as 100 USD per kg[72]. For Al alloys, it is estimated as 5 USD per kg[93]. Based on these values, the cost to recycle the airframe can be seen in Table 16.4.

Table 16.4: Airframe recycling costs

Component	Material	Mass (kg)	Recycling Cost ($ FY26)
Wing	61% CFR–PEEK, 39% Al–Li 2050	1,109.77	69,383
Tail	72% CFR–PEEK, 28% Al–Li 2050	294.99	21,576
Beams	Al–Li 2099	2,355.84	11,779
Bulkhead	Al–Li 2099	706.75	3,534
Skin	CFR–PEEK	3,769.35	376,935
Struts	CFR–PEEK	1,177.92	117,792
Longerons	CFR–PEEK	1,884.68	188,468
Airframes	Al–Li 2099	1,884.68	9423
Total		**13,183.98**	**798,891**

However, the material recovered through recycling will not be 100% of the original mass. In addition to this, by-to-fly (B2F) ratios must be re-applied to manufacture the new aircraft. As such, recycled CFR-PEEK is assumed to retain 80% of its mass[94], while Al alloys are assumed to retain 90% [95]. Based on these fractions, the final cost calculations are shown in Table 16.5.

[63] URL https://web.safran-group.com/ir2025/#page=1

[64] URL https://simpleflying.com/how-much-airbus-a320neo-cost-2026/

[65] URL https://www.aviationhunt.com/airbus-a320-ata-24/

[66] URL https://www.thalesgroup.com/en/solutions-catalogue/civil-aviation/flight-deck-avionics-equipment-functions

[67] URL https://www.ati.org.uk/wp-content/uploads/2021/08/insight(underscore)14-the-uk-cabin-opportunity.pdf

Table 16.5: Second generation aircraft material sourcing costs

Material	Post-Recycling Mass (kg)	Recycling Cost ($ FY26)	Total Required Mass (kg)	New Material Cost ($ FY26)	Total Cost ($ FY26)
CFR–PEEK	9,229.14	771,549	11,543.79	462,929	1,234,478
Al Alloys	3,904.84	27,342	5,818.81	47,849	75,191
Total	13,133.98	798,891	17,362.60	510,778	1,309,669
Total (+20%) (EUR FY26)		**747,761**		**478,088**	**1,225,850**

Comparing these results to the original material sourcing costs (and adding a 20% margin), the second generation of this aircraft will have a material procurement cost **27.5%** lower than the original. This shows that in the long run, recycling is beneficial in terms of not only sustainability but also profitability. While the flat difference does not affect total production cost too much (approximate EUR FY26 520,000 saved per aircraft), this adds up over time as aircraft sales numbers go up.

16.1.3. Direct Operating Costs (DOC)

Direct operating costs are considered the expenses that include providing the service and ensuring everything is in the correct conditions to fly. [68] Table 16.6 shows the breakdown of all the components contributing to the annual operating costs of EverWing, with a 20% contingency to account for components that have not reached TRL9 currently, reflecting uncertainty in green hydrogen pricing and PEM fuel cell maintenance intervals. Block hours represent the time from the moment the aircraft's brakes are released at the departure gate to the moment the brakes are set at the arrival gate [63], denoted as bh/yr. Based on a utilisation rate of 1850 flts/yr from section 15.2 block time and available seat kilometers (ASK) are calculated;

$$t_{block} = \frac{4000km}{850km/h} + 1h = 5.71 \text{ h/flight} = 10563.5 \text{ h/yr}$$

$$ASK = 150\text{pax} \times 1850\text{flts/yr} \times 4000\text{km} = 1\,110\text{M seat-km/yr}$$

SU is defined as service unit, which was calculated as seen in Equation 16.1, resulting in a SU of 44.3 SU/flight.

$$\text{SU} = \text{N} \cdot \text{d}, \quad \text{N} = \sqrt{\frac{\text{MTOM [tonnes]}}{50}}, \quad \text{d} = \frac{\text{range [km]}}{100} \tag{16.1}$$

CASK (cost per available seat-km) will be calculated using Equation 16.2, and is shown to comply with REQ-OPE-2.1.1 ($\leq$ 0.050 €/seat-km).

$$\text{CASK} = \frac{\text{DOC/yr}}{\text{ASK/yr}}, \quad \text{CASK}_{\text{no margin}} = 0.025 \text{ €/seat-km}, \quad \text{CASK}_{\text{margin}} = 0.030 \text{ €/seat-km} \tag{16.2}$$

Table 16.6: Annual Direct Operating Cost (DOC) of the BWB

Component	Price (M € FY26)	Explanation
Fuel (LH_2)	11.21	3 031 kg/flt from Table 8.7 with 1 850 flts/yr and 2 €/kg H_2 [15]
Flight Crew	3.69	350 €/bh $\times$ 10 564 bh/yr from IATA [96]
Cabin Crew	1.37	130€ /bh $\times$ 10 564 bh/yr with 3 crew [96]
Hydrogen ground operations	0.19	100 €/turn $\times$ 1 850 turns [15]
Fuel cells replacement	2.36	22 380 kW gross stack from Table 8.7 and 150 €/kW [15]
Airport services and ground handling	3.65	1 975 €/flt: landing (275 €) + pax (1 200 €) + ramp (500 €) with 1 850 flts/yr [96]
Insurance	0.6	0.4% $\times$ 150 M € maximum aircraft value from REQ-OPE-2.1.2 [96]
Navigation charges	4.75	From [74] 44.3 SU/flt at 58 €/SU, with 1 850 flts/yr
Total (with 20% margin)	**36.24**	27.82 M € $\times$ 1.20 = 33.38 M €

[68] URL: `https://www.globeair.com/g/direct-operating-cost-doc` [Cited 16 June 2026]

[69] URL: `https://www.lawinsider.com/dictionary/block-hour` [Cited 16 June 2026]

[70] URL: `https://ansperformance.eu/economics/cba/standard-inputs/latest/chapters/en_route_ans_costs.html` [Cited 17 June 2026]

16.2. Return on Investment

A return on investment (ROI) analysis will be performed to measure the profitability and the efficiency of the investment of the aircraft with respect to its cost. ROI is defined by Equation 16.3, expressed in percentage. A positive outcome represents that the investment generated a value in excess of cost, while a negative outcome shows a loss in value. The development costs were already estimated in section 16.3, leading to a gross value of 9 759 600 000 € and section 16.1 calculated that each unit of the BWB will cost 64 450 000 € to be produced, everything taking 2026 as the fiscal year.

$$\text{ROI} = \frac{\text{Net Return}}{\text{Cost of Investment}} \times 100 = \frac{n_{sold} \times (\text{Market Price} - \text{Production Costs}) - \text{Development Costs}}{n_{sold} \times (\text{Production Costs}) + \text{Development Costs}} \times 100 \tag{16.3}$$

In order to know the amount of aircraft that will be sold and the market price the BWB is expected to have, it is necessary to determine the market volume and the achievable market share of the product; which will be done in this section with the use of the market analysis from section 2.3.

16.2.1. Market Volume and Achievable Share

Market Volume

According to the market forecast Airbus conducted covering 2025-2045[71], the global demand for new aircraft resulted in 43 420 units, 34 250 of those being single-aisle narrow-body aircraft, yielding $\approx$ 1 712 new narrow bodies per year. The passenger traffic is expected to increase by 3.6% every year due to increases in trade, GDP and world population.[76] Based on the production window of the A320 (not accounting A320neo),[77] a production window of 25 years from the entry into service (2050-2075) is expected. This trend can be extrapolated to the assumed window, assuming there will be a continued growth in demand. Using the average 1 712 new aircraft per year and assuming a market growth of 1% annually, there will be $1\,712 \times (1.01)^{25} = 2\,196$ new aircraft per year between 2050-2075. This gives a demand of $2\,196 \times 25 = 54\,888$ new aircraft during the production window. Taking a conservative estimate, assuming the market demand does not grow, the demand would be $1\,712 \times 25 = 42\,800$. Taking a lower-end value in range, a demand for 47 000 new narrow-body aircraft will be used for the rest of the analysis.

Market Share

From the market analysis in section 2.3, the aviation market is governed as a duopoly, Airbus takes approximately 60% of the total share and roughly the rest is taken by Boeing [73]. Also, it was reasoned that the threat of new entrants in the market was very low due to considerably high barriers to entry. These include high capital requirements, long development cycles and a very complex certification process. Nevertheless, the net-zero target imposed by the ICAO [68] will give an advantage to zero-emission and remanufacturable aircraft, such as the BWB, compared to kerosene or SAF designs. The entrance of Comac in 2008 will be taken as reference, from Figure 16.1 it can be seen that Comac aircraft is forecasted to take 2% of the total narrow-body share by 2030. To adapt it to the BWB case in 2050 the regulatory advantage previously discussed needs to be taken into account, but also possible government subsidies to competitors, which will reduce the share the BWB attain. Furthermore, additional competitors may appear by 2050 and reduce the available share further. Thus, a share between 1-5% is a reasonable estimate.

A conservative, baseline and optimistic estimate will be taken from that range and the expected units sold will be calculated based on these and the demand from earlier, through $n_{sold} = 47\,000 \times$ Market Share. This is recorded in Figure 16.7.

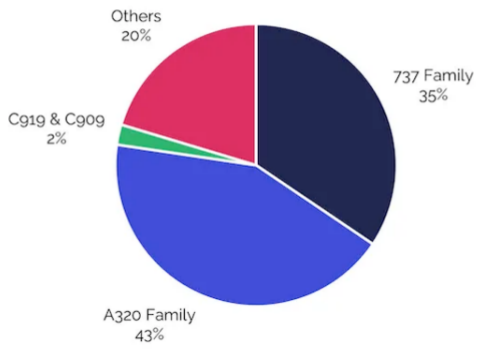

Source: IBA Insight

Figure 16.1: Expected Narrow-Body Share by 2030 [69]

Estimate	Market Share	Total sales, n_{sold}
Worst-case	1%	470
Assumed	**2%**	**940**
Baseline	3%	1 410
Optimistic	5%	2 350

Table 16.7: Estimates for market share and sales

16.2.2. Results and Expected Market Price

Due to the scarcity of information available about market prices of narrow-bodies by 2050, and the complexity of estimating a market price accounting for technology or design advantages and other factors, the market price will be determined based the current market price of the A320neo. Based on this price, the return on investment will be calculated through Equation 16.3. If it results in a positive ROI, the market price will be compared with the required 150M€ from REQ-OPE-2.1.2 in order to check compliance.

From the number of units that are going to be sold derived above and the costs already stated, Equation 16.3 yields:

$$\text{ROI} = \frac{940 \times \text{Market Price} - 70342.6}{70342.6} \times 100 \qquad \text{(in Million €)}$$

The current acquisition cost of the A320neo in 2026 is estimated to be 98 M€.[71] Accounting for technology and sustainability advantages the BWB will have with respect to its competitors, an initial market price estimate would be 105 M€. This leads to an ROI of 40.3%. If the market price is increased to 150 M€, assuming the same number of units are sold, the ROI would be 100.4%. There is no stakeholder requirement about ROI, thus the market price is kept as 105 M€, which complies with REQ-OPE-2.1.2 (acquisition cost $\leq$ 150M €). Based on these values, the break-even point occurs at a sales volume of 241 aircraft.

16.3. Post Project Gantt Chart

The post project Gantt chart shows the project development after the end of the DSE. Initially, there is a 14 year latency period for technological development. This is required for the TRL of technologies to mature, notably the storage and distribution of hydrogen, the material choices, the implementation of a blended wing body, and the implementation of fuel cells into conventional aircraft. This period is stimulated by investments from this project. The project then enters a detailed system design phase where complex systems are developed and thorough analyses are made. Then, a prototype phase where the principles discovered in the detail design phase are tested in smaller, cheaper prototypes. The first test aircraft is expected to be constructed in 2047, where the test aircraft phase will begin, starting a certification flight test campaign. Finally, the aircraft will be ready for distribution in 2049, and the first aircraft will enter the market in 2050. Certification plays a role in all design phases, starting in 2038 where the first discussions with the regulatory authorities are started, up until and after delivery of the aircraft.

The estimated cost of development is collected through each step in the development phases. These values are often propriety to aircraft manufacturers and therefore a detailed accurate breakdown is difficult to identify.

Whilst large contingencies are made at each step, project contingency management is critical. Currently this project uses 1.5 years less than the required 2050 after an 8.5 year development period. Which is equivalent to that of the A320. The cost of development also takes a 20% contingency to accommodate for unexpected costs in the development, providing a development cost of 9.7596 billion €.

Further analysis would have to be made with concrete work breakdown, and concrete accountancy, however this falls outside the scope of this report.

[71] URL: https://www.airbus.com/en/products-services/commercial-aircraft/global-market-forecast [Cited on 16 June 2026]
[72] URL: https://www.skyart.com/blog/airbus-a320-series-a-pioneer-of-modern-aviation [Cited on 16 June 2026]
[73] URL: https://safefly.aero/boeing-737-vs-airbus-a320-market-dynamics-2025/ [Cited on 16 June 2026]
[74] URL: https://www.icao.int/about-icao/Council/strategic-plan-2026-2050 [Cited on 16 June 2026]
[75] URL: https://www.aircraftinteriorsinternational.com/industry-opinion/market-forecast-comac-will-triple-aircraft-deliveries-by-2030.html[Cited on 16 June 2026]
[76] URL: https://www.macrotrends.net/stocks/charts/EADSY/airbus-se–/roi [Cited on 16 June 2026]
[77] URL: https://simpleflying.com/how-much-airbus-a320neo-cost-2026/ [Cited on 16 June 2026]

Project Phase	Task	Expected Duration	Expected cost (FY 2026)
Technolgy Maturity Phase	Development of novel propulsion unit technology	14 years	€ 2.500.000.000,00
	Development of novel materials for aviation	6 years	€ 200.000.000,00
	Development of liquid hydrogen safety protocols	8 years	€ 20.000.000,00
	Reasearch into aerodynamic principles surrounding blended wing body designs	6 years	€ 20.000.000,00
Detailed System Design Phase	Detailed Design of IPU components	1 year	€ 20.000.000,00
	Detailed Design of hydrogen components	1 year	€ 10.000.000,00
	Detailed Design of Aircraft Systems	1 year	€ 15.000.000,00
	Detailed Design of cockpit	6 months	€ 10.000.000,00
	Detailed aerodynamic design	1 year	€ 20.000.000,00
	Detailed aircraft aerodynamic simulations	1 year	€ 10.000.000,00
	Perform detailed propulsion system simulations	1 year	€ 10.000.000,00
	Develop Aircraft Software Architecture compliant with regulations	1 year	€ 10.000.000,00
	Perform System Safety and Compliance Simulations	1 year	€ 10.000.000,00
Prototype phase	Construct aircraft model and perform flight control tests	2 years	€ 30.000.000,00
	Construct model tank and perform functionallity tests	1 year	€ 10.000.000,00
	Perform material structural tests	1 year	€ 15.000.000,00
	Build fuselage demonstrator and perform laboratory tests	2 years	€ 500.000.000,00
	Develop aircraft software and program relevant controllers	1 year	€ 10.000.000,00
	Build propulsion unit demonstrator and perform laboratory tests	2 years	€ 1.000.000.000,00
	Build cockpit demonstrator and perform laboratory tests	2 years	€ 400.000.000,00
Test Aircraft Phase	Construct test aircraft	2 years	€ 3.000.000.000,00
	Perform independent and integrated software testing	2 years	€ 10.000.000,00
	Structural Load Tests	6 months	€ 20.000.000,00
	Powertrain Ground Tests	6 months	€ 20.000.000,00
	Aircraft System Integration Tests	6 months	€ 20.000.000,00
	Taxi Testing	6 months	€ 10.000.000,00
	Flight Test Campaign	1 year	€ 100.000.000,00
	Performance Testing	6 months	€ 50.000.000,00
Delivery	Manufacture servicable aircraft	1 year	€ -
	Install cabin interier for customer	3 months	€ -
Certification	Develop Certification Roadmap, approve with certifying authorities	4 years	€ 10.000.000,00
	Perfrom Preliminary safety assessments	1 year	€ 1.500.000,00
	Perform component and subsystem certification compliance tests and simulations	3 years	€ 30.000.000,00
	Perfrom aircraft system certification compliance tests	2 years	€ 30.000.000,00
	Perform saftey assessments for documented safety compliance	1 year	€ 1.500.000,00
	Finalise paperwork and gain type certificate	2 years	€ 10.000.000,00
			€ 8.133.000.000,00

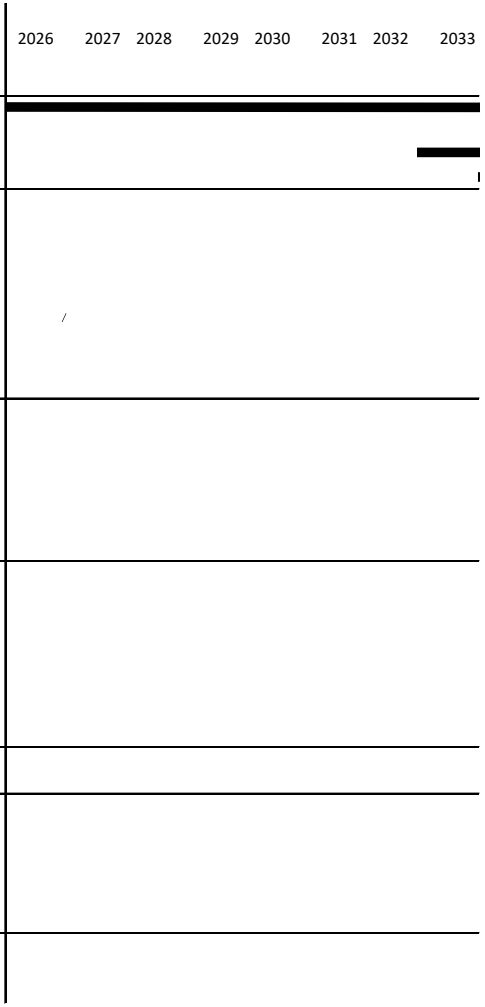

Figure 16.2: Project Gantt Chart (Page 1)

Figure 16.3: Project Gantt Chart (Page 2)

17. Product Compliance

17.1. Requirement Compliance

The compliance of the design is assessed through the requirements compliance matrix. It is a table that contains all the requirements imposed by the user and indicates with a tickmark when a requirement is met, providing a brief argumentation together with a cross-reference to reason whether or not the requirement is fulfilled. For those that are not compliant, the steps that will be taken to meet the requirement are indicated. Additionally, the verification method of each requirement will be recorded, according to chapter 18. These can be seen in Table 17.1.

The user requirement identifiers are categorised and abbreviated based on the categories shown on the right.

Requirement Abbreviations:

- REQ = Requirement
- USR = User
- PER = Performance
- SAR = Safety and Reliability
- SUS = Sustainability
- EB = Engineering Budget
- CST = Cost
- OTR = Other

Requirement identifiers use the following structure:

$\langle \text{ID} \rangle = \text{REQ} - \text{SOURCE} - \text{CATEGORY} - \text{NUMBER}$

Table 17.1: Compliance Matrix

Req. ID	Requirement	Comp.	Verification Method	Justification / Action
REQ-USR-PER-01	The aircraft shall have a capacity of 150 passengers	Yes	Demonstration	Cabin design resulted in an offered space for 150 passengers as shown in Figure 6.4
REQ-USR-PER-02	The aircraft shall have a nominal range of at least 4000km	Yes	Analysis	Based on the AEO fuel flow of 4×37.91 g/s from Table 8.7, a fuel mass of 3789 kg from Table 5.11 and a cruise speed of 236 m/s Table 5.7 it results in a maximum cruise range of 5897 km.
REQ-USR-PER-03	The aircraft shall have a cruise speed of Mach 0.8	Yes	Flight Test	Cruise speed suitable for Mach 0.8 Table 5.7
REQ-USR-SAR-01	The lifespan of the aircraft shall be at least 30 years	TBD	Analysis	The 30-year lifespan is used throughout as a design input, but a fatigue/damage-tolerance assessment needs to be added for the primary structure
REQ-USR-SAR-02	The aircraft shall have a dispatch reliability of at least 99.5%	Yes	Analysis	See section 14.4, dispatch reliability is comparable to that of an A320 (>99.5%)
REQ-USR-SUS-01	The aircraft shall only use renewable fuel/energy sources	Yes	Demonstration	Aircraft is powered purely from liquid hydrogen fuel cells as discussed in chapter 4.

Continued on next page

Table 17.1 – *continued from previous page*

Req. ID	Requirement	Comp.	Verification Method	Justification / Action
REQ-USR-SUS-02	The aircraft shall have zero emissions during operations	No	Flight Test	As reasoned in section 15.2, the CO_2 and NO_x are zero during operations, but contrails are not considered in the analysis and will produce emissions
REQ-USR-SUS-03	The aircraft shall fulfil expected EASA emission regulations for 2050 and beyond	Yes	Flight Test	EASA set limits to CO_2 and NO_x emissions during operations, and the BWB does not release any of those during operations as reasoned in section 15.2.
REQ-USR-SUS-04	Fine and ultra—fine particulate emissions shall be less than those seen in a large city by the year 2050	TBD/Yes	Test	An analysis into particulate emissions in a large city by 2050 needs to be done, together with a quantification of how much FP/UFP does the BWB emit, although it is expected to be lower due to the absence of combustion during operations, reducing by 60% total FP/UFP emissions.
REQ-USR-SUS-05	All parts of the aircraft shall be recycled or remanufactured into comparable parts for a similar aircraft. The only parts exempt of this requirement, are those power train components for which no circular path-ways are expected to be available by the year 2050	Yes	Demonstration	As discussed in chapter 13, all parts can be recycled or manfactured at least once into a new aircraft.
REQ-USR-SUS-06	Noise levels shall be similar to or lower than Airbus A320neo	TBD/Yes	Test	Through the qualitative analysis in subsection 5.3.5 it was strongly reasoned that BWB is expected to meet the requirement, but a quantitative assessment needs to be performed to reduce uncertainty.
REQ-USR-SUS-07	A high-level ex-ante Life Cycle Assessment (LCA) shall be performed	Yes	Demonstration	See section 15.2
REQ-USR-EB-01	The MTOM shall not exceed 80 000 kg	Yes	Demonstration	MTOM resulted in being 61 390 kg from subsection 5.3.3

Continued on next page

Table 17.1 – *continued from previous page*

Req. ID	Requirement	Comp.	Verification Method	Justification / Action
REQ-USR-EB-02	Required runway length at MTOW shall not exceed 2100 m in wet conditions	TBD	Analysis	A preliminary braking distance sizing is done in chapter 10, but it is assumed dry conditions and with several assumptions which bring considerable uncertainty.
REQ-USR-EB-03	Maximum wingspan shall be less than 40 m	Yes	Demonstration	Wingspan is 35.47 m from Figure 7.6
REQ-USR-EB-04	Maximum aircraft length shall be less than 40 m	Yes	Demonstration	Fuselage length is 21.4 m from chapter 6, plus an additional meter for engines going a little bit aft as shown in Table 6.3
REQ-USR-EB-05	Maximum turnaround time shall not exceed 45 minutes	Yes	Demonstration	As demonstrated in section 12.1, the expected turnaround time is expected to be 35 minutes, assuming we can refuel while boarding
REQ-USR-EB-06	The aircraft shall be able to be parked directly after a flight with near-empty tanks and/or batteries for a minimum of 12 hours without refuelling and/or recharging	Yes	Analysis / Demonstration	While aircraft may vent hydrogen when left stationary, there is no safety concern proven, and thus it can be left parked safely
REQ-USR-CST-01	The cost per available seat kilometre (CASK) shall not be higher than €0.050 per seat km	Yes	Analysis	CASK $= 0.030$ €/seat-km from subsection 16.1.3
REQ-USR-CST-02	Acquisition cost shall be less than 150M €	Yes	Demonstration	105M € of acquisition cost based on section 16.2
REQ-USR-OTR-01	The aircraft shall enter into service no later than 2050	Yes	Analysis	See Figure 16.2 and Figure 16.3
REQ-USR-OTR-02	The aircraft shall use technologies expected to each TRL9 before 2050	Yes	Demonstration / Analysis	See section 16.3

17.2. Sensitivity Analysis

The sensitivity analysis attempts to identify the parameters that are aircraft is sensitive to, for example a decrease in fuel cell efficiency of 10% might cause an increase in massflow of 25% due to the increase in required HEX sizing and corresponding mass. To reduce the work input the sensitivity analysis is focussed on parameters related to development risk. Notably a decrease in fuel cell performance, and a decrease in CFR-PEEK performance (these have been chosen due to their development uncertainty). As well as a direct result on the largest operational CO_2 contributor, the green H_2 production.

17.2.1. Fuel Cell Efficiency

The current fuel cell efficiency of 51.23% results in a total propulsion system mass of 7740 kg, however a reduction to 46.11% if the technology fails to mature results in a total propulsion system mass increases to 8025 kg. A decrease of 5.12% results in a system mass increase of 3.68%. This increase in mass whilst causing a shift in centre of gravity is relatively insignificant as an increase of just 285 kg can be comfortably mitigated.

17.2.2. CFR-PEEK material properties

The current minimum yield strength of CFR-PEEK from literature is 1200 MPa σ_y, this results in a wing box structural mass of 462.87 kg. By reducing the yield strength to CFRP-PEEK to 1080 MPa this results in a wing box structural mass, 467.29. This means that a reduction in material properties by 10% results in a increase in structural mass of 0.95%. This is accurate due to the limiting factor of the wing mass being the aluminium rather than the CFR-PEEK highlighting that the aircraft is not sensitive to the properties of this material.

17.2.3. H_2 production emissions

One key parameter that widely affects the results of the life-cycle assessment is the emission factor of green hydrogen. As discussed already in section 15.2 this vary depending on the supply chain, with different types of sourcing: wind, hydro, solar PV, the emission factor ranges from 0.5 - 3.6 kg CO_2-eq/kg H_2. A conservative estimate of 1.0 kg CO_2-eq/kg H_2, although there is evidence that by 2050 the supply chain will be wind-dominated. If sourcing does not reach the expected presence of wind energy by 2050, assuming the factor increases by 20%, then the total CCP burden of the aircraft will also increase roughly by 20%. Nevertheless, the burden in the operations phase will still be zero, as no CO_2/NO_x is emitted regardless, and throughout the total lifetime the burden will summate to 7.64 grams CO_2-eq/pax-km. This will still support the argument on offering considerably lower burden throughout the total lifetime compared to the A320neo, thus confirming the robustness of the results.

18. Project Methodology Verification and Validation

The reliability of the developed aircraft design tools and the resulting aircraft configuration were evaluated through a verification and validation process. Verification consists of unit and module testing of the individual tools, whereas validation involved comparing aircraft characteristics with analytical results, literature data and reference aircraft values.

18.1. Aircraft Development Model Functional Flow

A functional flow of the aircraft modelling tools is shown in Figure 18.1. Each block represents a Python script responsible for a specific aircraft design task, while the arrows indicate the transfer of data and dependencies between the different analyses.

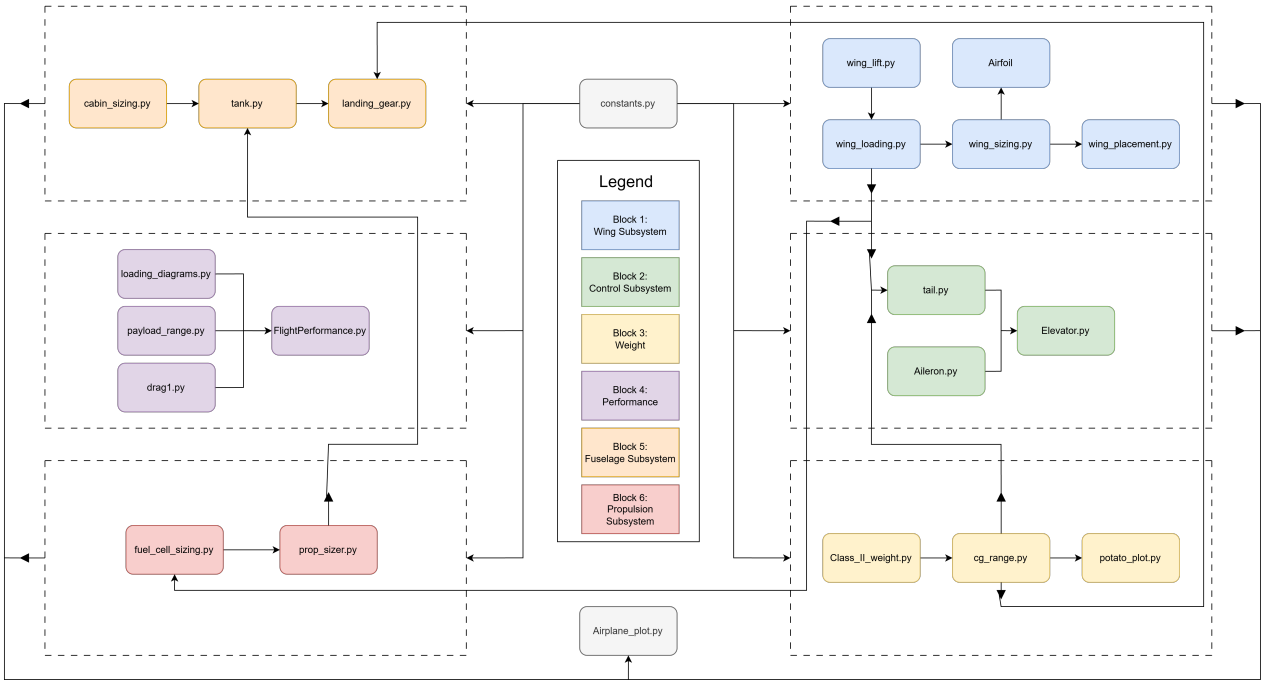

Figure 18.1: Diagram of the simulation code, showing the interaction between different code blocks

The workflow begins with a set of design assumptions and aircraft parameters. These inputs are used by the aerodynamic, control, weight, fuselage, performance and propulsion subsystems. Outputs generated by one analysis are transferred to subsequent code blocks where required, allowing dependencies between the different aircraft disciplines to be represented. The combined outputs are subsequently used to plot the preliminary aircraft design.

18.1.1. Code Hierarchy

To provide an effective verification campaign of the models and tools used, a distinct hierarchy definition of the software is created, as shown in Figure 18.2.

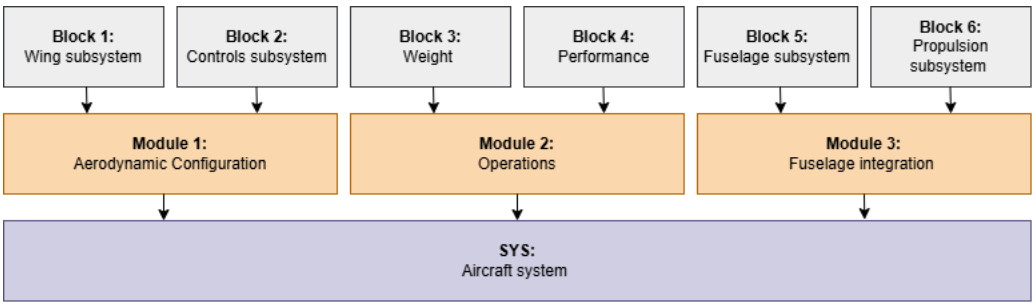

Figure 18.2: Code hierarchy of the preliminary design tool

The aircraft development model is organised into a hierarchy of code blocks, each representing a specific aircraft design discipline. Related code blocks are grouped into modules, allowing verification to be performed at both block and module level. This structure improves traceability by linking individual calculations to subsystem analyses.

- **Module 1: Aerodynamic Configuration** consists of the wing and controls subsystems. These blocks define the aircraft geometry, aerodynamic characteristics and control-surface configuration, representing the baseline aerodynamic design.
- **Module 2: Operations** consists of the weight and performance blocks. These analyses determine the aircraft layout, mass properties and stability characteristics, resulting in a feasible aircraft configuration.
- **Module 3: Fuselage Integration** consists of the fuselage subsystem and propulsion sizing block. These analyses define the propulsion architecture and its integration within the airframe, producing the final propulsion-system design.

The outputs of all three modules are combined within the Aircraft System (SYS), representing the complete aircraft design environment used for aircraft verification and validation.

18.2. Verification methods

Each block defined in the code hierarchy represents a separate unit that undergoes verification to confirm correct implementation of the methods and calculations. The blocks are grouped into three modules, allowing integrated testing of related aircraft design activities. To facilitate traceability throughout the verification and validation process, Blocks 1 to 6 are labelled B1 to B6, Modules 1 to 3 are labelled M1 to M3, and the complete aircraft design environment is labelled SYS. Verification is performed at both block and module level, while validation is performed by comparing the resulting aircraft characteristics against literature data and representative reference aircraft.

18.2.1. Unit Testing

Unit testing was performed on individual calculation and equations within each code block. The objective was to verify correct implementation of the mathematical relationships, input handling and numerical stability of the developed design tools. The unit tests performed are summarised in Table 18.1.

Table 18.1: Unit testing methods

ID	Test	Execution	Acceptance Criterion
U1	Null test	Execute functions using zero or empty inputs	No crashes; valid response returned
U2	Input validation	Provide invalid or non-physical inputs	Invalid inputs detected correctly
U3	Extreme value test	Evaluate functions at large and small inputs	Outputs remain valid and consistent
U4	Analytical test	Compare calculations with analytical solutions	Agreement within tolerance

18.2.2. Integrated Testing

Integrated testing was performed at module level to verify the correct interaction between the individual code blocks within each module. The objective was to confirm consistent data transfer and physically realistic outputs

when the aircraft design tools were executed as an integrated workflow. The integrated tests performed are summarised in Table 18.2.

Table 18.2: Integrated testing methods

ID	Test	Execution	Acceptance Criterion
I1	Interface test	Execute the module using outputs from preceding blocks	Inputs and outputs transferred correctly
I2	Physical test	Evaluate outputs for representative aircraft inputs	Outputs remain physically realistic
I3	Workflow test	Run the complete module sequence using final aircraft inputs	Module executes and produces usable outputs

18.3. Validation Methods

The validation process was conducted to assess whether the aircraft characteristics generated by the design tools were representative of a realistic regional transport aircraft. Since no experimental or flight test data were available, validation relied on comparisons with established aircraft data, engineering literature and expected physical behaviour. Three validation methods were used.

18.3.1. Wing Loading

Using the aircraft design point, wing loading W/S can be calculated based on MTOW and reference lifting area as:

$$\frac{M_{TOW}}{S_w + S_{fus}} \tag{18.1}$$

providing a value of approximately $1875\,N/m^2$. The A320 and 737-800 have wing loading values of around $6320\,kg/m^2$[80]. This is a large discrepancy that can be explained by the lifting fuselage characteristic of the blended wing body, which greatly increases the lifting area of the aircraft. If excluding the fuselage lifting area from the wing loading calculation, the value becomes $7620\,kg/m^2$. This is approximately 20% higher than that of the reference aircraft, but is close enough to provide confidence in the value achieved.

18.3.2. OEW Fraction

Another example of the validation process is the operating empty weight fraction $OEW/MTOW$. The aircraft produces and OEW fraction of:

$$\frac{OEW}{MTOW} = \frac{41596}{61390} = 0.678 \tag{18.2}$$

The calculated OEW/MTOW fraction of 0.678 is higher than the values typically observed for conventional regional transport aircraft, which generally range between 0.55 and 0.60 [80]. However, the result remains of the same order of magnitude and is considered physically plausible for a blended wing body configuration. Compared to conventional tube-and-wing aircraft, a BWB incorporates a larger integrated load carrying structure and accommodates a significant portion of the hydrogen fuel volume within the central body. These characteristics can increase the structural weight fraction while reducing the relative fuel mass required for a given mission. The result therefore suggests that the mass estimation methodology produces realistic aircraft mass characteristics and provides preliminary confidence in the validity of the sizing framework.

18.3.3. Cruise L/D Ratio

18.2 The aircraft has a cruise L/D ratio of 18.2. For comparable aircraft, the average cruise L/D lies in the range of 18.1-18.4[78]. While this would be a perfect validation result for a conventional aircraft, one of the main selling points for a blended wing body aircraft is a high L/D ratio, expected in the range of 22-26. However, this value can be explained though the extremely high wetted area, which causes large parasitic drag. In addition to this, some margin of error is to be expected due to simplifications in the aerodynamic analysis. As the result is still perfectly comparable to conventional aircraft and doesn't harm the overall aircraft performance, the cruise L/D can be considered validated.

18.4. Verification and Validation results

The validation results are summarised in Table 18.3. As can be seen, the obtained aircraft characteristics are of the expected order of magnitude and show reasonable agreement with reference aircraft and literature values. The results therefore provide preliminary confidence in the validity of the developed aircraft.

[78] URL `https://leehamnews.com/2014/11/04/fundamentals-of-airliner-performance-part-1/`

Table 18.3: Validation results

Metric	Aircraft Value	Expected Value	Assessment
Wing Loading	1875, 7620 excl. S_{fus}	6320	Acceptable; difference explained by BWB lifting body.
OEW fraction	0.678	0.55–0.60	Higher than conventional aircraft, but plausible.
Cruise L/D	18.2	18.1–18.5 conv.; 22–25 BWB	Within conventional range; low for BWB but acceptable.

The verification procedures described in section 18.2 were applied to the relevant code blocks and modules. Verification results are reported using the identifier convention introduced previously, for example the execution of Unit Test U3 on Block B4 is referenced as B4-U3. The results of the performed unit and module tests are presented in Table 18.4. For each test, the input, output, observed outcome and pass/fail assessment are documented. A test is considered successful when the corresponding acceptance criterion defined in Tables 18.1 and 18.2 is satisfied.

Table 18.4: Verification tests result table

Test ID	Input	Output	Pass Condition	Pass/Fail
Code block 1 'Wing subsystem' Unit tests				
B1-U1	Set wing area to 0	Error	Raise Error	Pass
B1-U2	Negative aspect ratio	Error	Raise Error	Pass
B1-U3	$S_{wing} = S_{ref}$ and $S_{wing} = 1$	$b = 35.4$ [m] and $b = 2$ [m]	Very large and small wingspan	Pass
B1-U4	Manual wing equations for span, root chord, tip chord and MAC	Code outputs agree with analytical hand calculations	Difference between code and analytical calculation is negligible.	Pass
Code block 2 'Controls subsystem' Unit tests				
B2-U1	Set elevator and ruddervator size to 0	$\ddot{\theta}_{to}$ = -44 deg/s	Large negative $\ddot{\theta}_{to}$	Pass
B2-U2	Negative elevator and ruddervator size	Error	Raise Error	Pass
B2-U3	Control surfaces placed at inboard and outboard span limits	Roll, pitch and yaw derivatives remain finite and change consistently with moment arm	Boundary cases produce physically consistent control derivatives	Pass
B2-U4	Elevator take-off rotation moment compared with moment-equilibrium hand calculation	Required elevator lift and moment have matching sign and order of magnitude	The hand calculated and code produced elevator lift and moment are similar.	Pass
Code block 3 'Weight' Unit tests				
B3-U1	Set payload mass to 0	Potato plot produces CG-range which is more aft than with payload.	Aft shift in CG-range	Pass
B3-U2	Negative payload, negative fuel mass or negative component mass	Error	Raise error	Pass
B3-U3	Set W_{OEW} to 95% of W_{TO} value and significantly reduce other masses	CG-range shifts more aft	Forward CG limit shifts aft	Pass
B3-U4	Calculate cg-range with only payload and no fuel	Calculated CG matches the potato diagram	Difference between coded CG and manual calculation shall be negligible	Pass
Code block 4 'Performance' Unit tests				
B4-U1	Set fuel mass to 0	Range is 0 from payload-range diagram	Range is 0 from payload-range diagram	Pass
B4-U2	Set $n_{max} = n_{min}$ in loading diagram	Manoeuvre envelope reduced to one line	Manoeuvre envelope reduced to one line	Pass
B4-U3	Set maximum fuel mass and maximum payload mass	Range at maximum fuel mass is maximum range, range at maximum payload mass is design range	Range at maximum fuel mass is maximum range, range at maximum payload mass is design range	Pass
B4-U4	Drag polar $C_D = C_{D0} + kC_L^2$ checked against manual calculation	Calculated drag coefficient matched model result	Drag coefficient calculation matches analytical equations for selected points	Pass
Code block 5 'Fuselage subsystem' Unit tests				
B5-U1	Cabin floor area set to zero	$l_{cabin} = 0$	Cabin Length reduces to zero	Pass
B5-U2	Negative cabin area	Error	Raise Error	Pass
B5-U3	Minimum and maximum available tank length	Tank radius and volume remain finite and positive for feasible lengths	Tank geometry shall remain physically realistic within available fuselage volume	Pass
B5-U4	Tank volume equation compared with manual calculation	Code volume agrees with analytical cylinder-volume calculation	Difference between coded and analytical volume is negligible	Pass
Code block 6 'Propulsion subsystem' Unit tests				
B6-U1	$P_{shaft} = 0$	Required fuel-cell power and hydrogen flow reduce to 0	Zero propulsion power and hydrogen flow	Pass
B6-U2	Set required shaft power to a negative value	Error	Raise Error	Pass

Continued on next page

Test ID	Input	Output	Pass Condition	Pass/Fail
B6-U3	Set required shaft power to the cruise and take-off values	Fuel-cell mass and hydrogen flow are higher for the take-off case	Propulsion-system size increases with required power	Pass
B6-U4	Calculate hydrogen flow manually from power, efficiency and hydrogen energy density	Manual hydrogen flow matches the code output	Difference between coded and manual hydrogen flow is negligible	Pass
Module 1 Integrated tests				
M1-I1	Pass wing geometry outputs to the control-surface sizing scripts	Span, chord, MAC and sweep are received by the control scripts	Correct exchange of wing geometry outputs	Pass
M1-I2	Use the final wing geometry for control-surface sizing	Aileron, elevator and ruddervator dimensions are generated	Control surfaces are successfully sized using the wing geometry	Pass
M1-I3	Run the complete wing and control workflow using the final aircraft inputs	Wing geometry and control-surface outputs are generated	Complete Module 1 workflow executes without errors	Pass
Module 2 Integrated tests				
M2-I1	Pass MTOW, OEW and CG outputs to the performance scripts	Aircraft masses and CG limits are received by the performance scripts	Correct exchange of weight and CG outputs	Pass
M2-I2	Use the final aircraft mass in the payload-range and climb calculations	Payload range, climb rate and service ceiling are generated	Performance results are generated using the final aircraft mass	Pass
M2-I3	Run the complete weight and performance workflow using the final aircraft inputs	CG envelope, payload-range diagram and climb results are generated	Complete Module 2 workflow executes without errors	Pass
Module 3 Integrated tests				
M3-I1	Pass tank volume and required power to the propulsion-sizing scripts	Tank volume and power requirements are received by the propulsion scripts	Correct exchange of fuselage and propulsion inputs	Pass
M3-I2	Use the final hydrogen requirement for tank and propulsion sizing	Tank dimensions, fuel-cell mass and hydrogen mass are generated	Tank and propulsion outputs are consistent with the hydrogen requirement	Pass
M3-I3	Run the complete fuselage and propulsion workflow using the final aircraft inputs	Fuselage, tank and propulsion-system outputs are generated	Complete Module 3 workflow executes without errors	Pass

19. Conclusion

Project Aim

The goal of this project was to 'Design a commercial 150-passenger, 4000 km range, net-zero emission aircraft for 2050 service entry with full end-of-life upcycling capabilities'. Therefore, the primary focus of the project was on the sustainability, recyclability, and re-manufacturability of the aircraft in design. Through an extensive trade-off, based on these key design drivers together with cost, aerodynamic, propulsive, and mass performance, the resulting design concept was a blended wing body aircraft named EverWing. A top-view schematic of the final design can be seen in Figure 19.1 and numerical details can be found in Table 19.1. A render of the EverWing can be seen in Figure 19.2.

Project Result

The aircraft consists of a large fuselage that acts as a lifting body, housing the passengers, cargo, and fuel. It also has a wing placed far aft, which provides lift. Control surfaces on the wing provide pitch and roll control. The fuselage also acts as a connection point for the tail and the four engines. The empennage was designed as a V-tail, as it would allow for additional pitch control, in addition to yaw control.

Table 19.1: Final design parameters

Parameter	Value
Length	21.4 m
Wingspan	35.5 m
MTOM	61390 kg
M_{cruise}	0.80
h_{cr}	12.2 km
L/D	18.2

EverWing is built using aluminium lithium alloys (such as Al-Li 2050, Al-Li 2099, and Al 2195) and Carbon Fibre Reinforced Polyether Ether Ketone (CFR-PEEK). After the aircraft has completed its service life, it will be returned to the manufacturer. Here, the aircraft gets disassembled, and each part is inspected for damage. Based on this inspection, the part is refurbished or recycled. The old aircraft thus re-enters the production cycle in the form of raw materials or re-manufactured parts.

The aircraft is powered by liquid hydrogen, stored in two tanks on the outboard sides of the fuselage and one tank aft of the cabin in the middle. By means of four independent fuel cells, the hydrogen is used to power four ducted fan engines, which are placed on the back of the fuselage. By using a hydrogen-electric powertrain, only water vapour is emitted, and the system emits no CO_2 and NO_X. Based on our design, the objective is feasible. Due to the limitations in time and facilities, real-life performance is not guaranteed to match the models.

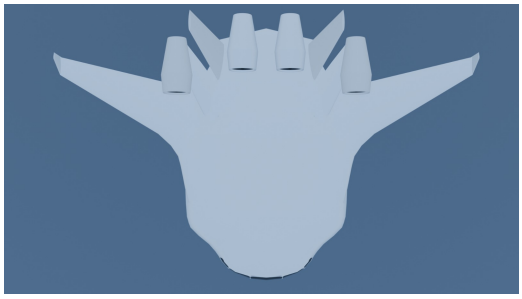

Figure 19.1: Final Design Top View

Figure 19.2: Final Aircraft Model EverWing

Project Difficulties

The project team ran into some technical difficulties throughout the design process, specifically the pressure bulkhead design, control surface design, and blended-wing body specific design, due to the lack of available data and empirical methods.

Recommendations

Further design efforts should aim to advance the technological maturity of concepts used in EverWing, by detailed subsystem design and thorough testing. Specific items requiring extra attention would be the propulsion subsystem, the selected materials, and the aerodynamic and structural implications of using a blended wing body instead of a conventional configuration. The aircraft additionally requires further designing, as the design presented in this report is high-level. Similarly, protocols must be finalised, regarding (hydrogen) safety and production, operational, and remanufacturing procedures.

References

[1] Shah, A., and Ansell, P. J., "Impact of Technology Maturation on Advanced Hydrogen Fuel Cell Aircraft," *Journal of Aircraft*, 2026, pp. 1–23. doi: 10.2514/1.C038714.

[2] Clark, L., and Gerhold, C., "Inlet noise reduction by shielding for the blended-wing-body airplane," *5th AIAA/CEAS Aeroacoustics Conference and Exhibit*, American Institute of Aeronautics and Astronautics, 1999. doi: 10.2514/6.1999-1937.

[3] Graver, B., Zheng, S., Rutherford, D., Mukhopadhaya, J., and Pronk, E., "Vision 2050: Aligning aviation with the Paris agreement," International Council on Clean Transportation, 2022.

[4] European Parliament and Council, "Regulation (EU) 2018/1139 on common rules in the field of civil aviation and establishing a European Union Aviation Safety Agency," Official Journal of the European Union, Jul. 2018.

[5] International Civil Aviation Organization, "Convention on International Civil Aviation," ICAO Doc 7300, 2006.

[6] International Air Transport Association, "IOSA Standards Manual (ISM)," ISM Ed 16 Rev 2, 2023.

[7] Keiser, D., Pupkes, B., and Freitag, M., "Passenger Expectations towards a Sustainable Aviation Industry," *Transportation Research Procedia*, Vol. 75, Dec. 2023, p. 189–197. doi: 10.1016/j.trpro.2023.12.022.

[8] Markatos, D., Psihoyos, H., Peerlings, B., Paletti, L., Boggero, L., Pantelas, P., Scheers, E., Söffing, L., Page, J., Pantelakis, S., Pasqualone, A., and Filippatos, A., "Systematic Identification of Stakeholder Needs for the Design of Sustainable Long-Range Aircraft of 2050," *Aerospace*, Vol. 13, No. 4, 2026, pp. 1–39. doi: 10.3390/aerospace13040299.

[9] International Air Transport Association, "Aircraft Technology Net Zero Roadmap," International Air Transport Association, Montreal, Canada, 2023.

[10] Li, S.-S., Yue, X., Li, Q.-Y., Peng, H.-L., Dong, B.-X., Liu, T.-S., Yang, H.-Y., Fan, J., Shu, S.-L., Qiu, F., and Jiang, Q.-C., "Development and Applications of Aluminum Alloys for Aerospace Industry," *Journal of Materials Research and Technology*, Vol. 27, Dec. 2023, pp. 944–983. doi: 10.1016/j.jmrt.2023.09.274.

[11] Krueger, R., and Bergan, A., "Advances in Thermoplastic Composites Over Three Decades: A Literature Review," NASA TM-20240005376, 2024.

[12] Anand, P., "Sustainable Materials in Aircraft Construction: A Viable Alternative to Aluminium?" *IOSR Journal of Mechanical and Civil Engineering*, Vol. 21, No. 5, 2024, pp. 9–11. doi: 10.9790/1684-2105020911.

[13] Seymour, K., Held, M., Stolz, B., Georges, G., and Boulouchos, K., "Future costs of power-to-liquid sustainable aviation fuels produced from hybrid solar PV-wind plants in Europe," *Sustainable Energy & Fuels*, Vol. 8, No. 4, 2024, p. 817. doi: 10.1039/D3SE00978E.

[14] Bell, A., Mannion, L. A., Kelly, M., Parker, R., Ghaani, M. R., and Dooley, S., "Life cycle CO2e intensity of power-to-liquid sustainable aviation fuel scenarios and specific use cases," *Advances in Applied Energy*, Vol. 20, Dec. 2025, p. 5. doi: 10.1016/j.adapen.2025.100248.

[15] Hoelzen, J., Koenemann, L., Kistner, L., Schenke, F., Bensmann, A., and Hanke-Rauschenbach, R., "H2-powered aviation – Design and economics of green LH2 supply for airports," *Energy Conversion and Management: X*, Vol. 20, Oct. 2023, pp. 1–36. doi: 10.1016/j.ecmx.2023.100442.

[16] Delpisheh, M., Moradpoor, I., Souhankar, A., Koutsandreas, D., and Shah, N., "Advancing the hydrogen economy: Economic, technological, and policy perspectives for a sustainable energy transition," *Renewable and Sustainable Energy Reviews*, Vol. 226, Jan. 2026, p. 2. doi: 10.1016/j.rser.2025.116238.

[17] Bhuiyan, M. H., and Siddique, Z., "Hydrogen as an alternative fuel: A comprehensive review of challenges and opportunities in production, storage, and transportation," *International Journal of Hydrogen Energy*, Vol. 102, Feb. 2025, p. 1031. doi: 10.1016/j.ijhydene.2025.01.033.

[18] Lee, B., Winter, L. R., Lee, H., Lim, D., Lim, H., and Elimelech, M., "Pathways to a Green Ammonia Future," *ACS Energy Letters*, Vol. 7, No. 9, 2022, pp. 3032–3038. doi: 10.1021/acsenergylett.2c01615.

[19] Kojima, Y., and Yamaguchi, M., "Ammonia as a hydrogen energy carrier," *International Journal of Hydrogen Energy*, Vol. 47, No. 54, 2022, pp. 22832–22839. doi: 10.1016/j.ijhydene.2022.05.096.

[20] International Aluminium Institute, "Global Aluminium Recycling: A Cornerstone of Sustainable Development," International Aluminium Institute, London, 2009.

[21] The Aluminum Association, "Environmental Product Declaration: Secondary Aluminum Ingot," The Aluminium Association, 2014.

[22] Hopewell, J., Dvorak, R., and Kosior, E., "Plastics recycling: challenges and opportunities," *Philosophical Transactions B*, Vol. 364, No. 1526, 2009, pp. 2115–2126. doi: 10.1098/rstb.2008.0311.

[23] Oliveux, G., Dandy, L., and Leeke, G., "Current status of recycling of fibre reinforced polymers: Review of technologies, reuse and resulting properties," *Progress in Materials Science*, Vol. 72, Jul. 2015, pp. 61–99.

[24] Meng, F., McKechnie, J., Turner, T. A., and Pickering, S. J., "Energy and environmental assessment and reuse of fluidised bed recycled carbon fibres," *Composites Part A: Applied Science and Manufacturing*, Vol. 100, Sep. 2017, pp. 206–214. doi: 10.1016/j.compositesa.2017.05.008.

[25] Sloan, I., Rios Romero, S., Ford, S., and Kooduvalli, K., "Embodied Energy of Pyrolysis and Solvolysis Processes for Recycling Carbon Fiber Reinforced Polymer Waste," *SAMPE Virtual Conference Proceedings*, 2020. doi: 10.33599/nasampe/s.20.0371.

[26] Faruk, O., Bledzki, A. K., Fink, H.-P., and Sain, M., "Biocomposites reinforced with natural fibers: 2000–2010," *Progress in Polymer Science*, Vol. 37, No. 11, 2012, pp. 1552–1596. doi: 10.1016/j.progpolymsci.2012.04.003.

[27] Schnell, M. C. A., "Existence and effectiveness perceptions of exit-barrier factors in liberalised airline markets," *Transportation Research Part E: Logistics and Transportation Review*, Vol. 42, No. 3, 2006, pp. 225–242. doi:

10.1016/j.tre.2004.10.001.

[28] Kappes, J. W., and Merkert, R., "Barriers to entry into European aviation markets revisited: A review and analysis of managerial perceptions," *Transportation Research Part E: Logistics and Transportation Review*, Vol. 57, Oct. 2013, pp. 58–69. doi: 10.1016/j.tre.2013.01.006.

[29] Raymer, D., "Enhancing aircraft conceptual design using multidisciplinary optimization," Ph.D. Thesis, Royal Institute of Technology, Stockholm, Sweden, 2002.

[30] Beck, N., Landa, T., Seitz, A., Boermans, L., Liu, Y., and Radespiel, R., "Drag Reduction by Laminar Flow Control," *Energies*, Vol. 11, No. 1, 2018, p. 252. doi: 10.3390/en11010252.

[31] Shah, A., and Ansell, P. J., "Modeling and Characterization of a Novel Propulsion System for Hydrogen Fuel Cell Aircraft," *AIAA SciTech Forum 2025*, Orlando, FL, 2025. doi: 10.2514/6.2025-0906.

[32] Gudmundsson, S., *General aviation aircraft design: applied methods and procedures*, Butterworth-Heinemann, Oxford, United Kingdom, 2014, Chap. 9.

[33] John David Anderson, *Aircraft Performance & Design*, McGraw-Hill Education, New York, 1999.

[34] Wu, Z., and Cao, Y., "Gust loads on aircraft," *The Aeronautical Journal*, Vol. 123, 2019, pp. 1216–1274. doi: 10.1017/aer.2019.48.

[35] Roskam, J., *Airplane Design, Part V: Component Weight Estimation*, DARcorporation, Lawrence, KS, 1989.

[36] Howe, D., *Aircraft Conceptual Design Synthesis*, Professional Engineering Publishing, London, 2000.

[37] Welstead, J., and Felder, J., "Conceptual Design of a Single-Aisle Turboelectric Commercial Transport with Fuselage Boundary Layer Ingestion," *54th AIAA Aerospace Sciences Meeting*, Reston, VA, 2016. doi: 10.2514/6.2016-1027.

[38] Ruijgrok, G. J., Voskuijl, M., and Varriale, C., *Elements of Airplane Performance*, TU Delft OPEN Publishing, Delft, The Netherlands, 2025.

[39] Newbury, S., "Academic Programme Research Findings And Recommendations," Aerospace Technology Institute, Rept. FZO-ACA-REP-0056, Cranfield, United Kingdom, 2022.

[40] Bos, A., "Aircraft Performance Summary Tables for BADA Revision 3.0," EUROCONTROL Experimental Centre, Brétigny-sur-Orge, France, 1998.

[41] Brown, M., and Vos, R., "Conceptual Design and Evaluation of Blended-Wing Body Aircraft," *2018 AIAA Aerospace Sciences Meeting*, American Institute of Aeronautics and Astronautics, Reston, Virginia, 2018. doi: 10.2514/6.2018-0522.

[42] Mo, Y., Ge, D., and He, B., "Experiment and optimization of the hat-stringer-stiffened composite panels under axial compression," *Composites Part B: Engineering*, Vol. 84, 2016, pp. 285–293. doi: 10.1016/j.compositesb.2015.08.039.

[43] CHEN, Z., ZHANG, M., CHEN, Y., SANG, W., TAN, Z., LI, D., and ZHANG, B., "Assessment on critical technologies for conceptual design of blended-wing-body civil aircraft," *Chinese Journal of Aeronautics*, Vol. 32, No. 8, 2019, pp. 1797–1827. doi: 10.1016/j.cja.2019.06.006.

[44] Ali, U., Okasha, M., Dief, T. N., ElSayed, M. S., and Kamra, M. M., "Blended wing body designs for aerodynamic, stability, and control optimization: A comprehensive review," *Transportation Engineering*, Vol. 22, No. 100397, 2025. doi: 10.1016/J.TRENG.2025.100397.

[45] Larkin, G., and Coates, G., "A design analysis of vertical stabilisers for Blended Wing Body aircraft," *Aerospace Science and Technology*, Vol. 64, 5 2017, pp. 237–252. doi: 10.1016/J.AST.2017.02.001.

[46] Whitcomb, R., "A design approach and selected wind-tunnel results at high subsonic speeds for wing-tip mounted winglets," NASA TN D-8260, 1976.

[47] Cabaleiro de la Hoz, C., Fioriti, M., and Boggero, L., "Performance and Reliability Evaluation of Innovative High-Lift Devices for Aircraft Using Electromechanical Actuators," *Aerospace*, Vol. 11, No. 6, 2024, p. 468. doi: 10.3390/aerospace11060468.

[48] Tzoumakis, G., Fotopoulos, K., and Lampeas, G., "Multi-Physics Digital Model of an Aluminum 2219 Liquid Hydrogen Aircraft Tank," *Aerospace*, Vol. 11, No. 2, 2 2024. doi: 10.3390/AEROSPACE11020161.

[49] Wang, C., Eisenreich, F., and Tomović, Z., "Closed-Loop Recyclable High-Performance Polyimine Aerogels Derived from Bio-Based Resources," *Advanced Materials*, Vol. 35, No. 8, 2023. doi: 10.1002/ADMA.202209003.

[50] Evkin, A. Y., and Lykhachova, O. V., "Design buckling pressure for thin spherical shells: Development and validation," *International Journal of Solids and Structures*, Vol. 156-157, 2019, pp. 61–72. doi: 10.1016/J.IJSOLSTR.2018.06.035.

[51] Renauld, N., "Design and Analysis of Inner Support Structures for Double-Walled Liquid Hydrogen Storage Vessels," M.S. Thesis, Delft University of Technology, Delft, Netherlands, 2024.

[52] The American Society of Mechanical Engineers, "Hydrogen Piping and Pipelines: ASME Code for Pressure Piping," The American Society of Mechanical Engineers, New York, NY, 2015.

[53] Webber, H., Llambrich, J., and Davoudi, H., "Thermal Management Roadmap Report," Aerospace Technology Institute, Rept. FZO-PPN-COM-0019, Cranfield, United Kingdom, 2022.

[54] Parello, R., Defoort, S., Bénard, E., and Gourinat, Y., "Integrating Cryogenic Tanks Model in Hydrogen Aircraft Design for Parametric Performance Analysis," *34th Congress of the International Council of the Aeronautical Sciences*, Firenze, Italy, 2024.

[55] Al-Shamma, O., Ali, R., and Hasan, H. S., "An instructive algorithm for aircraft elevator sizing to be used in preliminary aircraft design software," *Journal of Applied Engineering Science*, Vol. 15, No. 4, 2017, pp. 489–494. doi: 10.5937/JAES15-14829.

[56] Roskam, J., "Airplane Design Part VII: Determination of Stability, Control and Performance Characteristics: FAR and Military Requirements," *DARcorporation, Lawrence, KS*, 2002.

[57] Purser, P. E., and Campbell, J. P., "Experimental verification of a simplified vee-tail theory and analysis of available data on complete models with vee tails," Langley Memorial Aeronautical Laboratory, Langley field, VA, 1945.

[58] Galvão, F. L., "A Note on Glider Electric Propulsion," *Technical Soaring*, Vol. 36, No. 4, 10 2012, pp. 94–101.

[59] International Civil Aviation Organization, *Aerodromes: international standards and recommended practices. Volume I, Aerodrome design and operations*, 2009.

[60] Airbus S.A.S., "A319 Aircraft Characteristics – Airport and Maintenance Planning," Airbus S.A.S., Blagnac Cedex, France, 2017.

[61] Li, J., Yu, Z., Huang, Y., and Li, Z., "A review of electromechanical actuation system for more electric aircraft," *2016 IEEE International Conference on Aircraft Utility Systems (AUS)*, Institute of Electrical and Electronics Engineers, 2016, pp. 490–497. doi: 10.1109/AUS.2016.7748100.

[62] Qiao, G., Liu, G., Shi, Z., Wang, Y., Ma, S., and Lim, T. C., "A review of electromechanical actuators for More/All Electric aircraft systems," *Proceedings of the Institution of Mechanical Engineers, Part C: Journal of Mechanical Engineering Science*, Vol. 232, No. 22, 2018, pp. 4128–4151. doi: 10.1177/0954406217749869.

[63] Dell'Amico, A., and Reichenwallner, C., "A Conceptual Comparison of Hydraulic and Electric Actuation Systems for a Generic Fighter Aircraft," *Aerospace*, Vol. 12, No. 1, 2024, p. 1. doi: 10.3390/aerospace12010001.

[64] Li, Z., Hamidi, A. S., Yan, Z., Sattar, A., Hazra, S., Soulard, J., Guest, C., Ahmed, S. H., and Tailor, F., "A circular economy approach for recycling Electric Motors in the end-of-life Vehicles: A literature review," *Resources, Conservation and Recycling*, Vol. 205, 2024, p. 107582. doi: 10.1016/j.resconrec.2024.107582.

[65] Currey, N. S., *Aircraft Landing Gear Design: Principles and Practices*, American Institute of Aeronautics and Astronautics, Washington, DC, 1988.

[66] ten Damme, L., van Put, M., and Gangoli Rao, A., "Simulation of the refuelling process for an LH2-Powered commercial Aircraft: Part 2 - Refuelling time of the Airbus ZEROe turboprop concept," *International Journal of Hydrogen Energy*, Vol. 216, 2026, p. 153582. doi: 10.1016/J.IJHYDENE.2026.153582.

[67] Molkov, V., Ebne-Abbasi, H., and Makarov, D., "Liquid hydrogen refuelling at HRS: Description of sLH2 concept, modelling approach and results of numerical simulations," *International Journal of Hydrogen Energy*, Vol. 93, 2024, pp. 285–296. doi: 10.1016/J.IJHYDENE.2024.10.392.

[68] Huaguo, C., Cheuk Lun, and Denvid, L., "Deterioration Mechanisms and Advanced Inspection Technologies of Aluminum Windows," , 2022.

[69] Egorov, A. V., Polyakov, V. V., Salita, D. S., Kolubaev, E. A., Psakhie, S. G., Chernyavskii, A. G., and Vorobei, I. V., "Inspection of aluminum alloys by a multi-frequency eddy current method," *Defence Technology*, Vol. 11, No. 2, 2015, pp. 99–103. doi: 10.1016/J.DT.2014.12.002.

[70] Kennedy, S. M., Jeen Robert, R. B., Malkiya Rasalin Prince, R., Hikku, G. S., and Kaliraj, M., "A comprehensive overview of the fabrication and testing methods of FRP composite pipes," *MethodsX*, Vol. 13, 2024, p. 102990. doi: 10.1016/J.MEX.2024.102990.

[71] Lange, R., and Mook, G., "Structural analysis of CFRP using eddy current methods," *NDT & E International*, Vol. 27, No. 5, 1994, pp. 241–248. doi: 10.1016/0963-8695(94)90128-7.

[72] Teltschik, J., Matter, J., Woebbeking, S., Jahn, K., Borja Adasme, Y., Van Paepegem, W., Drechsler, K., and Tallawi, M., "Review on recycling of carbon fibre reinforced thermoplastics with a focus on polyetheretherketone," *Composites Part A: Applied Science and Manufacturing*, Vol. 184, 2024. doi: 10.1016/j.compositesa.2024.108236.

[73] European Aluminium, "Environmental Profile Report 2024: Executive Summary," European Aluminium, Brussels, Belgium, 2025. Version 2.0.

[74] SAE International, "Guidelines and Methods for Conducting the Safety Assessment Process on Civil Airborne Systems and Equipment," SAE Aerospace Recommended Practice, 1996. doi: 10.4271/ARP4761.

[75] U.S. Department of Transportation Federal Aviation Administration, "Advisory Circular 25.1309-1B," , 2024.

[76] Rahn, A., Schuch, M., Wicke, K., Sprecher, B., Dransfeld, C., and Wende, G., "Beyond flight operations: Assessing the environmental impact of aircraft maintenance through life cycle assessment," *Journal of Cleaner Production*, Vol. 453, 2024. doi: 10.1016/j.jclepro.2024.142195.

[77] Hoff, T., Becker, F., Dadashi, A., Wicke, K., and Wende, G., "Implementation of Fuel Cells in Aviation from a Maintenance, Repair and Overhaul Perspective," *Aerospace 2023, Vol. 10, Page 23*, Vol. 10, No. 1, 2022, p. 23. doi: 10.3390/AEROSPACE10010023.

[78] Meissner, R., Sieb, P., Wollenhaupt, E., Haberkorn, S., Wicke, K., and Wende, G., "Towards climate-neutral aviation: Assessment of maintenance requirements for airborne hydrogen storage and distribution systems," *International Journal of Hydrogen Energy*, Vol. 48, No. 75, 2023, pp. 29367–29390. doi: 10.1016/J.IJHYDENE.2023.04.058.

[79] Aircraft Commerce, "A320 family maintenance analysis & budget," *Aircraft Commerce*, Vol. 1, No. 44, February/March 2006, pp. 18–31.

[80] Airbus S.A.S., "A320 Aircraft Characteristics – Airport and Maintenance Planning," Airbus S.A.S., Blagnac Cedex, France, 2025.

[81] Garcia Garriga, A., "Aerospace Life Cycle Assessment (LCA): Framework for improved connectivity," International Aerospace Environmental Group, 2025.

[82] Haile, S. M., "Materials for fuel cells," *Materials Today*, Vol. 6, No. 3, 2003, pp. 24–29. doi: 10.1016/S1369-7021(03)00331-6.

[83] Gao, F., Nie, Z., Yang, D., Sun, B., Liu, Y., Gong, X., and Wang, Z., "Environmental impacts analysis of titanium sponge production using Kroll process in China," *Journal of Cleaner Production*, Vol. 174, 2018, pp. 771–779. doi: 10.1016/j.jclepro.2017.09.240.

[84] Yilmaz, G., Sadvakasova, A. K., Kossalbayev, B. D., Bauenova, M. O., Zharmukhamedov, S. K., Ziyayeva, G. K., Zaletova, D. E., Alharby, H. F., and Allakhverdiev, S. I., "Hydrogen energy development in Turkey: Challenges and opportunities," *International Journal of Hydrogen Energy*, Vol. 52, 2024, pp. 1304–1311. doi: 10.1016/j.ijhydene.2023.11.230.

[85] Howe, S., Kolios, A., and Brennan, F., "Environmental life cycle assessment of commercial passenger jet airliners," *Transportation Research Part D: Transport and Environment*, Vol. 19, 2013, pp. 34–41. doi: 10.1016/j.trd.2012.12.004.

[86] Ajeeb, W., Costa Neto, R., and Baptista, P., "Life cycle assessment of green hydrogen production through electrolysis: A literature review," *Sustainable Energy Technologies and Assessments*, Vol. 69, 2024, p. 103923. doi: 10.1016/j.seta.2024.103923.

[87] Airbus S.A.S., "A320 FAMILY: the most successful aircraft family ever," Airbus S.A.S., Blagnac Cedex, France, 2021.

[88] Duflou, J. R., Tekkaya, A. E., Haase, M., Welo, T., Vanmeensel, K., Kellens, K., Dewulf, W., and Paraskevas, D., "Environmental assessment of solid state recycling routes for aluminium alloys: Can solid state processes significantly reduce the environmental impact of aluminium recycling?" *CIRP Annals*, Vol. 64, No. 1, 2015, pp. 37–40. doi: 10.1016/j.cirp.2015.04.051.

[89] Osman, A. I., Nasr, M., Mohamed, A. R., Abdelhaleem, A., Ayati, A., Farghali, M., Al Muhtaseb, A. H., Al Fatesh, A. S., and Rooney, D. W., "Life cycle assessment of hydrogen production, storage, and utilization toward sustainability," *WIREs Energy and Environment*, Vol. 13, No. 3, 2024. doi: 10.1002/wene.526.

[90] Chung, T.-C., and Li, H., "Carbon Fiber Precursors and Production Process," University Park, PA, U.S. Patent 11,987,707 B2, Issued 21 May 2024.

[91] ICAO Committee on Aviation Environmental Protection (CAEP), "Report on Operational Opportunities to Reduce Climate Effects of Contrails and Other Non-CO2 Emission," ICAO, Montreal, Canada, 2025.

[92] Lequeu, P., Smith, K. P., and Daniélou, A., "Aluminum-Copper-Lithium Alloy 2050 Developed for Medium to Thick Plate," *Journal of Materials Engineering and Performance*, Vol. 19, No. 6, 2010, pp. 841–847. doi: 10.1007/s11665-009-9554-z.

[93] Wasilenski, A., and Cooper, D., "Assessing the potential for closed loop recycling of end-of-life aerospace aluminum alloys in the United States," *Procedia CIRP*, Vol. 135, 2025, pp. 187–194. doi: 10.1016/j.procir.2025.02.129.

[94] Xing, M., Fu, S., Shembekar, A. P., and Ray, D., "Recycling of carbon fibre/PEKK laminates via glass transition assisted mechanical delamination," *Composites Part B: Engineering*, Vol. 310, 2026. doi: 10.1016/j.compositesb.2025.113155.

[95] Samuel, M., "A new technique for recycling aluminium scrap," *Journal of Materials Processing Technology*, Vol. 135, 2003, pp. 117–124. doi: 10.1016/S0924-0136(02)01133-0.

[96] Jenkinson, L. R., Simpkin, P., and Rhodes, D., *Civil Jet Aircraft Design*, American Institute of Aeronautics and Astronautics, London, 1999.

A. Requirements

A.1. Stakeholder Requirements

Table A.1: Stakeholder Requirements

ID	Requirement Description	Type
REQ-REG-1	The aircraft shall demonstrate a zero lifecycle environmental impact when entering into service in 2050	Functional
REQ-OPE-1	The aircraft shall be certified for commercial service	Operational
REQ-OPE-2	The aircraft shall be competitive in the A320-class	Constraint
REQ-OPE-3	The aircraft shall enter into service by 2050	Constraint
REQ-AIR-1	Applicable airport operational rules and restrictions shall be complied with	Operational
REQ-AIR-2	The aircraft shall operate using standard A320-class airport infrastructure	Functional
REQ-PAS-1	Passengers shall have a comfortable and safe in-flight experience	Operational
REQ-MAN-1	The production process shall be safe and feasible	Functional

A.2. Mission Requirements

Table A.2: Mission Requirements

ID	Requirement Description
REQ-REG-1.1	Net-zero emissions shall be achieved during all in-service operations
REQ-REG-1.2	The aircraft shall be designed to be fully re-manufactured and/or recycled at end of life, excluding the powertrain components
REQ-REG-1.3	The aircraft shall demonstrate net-zero lifecycle impact through an ex-ante Life Cycle Assessment
REQ-OPE-1.1	All ground and flight operations shall be safe for all souls on board
REQ-OPE-2.4	A nominal operational lifetime of at least 30 years shall be provided.
REQ-OPE-2.1	The aircraft shall be affordable for operators
REQ-OPE-2.2	The aircraft shall comply with A320-class operational targets
REQ-AIR-1.1	Applicable airport safety, emissions, noise, and operational regulations shall be complied with during all airport procedures
REQ-AIR-2.2	The aircraft shall be compatible with available airport boarding systems
REQ-AIR-2.3	The aircraft shall be compatible with available airport energy systems
REQ-PAS-1.2	Comfortable travel shall be provided for passengers
REQ-MAN-1.2	The manufacturing process shall be safe
REQ-MAN-1.3	The manufacturing process shall be feasible

A.3. System Requirements

Table A.3: System Requirements

ID	Requirement Description
REQ-REG-1.1.4	During all in-service operations the aircraft shall achieve net-zero CO_2 emissions
REQ-REG-1.1.5	The aircraft shall comply with EASA emission regulations at service entry in 2050 and beyond
REQ-REG-1.1.6	The aircraft shall achieve a contrail reduction of TBD% compared to A320 under TBD atmospheric conditions
REQ-REG-1.1.8	During all in-service operations the aircraft shall achieve net-zero NO_X emissions
REQ-REG-1.2.3	At end-of-life aircraft components shall be removable without structural damage
REQ-REG-1.2.6	All selected aircraft materials shall be compatible with remanufacturing and/or recycling processes available for end-of-life aircraft processing
REQ-REG-1.2.5	All materials and components shall be traceable throughout their lifetime
REQ-OPE-1.1.1	The aircraft shall detect system failures during all flight and ground phases according to TBD failure detection coverage and response time
REQ-OPE-1.1.2	The aircraft shall provide flight crew alerts for all critical failures
REQ-OPE-1.1.3	The aircraft shall support safe flight and landing procedures after a failure detection
REQ-OPE-1.1.4	The aircraft shall maintain controllability and stability during operating conditions
REQ-OPE-1.1.5	The aircraft structure shall withstand all limit loads without structural failure
REQ-OPE-1.1.6	All safety-critical systems shall include fail-safe architecture
REQ-OPE-1.1.7	The aircraft shall maintain controllability under crosswind landing conditions up to TBD knots
REQ-OPE-1.1.8	The aircraft shall provide situational-awareness metrics to the flight crew during all relevant flight phases
REQ-OPE-1.1.9	The aircraft shall enable the evacuation of all passengers and crew within 90s
REQ-OPE-1.1.10	The aircraft shall comply emergency evacuation requirements of CS25.800-820
REQ-OPE-1.1.11	The primary structure shall be able to withstand bird-strikes and Foreign Object Debris (FOD)
REQ-OPE-1.1.12	The emergency exits on each side of the fuselage must include at least two Type I or larger and two Type II or larger exits
REQ-OPE-1.1.13	At least one floor-level exit shall be located on each side near each end of the cabin
REQ-OPE-1.1.14	Passageways leading to Type I, Type II, or Type C emergency exits shall be unobstructed and at least 51 cm wide
REQ-OPE-1.1.15	cross-aisles shall be unobstructed and at least 51 cm wide between main aisles
REQ-OPE-1.1.16	Passenger aisles shall be at least 51 cm wide at 64 cm and more from the floor
REQ-OPE-1.1.17	No more than 3 seats abreast shall be placed on each side of an aisle, when accessible by a single aisle
REQ-OPE-1.1.18	No more than 6 seats abreast shall be placed on each side of an aisle, when accessible by two aisles
REQ-OPE-1.1.19	At least one floor-level exit must be located on each side near each end of the cabin
REQ-OPE-1.1.20	Downward visibility forward from the cockpit shall be at least 17 degrees from the horizontal datum plane
REQ-OPE-1.1.21	Upward visibility forward from the cockpit shall be at least 21 degrees from the horizontal datum plane
REQ-OPE-1.1.22	Lateral visibility from the cockpit shall be at least 120 on each side of the aircraft
REQ-OPE-1.1.23	Downward visibility at 90^o shall be 27^o from the horizontal datum plane
REQ-OPE-2.4.1	Routine maintenance tasks shall be completed within periods of TBD weeks
REQ-OPE-2.4.2	Performance degradation shall be limited to a level of TBD% per TBD years

Continued on next page

ID	Requirement Description
REQ-OPE-2.4.3	All aircraft components requiring scheduled maintenance or inspection shall be accessible without structural disassembly
REQ-OPE-2.1.1	The aircraft shall achieve a cost per available seat-kilometre not higher than €0.050/seat-km
REQ-OPE-2.1.2	The acquisition cost of the aircraft shall not exceed 150M EUR
REQ-OPE-2.2.1	The aircraft shall be capable of sustained cruise at Mach 0.8
REQ-OPE-2.2.2	The aircraft shall achieve a standard operational range of 4000 km
REQ-OPE-2.2.3	The aircraft shall be capable of carrying a minimum of 150 passengers
REQ-OPE-2.2.4	Aircraft cargo systems shall be compatible with standard baggage and container handling equipment in 2050 and beyond
REQ-OPE-2.2.5	Aircraft shall have a MTOW not larger than 80,000 kg
REQ-OPE-2.2.6	Aircraft shall have a maximum wingspan of 40 m
REQ-OPE-2.2.7	Aircraft shall have a maximum length of 40 m
REQ-OPE-2.2.8	The aircraft shall provide a rate of climb of at least TBD m/s
REQ-OPE-2.2.9	Aicraft shall have a dispatch reliability of at least 99.5%
REQ-OPE-2.2.10	Aircraft turnaround time shall be less than 45 minutes
REQ-OPE-2.2.11	Aircraft shall sustain utilisation rates higher than the A320 during its operational lifetime
REQ-OPE-2.2.12	The aircraft shall not consume fuel/energy at a rate higher than TBD MJ/pax-km
REQ-OPE-2.2.13	The aerodynamic design of the wing shall achieve a zero-lift drag coefficient C_{D_0}, not higher than TBD under clean cruise configuration at Mach 0.8
REQ-OPE-2.2.14	The aircraft wing subsystem shall achieve a cruise lift-to-drag ratio, L/D of at least TBD at Mach 0.8
REQ-OPE-2.2.15	Aircraft shall have a required runway length not larger than 2100m at MTOW under ISA conditions
REQ-OPE-2.3.1	Aircraft shall have a W/S ratio $\leq$ 1875
REQ-OPE-2.3.2	Aircraft shall have a W/P ratio $\leq$ 0.05035
REQ-AIR-1.1.1	Fine and ultra-fine particulate emissions shall be less than those seen in a large city by the year 2050
REQ-AIR-1.1.2	The aircraft shall be compatible with standard airport ground logistics in 2050
REQ-AIR-1.1.3	Aircraft shall not exceed noise levels of 92 dB during landing
REQ-AIR-2.2.1	Aircraft shall be compatible with standard airport gate dimensions
REQ-AIR-2.2.2	Aircraft shall be compatible with standard airport boarding systems
REQ-AIR-2.3.1	Aircraft shall be compatible with standard airport ground power units
REQ-AIR-2.3.2	Aircraft shall be compatible with standard airport refuelling interfaces
REQ-PAS-1.2.1	The aircraft pressurisation system shall maintain a cabin pressure 81.2 kPa, during normal flight operations, up to maximum operating altitude
REQ-PAS-1.2.2	The aircraft shall limit the cabin noise level to a maximum of TBD dB during taxi, take-off, cruise, approach, and landing, measured at seated passenger ear height
REQ-PAS-1.2.3	The passenger cabin shall include seating for 150 passengers and additional crew
REQ-PAS-1.2.4	The aircraft shall provide at least TBD lavatories accessible to passengers during cruise
REQ-PAS-1.2.5	The aircraft shall provide stowage volume for carry-on baggage of at least TBD L per passenger in overhead bins or equivalent certified cabin storage available in 2050
REQ-PAS-1.2.6	The environmental control system shall maintain cabin air temperature between TBD °C and TBD °C during normal ground and flight operations
REQ-PAS-1.2.7	The aircraft shall limit passenger cabin vibration metric to TBD, measured at the seat during taxi, take-off, cruise, approach, and landing
REQ-MAN-1.3.1	The aircraft shall enable modular manufacturing and assembly of major aircraft sections

Continued on next page

ID	Requirement Description
REQ-MAN-1.3.2	The aircraft architecture shall allow configuration variants without redesign of the primary load-bearing structure
REQ-MAN-1.2.1	The manufacturing process shall abide by local labour laws
REQ-MAN-1.1.3	The aircraft shall limit the use of materials classified as scarce, critical, or rare-earth-dependent to TBD% of aircraft operating empty mass

A.4. Subsystem Requirements

Table A.4: Subsystem Requirements

ID	Requirement Description
REQ-AIR-1.1.2.1	The landing gear system shall enable towing, pushback, taxiing, braking and steering during airport operations
REQ-AIR-1.1.2.2	The energy storage system shall allow the aircraft to remain parked for at least 12 h after flight with near empty tanks/batteries
REQ-REG-1.1.5.1	At most 30% of the energy carrier shall be conventional jet fuel no later than 2050
REQ-REG-1.1.5.2	The aircraft shall actively monitor CO_2, NO_x and contrail related emissions during all flight phases with a measurement accuracy of TBD%
REQ-PAS-1.2.3.1	The passenger cabin shall provide each passenger seat with a minimum seat pitch of 76 cm in the nominal 150-passenger layout
REQ-PAS-1.2.3.2	The passenger cabin shall a minimum seat width of 43 cm in the nominal 150-passenger layout
REQ-LG-1.1.4.1	the nose gear shall support at least 8% of the MTOW during ground operations
REQ-LG-2	The nose gear shall support at most 15% of the MTOW during ground operations
REQ-LG-3	The centre of gravity of the aircraft during all ground operations shall be within the plan-form defined by the location of the landing gear
REQ-LG-4	The aircraft shall have a limit tip-over bank angle of at least 10°
REQ-LG-5	The aircraft shall have a scrape-angle of at least 12°
REQ-LG-6	The aircraft cg shall remain in front of the main landing gear in all conditions, including during a pitch angle of 15°
REQ-LG-7	The landing gear subsystem shall not impede the control surface deployment, or the structural integrity of the wing box
REQ-LG-8	The landing gear shall absorb a vertical load for a design touchdown rate of 12 fps (CS 25.723)
REQ-LG-9	The landing gear shall be retractable
REQ-ESS-1	The energy supply and storage system shall have a mass $\leq$ 19795.8
REQ-PRP-1	The propulsion system shall have a mass $\leq$ 9155.8 kg
REQ-AFR-1	The airframe shall have a mass $\leq$ 20957.2 kg
REQ-CBN-1	The cabin interior shall have a mass $\leq$ 20957.2 kg
REQ-AVN-1	The avionics and electrical system shall have a mass $\leq$ 5286.6 kg
REQ-MCH-1	The mechanical systems shall have a mass $\leq$ 3619.3 kg

B. Formulas and Relations

B.1. Torenbeek's Procedure

All formulas listed in this section are only applicable to imperial units (lbs, ft, etc.) [35] [36]

Wing subsystem

$$W_w = 0.0017\, W_{MZF} \left(\frac{b}{\cos\Lambda_{1/2}}\right)^{0.75} \left[1 + \left(\frac{6.3\cos\Lambda_{1/2}}{b}\right)^{1/2}\right] (n_{ult})^{0.55} \left(\frac{bS_w}{t_r W_{MZF}\cos\Lambda_{1/2}}\right)^{0.30} \tag{B.1}$$

- For spoilers and speed brakes, 2% should be added
- If the landing gear is not mounted under the wing, the weight should be reduced by 5%
- If Fowler flaps are used, the weight should be increased by 2%

Empennage subsystem

$$W_v = S_v \left[3.81 \left\{(S_v)^{0.2} V_D/1000 \left(\cos\Lambda_{1/2_v}\right)^{1/2}\right\} - 0.287\right] \tag{B.2}$$

$$\tan\Lambda_n = \tan\Lambda_m - \frac{4}{AR}\left[(n-m)\frac{1-\lambda}{1+\lambda}\right] \tag{B.3}$$

Fuselage subsystem

$$W_f = 0.021\, K_f \left(\frac{V_D l_h}{w_f + h_f}\right)^{1/2} (S_{fgs})^{1.2} \tag{B.4}$$

With constant K_f taking the following values;

- = 1.08 for a pressurised fuselage
- = 1.07 if the main landing gear is attached to the fuselage

If the design is equipped with more than one factor above, the effect is multiplicative.

$$M_{LIFTSUR} = C_1 \left[A^{0.5} S^{1.5} \sec\Lambda_{c/4} \left(\frac{1+2\lambda}{3+3\lambda}\right) \frac{m_{MTO}}{S} n_{ult}^{0.3} \left(\frac{V_D}{t/c}\right)^{0.5}\right]^{0.9} \quad \text{kg} \tag{B.5}$$

Powertrain subsystem

$$W_{pwt} = W_{nac} + W_{fan} + W_{eng}\cdot N_e + W_{apsi} \tag{B.6}$$

$$W_{nac} = 0.065 T_{TO} \tag{B.7}$$

$$T_{TO} = \frac{W_{MTO} \div \frac{W}{P}}{V_{TO}} \tag{B.8}$$

$$W_{fan} = \frac{P_{shaft}}{SP_{fan}} N_e \tag{B.9}$$

$$W_{eng} = W_{fc} + W_{hex} + W_{mot} + W_{cem} \tag{B.10}$$

$$W_{apsi} = 36 N_e (\frac{dW_{LH_2}}{dt})_{TO} \tag{B.11}$$

Landing Gear subsystem

$$W_g = K_{g_r}\left\{A_g + B_g\left(W_{MTO}\right)^{3/4} + C_g W_{MTO} + D_g\left(W_{MTO}\right)^{3/2}\right\} \tag{B.12}$$

Fixed Equipment

$$W_{feq} = W_{fco} + W_{els} + W_{iae} + W_{api} + W_{ox} + W_{fur} + W_{bc} + W_{paint} + W_{misc} \tag{B.13}$$

$$W_{fco} = 0.64\left(W_{MTO}\right)^{2/3} \times \begin{cases} 1.2 & \text{if leading edge devices are employed} \\ 1.15 & \text{if lift dumpers are employed} \end{cases} \tag{B.14}$$

$$W_{iae} = 0.575\left(W_{OEW}\right)^{0.556}\left(R_{ferry}\right)^{0.25} \quad \text{(B.18)}$$

$$W_{els} = 10.8\left(V_{pax}\right)^{0.7}\left\{1 - 0.018\left(V_{pax}\right)^{0.35}\right\} \quad \text{(B.15)}$$

$$W_{ox} = 30 + 1.2N_{pax} \quad \text{(B.19)}$$

$$W_{api} = 6.75\left(l_{pax}\right)^{1.28} \quad \text{(B.16)}$$

$$W_{fur} = 0.211\left(W_{MTO} - W_{LH_2}\right)^{0.91} \quad \text{(B.17)}$$

$$W_{paint} = \rho_{paint,areal} \times S_{wet} \quad \text{(B.20)}$$

B.2. Performance Analysis

[38]

Performance Diagram

$$V = \sqrt{\frac{2W}{\rho S C_L}} \quad \text{(B.21)}$$

$$C_D = C_{D_0} + \frac{C_L^2}{\pi A R e} \quad \text{(B.24)}$$

$$D = \frac{C_D}{C_L}W \quad \text{(B.22)}$$

$$C_L = \sqrt{\frac{C_{D_0}}{\pi A R e}} \quad \text{(B.23)}$$

$$C_L = \sqrt{\frac{3C_{D_0}}{\pi A R e}} \quad \text{(B.25)}$$

Climb Ceilings and Effect of Altitude

$$ROC = \frac{P_a - P_r}{MTOW} \quad \text{(B.26)}$$

$$P_a = P_{a_{SL}}\left(\frac{\rho}{\rho_{SL}}\right)^n \quad \text{(B.27)}$$

Time to Climb

$$t_{cl} = \int_0^{H_{cr}} \frac{dH}{ROC_{max}} \quad \text{(B.28)}$$

B.3. Longitudinal stability

All formulas listed in this section are used for the longitudinal stability analysis.

Moment equilibrium

$$M_{res} = \frac{1}{2}\rho V_{cr}^2 S_{ref} C_m \bar{c}_{ref} = L_f(X_{cg} - X_f) + L_w(X_{cg} - X_w) + L_r(X_{cg} - X_r) + M_{ac,f} + M_{ac,w} - F_t(Z_e) = 0 \quad \text{(B.29)}$$

Pitching moment coefficient and pitch slope

$$\begin{aligned} C_m = {} & C_{Lf_\alpha} \cdot (\alpha - \alpha_{0,f}) \cdot \frac{S_f}{S_{ref}}\left(\frac{X_{cg} - X_f}{\bar{c}_{ref}}\right) + (C_{Lw_\alpha} \cdot (\alpha - \alpha_{0,w}) + C_{Lw,\delta} \cdot \delta_e)\frac{S_w}{S_{ref}}\left(\frac{X_{cg} - X_w}{\bar{c}_{ref}}\right) \\ & + \left(C_{Lr_\alpha}\left(\alpha \cdot (1 - \frac{d\epsilon}{d\alpha}) - \alpha_{0,r} + \alpha_i\right) + C_{Lr_\delta} \cdot \delta_r\right)\frac{S_r \cos^2\phi}{S_{ref}}\left(\frac{X_{cg} - X_r}{\bar{c}_{ref}}\right)\left(\frac{V_r}{V_{cr}}\right)^2 \\ & + \frac{S_f}{S_{ref}} C_{mac,f}\frac{\bar{c}_f}{\bar{c}_{ref}} + \frac{S_w}{S_{ref}} C_{mac,w}\frac{\bar{c}_w}{\bar{c}_{ref}} = 0 \end{aligned} \quad \text{(B.30)}$$

$$\begin{aligned} \frac{dC_m}{d\alpha} = {} & C_{Lf_\alpha}\frac{S_f}{S_{ref}}\left(\frac{X_{cg} - X_f}{\bar{c}_{ref}}\right) + C_{Lw_\alpha}\frac{S_w}{S_{ref}}\left(\frac{X_{cg} - X_w}{\bar{c}_{ref}}\right) \\ & + C_{Lr_\alpha}\frac{S_r \cos^2\Gamma_{tail}}{S_{ref}}(1 - \frac{d\epsilon}{d\alpha})\left(\frac{X_{cg} - X_r}{\bar{c}_{ref}}\right)\left(\frac{V_r}{V_{cr}}\right)^2 \end{aligned} \quad \text{(B.31)}$$

Center of gravity and Neutral point

$$X_{cg} = \frac{\sum_{i=1}^{n} M_i \cdot X_{cg,i}}{\sum_{i=1}^{n} M_i} = \frac{\sum_{i=1}^{n-1} M_i \cdot X_{cg,i} + M_{wing} \cdot X_{cg,wing}}{\sum_{i=1}^{n} M_i} \tag{B.32}$$

$$X_{cg,wing} = 0.4 \cdot \bar{c}_w + X_{LEMAC} \tag{B.33}$$

$$X_{np} = \frac{C_{L\alpha,f}\left(\frac{S_f}{S_{\text{ref}}}\right) X_{\text{ac},f} + C_{L\alpha,w}\left(\frac{S_w}{S_{\text{ref}}}\right) X_{\text{ac},w} + C_{L\alpha,r}\left(\frac{S_r \cos^2 \Gamma_{tail}}{S_{\text{ref}}}\right)\left(1 - \frac{d\varepsilon}{d\alpha}\right) X_r \left(\frac{V_r}{V_{cr}}\right)^2}{C_{L\alpha,f}\left(\frac{S_f}{S_{\text{ref}}}\right) + C_{L\alpha,w}\left(\frac{S_w}{S_{\text{ref}}}\right) + C_{L\alpha,r}\left(\frac{S_r \cos^2 \Gamma_{tail}}{S_{\text{ref}}}\right)\left(1 - \frac{d\varepsilon}{d\alpha}\right)\left(\frac{V_r}{V_{cr}}\right)^2}. \tag{B.34}$$

Ruddervator deflection

$$\begin{aligned}\delta_r = -\frac{1}{\frac{S_r \cos^2 \Gamma_{tail}}{S_{ref}} C_{Lr,\delta}\left(\frac{X_{cg} - X_r}{\bar{c}_{ref}}\right)\left(\frac{V_r}{V_{cr}}\right)^2} \Bigg[& C_{Lf_\alpha}(\alpha - \alpha_{0,f}) \frac{S_f}{S_{ref}} \left(\frac{X_{cg} - X_{ac,f}}{\bar{c}_{ref}}\right) \\ & + \left(C_{Lw_\alpha}(\alpha - \alpha_{0,w}) + C_{Lw,\delta}\delta_e\right) \frac{S_w}{S_{ref}} \left(\frac{X_{cg} - X_{ac,w}}{\bar{c}_{ref}}\right) \\ & + \frac{S_f}{S_{ref}} C_{mac,f} \frac{\bar{c}_f}{\bar{c}_{ref}} + \frac{S_w}{S_{ref}} C_{mac,w} \frac{\bar{c}_w}{\bar{c}_{ref}} \\ & + \frac{S_r \cos^2 \Gamma_{tail}}{S_{ref}} C_{Lr_\alpha}\left(\alpha\left(1 - \frac{d\epsilon}{d\alpha}\right) - \alpha_{0,r} + \alpha_i\right)\left(\frac{X_{cg} - X_r}{\bar{c}_{ref}}\right)\left(\frac{V_r}{V_{cr}}\right)^2 \Bigg].\end{aligned} \tag{B.35}$$